TECHNICAL UNIVERSITY OF MUNICH

TUM SCHOOL OF COMPUTATION, INFORMATION AND TECHNOLOGY

Near-Field Measurement and Transformation of Modulated Electromagnetic Fields using Uncrewed Aerial Vehicles

Fabian Tobias Faul

Vollständiger Abdruck der von der TUM School of Computation, Information and Technology der Technischen Universität München zur Erlangung des akademischen Grades eines

Doktors der Ingenieurwissenschaften

genehmigten Dissertation.

Vorsitz:		Prof. Dr.-Ing. habil. Dr. h.c. Alexander W. Koch
Prüfer der Dissertation:	1.	Prof. Dr.-Ing. Thomas Eibert
	2.	Prof. Dr. Frank Gronwald

Die Dissertation wurde am 18.03.2024 bei der Technischen Universität München eingereicht und durch die TUM School of Computation, Information and Technology am 10.09.2024 angenommen.

Abstract

The determination of the far-field (FF) radiation pattern of an antenna from measurements of its near-field (NF) is a common task in the field of antenna characterization and validation. In this context, NF measurements performed on-site are of great interest, as they are able to significantly extend the capabilities of traditional antenna characterization where measurements in anechoic chambers are comparatively inflexible. Such on-site or in-situ measurements benefit from the development and availability of uncrewed aerial vehicles (UAVs) as they can reach almost any position without further restriction. Most UAV-based NF measurements in the literature use a magnitude-only measurement approach which simplifies the measurement setup but requires a phaseless NF to FF transformation (NFFFT) to reveal the FF radiation pattern in the post-processing. However, phaseless NFFFT algorithms are neither reliable yet, nor do they achieve accuracy levels comparable to those obtained with complex field values. The idea of coherent UAV-based NF measurements, i.e., the magnitude and phase of the electromagnetic field are recorded, has been around for some time but was never realized and tested. Coherent UAV-based measurements allow for the employment of advanced time-harmonic NFFFTs which have a high accuracy and offer additional features like the consideration of scattering objects or a conductive ground. Therefore, as part of this work, a fully coherent UAV-based NF measurement setup has been built up using consumer electronic components for the UAV. The setup is described in detail where planar and cylindrical field measurements are presented. Here, it has been shown for the first time that a reasonable error level of -30 dB can be achieved in in-situ NF measurements while maintaining the flexibility of a UAV-based setup. Nevertheless, there are potential error sources in the measurement setup, especially due to the addition and replacement of components in comparison to traditional NF measurements in anechoic chambers. Accordingly, an extensive error analysis is given with a focus on the differences of the UAV-based setup in comparison to traditional NF measurement setups. Within this analysis, measurements and simulations have been performed to reveal the impact of the single components on the measured NF which is the foundation of any future improvement.

The second part of this thesis is dedicated to the measurement of modulated field signals. This problem arises, e.g., when it comes to the measurement of mounted antennas in their real operating environment or large reflector antennas that cannot be characterized by traditional methods due to their size. For some of these situations it might not be possible, or sometimes even not desired, to feed the antenna under test (AUT) with a test signal. Measuring antennas during their normal operation state means that there is also a need to process modulated field signals while, at the same time, it is beneficial to use the sophisticated time-harmonic NFFFT algorithms to obtain the FF radiation pattern. Therefore, two approaches for the measurement and transformation of continuously modulated fields are discussed and characterized that allow for the usage of time-harmonic NFFFTs. In the discussion it becomes clear that a measurement approach with a measurement time that is much shorter than the modulation period of the antenna operating signal is most suitable for field measurements with UAVs. Accordingly, this approach is further investigated where its feasibility is demonstrated by numerical simulations and measurements in a controlled environment. In addition, the limitations of the measurement approach are shown from which guidelines for its practical usage are drawn. Eventually, the two parts of this thesis, namely coherent

UAV-based NF measurements and the measurement of modulated fields, are ultimately combined in the discussion of UAV-based NF measurements of an air navigation system. Here, a measurement system was set up and tested while initial test measurements confirm that the chosen measurement approach is principally suitable for the characterization of such air navigation systems.

Kurzfassung

Die Bestimmung der Fernfeld (FF)-Strahlungseigenschaften einer Antenne aus Messdaten, die im Nahfeld (NF) gewonnen werden, ist eine übliche Aufgabenstellung in Bezug auf die Charakterisierung und Validierung von Antennen. Hierbei sind NF-Messungen, die am Einsatzort der Antenne durchgeführt werden, von großem Interesse, da sie die Möglichkeiten der traditionellen Antennencharakterisierung erheblich erweitern indem auch Einflussfaktoren der Umgebung berücksichtigt werden können, während Messungen in reflexionsarmen Messkammern vergleichsweise unflexibel sind. Solche Messungen vor Ort profitieren von der Entwicklung und Verfügbarkeit unbemannter Luftfahrzeuge (UAVs), da diese fast jede Position ohne nennenswerte Einschränkungen erreichen können. Die meisten in der Literatur dargestellten UAV-basierten NF-Messungen verwenden einen phasenlosen Messansatz, der den Messaufbau zwar vereinfacht, gleichzeitig aber eine phasenlose NF-FF-Transformation (NFFFT) erfordert um das FF-Strahlungsdiagramm im Nachgang zu berechnen. Die phasenlosen NFFFT-Algorithmen sind bisher jedoch weder zuverlässig noch erreichen sie die Genauigkeit, die sich mit ihren kohärenten Gegenstücken erreichen lässt. Die Idee kohärenter UAV-basierter Feldmessungen, bei denen Betrag und Phase des elektromagnetischen Feldes aufgezeichnet werden, gibt es schon seit einiger Zeit, wobei entsprechende Ansätze bisher nicht realisiert wurden. Kohärente UAV-basierte NF-Messungen ermöglichen den Einsatz fortschrittlicher zeitharmonischer NFFFTs, die eine hohe Genauigkeit aufweisen und zusätzliche Funktionen wie die Berücksichtigung von streuenden Objekten oder eines leitenden Bodens bieten. Daher widmet sich der erste Teil dieser Arbeit der Beschreibung eines vollständig kohärenten UAV-basierten Messaufbaus, der für planare und zylindrische Messungen verwendet wurde, die ebenfalls beschrieben werden. Hierbei wird gezeigt, dass ein akzeptables Fehlerniveau von $-30\,\mathrm{dB}$ auch in in-situ-Messungen erreicht werden kann, während die Flexibilität des UAV-basierten Messaufbaus gewahrt bleibt. Dennoch gibt es potentielle Fehlerquellen im Messaufbau, die insbesondere durch das Hinzufügen und Austauschen von Komponenten im Vergleich zu traditionellen NF-Messaufbauten in reflexionsarmen Kammern entstehen. Entsprechend wird eine Fehleranalyse vorgestellt, die sich vor allem auf die Unterschiede zwischen einem NF-Messsystem mittels UAV und solchen in reflexionsarmen Räumen konzentriert. Im Rahmen der Analyse wurde durch Messungen und Simulationen der Einfluss der einzelnen Komponenten auf die gemessenen NF-Daten ermittelt, was die Grundlage für zukünftige Weiterentwicklungen des Messsystems darstellt.

Der zweite Teil dieser Arbeit befasst sich mit der Messung von modulierten Feldsignalen. Dieses Problem stellt sich beispielsweise bei der Messung von Antennen in ihrer realen Betriebsumgebung oder von großen Reflektorantennen, die aufgrund ihrer Größe nicht in reflexionsarme Räume gebracht und mit herkömmlichen NF-Messsystemen charakterisiert werden können. Darüberhinaus ist es in manchen Situationen nicht möglich oder nicht erwünscht die zu prüfende Antenne mit einem Testsignal zu speisen. Die Messung von Antennen in ihrem normalen Betriebszustand bedeutet, dass auch modulierte Signale verarbeitet werden müssen, während es gleichzeitig von Vorteil ist die hochentwickelten zeitharmonischen NFFFT-Algorithmen zu verwenden. Entsprechend werden im zweiten Teil dieser Arbeit zwei Ansätze zur Messung und Transformation von kontinuierlich modulierten Feldern diskutiert, die zusammen mit zeitharmonischen NFFFTs verwendet werden können. In der Diskussi-

on zeigt sich deutlich, dass ein Messansatz mit einer Messzeit die kürzer ist als die Modulationsdauer des Antennenbetriebssignals für Feldmessungen mit UAVs am besten geeignet ist. Entsprechend wird ein solcher Ansatz weiter untersucht, wobei Messungen in einer kontrollierten Umgebung die Anwendbarkeit des Messverfahrens zeigen. Weiterhin wurde der Ansatz mit Hilfe numerischer Simulationen kritisch auf seine Grenzen hin untersucht und es wurden Richtlinien für die praktische Anwendung des Messverfahrens abgeleitet. Die beiden großen Themenkomplexe dieser Arbeit, nämlich die kohärente NF-Messung mithilfe von UAVs und die Messung modulierter Felder, werden letztlich in der Diskussion von UAV-basierten NF Messungen an einem Flugnavigationssystem kombiniert. Hierzu wurde ein geeignetes Messsystem aufgebaut und getestet, wobei erste Testmessungen zeigen, dass der gewählte Messansatz grundsätzlich für die Charakterisierung von Flugnavigationssystemen geeignet ist.

Preface and Acknowledgment

"If I find 10,000 ways something won't work, I haven't failed. I am not discouraged, because every wrong attempt discarded is another step forward."
— Thomas A. Edison

Talking about 10 000 ways in which something does not work sounds to me like a perfect description of how UAV-based field measurements are realized. Even though the principle is simple, there are several things that can go wrong - and they will go wrong - ranging from faulty cables to drone crashes, where, fortunately, the latter happened just once. Therefore, I am grateful to complete this work with successful coherent UAV-based near-field measurements. It is the result of hundreds of UAV flight hours, numerous measurements and extensive field transformations and, overall, a good summary of the work I did during my time at the Chair of High-Frequency Engineering at the Technical University of Munich.

I would like to thank Prof. Dr. Thomas Eibert for giving me the opportunity to carry out this work. At the beginning, it was by far not clear what we could achieve and where this would lead to. I am all the more grateful for his unwavering support and advice throughout the years. A very special "thank you" goes to Thomas Mittereder, who helped me with the realization of every measurement setup, who accompanied me during most of the measurements and who remained patient and supportive, even if I only needed to perform this one last measurement, which made us come home late in the evening. Moreover, I would like to thank my former colleagues at the Chair of High-Frequency Engineering for all the fruitful discussions and many rounds of table football. My thanks go to Arslan Azhar, Dr. Bernd Hofmann, Dr. Safiullah Khan, Dr. Josef Knapp, Dr. Jonas Kornprobst, Dr. Ole Neitz, Dr. Alexander Paulus, Dr. Uwe Siart and Jonas Weindl, among others. In addition to my colleagues, I would also like to thank the students who contributed to this work. Florian Muhr investigated the mutual coupling between the field probe antenna and the UAV itself, Jana Daubmeier investigated the errors that occur when dealing with modulated fields, while Daniel Korthauer was of great help in making the UAV hardware more solid and performing various measurements in the anechoic chamber.

Last but not least, I would like to thank my parents and my family for encouraging me along the way and for always supporting me, no matter what I do. The biggest thanks go to my wife Deborah, who has been with me throughout this whole journey and who often took daily tasks off my shoulders such that I could focus on my work.

I don't want to finish without saying a few words about music. Music always played a special role in my life and it was also listening to music that kept me in a good mood during long programming sessions and difficult hardware troubleshooting. Therefore, I would like to posthumously thank Ludwig van Beethoven for his symphonies and especially the baroque composers Claudio Monteverdi, Johann Kuhnau, Heinrich Ignaz Franz Biber and Johann Sebastian Bach for their great cantatas, chorales and masses.

Munich, Germany
December 2024

Fabian Faul

Contents

Part I

Prelude

Chapter 1

Introduction

The antenna is one of the most important and, at the same time, one of the most critical components of a wireless communication system. It is the component which is employed to transmit or receive electromagnetic waves, where a carefully designed antenna can enhance the overall performance of a wireless system considerably.

1.1 Historical Background

The foundations for the theory of antennas and electromagnetic waves in general have been given in 1864 by James Clerk Maxwell when he published a set of equations that unified the theories of electricity and magnetism, nowadays known as *Maxwell's Equations*. However, it took another decade until Heinrich Rudolph Hertz presented an apparatus that proved Maxwell's theory as it produced sparks at the center gap of a dipole which could be detected in the gap of a nearby but separate electric loop [Kraus 1985]. Still, the technology remained mainly experimental until Guglielmo Marconi announced the first successful transatlantic wireless transmission of a message in 1901 and commercialized the communication using radio waves in the following years [Brittain 2004]. While Marconi used wires attached to kites and masts for his experiments, World War II ushered in a new era of antennas in which reflector and horn antennas were widely used. At the same time, the invention of new microwave sources, such as the klystron and magnetron, enabled the usage of higher frequencies [Balanis 1992]. Starting in the 1960's, the development and design of antennas was accompanied by numerical simulations to predict and analyze the behavior of an antenna structure. However, the testing and verification of a realized antenna is still an important and, in certain cases, demanding task.

The parameters of an antenna under test (AUT) are ideally determined when the antenna is illuminated by plane waves which is due to the definition of the antenna parameters. The simplest practical method to create a plane wave is with the help of a second antenna which is placed far away from the AUT since the curvature in the far field (FF) of any antenna can be accepted to be locally planar. Such FF measurements are the oldest and most direct method of antenna characterization, where the antenna parameters are revealed instantly during the measurement. By rotating the AUT, a second static antenna, the field probe, can be used to determine the full radiation pattern while both antennas can be in either transmit or receive mode since the antenna parameters and operation are reciprocal. However, reaching the FF condition of an antenna can easily require a distance of several tens or hundreds of meters, depending on the antenna size and the measurement frequency. Thus, FF ranges are usually large open spaces which cause other drawbacks as the environment will have an impact on the measurement results, e.g., external noise will interfere with the measurement signal or reflections from the ground will alter the measured field value. Hence, there have been several approaches to treat the single disturbances, like elevated ranges, slanted

ranges or reflection ranges as well as measurements in shielded chambers [Qureshi 2013a]. In the 1960's, the compact antenna test range (CATR) was invented at the Georgia Institute of Technology which is a quasi-FF measurement system [Joy 1988]. It allows the characterization of antennas at frequencies where the FF distance with respect to the AUT cannot be reached as large distances would be required. Within the CATR, the radiated waves of a source antenna are collimated by one or more reflectors in such a way that a locally plane wavefront illuminates the AUT. Therefore, the CATR combines all the advantages of FF measurements, but without the requirement of large distances, together with the benefits of an indoor measurement system that can be fully isolated from the environment in terms of weather conditions and external noise. Almost contemporaneous to the development of the CATR, antenna measurements in the near field (NF) of the AUT have been explored. In 1960, researchers from Scientific-Atlanta presented a comparison of an antenna FF pattern obtained from FF measurements in comparison to NF measurements on a planar surface from which the FF was calculated in the post-processing with the help of a Fourier transform. In the following decades, NF measurements have been further developed and improved and are nowadays an established technology. NF measurements of antennas are commonly performed in non-reflecting or anechoic chambers which are shielded from the outer environment and provide an acceptable approximation of free space. These conditions allow the development of very precise NF measurement techniques since external effects and reflections can be almost fully dismissed with the help of absorbers. However, measurements carried out in the NF do not deliver the antenna parameters in real-time since an additional post-processing step is required to calculate the FF radiation pattern of the AUT. This calculation is known as the near-field to far-field transformation (NFFFT) and is still, over 60 years later, an active field of research. Even if first NF measurements of antennas have been carried out in the 1960's, the technology gained considerable interest in the last decades as computing power became cheaper and is now easier accessible.

Considering the advantages and disadvantages of the different methods for antenna characterization, still all of the mentioned measurement setups are used as they are all useful depending on the situation and frequency range of interest. NF measurements are usually employed for higher frequencies whereas outdoor FF ranges are almost only applicable for the measurement of low frequencies due to the sensitivity to weather conditions and, primarily, also since very large chambers would be needed in this case. In general, antenna measurements have become more important over the years as the accurate knowledge about the radiation behavior of an antenna is becoming more important to improve the performance of wireless sensors or communication systems. As pointed out by Balanis [1992], "antenna design may have been considered a secondary issue in overall system design" in former times while it plays a decisive role nowadays. A good knowledge of the antenna behavior is especially important when it comes to antenna arrays and beam shaping which are largely used in recent communication standards.

1.2 In-situ Measurements

NF and FF ranges have in common that they are set up at some specific location while the AUT is brought to the measurement system. This means that large or immobile antennas cannot be measured, which is especially true for NF ranges as the size of the anechoic chamber ultimately limits the size of the AUT. Anechoic chambers provide an echo-free environment and are a defined and acceptable approximation of free space. However, measuring the performance of an antenna under near-ideal conditions can distort the actual parameters, as the operating environment of the antenna may have a severe impact on the antenna performance due to mounting structures or nearby scatterers. This is why a considerable interest for the realization of in-situ, also called on-site, measurements has come up over the years. There have been many approaches which tackle different problems of conventional NF or FF ranges. The measurement of large reflector antennas with diameters of about 2 m to 20 m, for example, is complicated regarding the given measurement ranges. The size of the anechoic chamber of an NF range is often too

small, while FF ranges are not applicable for measurements with high accuracy due to ground reflections and external noise. Additionally, the dynamic range of FF setups is limited, especially for higher frequencies. To cope with this, Steiner et al. built and presented a cylindrical outdoor NF range in 1993 [Steiner and Fritzel 1993; Steiner et al. 1994]. It consisted of a 36 m high diamond-shaped scanner tower made of concrete and an azimuth positioner turntable which was specified for AUT diameters of 20 m while the whole system had an operational frequency range of 1 GHz to 20 GHz. The measurement setup included an auto alignment system of the AUT and probe antenna to ensure an almost cylindrical scan plane. The shape of the scan plane is a constraint of NFFFTs that are based on the fast Fourier transform (FFT) as a perfect planar or cylindrical measurement surface is assumed by the algorithms. With the development of NFFFT algorithms which are based on equivalent sources or currents, the measurement and transformation of the field on arbitrary surfaces becomes possible. This development paves the way for real mobile in-situ NF measurement setups. In the past, there have been many approaches for the realization of such mobile field measurement setups. One of the simplest approaches is a transportable planar scanner which can be brought to the AUT [Eibert et al. 2013]. Similar, but even simpler, is a free-hand setup where the probing antenna is moved in the NF of the AUT by an operator. However, the accuracy of these setups is limited due to the lack of probe orientation data in Faul et al. [2020] or due to a magnitude-only measurement setup in Álvarez-Narciandi et al. [2021]. Still, the advantage of such free-hand measurement systems is the narrow space usage and especially the mobility. Despite delivering measurement results with high accuracy, these systems may be useful for quick tests of the functionality of antennas, e.g., an operational check of the antennas of a satellite after transportation or the detection of pattern changes of mobile base stations after maintenance. A more sophisticated realization of in-situ measurements uses an overhead crane as described by Steiner et al. [2015] and Geise et al. [2019]. The crane moves a portable measurement gondola along a predefined measurement surface while its actual position is determined by a laser tracking system. The gondola itself contains the field probing antenna and some radio frequency (RF) equipment. It has an overall size of about 1 m and can be tilted and rotated in azimuth and elevation, which allows the measurement on planar, cylindrical and spherical surfaces. However, the flexibility of the overall measurement system is limited since the knowledge of the crane-gondola transfer function, i.e., the behavior of the gondola with respect to the crane control signal, is necessary to plan a scan trajectory. This allows only the usage of very specific cranes or causes an excessive overhead to measure the behavior of the crane and the gondola. Still, all of the presented measurement setups fail, or at least require excessive expenses, when it comes to the in-situ characterization of large antennas, like, e.g., reflectors for space observation or antenna systems as found in air navigation. The idea to employ aircrafts for such antenna characterizations has been around for a long time. First measurements were made in 1963, when a battery-powered transmitter together with a dipole antenna was towed by an aircraft, which in turn orbited the AUT [Barnes 1963]. The field received by the AUT was measured on the ground while the azimuth and elevation angles of the aircraft were recorded by an operator using an optical device. Since such aircraft-based measurements require significant effort, it was not until the introduction of uncrewed aerial vehicles (UAVs) that the field of in-situ measurements gained considerable interest. UAVs enable new possibilities due to their mobility and flexibility, while the costs are significantly lower than for fixed measurement setups. Furthermore, there is no need to rotate the AUT in UAV-based measurements, as the UAV is able to reach almost any position without further restrictions and, therefore, the field can be theoretically measured on any surface around the AUT. Since Fritzel et al. [2002] proposed in-situ measurements with UAVs in 2002, several different realizations of UAV-based antenna measurements for different frequency ranges have been published.

In general, most field measurement setups can be divided into two subsystems: the positioning part and the RF subsystem. These two system parts and their interaction become more obvious in UAV-based field measurements, as shown by the diagram in Fig. 1.1. The positioning subsystem includes the UAV and all other measurement equipment and sensors to determine the position and orientation of the field

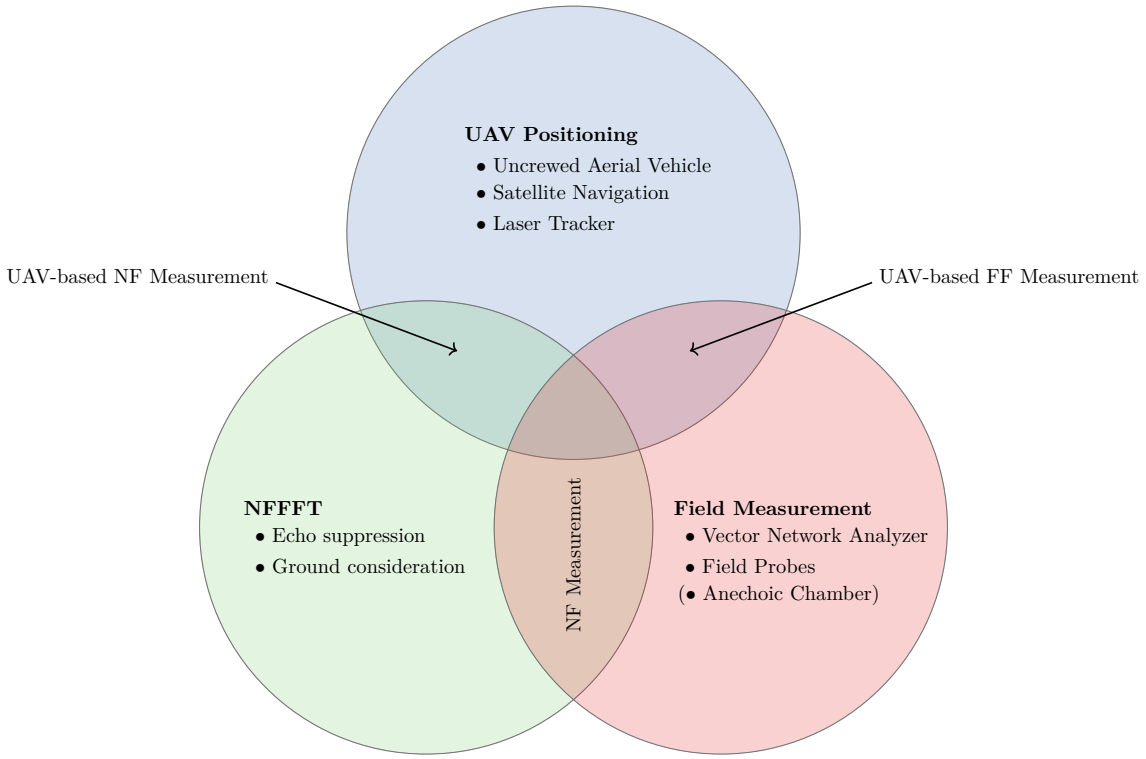

Figure 1.1: Different parts of a UAV-based field measurement system. The positioning (blue, top) includes the UAV and position measurement systems. The RF part (red, right) comprises all RF equipment that is necessary to measure an electromagnetic field. The NFFFT (green, left) extends the capabilities of the measurement as echo suppression and ground consideration becomes possible.

probe. The RF subsystem, in contrast, includes all parts related to the field measurement, such as cables, antennas and the measurement receiver itself. The combination of the UAV-based positioning with a field measurement system allows to measure the field magnitude in the FF, such as in FF ranges. Furthermore, if an NFFFT is added to this measurement system, UAV-based NF measurements can be performed which, however, require a higher precision for the determination of position and orientation of the field probe in comparison to FF measurements. Still, the benefit of NF measurements or, more precisely, of the usage of advanced NFFFT, is that the non-ideal environment of UAV-based field measurements can be taken into account as the suppression of scatterers and the consideration of the ground becomes possible.

During the last years, UAV-based field measurements have been presented for various frequency ranges [Virone et al. 2014; Chang et al. 2015; Paonessa et al. 2016; García-Fernández et al. 2017; Bolli et al. 2018; García-Fernández et al. 2018b, 2019a,b; Culotta-López et al. 2021]. While most of these measurements have been performed in a single-frequency manner for antenna characterization, UAV-based field measurement systems for specific applications have also been presented, like, e.g., the measurement of the coverage of cellular networks [Teng et al. 2015]. Other applications concern the verification of air navigation signals in space and the detection of possible interference [Schrader et al. 2016, 2019; Sommer et al. 2020]. Further, there are related applications which, e.g., employ UAVs to detect objects under the surface with the help of ground penetrating radar [Engel et al. 2021; García-Fernández et al. 2021]. All mentioned realizations of UAV-based measurement systems are implemented in a phaseless magnitude-only manner with limited accuracy. Coherent UAV-based NF measurements, however, can improve the accuracy of in-situ antenna characterizations. This has been demonstrated in coherent but

single-frequency UAV-based NF measurements that are discussed in this work. Furthermore, coherent measurements can open new opportunities in the field of antenna diagnostics, which is exemplary discussed in measurements where the AUT was fed with a modulation signal.

1.3 Scope and Outline of this Thesis

This thesis focuses on coherent UAV-based NF measurements, i.e., NF measurements including magnitude and phase of the field. However, before discussing the specialties of UAV-based NF measurements, some theoretical background is recapitulated. The most important characteristics of antennas are reviewed in Chapter 2, before the basics of NF antenna measurement systems are described. Furthermore, Chapter 3 recalls the fundamentals of UAVs. After the introductory theoretical background in the first part of this thesis, the second part deals with UAV-based measurements themselves. First, a UAV-based NF measurement setup is presented alongside its components in Chapter 4. The clear benefit of the presented setup is the applicability of well-known NFFFT algorithms such as those used for NF measurements in anechoic chambers, since the complex field values are available. Results of measurements using the described setup are discussed in Chapter 5. Here, a comparison of measurements on a planar and a cylindrical measurement geometry is given. Several components are replaced or newly introduced in the presented UAV-based measurement setup in comparison to traditional NF measurements in anechoic chambers. This inevitably introduces new error sources and uncertainties into the measurement system that need to be understood and characterized to allow for an educated improvement of the overall system performance. Therefore, an analysis of the most important sources for errors and uncertainties within the given UAV-based measurement setup is discussed in Chapter 6. The third part of the thesis deals with another problem that comes alongside in-situ NF measurements. Since in-situ or UAV-based field measurements are aimed to be performed at the place where the AUT is regularly installed, the need to tackle modulated field signals arises. Up to this point in the thesis, only single-frequency field measurements are discussed. Therefore, approaches for the measurement and transformation of modulated fields using a time-harmonic NFFFT are examined in Chapter 7. Here, especially the applicability of one approach is demonstrated by simulations and measurements, while also its limitations and constraints are investigated. Finally, in Chapter 8, UAV-based NF measurements are brought together with the methods for the measurement of modulated fields regarding the verification of an air navigation system, the VHF Omnidirectional Radio Range (VOR). In this chapter, a concept for the NF measurement of the Doppler VHF Omnidirectional Radio Range (DVOR) is presented while simulations show its applicability. First measurements are described while the gained results support the measurement approach. In the end, in Chapter 9 an overall conclusion is drawn together with a suggestion for future research and open points in the field of UAV-based field measurements.

Chapter 2

Traditional Near-Field Measurements

The purpose of antenna measurements is the characterization of the electromagnetic radiation behavior of an AUT. This is usually done through the determination of specific properties, e.g., the radiation pattern of an antenna which is one of the most important characteristics of any antenna. Beside the direct measurement of the radiation in the FF and other more complex measurement setups, like the CATR, NF measurements are nowadays a well-established approach for the characterization of antennas. NF measurements are commonly performed in anechoic chambers which provide an acceptable approximation of free space. Within NF antenna measurements, the electromagnetic field is measured in the vicinity of the AUT from which the FF is calculated in a subsequent post-processing step. For this, an NFFFT is employed which can be of various implementations. However, technically, the NFFFT is not part of the NF measurement itself but a necessary post-processing step to reveal the FF. Both parts, the actual measurement of the NF as well as the NFFFT, are described in this chapter after the recapitulation of some antenna basics. There are a variety of books and other publications available in the literature that deal with NF antenna measurements and NFFFTs. Among others, this chapter is based on Slater [1991], Parini et al. [2020a] and Parini et al. [2020b].

2.1 Antenna Characteristics

There are numerous definitions given in the literature of what an antenna exactly is. The *IEEE Standard Definitions of Terms for Antennas* [IEEE 1969] describes an antenna as "a means for radiating or receiving radio waves". In other words, an antenna is a component or transducer which realizes the transition of an unguided electromagnetic wave, e.g., a wave propagating in free space, and a guided wave in a waveguide structure, e.g., a transmission line. There are numerous types of antennas, ranging from simple wire antennas to well-designed parabolic reflectors. In general, the behavior of antennas is reciprocal, i.e., their key properties are similar in transmit and receive mode. Even if this does not seem to be true for active antennas or antenna arrays, it applies, strictly speaking, also in this case since the isolated radiating structure is still reciprocal and only the feed network is controlled to change the power fed to the actual radiator.

2.1.1 Radiation Pattern, Directivity and Gain

The radiation pattern is one of the most important characteristics of any antenna. It describes the spatial variation of the field or power density around the antenna and is given in a mathematical or graphical form. In most cases, the radiation pattern is determined for the FF while spherical coordinates are commonly used. Figure 2.1 shows an example of a radiation pattern in spherical coordinates where,

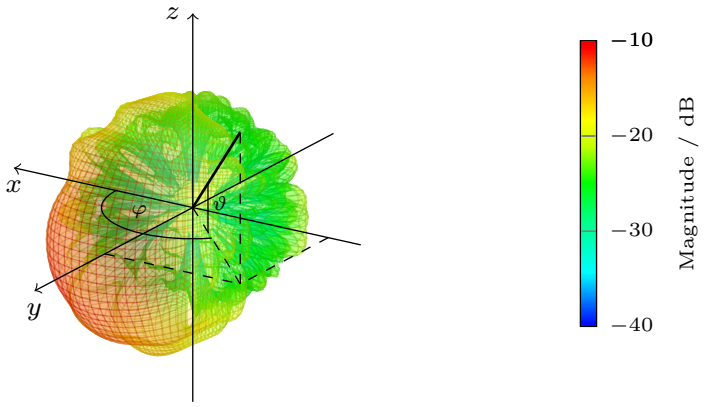

Figure 2.1: Exemplary FF radiation pattern of the electrical field E_ϑ of an antenna in spherical coordinates dependent on elevation ϑ and azimuth φ. The radiation pattern varies with increasing distance to the antenna.

e.g., the point $\boldsymbol{p}$ can be described as (r, ϑ, φ). The FF of an antenna is approximated for $r \to \infty$ where the radiated electromagnetic wave is assumed to be a locally plane wave. This implies that there is no field component in propagation direction in the FF, i.e., $\boldsymbol{E_r} = 0$ and $\boldsymbol{H_r} = 0$, while the transversal components of the electric and magnetic fields are orthogonal. The electric and magnetic fields, $\boldsymbol{E}$ and $\boldsymbol{H}$, at point $\boldsymbol{p}$ can be described as

$$\boldsymbol{E}(\vartheta, \varphi) = E_\vartheta(\vartheta, \varphi)\hat{\boldsymbol{u}}_\vartheta + E_\varphi(\vartheta, \varphi)\hat{\boldsymbol{u}}_\varphi\,, \tag{2.1}$$

$$\boldsymbol{H}(\vartheta, \varphi) = H_\vartheta(\vartheta, \varphi)\hat{\boldsymbol{u}}_\vartheta + H_\varphi(\vartheta, \varphi)\hat{\boldsymbol{u}}_\varphi\,, \tag{2.2}$$

where $\hat{\boldsymbol{u}}_\vartheta$ and $\hat{\boldsymbol{u}}_\varphi$ are the unit vectors in ϑ- and φ-directions.

A measure for the electromagnetic radiation in a certain direction is the directivity $D(\vartheta, \varphi)$ of an antenna. According to the *IEEE Standard for Definitions of Terms for Antennas* [IEEE 2014], the directivity describes the ratio between the power density $\boldsymbol{S}(\vartheta, \varphi)$ radiated in a certain angular direction to the total power P_{rad} radiated by the antenna averaged over all directions. It is given by

$$D(\vartheta, \varphi) = \frac{|\,\boldsymbol{S}(\vartheta, \varphi)|}{\frac{P_{\text{rad}}}{4\pi}} = \frac{|\,\boldsymbol{S}(\vartheta, \varphi)|}{\left|\,\boldsymbol{S}_{\text{i}}(\vartheta, \varphi)\right|}\,. \tag{2.3}$$

It is common to describe the directivity of an antenna in relation to the power density $\boldsymbol{S}_{\text{i}}(\vartheta, \varphi)$ of an isotropic radiator. The isotropic radiator is a theoretical point source which radiates with an equal power distribution over a sphere, respectively 4π sr. The definition of the directivity with respect to an isotropic radiator is equal to (2.3). Often, the term directivity is only referred to the maximum directivity which will be referred to as D_{max} in the following. For an isotropic radiator, it is obvious that D is identical for all angular directions and also equal to D_{max}. However, the maximum directivity of an antenna is of interest as it is a measure how focused the radiated energy is. Typical maximum directivities are in the range of a few decibel for dipoles and up to about 40 dBi or even much more for reflector antennas, where the i in dBi states that the isotropic radiator is used as reference.

In general, the mathematical representation of the radiation pattern is a function of spatial coordinates where usually the electric field, power density or directivity of an antenna is described in the FF. The most common visualization of a radiation pattern is a three-dimensional (3D) plot as depicted in Fig. 2.1, while it is also common to show only cuts of the 3D pattern at certain angles in ϑ and φ. Figure 2.2 shows a cut at $\vartheta = 90°$ of the radiation pattern in Fig. 2.1 as polar plot. The pattern cut consists of

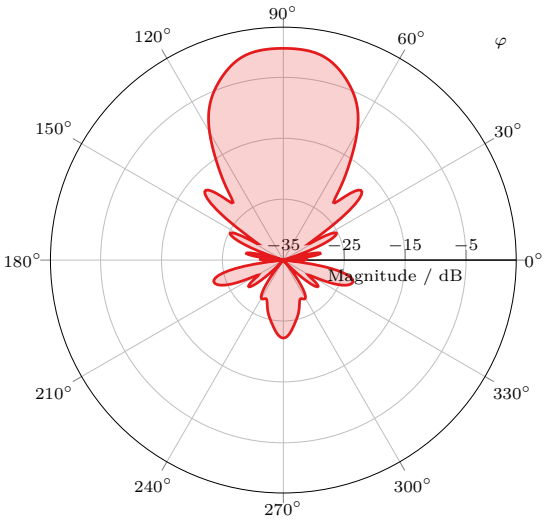

Figure 2.2: Phi-cut of the antenna radiation pattern of Fig. 2.1 at $\vartheta = 90°$ visualized as 2D polar plot.

several lobes which represent the power radiated in the different angular directions. The direction of strongest radiation, i.e., the direction of the maximum directivity, is called main lobe or main beam.

Beside the directivity, another important measure is the gain G of an antenna. The gain is closely related to the directivity and takes additionally the antenna efficiency into account. It is given by

$$G = \xi D = \frac{P_{\text{rad}}}{P_{\text{in}}} D \,, \tag{2.4}$$

where the antenna efficiency ξ is the ratio of the power radiated by an antenna P_{rad} to the power which is delivered to this antenna P_{in}.

2.1.2 Input Impedance and Reflection Coefficient

In the world of electrical circuit theory, an antenna is an element that has a certain reactance, inductance and capacitance, while it interacts with the circuit it is integrated in. Primarily, the input impedance of an antenna is of interest as it defines the matching of the antenna to the external circuit, e.g., the transmission line, it is connected to. The input impedance Z_{A} can be written in terms of a resistance R_{A} and a reactance X_{A} as

$$Z_{\text{A}} = R_{\text{A}} + \text{j} X_{\text{A}} \,. \tag{2.5}$$

If a generator with impedance Z_{G} is connected to the input terminals of the antenna, then a portion of the supplied power is reflected at the input terminals of the antenna if the input impedance of the antenna Z_{A} and the generator Z_{G} are not matched. This is described by the reflection coefficient Γ which is the ratio of the amplitude of the reflected wave to the amplitude of the incident wave. It can also be given in terms of generator and antenna impedances which denotes to

$$\Gamma = \frac{Z_{\text{A}} - Z_{\text{G}}}{Z_{\text{A}} + Z_{\text{G}}} \,. \tag{2.6}$$

The reflection coefficient is commonly given in logarithmic scale in decibel which is

$$\Gamma_{\text{dB}} = 20 \log_{10} |\Gamma| \,. \tag{2.7}$$

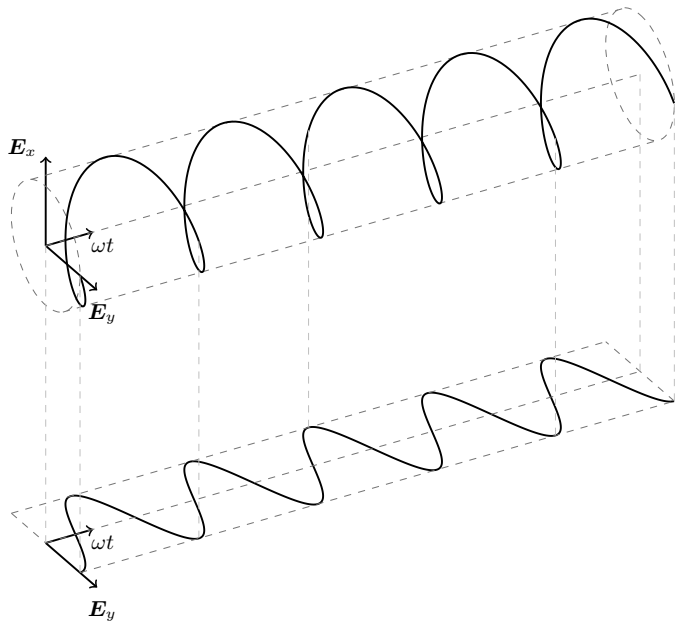

Figure 2.3: Trace of the electric field vector along the traveling direction of a right hand circular polarized wave over time. The electrical field in a certain direction can be derived by projection of the 3D field over time, as shown for the field along the y-axis.

Especially in antenna design, it is also common to express the matching of the antenna to the electrical feeding network in terms of the voltage standing wave ratio (VSWR). It is related to the reflection coefficient Γ and given by

$$VSWR = \frac{1 + |\Gamma|}{1 - |\Gamma|} . \tag{2.8}$$

The VSWR is always a positive real number where lower values mean a better matching of the antenna to the feeding network. The antenna is perfectly matched when $VSWR = 1$, while no power is reflected in this case.

2.1.3 Polarization

The polarization of an electromagnetic wave is defined via the direction of the the electric field. For example, a plane wave traveling in positive z-direction is described by

$$\boldsymbol{E} = E_0 \hat{\boldsymbol{u}}_x \, \mathrm{e}^{\mathrm{j}(\omega t - kz)} , \tag{2.9}$$

where E_0 is a constant field value, $\omega = 2\pi f$ the angular and f the temporal frequency. Furthermore, $k = {}^{2\pi z}/_{\lambda}$ is the wavenumber that depends on the wavelength λ. The electric field is oscillating only in x- and the magnetic field in y-direction while both, E and H, are perpendicular to the propagation direction. Therefore, the wave described by (2.9) is said to be linearly polarized in x-direction. A wave can also be circularly or elliptically polarized which means that the oscillation changes its direction during propagation, respectively over time. The example of a right-handed, circularly polarized wave is illustrated in Fig. 2.3. In general, the polarization of a polarized wave can always be classified as elliptical which includes the circular polarization as a limiting case for $|E_x| = |E_y|$ and a phase difference of 90° between E_x and E_y. Also, the linear polarization can be represented by the elliptical polarization,

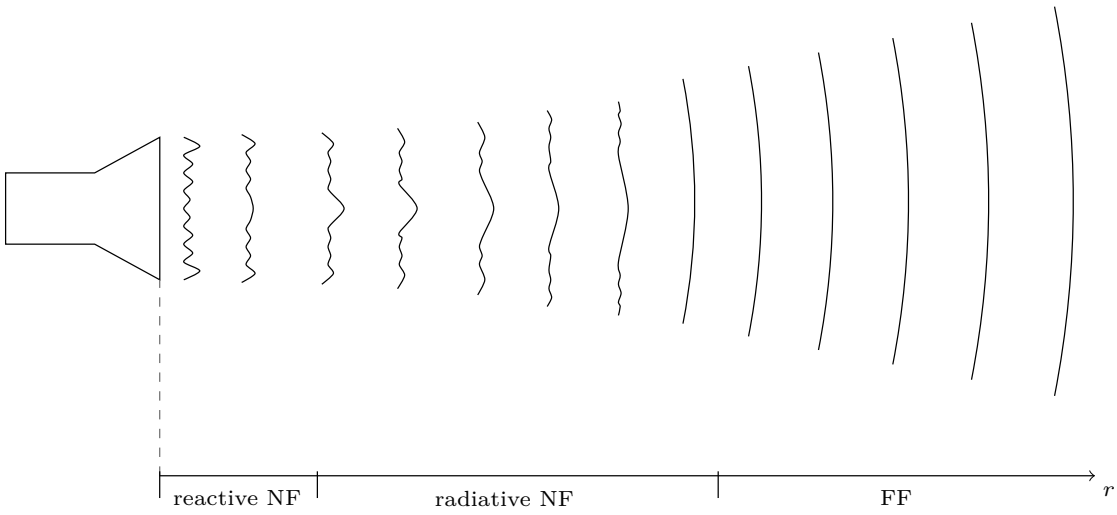

Figure 2.4: Field regions of an electromagnetic wave changing with the distance from the transmitting or receiving antenna.

e.g., in x-direction for $E_y = 0$.

Overall, the polarization of an antenna is an important characteristic as it defines which field component of an electromagnetic wave is received by an antenna, e.g., a linearly polarized antenna in x-direction will only receive the parts of a wave which are oscillating in x-direction and no wave components in y-direction. A polarization mismatch arises, if the polarization of an antenna is not the same as the polarization of an incoming wave. Indeed, this is the case for almost any practical case. Assuming that the electric field of an antenna can be written as

$$\boldsymbol{E}_\mathrm{A} = E_\mathrm{A}\hat{\boldsymbol{u}}_\mathrm{A}\,, \tag{2.10}$$

and the electric field of the incoming wave as

$$\boldsymbol{E}_\mathrm{w} = E_\mathrm{w}\hat{\boldsymbol{u}}_\mathrm{w}\,, \tag{2.11}$$

where $\hat{\boldsymbol{u}}_\mathrm{A}$ and $\hat{\boldsymbol{u}}_\mathrm{w}$ are the unit vectors of the antenna polarization and the incoming wave, respectively. The mismatch between the antennas can be expressed in terms of the polarization loss factor (PLF). It is given by

$$PLF = \left|\,\hat{\boldsymbol{u}}_\mathrm{A}\cdot\hat{\boldsymbol{u}}_\mathrm{w}\right| = |\cos\psi|\,, \tag{2.12}$$

where ψ is the angle between the two unit vectors $\hat{\boldsymbol{u}}_\mathrm{A}$ and $\hat{\boldsymbol{u}}_\mathrm{w}$.

2.2 Field Regions

The properties of an electromagnetic field radiated by an antenna change with the distance from that antenna. In general, three different field regions are distinguished as visualized in Fig. 2.4. The region in the immediate vicinity of the antenna is called the reactive NF where propagating waves and non-propagating evanescent fields can exist. The reactive NF extends from any conductive part of the antenna where the stored non-propagating energy can couple in an inductive or capacitive manner when another conductor is brought into this area. The second field region is the radiating NF, in which radiating

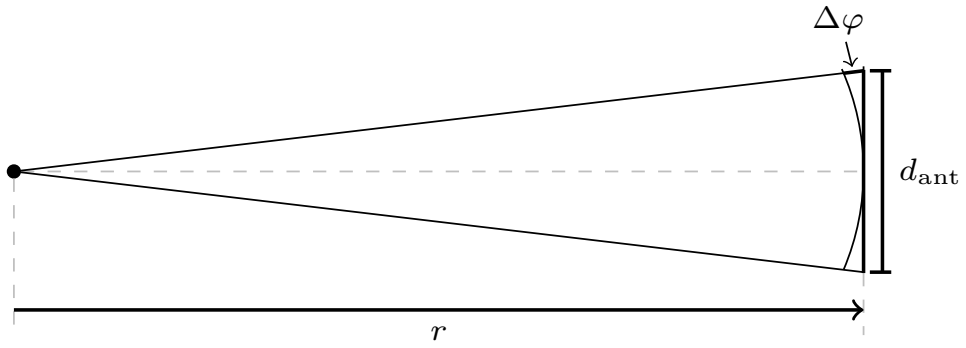

Figure 2.5: Curvature of the phase front of a radiating isotropic source in the FF. The difference $\Delta\varphi$ between the real curvature and the ideal planar phase front over the aperture of diameter d_{ant} of a receiving antenna defines the FF distance of the antenna.

field components are dominant over their non-radiating counterparts. NF measurements are usually performed in the radiating NF. The FF of an antenna is the region in which the field distribution does not change anymore with increasing distance r to the antenna and the wavefront can be seen as locally plane wave. The distance at which the FF begins is usually given in dependence on the maximum aperture dimension of the antenna d_{ant} as $r \geq {}^{2d_{\mathrm{ant}}^2}/_{\lambda}$. The derivation of this FF distance is recapitulated in the following while it can also be found in Parini et al. [2020a] and Selvan and Janaswamy [2017]. The phase of a plane wave is equal everywhere on a plane perpendicular to the propagation direction. Moreover, the phase of a spherical wave is equal everywhere on a sphere for an arbitrary but fixed radius. A phase difference, or accepted phase error, $\Delta\varphi$ arises when an originally spherical wave is treated locally as it was a plane wave. Figure 2.5 illustrates a situation in which an isotropic source illuminates the receiving AUT with aperture size d_{ant}. The phase in the horizontal extension of the isotropic source is given by

$$\varphi_{\mathrm{center}} = \frac{2\pi}{\lambda} r\,, \tag{2.13}$$

where r is the distance of the source to an observation plane with extension d_{ant} that is equal to the aperture size of the AUT. The phase on the edge of the curved wavefront is given by

$$\varphi_{\mathrm{curved}} = \frac{2\pi}{\lambda} \sqrt{r^2 + \left(\frac{d_{\mathrm{ant}}}{2}\right)^2}\,. \tag{2.14}$$

The phase difference $\Delta\varphi$ between the perfect planar and the actual curved wavefront results from the subtraction of (2.13) from (2.14). It is

$$\Delta\varphi = \frac{2\pi}{\lambda} \left(\sqrt{r^2 + \left(\frac{d_{\mathrm{ant}}}{2}\right)^2} - r \right). \tag{2.15}$$

An expansion of (2.15) into a Taylor series and taking only the first term leads to

$$\Delta\varphi \approx \frac{\pi d_{\mathrm{ant}}^2}{4\lambda r}\,. \tag{2.16}$$

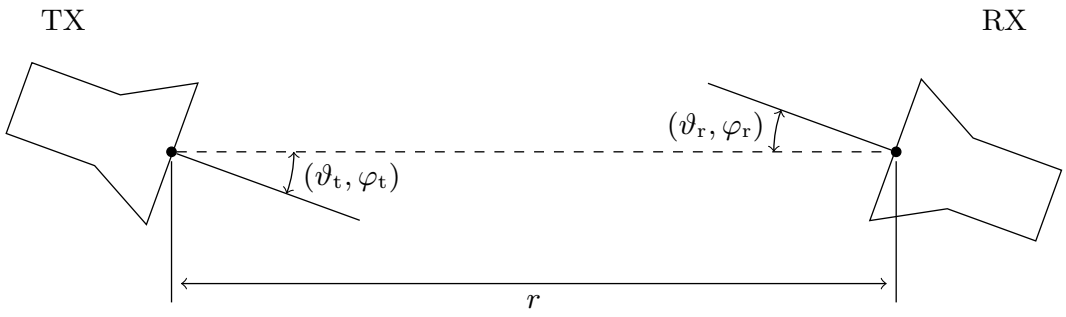

Figure 2.6: Wireless link consisting of a transmitting (TX) and a receiving antenna (RX). The mutual positioning of the two antennas is given by the distance r and the orientation angles $(\vartheta_{\mathrm{t/r}}, \varphi_{\mathrm{t/r}})$.

The distance at which the FF begins is normally defined as the distance where the maximal phase change $\Delta\varphi$ across the AUT aperture is 22.5° which is equal to $\lambda/16$ [Slater 1991]. Therefore, inserting the condition of $\Delta\varphi \leq 22.5° \triangleq \frac{\pi}{8}\mathrm{rad}$ as maximum phase error across the aperture, finally leads to

$$r \geq \frac{2d_{\mathrm{ant}}^2}{\lambda}\,, \tag{2.17}$$

where the case of the equal sign is the FF distance which should be taken into account as a minimum distance to operate under FF conditions.

2.3 Friis Transmission Equation

The power density S_t radiated by an antenna and observed at a distance r in the angular direction $(\vartheta_\mathrm{t}, \varphi_\mathrm{t})$ can be written as

$$S_\mathrm{t} = \frac{P_\mathrm{t} G_\mathrm{t}(\vartheta_\mathrm{t}, \varphi_\mathrm{t})}{4\pi r^2}\,, \tag{2.18}$$

where P_t is the power supplied to and G_t the gain of the transmitting antenna. The power P_r collected by an antenna in receive mode can be expressed in terms of the power density S of the incoming wave and an effective antenna aperture A_{eff} by

$$P_\mathrm{r} = S A_{\mathrm{eff}}\,. \tag{2.19}$$

The effective aperture describes the power which is measured at the terminals if a plane wave is incident on the antenna. It can also be written regarding the gain G_r of the antenna

$$A_{\mathrm{eff}} = \left(\frac{\lambda^2}{4\pi}\right) G_\mathrm{r}(\vartheta_\mathrm{r}, \varphi_\mathrm{r})\,, \tag{2.20}$$

where $(\vartheta_\mathrm{r}, \varphi_\mathrm{r})$ is the direction of the incident wave. Figure 2.6 shows a simple wireless link consisting of a transmitter (TX) and a receiver (RX). The power P_r collected by the receiving antenna in relation to the power P_t supplied to the transmitting antenna can be calculated by combining (2.18) to (2.20). It is

$$P_\mathrm{r} = \left(\frac{\lambda^2}{4\pi}\right) G_\mathrm{r}(\vartheta_\mathrm{r}, \varphi_\mathrm{r}) S_\mathrm{t} = \left(\frac{\lambda}{4\pi r}\right)^2 G_\mathrm{r}(\vartheta_\mathrm{r}, \varphi_\mathrm{r}) G_\mathrm{t}(\vartheta_\mathrm{t}, \varphi_\mathrm{t}) P_\mathrm{t}\,. \tag{2.21}$$

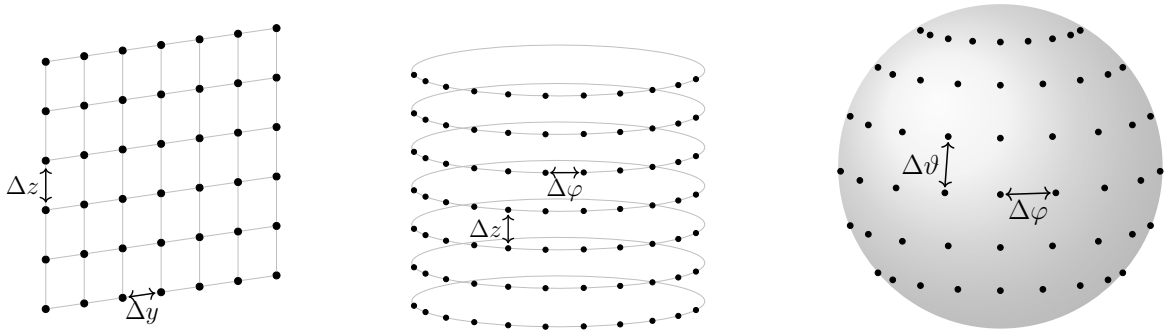

(a) (b) (c)

Figure 2.7: Typical scan geometries that are used in NF antenna measurements in anechoic chambers, where the choice, whether a planar, cylindrical or spherical geometry is used, depends on the AUT and the implementation of the measurement system.

The last part of (2.21) is the most common form of the Friis transmission equation which has been named after Harald T. Friis who developed the formula in 1946 [Friis 1946] in a slightly different form using only the effective apertures of the antennas instead of the antenna gains. In practical applications, it is also common to express (2.21) in terms of directivity instead of gain, considering the relation given in (2.4). However, the Friis transmission equation assumes that the incident wave is a plane wave which is only satisfied in the FF of the transmitting and receiving antennas. The formula is therefore only applicable for distances equal or greater than the FF distance. The resulting powers calculated from (2.21) assume that no reflection occurs due to impedance mismatch on either of the antennas as well as that the polarizations of both antennas are matched. If all of these mismatches are additionally included, (2.21) extends to

$$P_\mathrm{r} = \left| 1 - \Gamma_\mathrm{r} \right| \left| 1 - \Gamma_\mathrm{t} \right| \left| \cos\psi \right| \left(\frac{\lambda}{4\pi r} \right)^2 G_\mathrm{r}(\vartheta_\mathrm{r}, \varphi_\mathrm{r}) G_\mathrm{t}(\vartheta_\mathrm{t}, \varphi_\mathrm{t}) P_\mathrm{t} \,, \tag{2.22}$$

where Γ_r and Γ_t are the reflection coefficients of the antennas due to impedance matching and ψ is the polarization-mismatch angle between the two antennas as described in Section 2.1.3.

2.4 Near-Field Measurement Ranges

Reviewing the literature, there are many ways how NF measurements can be realized. However, most of the differences are due to the chosen scan geometries and the employed measurement equipment. The scan or measurement geometry defines the spatial positions to which the probing antenna is moved as the field of the AUT is measured. In principal, there are three basic scan geometries which are commonly established: planar, cylindrical and spherical. They are schematically depicted in Fig. 2.7.

The planar measurement geometry is by far the simplest, as the field probe is moved on a plane in front of the oftentimes static AUT, measuring its field. NF measurements are usually performed with some distance between the AUT and the field probe to avoid any mutual interaction between the two antennas and also the measurement of strong reactive fields. A rectangular scanning grid is commonly used where the field probe is moved horizontally and vertically to the measurement locations $\boldsymbol{r} = (y, z)$ of the planar grid [IEEE 2012]. The main disadvantage of a planar measurement setup is that the AUT and the field probe do not face each other at all measurement locations, i.e., the orientation of the two antennas with respect to the measurement plane does not change with their displacement. As a result,

the radiation pattern of the field probe is found again within the recorded NF data. In addition, it must be considered that the probing antenna integrates the NF around a desired measurement position $\boldsymbol{r}$ rather than measuring the field only at exactly this position $\boldsymbol{r}$. Hence, the voltage at the probe ports $U(\boldsymbol{r})$ can be expressed as

$$U(\boldsymbol{r}) = \oiiint_{V_{\text{prob}}} \boldsymbol{w}_{\text{prob}}(\boldsymbol{r}) \cdot \boldsymbol{E}(\boldsymbol{r}) \, \mathrm{d}V \,, \tag{2.23}$$

where $\boldsymbol{E}(\boldsymbol{r})$ is the electric field at position $\boldsymbol{r}$, $\boldsymbol{w}_{\text{prob}}(\boldsymbol{r})$ the weighting factor and V_{prob} the volume of the probing antenna. The NF can, principally, not be measured at a single position as this would require a very small probe, i.e., a Hertzian dipole, which entails that the measured field is always subject to the influence of the field probe [Joy and Paris 1972]. To reduce this probe influence, the spatial weighting of the measured field distribution by the field probe needs to be considered in the post-processing during the NFFFT. This is commonly known as probe correction.

In comparison to planar measurements, the influence of the field probe on the measured NF is lower for a cylindrical scan geometry. Within a cylindrical NF measurement, the field probe is moved on a cylinder around the AUT. In addition, the field probe is rotated around its vertical axis such that it always points to the center of the measurement cylinder while moving on a circular path around it. The center of the measurement cylinder does not necessarily have to coincide with the position of the AUT, but it often does. As a consequence of the fact that the field probe points always to the rotation center of the cylinder, respectively to the AUT, the influence of the probe pattern is significantly lowered in horizontal direction as the probe antenna is illuminated from a far smaller range of incident angles in comparison to planar measurements. However, this is only true in horizontal and not in vertical direction, where, in the latter case, the probe influence on the measured field is similar to the case of a planar scan grid. The probe influence is further reduced when a spherical measurement geometry is considered. Here, the field probe virtually moves around the AUT on a spherical measurement grid, where in reality the field probe is commonly fixed and the AUT is rotated around multiple axes. As a result, the probe influence is minimized as the incident angles are minimized from which the probe antenna is illuminated by AUT field. The result is similar to a weighting of all field values with the same factor. Still, NF measurements are realized with the different measurement geometries since each one has advantages and disadvantages. The choice of the scan geometry often depends mostly on the AUT. In general, the full knowledge about the radiation of an antenna, or any other radiating object, is only achieved if the complex field is measured on a closed surface around this antenna. Still, an open measurement surface can be used instead of a closed one if the antenna is highly directive and it is known that the radiation in a certain spatial direction is low, i.e., only the field in direction of the main beam of the AUT is relevant. An open surface can also be used if the radiation shall only be measured in a certain direction, which is possible as the calculated FF is commonly only valid in the direction in which the NF has been measured. This angular range in which the calculated FF is valid can be estimated by basic geometry as depicted in Fig. 2.8. Assuming a planar measurement geometry, the valid angles α and β for the upper and lower part of the measurement surface are given by

$$\alpha = \arctan\left(\frac{\frac{d_{\text{ant}}}{2} + \Delta h_{\text{meas,up}}}{d_{\text{meas}}}\right), \tag{2.24}$$

and

$$\beta = \arctan\left(\frac{\frac{d_{\text{ant}}}{2} + \Delta h_{\text{meas,dwn}}}{d_{\text{meas}}}\right), \tag{2.25}$$

where $\Delta h_{\text{meas,up}}$ and $\Delta h_{\text{meas,dwn}}$ are the upper and lower parts of the measured field geometry that exceeds

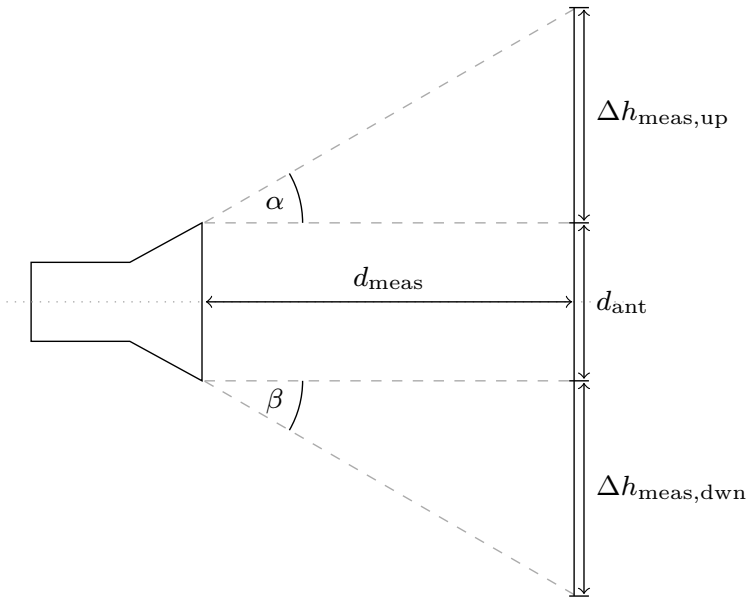

Figure 2.8: Side view of a horn antenna. The valid angles of the FF radiation pattern can be determined from the measured NF data by extrapolation of the angular coverage of the measured field.

the size of the AUT aperture d_{ant}. Moreover, it must be considered that in measurements with an open surface, the missing field outside of the valid angles causes some errors even within the valid angles [Newell 1988]. In general, the NF shall have decayed at the edges of the scan plane to the desired level of interest, e.g., the field at the scan edges shall be 40 dB lower than the highest field value if such low levels are of interest. Additionally, this also determines the observable FF error [Slater 1991].

As described by Parini et al. [2020a], the RF system of an NF test range can be seen as a two-arm microwave interferometer where both antennas, AUT and field probe, are inserted in one arm. However, a practical measurement setup is usually realized with the help of a vector network analyzer (VNA) which measures the transmission parameter between the AUT and the field probe. A schematic drawing of the RF part of a typical NF measurement system is depicted in Fig. 2.9 (a). Within the measurement setup, either the AUT or the field probe can be transmitting while the other antenna is receiving. This is only applicable for passive antennas due to their reciprocity. However, depending on the requirements and

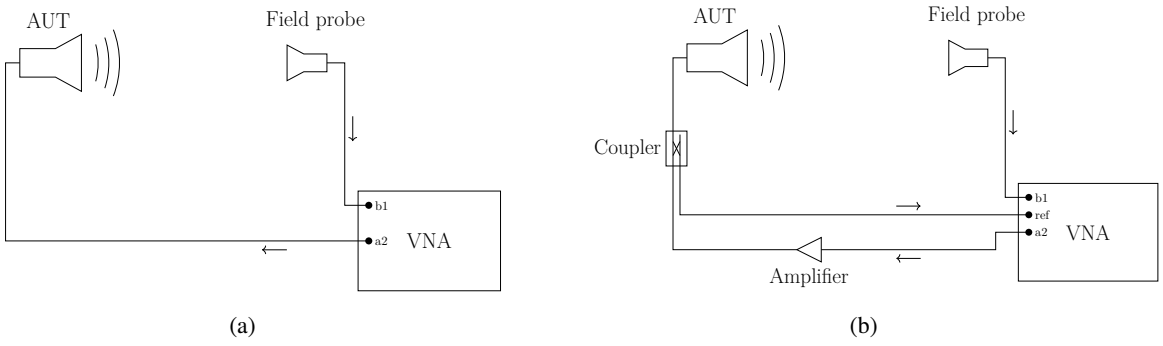

Figure 2.9: Schematic of the RF part of a simple NF measurement setup (a) and of an advanced NF setup (b) in which a reference signal is routed back from the AUT to the VNA.

goals, the actual implementation of the RF setup can vary and also be different from the one shown in Fig. 2.9 (a). Often, amplifiers and mixers are inserted to the signal paths to ensure that the influences of the coaxial cables and all other RF components are minimized. The RF signal diagram of a more advanced NF setup is depicted in Fig. 2.9 (b). Here, the AUT is transmitting while the generator signal is amplified outside of the VNA with the help of an additional amplifier. To compensate the impact of the amplifier, the generator signal is routed back to the channel reference input of the VNA. Moreover, all devices are usually connected by coaxial SMA cables for which a high quality is crucial to prevent phase distortions of the measurement signal. Equally important as the RF part of the measurement system is the positioning system that rotates and moves the field probe and, depending on the actual implementation, also the AUT. Here, sophisticated positioning systems are used that are chosen in accordance to the desired measurement frequency since the positioning accuracy ultimately limits the maximum measurement frequency. As an example, the anechoic chamber of the Technical University of Munich (TUM) has been designed for NF antenna measurements up to 26.5 GHz while the rotational positioners and the linear stage have a specified accuracy of about 0.09° and 50 µm, respectively [NSI 2008, 2014].

Antenna measurements would be ideally performed in free space, as there are no scattering objects and no reflections occur. Since this theoretical goal cannot be achieved, NF measurements are commonly performed in the controlled environment of anechoic chambers. These measurement chambers are equipped with electromagnetic absorbers to suppress reflections such that they are negligible. Electromagnetic absorbers exist of various materials and shapes, where pyramid foam absorbers are often used in measurement chambers. Due to their geometrical dimensions, the absorbers work only in a dedicated frequency range and must be selected according to the desired measurement frequencies and the size of the measurement chamber.

2.5 Near-Field to Far-Field Transformation

The NF measurement of an antenna is usually followed by a post-processing step in which the FF radiation pattern is determined. This calculation is commonly known as the NFFFT and has been an active field of research for many decades. The exact implementation of an NFFFT can be of various form, which is also true for the robustness, accuracy and characteristics of the available implementations. The basic approach of most NFFFTs is the replacement of the AUT or, more generally, the radiating object by equivalent sources. The equivalent sources are determined from the measured field values, and finally the FF can be calculated from these sources. Similar to the implementation of the NFFFT itself, the used equivalent sources can be of different form. For the transformation of the field, methods of modal expansion are usually used. Depending on the measurement geometry, planar, cylindrical or spherical waves are used as equivalent sources, although in principle any measurement geometry is possible.

Taking the example of plane wave propagation, the radiating field of the transmitting antenna is represented by plane waves. These plane waves are translated to the location of the receiving antenna where they are multiplied by the receiving pattern of the field probe. Thereby, each plane wave causes only one incident plane wave on the field probe in the same direction. If the measured field is band-limited in x- and y-direction to the respective propagation constants k_{x0} and k_{y0}, then a finite sample spacing of Δx and Δy will be sufficient to reconstruct the entire field if a rectilinear acquisition scheme is applied. According to Parini et al. [2020a], the sampling is given by

$$\Delta x = \frac{\pi}{k_{x0}} \tag{2.26}$$

and

$$\Delta y = \frac{\pi}{k_{y0}} \tag{2.27}$$

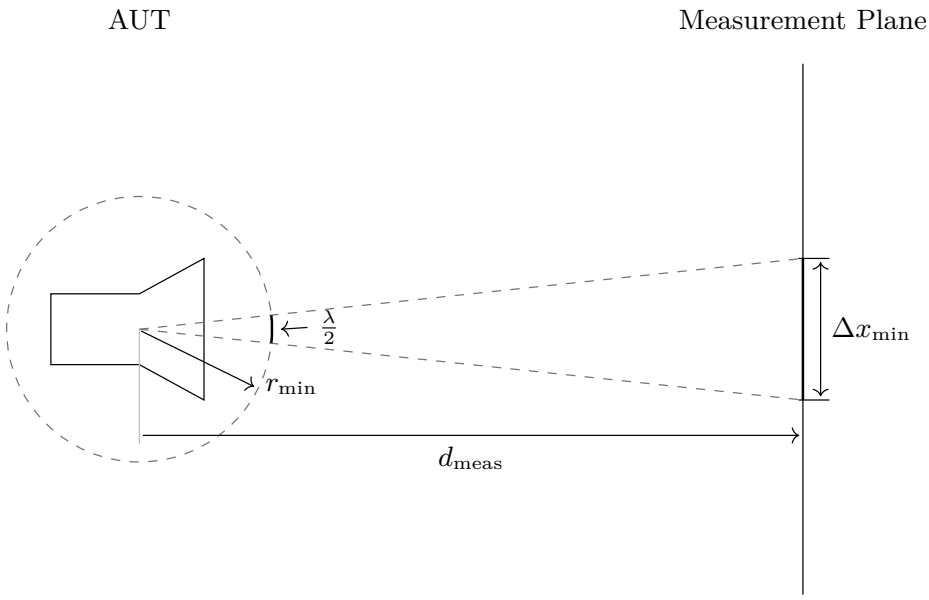

Figure 2.10: Projection of the required field sampling from the minimal sphere to the measurement plane within the NFFFT.

in x- and y-direction, where

$$k_{x0} = k_{y0} = \frac{2\pi}{\lambda} \tag{2.28}$$

applies for homogeneous plane-wave spectra. This leads to a minimum sampling distance of

$$\Delta x = \Delta y = \frac{\lambda}{2}, \tag{2.29}$$

which is similar to the Nyquist-Shannon sampling theorem [Girod et al. 2001]. The wavelength $\lambda = {}^{c}/_{f}$ corresponds to the measurement frequency f, considering the speed of light c. However, the requirement of the sampling theorem is only valid on the minimal sphere, a sphere which encloses all parts of the AUT, but narrowly and without any additional space. As the measurement positions move further away from the positions on the minimal sphere, also the requirement of the sampling theorem is relaxed. This is a consequence of the fact that an electromagnetic wave does not change its direction of propagation in free space as long as it is not forced to do so, e.g., by external fields or scattering objects. Therefore, the intercept theorem is applicable where the angular sampling distance of the field is preserved and can be projected from the minimal sphere to the measurement plane [Qureshi et al. 2013b]. This is schematically depicted in Fig. 2.10. Regarding the arrangement in the given example, the sampling distance between two measurement positions on the measurement plane must not exceed

$$\Delta x_{\min} = \frac{d_{\text{meas}}}{r_{\min}} \frac{\lambda}{2}, \tag{2.30}$$

where $r_{\min}$ is the radius of the minimal sphere and d_{meas} the distance from the center of the sphere to the measurement plane. Still, the exact treatment of over- or undersampled field parts depends on the explicit implementation of the NFFFT.

Beside a plane wave representation, equivalent currents on the surface of the antenna geometry can also be employed as equivalent sources. Equivalent currents are a powerful source representation since

gaining diagnostic data of the AUT is often similar to determining equivalent currents on the surface of the antenna. Such equivalent currents as sources are following Huygens' principle which states that the field outside a closed volume can be calculated if the tangential fields on the corresponding closed surface are known. However, an open measurement surface may be used instead of a closed one if it is known that the radiation in a particular direction is low or if only the radiation in a certain direction is of interest [Eibert et al. 2015].

Throughout this thesis, the fast irregular antenna field transformation algorithm (FIAFTA) is employed as NFFFT, which has been developed at the Chair of High-Frequency Engineering of the TUM [Eibert and Schmidt 2009; Eibert et al. 2010, 2015]. The FIAFTA is a computationally efficient NFFFT implementation that can handle field data on arbitrary measurement grids. The working principle of the algorithm is based on a plane-wave approach as the radiated AUT fields are translated into propagating plane waves that are directly incident on the field probe, meaning that the algorithm works with the FF of the probe. Furthermore, this implies that the FF radiation pattern of the probe can be directly taken into consideration for the weighting of the measured field values which ensures full probe correction with comparably low computational complexity. One of the main differences in comparison to conventional NFFFT algorithms based on the FFT is that the FIAFTA is able to handle irregular and arbitrarily sampled NF data. This becomes especially important when in-situ measurements are considered since, in that case, it is commonly hard to precisely maintain a measurement grid. Besides a full probe correction and the acceptance of irregular measurement positions, the FIAFTA includes features that enable accurate in-situ NF measurements, like the consideration of external scatterers [Yinusa and Eibert 2013] and conducting ground [Eibert and Mauermayer 2018; Mauermayer and Eibert 2018]. Scatterers are almost omnipresent in real measurement environments since the AUT and the field probe are to be mounted somewhere and the holding structure can usually not be sufficiently covered by absorbing material. This scenario is even worse in in-situ measurements where an AUT might be mounted in an inconvenient way for NF measurements. For this, the scattering objects can also be considered as equivalent sources which are, similar as the other equivalent sources, contributing to the measured field values. Eventually, the only difference between scatterers and the AUT sources is that only the latter are taken into account when the FF radiation pattern is calculated. In this way, the FIAFTA is able to calculate the free-space radiation pattern of the AUT without the contribution of the disturbing scatterers. In a similar manner, the FIAFTA takes reflecting ground into account where arbitrary values of permittivity and permeability can be specified.

2.6 Calculation of the Measurement Error

The NF or resulting FF radiation pattern from a measurement is commonly compared to some reference field for the evaluation of the quality of the measurement. The reference is often a numerical simulation, e.g., in antenna design, or a previously conducted measurement of the same antenna. Usually, the deviation between the actual measurement and the reference is calculated which, in the first place, states how well both measurements or fields match. This deviation is often given in decibels and can be calculated as

$$\epsilon_{\mathrm{abs}} = 20\log\left|\left|\frac{\boldsymbol{E}_{\mathrm{ref}}}{\max\left(|\,\boldsymbol{E}_{\mathrm{ref}}|\right)}\right| - \left|\frac{\boldsymbol{E}_{\mathrm{meas}}}{\max\left(|\,\boldsymbol{E}_{\mathrm{meas}}|\right)}\right|\right|, \tag{2.31}$$

where $\boldsymbol{E}_{\mathrm{meas}}$ and $\boldsymbol{E}_{\mathrm{ref}}$ are the complex field vectors of the measurement and the reference for a single measurement position or FF direction. A complex field value contains magnitude and phase of the field in comparison to scalar values which lack the phase information. Further, in (2.31), $\max(\boldsymbol{x})$ is the maximum function that delivers the maximum among all values in the array or series $\boldsymbol{x}$. While (2.31) reveals the deviation and, therefore, possible errors in the measurement, it is only based on the

field magnitude and does not include its phase, i.e., a phase difference does not contribute to the error calculated by (2.31). For this, (2.31) can be reformulated to

$$\epsilon_{\mathrm{cmplx}} = 20\log\left| \frac{\boldsymbol{E}_{\mathrm{ref}}}{\mathrm{maxc}\left(\boldsymbol{E}_{\mathrm{ref}}\right)} - \frac{\boldsymbol{E}_{\mathrm{meas}}}{\mathrm{maxc}\left(\boldsymbol{E}_{\mathrm{meas}}\right)} \right|. \tag{2.32}$$

The function $\mathrm{maxc}(\boldsymbol{x})$ reveals the complex value of an array $\boldsymbol{x}$ at the absolute maximum, i.e.,

$$\mathrm{maxc}(\boldsymbol{x}) = x_i \quad \text{where} \quad \left| x_i \right| = \max(|\boldsymbol{x}|)\,. \tag{2.33}$$

Obviously, (2.32) is more restrictive and sensitive regarding the deviation since the magnitudes and phases of the fields are taken into account. Still, both error measures are valuable and important while the comparison of the calculated deviation from (2.31) and (2.32) provides insights on how much the deviation or error is related to the phase. However, the more relaxed error measure of (2.31) is commonly used in the literature for the evaluation of antenna measurements.

2.7 Chapter Summary

In this chapter, the essential properties of antennas were reviewed. It was outlined that the FF radiation pattern is one of the most important characteristics, although additional properties must be taken into account. Furthermore, the Friis transmission equation was discussed which allows for the direct calculation of the power received by an antenna in dependence on the power transmitted by another antenna. Another part of this chapter dealt with the basics of NF measurements. Here, the measurement setup in terms of used hardware for the positioning of the antennas as well as the RF part have been briefly described. It was outlined that typical measurement arrangements include planar, cylindrical and spherical scan geometries where any kind of truncated NF measurement scheme leads to limited valid angles of the resulting FF. Moreover, the NFFFT was briefly discussed which, strictly speaking, is not part of the actual NF measurements but a mandatory post-processing step if the FF, or any other information related to the equivalent sources, is of interest. Eventually, a definition was given for the calculation of the deviation between two fields, with and without consideration of the phase. These formulas will be referred to throughout all following chapters of this thesis.

Chapter 3

Uncrewed Aerial Vehicles

The field of uncrewed aerial vehicles (UAVs), also known as unmanned aerial vehicles or drones, is manifold regarding the types and working principles of the flying vehicles. On the one side, there are fixed wing drones which are based on the lift created by pressure differences above and below the wing, just as for normal crewed planes [Valavanis and Vachtsevanos 2015]. On the other side, there are rotorcraft UAVs which work with lift that is generated by rotating rotor blades [Mahony et al. 2012]. More advanced models are capable of vertical take-off and landing (VTOL) and combine fixed wing with rotorcraft technology [Stahl et al. 2018]. Nowadays, multirotors, also called multicopters or simply copters, are the most common type of UAVs among end users. They are used for all kinds of applications, ranging from photography to agricultural seeding. For the UAV-based antenna measurements in this thesis, only multirotors have been used. Therefore, in the following, the term *UAV* refers only to this type.

3.1 Multirotor Operation Principle

In general, multirotors can be of various type, ranging from single-rotor models like helicopters to octocopters and beyond. Among the consumer devices, quad- and hexacopter are widely spread, i.e., copters with four or six rotors. Figure 3.1 shows the frames and rotor arrangement of a hexa- and an octocopter together with the respective rotation direction of the rotor blades. In the figure, it can be seen that the rotors next to each other are spinning in different directions which is necessary to stabilize the copter. In contrast to fixed wing UAVs, the propulsive force of copters is purely provided by the spinning rotors which work with the same principle as wings, i.e., they create uplift due to a difference in air pressure above and below the rotor blade. However, the rotor blades of copters usually have a fixed pitch in comparison to the wings of planes which are adjustable in terms of pitch. This leads to the situation that the uplift, or thrust, of a copter can only be controlled by the rotation speed of the rotor blades. Besides the thrust, a UAV is usually controlled by the pitch, roll and yaw angles which are rotations around the three principal axis of an aircraft. These principal axis, that form a right-handed coordinate system, are illustrated in Fig. 3.2 for the case of a hexacopter together with the corresponding orientation angles.

As already mentioned, the thrust can be adjusted by the change of the rotation speed of the rotor blades. If all rotors spin at the same speed and the generated air pressure creates an upward force, the copter moves vertically upward, assuming that there is no external force like wind. Similarly, reducing the rotation speed of all rotors lowers the upward force and makes the copter descending. As shown in Fig. 3.1, the rotors are spinning in different directions, clockwise and counter-clockwise, while they are mounted in an alternating manner. Therefore, it is important that all rotors are spinning with the same speed for a vertical movement as this neutralizes the torque that is transferred from the rotors onto the

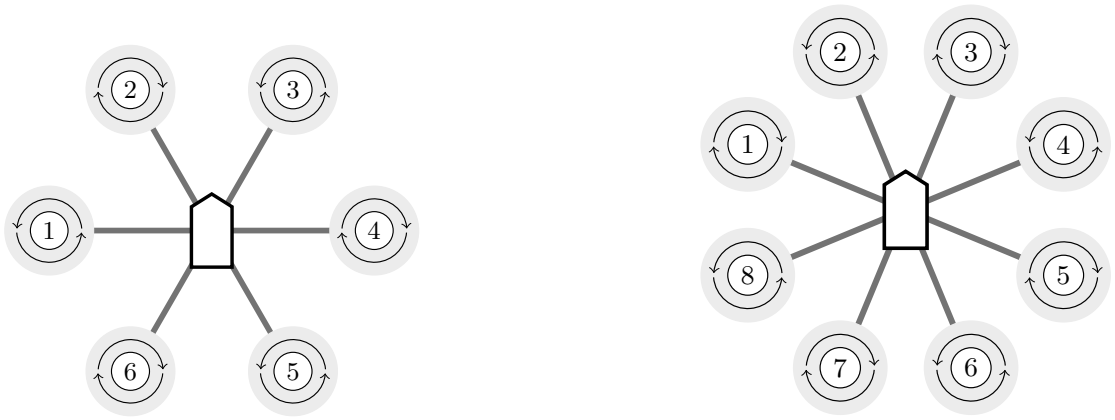

(a) (b)

Figure 3.1: Typical arrangement of the rotors/motors of a hexacopter (a) and an octocopter (b). The rotation direction of the rotor blades is indicated where two adjacent rotors are spinning in opposite directions.

frame. However, the rotation around the vertical yaw axis can be achieved by intentionally mismatching the rotation speed of the clockwise and counter-clockwise rotors, depending on the direction in which the copter shall be turned. Tilting the copter around the transverse pitch or longitudinal roll axis, for the flight to the front, back or side of the copter, can be achieved by simultaneously increasing the rotation speed of the rotors on the opposite side of the axis.

As the rotors of a copter are always spinning to move the copter or keep it in place, the UAV is not able to maneuver or land safely when the rotors stop working. However, hexa- and octocopters may have enough redundancy in their rotors and motor thrusts such that they can theoretically land safely if a single motor is failing [Du et al. 2015].

3.2 Components of a Multirotor

Even if the exact implementation of a multirotor can vary, some components are always present as they build the foundation for the operation of such a flying vehicle. Figure 3.3 shows a schematic overview of these components, which can be grouped into sensors that provide input to the flight controller and actuators that are controlled by the flight controller. The flight controller itself does not belong to any of the aforementioned groups and can be seen as separate category. All of the depicted components are briefly reviewed in the following.

3.2.1 Rotors and Motors

The rotors are obviously a key component of any multirotor as they produce torque and thrust which enables the controlled movement in the air. The rotors usually have a fixed pitch or angle of attack, while their length needs to be chosen with respect to the frame size and desired payload of the copter. A single rotor comprises multiple rotor blades where, most often, rotors consist of only two blades. Furthermore, the material of the rotors is crucial for their performance. Smaller UAVs commonly use plastic rotors while more professional UAVs use rotors made of carbon-fiber. In general, carbon-fiber rotors are more expensive but they are also lighter and stronger which reduces the overall mass of a copter and hinders

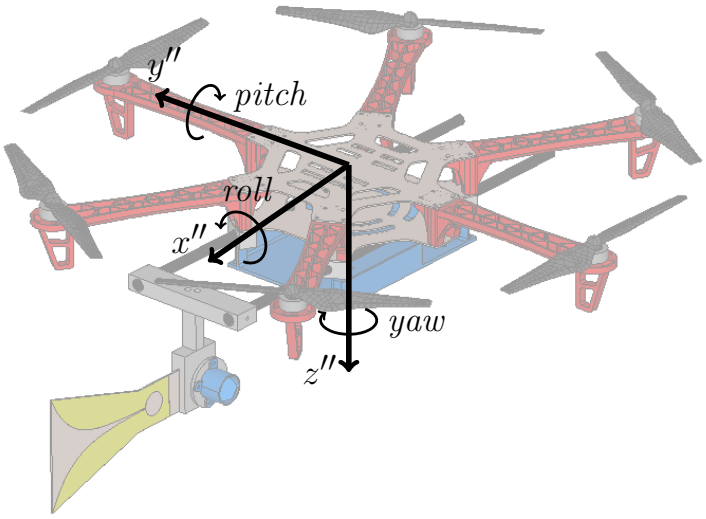

Figure 3.2: Principal axes of a UAV for the example of a hexacopter. The rotations roll (around x''), pitch (around y'') and yaw (around z'') are the foundation for control of any UAV and are also indicated.

the bending of the single rotor blades. Carbon-fiber rotors are also said to produce less vibration in comparison to their counterparts made of plastic [Quan 2017]. Most multirotors, and also the ones used in this thesis, are designed in a way that the rotors are directly mounted onto the motor shafts which are used to convert electrical energy into rotation energy. The employed motors within consumer-grade copters are usually brushless direct current (DC) servomotors due to their simple working principle and low costs. Servomotors are commonly controlled using pulse width modulation (PWM) signals to tune them to a specific rotation speed. This requires, intermediate electronic speed controllers (ESCs) which are separate components in the copter setup. An ESC connects the flight controller and the motor, converting the PWM signal into voltage levels that are provided to the servomotor. Usually, one ESC can drive one servomotor while they are sometimes directly integrated into the motors. In general, the ESCs are selected considering the compatibility to the motors and are crucial regarding an optimization of the motor performance. Still, the motor efficiency varies and is largely influenced by the chosen rotor type, while the rotor performance itself highly depends on the speed and torque of the motor. This is also the reason why motors and rotors need to be carefully selected and matched. Regarding Fig. 3.3, the motors and connected ESCs are the most important components on the actuator-side of the flight controller.

3.2.2 Flight Controller and Sensors

The motors need to be actively controlled since the stability and flight operation of any multicopter is based on the differences in thrust and torque of the single rotors. For this an electronic flight controller is employed to regulate the rotation speed of the single motors, where this regulation is only possible if the flight controller gets information about the orientation of the copter. Therefore, the flight controller uses several internal and external sensors to determine the state of the multirotor. These sensors build the foundation for the operation of a multirotor and are on the input side in Fig. 3.3. Foremost, gyroscopes and accelerometers are used to determine the horizontal orientation of the copter and the changes

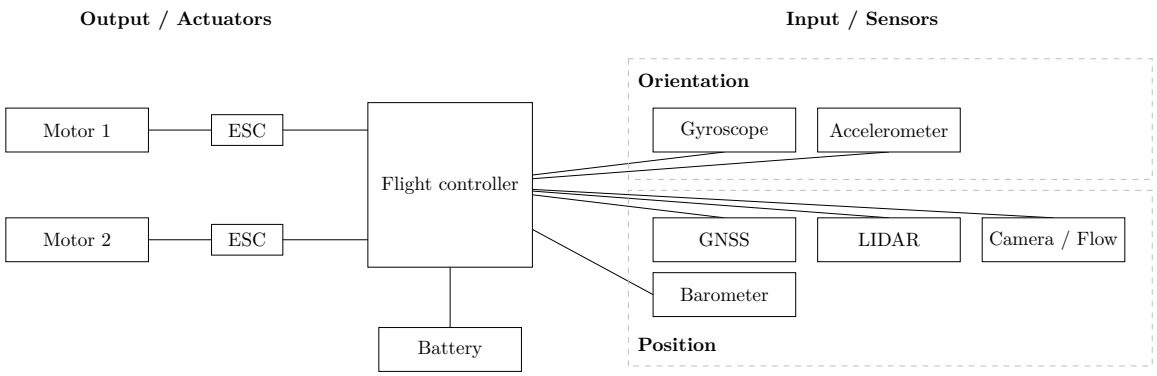

Figure 3.3: Schematic overview of the most important components of a typical UAV and their relation to the flight controller. The motors and their control electronics are on the output or action side of the flight controller, while several different sensors provide input to the flight controller.

therein. This allows for an automatic horizontal leveling of the multirotor, while intentional changes can be commanded by an external remote control to fly and guide the multirotor in a specific direction. Advanced flight controllers can run flight software packages that allow for more sophisticated flight operations up to fully autonomous flights. Such semi-autonomous or fully autonomous flights require additional information about the horizontal and vertical position of the copter as well as its orientation with respect to its surrounding environment. For this, a compass can be used to detect the orientation of the copter around its vertical yaw axis with respect to the world or global navigation satellite system (GNSS) coordinate system since the magnet field of the earth is detected. In addition, a barometer is able to determine the flight height over ground by sensing air pressure. Furthermore, a light detection and ranging (LIDAR) system can be used to determine the position of the multicopter relative to some nearby device by scanning surrounding objects and calculating the position change. In a similar way, a camera can also be used to map the environment and determine the relative position of the copter which, however, may involve intensive computing power. Also, GNSS can be used to determine the position of a copter. The advantage of GNSS over LIDAR or a camera is that it can deliver a global unambiguous position without the need for a fixed reference position.

3.2.3 Batteries and Energy Consumption

Carefully looking at Fig. 3.3 reveals that all listed UAV components are electrically powered while their individual energy consumption is very diverse, e.g., the motors need significantly more energy than a gyroscope. For this, batteries are employed to provide the necessary electrical energy to all components. Commonly, lithium polymer (LiPo) batteries are chosen as they have a significantly higher energy density than other battery types. A LiPo cell has a nominal voltage of 3.7 V which reaches 4.2 V or even 4.35 V when fully charged, depending on the exact LiPo type. Still, to provide a sufficient voltage level to all copter components, several LiPo cells are usually connected in series and also in parallel to extend the battery capacity. However, the usage of batteries as power source is limited since a higher energy capacity comes along with more weight which again increases energy consumption due to the overall mass of the UAV. Therefore, it is important to choose the used battery in accordance to all other components of the UAV, including the frame itself. Nevertheless, it is not surprising that other approaches have also been tried to provide energy to a copter. One idea of using a small combustion engine as power source can be found in the literature [Fritzel et al. 2019; Pavković et al. 2020]. Despite rotating the rotors directly, the combustion engine drives a generator to produce electrical energy which is finally able to power all electronic components as if a battery was used. Still, combustion engines are

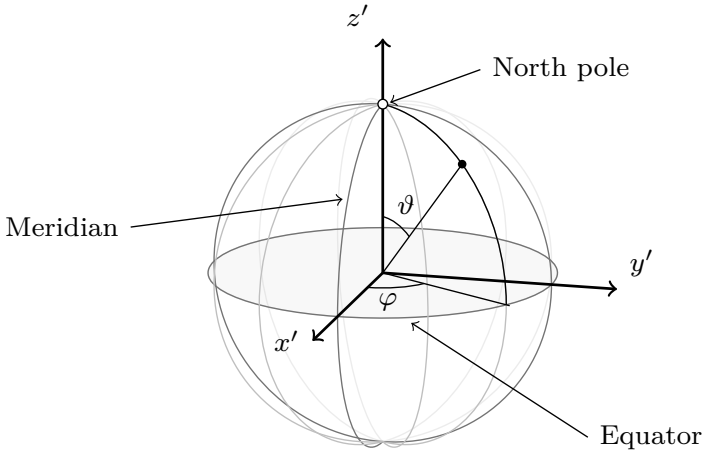

Figure 3.4: Global coordinate system used by GNSSs. Positions are usually described in terms of their latitude φ, longitude ϑ and altitude.

very rarely used when it comes to copters. Another idea are tethered copters which use a power line to the ground [Zikou et al. 2015; Walendziuk et al. 2020]. Such an implementation theoretically allows an unlimited flight time, while it reduces the action radius of the copter at the same time. However, the solution is ideal and also actively used for applications which do not need a large action radius.

3.3 Global Navigation Satellite System

Any location on earth can be described as position of an appropriate global coordinate system, a geodetic system. There are multiple geodetic systems where the World Geodetic System 1984 (WGS 84) is the current standard and also used by satellite navigation, including the Global Positioning System (GPS). The WGS 84 is a three-dimensional, right-handed Cartesian coordinate system (x', y', z') where the origin is in the mass center of a reference ellipsoid which approximates the earth's surface. The axes of the coordinate system are aligned with the intersection of the equator and Greenwich meridian, 90° to the east of that and to the geometrical north pole [Zogg 2011]. However, positions within the WGS 84 are commonly described by elliptical coordinates, i.e., by the latitude ϑ as angle between the y' and z' axes, the longitude φ as angle between the x' and y' axes and the elliptical height. In addition, the deviation between the ellipsoid and the actual surface of the earth has to be taken into account. This deviation is considered by the geoid, a mathematical model of the earth's surface that goes back to Carl Friedrich Gauß [Defense Mapping Agency 1991].The coordinate system is illustrated in Fig. 3.4. The actual determination of the position from satellite navigation is based on triangulation and the runtime of the signals from the satellites to the receiver. A minimum of four satellite signals is necessary for the calculation of the receiver position. The position accuracy can be further increased if more satellite signals are received, including signals from satellites of the GPS, BeiDou navigation satellite system (BDS), GLONASS and Galileo.

Regarding the usage and processing of the satellite positions, there are two standard problems in geometric geodesy: determining the coordinates of a position from an offset relative to another position, the direct geodetic problem, and calculating the distance and bearing between two given coordinates, the indirect geodetic problem.

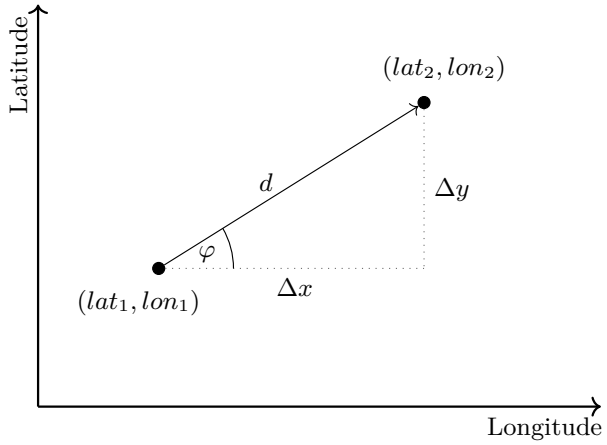

Figure 3.5: Situation of finding the coordinates (lat_2, lon_2) of a position where the offset $(\Delta x, \Delta y)$ from a reference position (lat_1, lon_1) is given. The altitude of this example is considered to be constant $alt = const.$ and the distance between the two locations is very small in comparison to the radius of the earth.

3.3.1 Direct Geodetic Problem

The direct geodetic problem describes the problem of finding the coordinates of a position that is given in terms of distance and angle from reference coordinates. While the solution of this problem is almost trivial in 2D coordinates and can be solved by pure trigonometry, finding the target coordinates becomes much more complex on a sphere. There are several approaches and formulas for the calculation of the target coordinates where the direct form of Vincenty's formula is well known [Vincenty 1975]. It is an iterative approach which is based on the assumption that the figure of the earth is an oblate spheroid resulting in a good accuracy in comparison to other methods. However, most methods are a good approximation for small distances while they can be off from the accurate coordinates when the distance becomes longer. Considering UAV flights of a few tens or hundreds of meters, the accuracy of most of the calculation approaches are acceptable. This applies also to the determination of the new coordinates following a rhumb line, i.e., a path of constant bearing which crosses all meridians at the same angle. Considering the case that the coordinates of a reference position $\left(lat_1, lon_1, alt_1\right)$ are given and the coordinates of a position $\left(lat_2, lon_2, alt_2\right)$ shall be found. Further, the target position is located at a distance of d meters with bearing angle φ from the reference position. The situation is depicted in 2D top view in Fig. 3.5. Eventually the coordinates of the target position $\left(lat_2, lon_2, alt_2\right)$ are given by

$$\begin{aligned} lat_2 &= lat_1 + \frac{d}{r_{\text{earth}}} \frac{180}{\pi} \cos\varphi \\ &= lat_1 + \frac{\Delta x}{r_{\text{earth}}} \frac{180}{\pi}, \end{aligned} \tag{3.1}$$

$$\begin{aligned} lon_2 &= lon_1 + \frac{d}{r_{\text{earth}}} \frac{180}{\pi} \frac{\sin\varphi}{\cos\left(lat_1\right)} \\ &= lon_1 + \frac{\Delta y}{r_{\text{earth}}} \frac{180}{\pi} \frac{1}{\cos\left(lat_1\right)}, \end{aligned} \tag{3.2}$$

$$alt_2 = alt_1 + \Delta z, \tag{3.3}$$

where the radius r_{earth} is chosen as the mean radius of the earth being 6 371 008.8 m according to Moritz [2000]. The Δx and Δy components are considered to be distances on axes that are parallel to the meridian and equator, respectively longitude and latitude axes, of the WGS 84 coordinate system while Δz is meant to be in normal direction out from the earth surface. This calculation of GNSS coordinates from relative distances is used in the Ardupilot flight software package [ArduPilot 2022] and has also been employed for the relative flight tests in this thesis.

3.3.2 Indirect Geodetic Problem

For most applications the absolute distance between two GNSS coordinates is relevant instead of the coordinates themselves, e.g., when flying 100 m with a UAV in a certain direction. The problem of finding this distance between two coordinates is known as the indirect geodetic problem. Similar as for the direct problem, several approaches exist, like another formula of Vincenty's formulae which again works with an iterative approach. However, a much simpler solution for the problem is given by the Haversine function which returns the greater circle distance between two coordinates $\left(lat_1, lon_1, alt_1\right)$ and $\left(lat_2, lon_2, alt_2\right)$. It is less accurate in comparison to Vincenty's formula but an acceptable approximation for rather short distances that occur in UAV flights, like they are considered in this thesis. The Haversine function is given by

$$\text{hav}\left(lat_1, lon_1, lat_2, lon_2\right) = d = 2r_{\text{earth}} \arcsin\left(\sqrt{\sin^2\left(\frac{\Delta lat}{2}\right) + \cos(lat_1)\cos(lat_2)\sin^2\left(\frac{\Delta lon}{2}\right)}\right), \tag{3.4}$$

where $\Delta lat = lat_2 - lat_1$ and $\Delta lon = lon_2 - lon_1$ are the differences in latitude and longitude, respectively. Beside (3.4), there is a second version of the Haversine formula which uses the tangent instead of the sine-function. It denotes to

$$\text{hav}\left(lat_1, lon_1, lat_2, lon_2\right) = d = 2r_{\text{earth}} \arctan\left(\frac{\sqrt{a}}{\sqrt{1-a}}\right), \tag{3.5}$$

with

$$a = \sin^2\left(\frac{\Delta lat}{2}\right) + \cos\left(lat_1\right)\cos\left(lat_2\right)\sin^2\left(\frac{\Delta lon}{2}\right). \tag{3.6}$$

Sometimes not only the distance between two GNSS coordinates is of interest but also the distance along each axis as depicted in Fig. 3.5. The respective components along the axes can be calculated by

$$\Delta x = \text{hav}\left(lat_1, lon_1, lat_1, lon_2\right) \begin{cases} 1 & \text{for } lon_2 \geq lon_1 \\ -1 & \text{for } lon_2 < lon_1 \end{cases}, \tag{3.7}$$

and

$$\Delta y = \text{hav}\left(lat_1, lon_1, lat_2, lon_1\right) \begin{cases} 1 & \text{for } lat_2 \geq lat_1 \\ -1 & \text{for } lat_2 < lat_1 \end{cases}. \tag{3.8}$$

3.3.3 Differential Satellite Navigation and Real-Time Kinematic System

The working principle of GNSS inherently comes with multiple uncertainties and error sources due to the fact that the position information is calculated from satellite signals. On the one hand, there are errors like the imprecise knowledge of the exact satellite position or slightly erroneous time bases within the satellites. On the other hand, there are errors in the channel the satellite signals have to travel through.

Especially the influence of ionosphere and troposphere can be large and needs to be compensated. Moreover, also reflections and multipathing can be problematic as well as the noise of the GNSS receiver itself [Zogg 2011]. There are multiple approaches for the treatment of the different error sources, like the simultaneous measurement at two frequencies or the correction of influences of the ionosphere using physical models. Furthermore, the comparison of the determined GNSS position with one or more reference stations can eliminate several errors. This comparison is commonly known as differential GNSS (DGNSS) or, due to the fact that it was most often used together with GPS in the past, as differential GPS (DGPS). DGNSS provides correction data for enhancement of the position measured by a GNSS receiver. The principle of DGNSS is based on a reference station that is located at a known position and can, therefore, determine the offset between its actual position and the currently measured GNSS position. With this information, correction data can be provided to the GNSS receivers for consideration and enhancement of their own measured position. The correction data can be either considered in the post-processing of position measurements or in real-time where the latter one requires a communication channel between the GNSS receiver and the reference station. A related method for accurate satellite navigation is real-time kinematic (RTK) positioning which uses a similar working principle as DGNSS but employs an own reference base station. This base station is usually placed at a fixed location which can be different for different operation scenarios. There are significant differences between RTK and DGNSS from a technical perspective. RTK is based on phase measurements of the carrier signal where DGNSS has traditionally been based on differential pseudorange code measurements to determine the offsets to the satellites [Landau et al. 2009]. The practical implementation of an RTK system consists of a minimum of one base station as reference and another GNSS receiver which is usually moved to the measurement locations. The communication for the correction data is typically realized as wireless channel in the ultra high frequency (UHF) band.

3.4 Chapter Summary

Since UAVs play a key role in this thesis, some of their basics have been reviewed in this chapter. Besides the operation principle of multirotors, the most important components and their interaction have been briefly described. It has been outlined that the rotors as well as the motors are crucial for the performance of a copter and need to be chosen in accordance with the UAV. Furthermore, the world geodetic system has been reviewed since all autonomous flights throughout the following chapters are based on GNSSs. The two geodetic problems, of finding coordinates that advance from other coordinates and determining the distance between two coordinates, have been discussed as well as approximations which are applicable of only small flight distances are relevant, like for UAV-based field measurements.

Part II

UAV-based Near-Field Measurements

Chapter 4

UAV-based Measurement Setup

Recent advances in the field of UAVs have opened up new possibilities in various areas, e.g., ranging from additional site information in disaster relief to autonomous seeding and fertilizer spraying in agriculture. Among others, UAVs have also elevated the field of in-situ antenna measurements as they are very flexible and mobile while, at the same time, they can carry field probes together with some measurement equipment to almost any position without further restrictions. First UAV-based field measurements have been been presented by Virone et al. in 2014 at very high frequency (VHF) and UHF [Virone et al. 2014; Paonessa et al. 2016]. The authors placed a measurement receiver on the UAV to collect the field data, while the position of the UAV, and, therefore, the field probe, was recorded by a laser tracker situated on the ground. In a later publication, the same authors substituted the laser tracker with a RTK GNSS for the measurement of a low frequency radio telescope at VHF frequencies [Bolli et al. 2018]. In the following years, several measurements at higher frequencies in the L-band [Chang et al. 2015], S-band [García-Fernández et al. 2017, 2018a] and C-band [García-Fernández et al. 2017, 2019a,b] have been presented, where different types of antennas, e.g., horn and reflector antennas, were employed as AUTs. All of these measurements have been carried out as magnitude-only measurements, with a receiver on the UAV while the AUT was transmitting. In 2016, Fritzel et al. [2016] proposed a UAV-based measurement setup which allows for coherent in-situ measurements, i.e., the measurement of the field magnitude and phase. For this, they came up with the usage of an optical fiber link that connects a measurement receiver on the ground to the field probe on the UAV. They also proposed the usage of a laser tracker to determine the measurement positions, which enables measurements at higher frequencies due to the highly accurate determination of the UAV position.

Even if the concept has been proposed back in 2016, it remained only a concept and has never been realized. Therefore, this chapter discusses the realization and implementation of such a coherent UAV-based NF measurement system, while measurement results are given in Chapter 5.

4.1 Overview and Radio Frequency Setup

The setup for coherent UAV-based NF measurements consists of two main parts: the flying platform or UAV, which carries the field probe while flying along the measurement path, and the ground station, which contains all instruments for data recording and control. On another level, the measurement setup can be divided into a flight part, which includes all electronics related to the flight control, and an RF part which involves the antennas and the measurement equipment. An overview of the measurement setup in form of a block diagram is shown in Fig. 4.1. Obviously, one of the key components of the whole measurement setup is the UAV itself as it moves the field probe along a predefined path to the desired measurement positions. The field probe, a Vivaldi antenna made out of PCB, is mounted to the

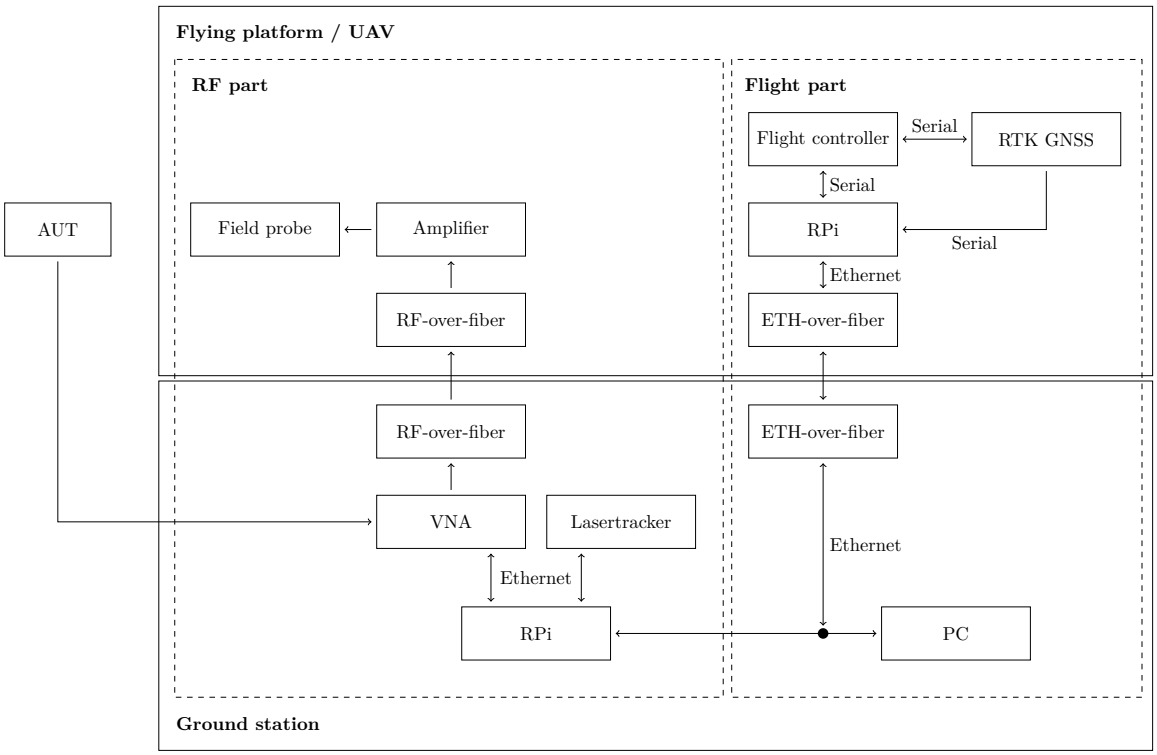

Figure 4.1: Block diagram of the UAV-based field measurement setup. All relevant components are represented while the classification into components that belong to the RF system and others which belong to the flight system is indicated (dashed boxes). Additionally, the order of the single components indicate whether they are located on the flying platform or on the ground during operation (solid boxes).

front of the UAV as depicted in Fig. 4.2. The measurement setup is capable of measuring the complex transmission parameter between the AUT and the field probe in magnitude and phase. For this, the probe on the UAV is connected to a VNA on the ground via an RF-over-fiber link, while the VNA is also connected to the AUT via an SMA-cable. For the measurements, the employed VNA was a two port analyzer of type R&S ZVL [R&S 2022f], while a commercial RF-over-fiber link was used [ViaLiteHD 2020]. In traditional NF measurements in anechoic chambers, the probing antenna is moved precisely to the desired measurement positions using highly sophisticated positioning systems. This is a conceptual difference in comparison to UAV-based measurements, since the UAV will fly only approximately along a desired path, while the actual measurement positions are determined using an external position measurement system. In order to precisely determine the position of the UAV, a laser tracker of type FARO Vantage [FARO 2016] is employed. Both, the laser tracker and the VNA, are triggered simultaneously and are read-out by a Raspberry Pi (RPi). The measured position and field data is stored on the RPi as well as streamed to the local network using a multicast approach. This allows all devices and applications in the network to access the data which can be used, e.g., for real-time plotting of the measured field or for a dynamic control of the flight path depending on the measured field data.

The dynamic range of a measurement setup describes the ratio of the field maximum and minimum that can be detected without the field signal clipping or vanishing in the noise floor. For the described RF part of the UAV-based setup, the dynamic range is mainly determined by the VNA while the RF-over-fiber link can reduce the possible dynamic range. Even if the overall link budget of the RF-over-fiber link is 0 dB, according to the specifications of the manufacturer, the fiber link has a noise figure of 23.5 dB

Figure 4.2: Hexacopter during measurement flight with vertically polarized field probe mounted at the front. The prism reflector target is placed at the front of the UAV and next to the probe antenna where a stable line-of-sight to the laser tracker can be ensured. Also, the optical fiber that connects the UAV with the ground in terms of control and RF signals is visible.

[ViaLiteHD 2020] which, in fact, reduces the dynamic range by about the same amount. To cope with this, the unidirectional RF-over-fiber link is used such that the probe is transmitting while the AUT works as receiver. This has no impact on the measurement results since antenna measurements are reciprocal. In turn, the advantage is that the influence of the noise figure of the RF-over-fiber link on the dynamic range is reduced as the fiber converters are fed with a constant power level from the VNA. Depending on the measurement distance, an additional power amplifier is inserted in the signal path right before the transmitting probe antenna.

The RF part of the measurement setup has been tested independently of the UAV. For this, NF measurements have been performed in a sports facility of the TUM, where, instead of a UAV, an operator person was moving the probing antenna around the AUT. Despite the fact that the orientation of the field probe was only maintained by feeling and, therefore, prone to errors, an FF error level of $-20\,\mathrm{dB}$ could be reached. Even though this error level is far from what is achieved in NF measurements in anechoic chambers, the manual measurements proved the functionality of the described RF part of the measurement setup. In addition, such a manual and highly mobile measurement system may be useful for fast on-site operation checks of antennas after they have been installed or transported. The corresponding measurement results have been published in Faul et al. [2020].

4.2 Flight Part of the Measurement Setup

The main task of the flight part of the measurement system is the movement of the field probe on a predefined measurement surface. The realization with UAVs is promising as they provide a high flexibility for the realization of arbitrary measurement surfaces. A hexacopter, comprising six glass fiber-based rotors and built on the DJI Flamewheel 550 frame [DJI 2022], is used within the measurement setup. Beside the frame itself, the flight controller, together with the control software, is one of the most important parts of any UAV as they define the capabilities of the flying platform. Therefore, the Ardupilot

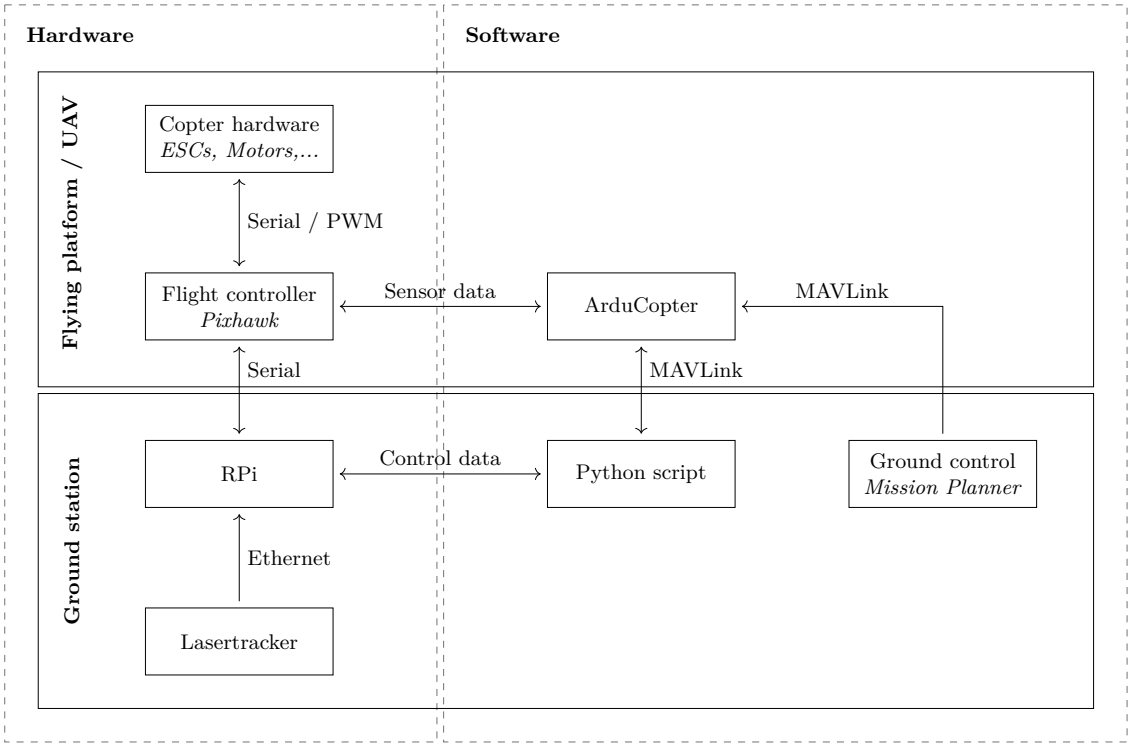

Figure 4.3: Block diagram showing the interaction between software and hardware components where it is also indicated whether the single parts belong to the flying platform or to the ground station.

flight software [ArduPilot 2022] was used on a Pixhawk Cube [PX4 2022] flight controller. Pixhawk is an open hardware controller, especially designed for the control of autonomous vehicles. The main advantages of the board are the redundant internal sensors and processors, as well as its flexibility in terms of external connections. Ardupilot, in turn, is an open-source control software that supports the control of many kinds of autonomous vehicles, e.g., multicopters, rovers and boats. It is fully configurable and, since there is a large community behind the software project, many hardware platforms and various sensors are supported. The interface to the flight software is a companion software that runs on a personal computer (PC), the ground control station (GCS). The GCS allows the access and monitoring of all parameters during flight. At the same time, additional customized scripts and programs can connect to the flight controller to either read and change flight parameters or send control commands. The connections and interactions between the different hardware and software components of the UAV are depicted in Fig. 4.3. One of the strengths of Ardupilot is the fully autonomous flight, i.e., flying along predefined paths without the need of any manual control. There are different flight modes for different levels of autonomy and user interaction. Except for a tuning of the UAV and pre-measurement flight tests, only the autonomous modes have been used for the flight tests and measurements.

Since an autonomous flight requires information about the position and orientation (6D-position) of the vehicle, the employed UAV is equipped with two GNSS receivers and two compasses, while the inertial measurement unit (IMU) of the flight controller contains multiple redundant gyroscopes and accelerometers. The redundancy of the different sensors does not only prevent possible sensor failures but allows an improved estimation of the UAV state. A fully autonomous flight is defined by a list of waypoints which are sequentially approached by the UAV. The individual waypoints, which consist of GPS position and heading information, can be defined either before the flight or dynamically, one at a time, each time a waypoint is reached. The accuracy with which the UAV follows the given flight path

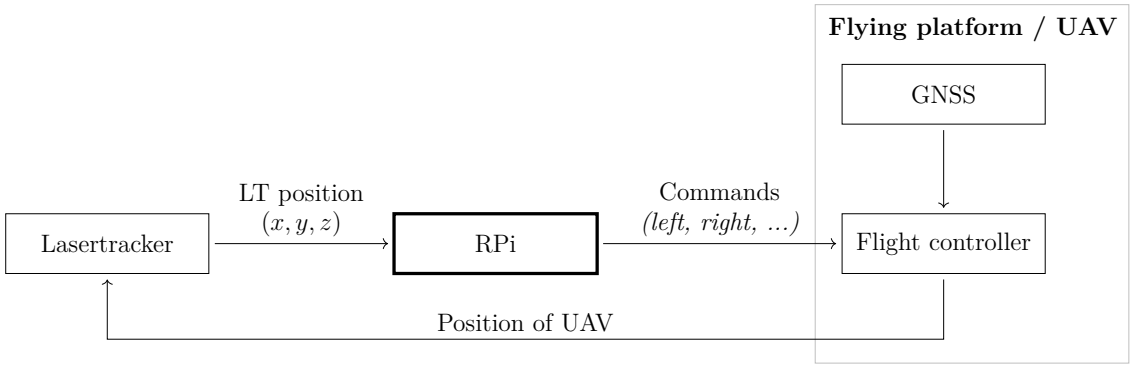

(a)

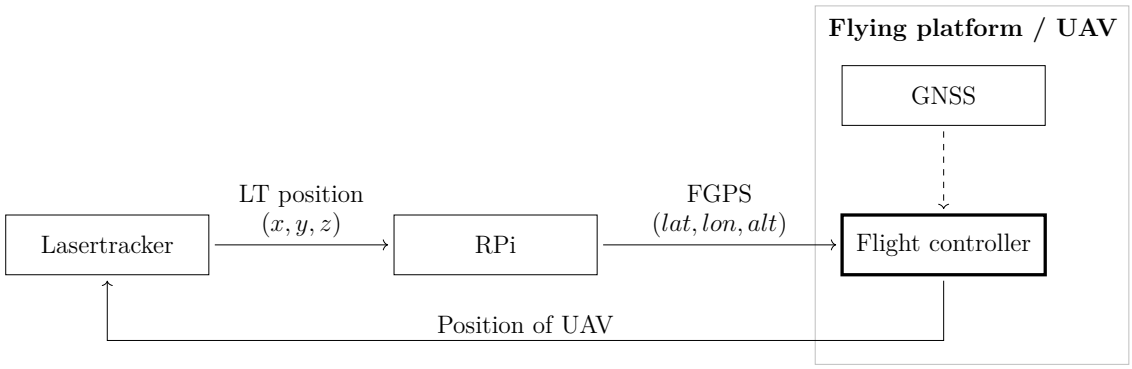

(b)

Figure 4.4: Block diagrams showing two different methods for UAV control by using position data from the laser tracker on the ground. Within the relative guidance setup, flight commands are sent from the RPi to the flight controller (a), while GNSS positions are sent to the flight controller in the FGPS setup (b). The leading component is marked with thicker lines, i.e., the component where the calculation of the flight commands from the position information is performed.

depends on several conditions where, foremost, the precision of the GNSS position data plays a major role. Therefore, the standard GNSS precision is often enhanced with the help of an RTK setup, where the used receiver boards [u-blox 2022] reach a position accuracy of about 3 cm to 5 cm.

During the construction of the UAV-based field measurement system, the idea to employ the laser tracker also for flight control came up, as it is used anyway for the measurement of the field position and its precision is several orders of magnitude better than that of an RTK GNSS. However, the usage of the laser tracker position data for flight navigation requires an external control loop or, at least, some pre-processing of the laser tracker positions before it is sent to the flight controller. Two examples of possible implementations are schematically shown in Fig. 4.4. An external control loop, as depicted in Fig. 4.4 (a), processes the position data of the laser tracker while specific flight commands for appropriate movements are sent to the UAV. The implementation of the control loop is straightforward due to the network-based distribution of the laser tracker position data, while the actual calculations can be implemented either on the ground site or on the RPi onboard of the UAV. However, the explicit realization and following flight tests revealed that the dead times, which are due to the measurement and calculation of the positions, are critical and that a more advanced control loop model is needed, especially to cope with fast UAV movements. Another idea for the usage of the laser tracker position for flight navigation is shown in Fig. 4.4 (b). Here, the laser tracker position data are transformed into GPS coordinates, as

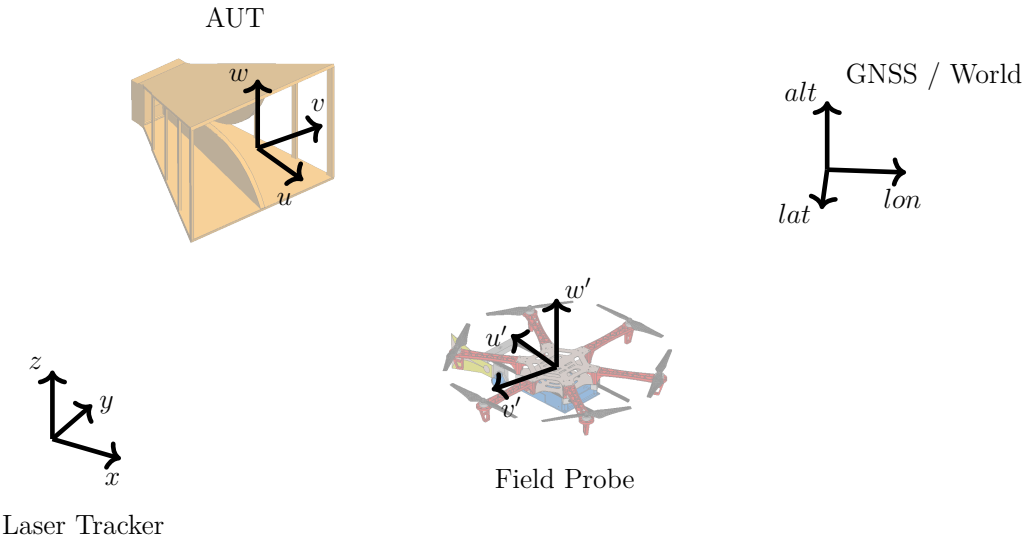

Figure 4.5: Different Cartesian coordinate systems used within the UAV-based measurement setup. The leading AUT coordinate system (u, v, w) is shown opposite of the UAV coordinate system (u', v', w') as they are linked by default to each other. The laser tracker positions (x, y, z) as well as the GNSS or world coordinate system (lat, lon, alt) describe the location of the UAV and need to be converted into the AUT coordinate system.

described in Section 3.3, and then provided to the flight controller as if it was an external GPS receiver. This approach is called fake GPS (FGPS) because of the non-existing GPS receiver. Both approaches, the external control loop and the FGPS, have the advantage that they can theoretically be realized and used in flights with bad or no GNSS reception such as inside of anechoic chambers. However, the practical use cases of UAV-based NF measurements are outdoor in-situ measurements, where environmental effects and weather conditions, like wind gusts, have a much higher impact on the accuracy of the flight path than the usage of a laser tracker over an RTK. Therefore, the RTK GNSS position was used for flight navigation, while the laser tracker was only employed for the determination of the measurement locations.

4.3 Position and Orientation

The measurement setup contains four different coordinate systems that are shown in Fig. 4.5. The main coordinate system of the measurement setup (u, v, w) is defined relative to the AUT, with the origin in the center of the aperture of the AUT. The u-axis points into the direction of the main beam and the v-axis to the left of the AUT. Similar as in NF measurements in anechoic chambers, a second coordinate system (u', v', w') is defined locally according to the main beam of the probe. This local probe coordinate system is locked to the UAV and can be seen as a re-definition of the body-fixed UAV coordinate system described in Section 3.1. The orientation of the probe at the different measurement positions, is described by the three rotations around the principal axes of the UAV, where at $(\vartheta, \varphi, \chi) = (90°, 0°, 0°)$, the AUT and probe coordinate systems face each other. In general, the roll, pitch and yaw angles of the UAV correspond with ϑ, φ and the polarization χ if the vertical w-axis of the AUT coordinate system

is congruent with the alt-axis of the GPS coordinate system. The relations are given by

$$\vartheta_{\text{prob}} = 90° - pitch\,, \tag{4.1}$$

$$\varphi_{\text{prob}} = yaw_{\text{offs}} - yaw\,, \tag{4.2}$$

$$\chi_{\text{prob}} = roll\,, \tag{4.3}$$

where yaw_{offs} is an offset angle that is determined during the alignment of the measurement setup.
In addition to the aforementioned coordinates, there is also the coordinate system of the laser tracker (x, y, z) in which the laser tracker itself is in the origin. The laser tracker coordinates $\boldsymbol{r}_{\text{lt}}$ can be transformed to the AUT coordinate system $\boldsymbol{r}_{\text{aut}}$ by

$$\boldsymbol{r}_{\text{aut}} = \boldsymbol{R}_{\text{z}}(\alpha)\boldsymbol{R}_{\text{y}}(\beta)\boldsymbol{R}_{\text{x}}(\gamma)\left(\boldsymbol{r}_{\text{lt}} + \boldsymbol{b}\right)\,, \tag{4.4}$$

where $\boldsymbol{R}_i(\alpha)$ is a rotation about the angle α around the i-axis, with $i \in \{x, y, z\}$, and $\boldsymbol{b}$ a translation vector. Furthermore, there is also the GNSS, or world, coordinate system (lat, lon, alt) which is used by the UAV for flight navigation. Similar to (4.4), the GNSS coordinates can also be transformed to the AUT coordinate system. The rotation angles and the translation are determined by an appropriate alignment procedure. Within the field measurements, this is done by the measurement of several positions on the UAV with the laser tracker and the simultaneous recording of the GNSS position and the orientation angles. Normally, the vertical z-axis of the laser tracker matches with the vertical alt-axis of the world system if the laser tracker has been aligned and placed carefully on stable ground.

4.4 Data Synchronization

Within the UAV-based measurement setup, the field, position and orientation data are all obtained from different sources – from the VNA, the laser tracker and the UAV, respectively. As described in Section 4.1, the VNA and the laser tracker are triggered together by a RPi which also collects the data from the two measurement devices. This ensures that the field and position data correspond to each other. In contrast, the flight controller of the UAV cannot be triggered, which raises the necessity of a synchronization procedure to match the data obtained from the different data sources. In the following, three different synchronization approaches are described: the synchronization of the data using a global timestamp, using the laser tracker positions and with the help of an RF switch.

4.4.1 Synchronization by GPS Timestamp

The easiest way to match the orientation data from the UAV to the position and field data, obtained from the laser tracker and the VNA, is the usage of a global timestamp throughout the measurement system. The UAV assigns a GPS timestamp to all of its parameters and values and, therefore, also to the orientation data. The laser tracker and VNA are triggered with a common signal from the RPi, which also assigns a timestamp to the position and field data after they are retrieved from the measurement devices. This timestamp, though, depends on the time of the RPi's clock which is normally not synchronized with anything but can be synchronized to GPS time with the help of a suitable GNSS receiver. However, on the one hand, the RPi has no input/output (IO) ports that can be used for real-time tasks and, therefore, an uncertainty between the time of the trigger pulse and the assignment of the timestamp arises. On the other hand, the general-purpose input/output (GPIO) pins of the RPi, that are used to create the trigger signal, have a latency in the order of sub-milliseconds, which is negligible within the measurement setup. In addition to the time uncertainties regarding the timestamp of the laser tracker and the VNA, there is also an uncertainty regarding the timestamps of the orientation data. The time of the UAV is obtained

from the GNSS receiver, where the exact latency due to cables and signal converters between the GNSS receiver and the flight controller is not known. Bringing all together, the absolute error regarding the timestamps is expected to be in the order of a few ten to hundred milliseconds. Since the offset between the timestamps is the same for all measurement data, and the orientation of the UAV does not change rapidly and is similar during the whole measurement, the timestamp offset might only have a minor effect on the accuracy of the FF resulting from the NF measurement. Nonetheless, it must be the goal to eliminate all error sources to ensure an even higher accuracy of the measurement setup.

4.4.2 Synchronization by Lasertracker

The offset between the timestamps of the UAV and the RPi on the ground can also be found by matching the position data of the laser tracker to the recorded GNSS flight path of the UAV. For this, the GNSS positions (lat, lon, alt) are converted to Cartesian coordinates $\tilde{\boldsymbol{r}} = (\tilde{x}, \tilde{y}, \tilde{z})$, according to (3.7) and (3.8), and relative to a position $\tilde{\boldsymbol{r}}_0$. Further, the static offset vector from the flight controller to the laser tracker target is corrected by calculating the offset vector for every GNSS position with the corresponding orientation angles. Given the corrected relative GNSS positions $\tilde{\boldsymbol{r}}_{\mathrm{corr}}$, the translation and rotation between $\tilde{\boldsymbol{r}}_{\mathrm{corr}}$ and the laser tracker position $\boldsymbol{r}_{\mathrm{lt}}$ is calculated as

$$\boldsymbol{r}_{\mathrm{lt}} = \boldsymbol{R}_{\mathrm{z}}(\alpha)\boldsymbol{R}_{\mathrm{y}}(\beta)\boldsymbol{R}_{\mathrm{x}}(\gamma)\left(\tilde{\boldsymbol{r}}_{\mathrm{corr}} + \boldsymbol{b}_{\mathrm{offs}}\right) \ , \tag{4.5}$$

where $\boldsymbol{b}_{\mathrm{offs}}$ is the translation offset vector and $\boldsymbol{R}_i(\alpha)$ a matrix that rotates a vector $\boldsymbol{r}$ about the angle α around the i-axis, where $i \in \{x, y, z\}$. The translation and rotation between $\boldsymbol{r}_{\mathrm{lt}}$ and $\tilde{\boldsymbol{r}}_{\mathrm{corr}}$ can be found by minimizing (4.5) for all positions together. It is given by

$$\underset{\substack{\boldsymbol{b}_{\mathrm{offs}} \in \mathbb{R}^3 \\ \{\alpha,\beta,\gamma\} \in \mathbb{R}}}{\text{minimize}} \sum_n \left[\boldsymbol{R}_{\mathrm{z}}(\alpha)\boldsymbol{R}_{\mathrm{y}}(\beta)\boldsymbol{R}_{\mathrm{x}}(\gamma)\left(\tilde{\boldsymbol{r}}^{\,n}_{\mathrm{corr}} + \boldsymbol{b}_{\mathrm{offs}}\right) - \boldsymbol{r}^{\,n}_{\mathrm{lt}}\right]^2 \ , \tag{4.6}$$

where all measurement positions are added and, e.g., $\boldsymbol{r}^{\,n}_{\mathrm{lt}}$ is the nth position recorded by the laser tracker. After the matching of the GNSS flight path and the laser tracker positions, the offset in the timestamps is found by comparing the two time bases. Within the measurement setup, this approach is used for the enhancement of the synchronization regarding the global GPS timestamp.

4.4.3 Synchronization by RF Switch

The required position accuracy within the measurement setup depends on the measurement frequency as pointed out in Chapter 2. According to the rule of thumb, which requires a position accuracy of $\lambda/50$ for an FF error of about -50 dB, the position must be resolved up to 6 cm for a NF measurement at 100 MHz. As this requirement can be fulfilled by the RTK GNSS, the laser tracker is not used for measurements at low frequencies. However, this also drops the possibility to synchronize the data via the position as described before, while the problem changes to synchronizing the field data with the UAV, respectively GNSS positions. A possibility to synchronize the data and to find the time offset between the UAV and the RPi on the ground is with the help of an RF switch in the VNA signal path that is controlled by the flight controller of the UAV. A change of the switch state can be easily seen on the VNA, while the control signal of the switch can be retrieved from the UAV logfiles. Both signals can then be shifted in time until the patterns of the switch and control signals match. In this case, the adjusted time is the time delay. A comparison of the field signal with the control signal is shown in Fig. 4.6. The two main sources of uncertainty within this approach of synchronization are the exact switching time of the RF switch and the time delay between the recorded control signal and the actual control output. For the measurement in Fig. 4.6, an RF switch of type NXP SA630 [NXP 2014] has been used. Its switch delay

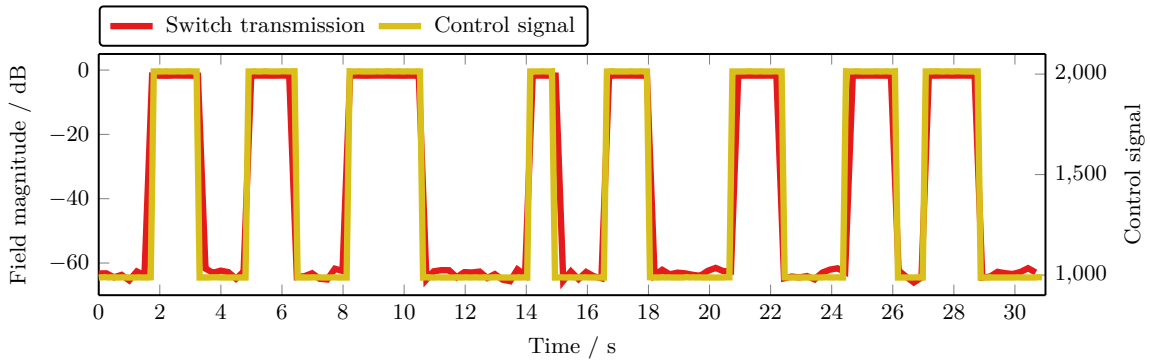

Figure 4.6: Comparison of the RF transmission signal of an RF switch with its control signal. The switch pattern has been chosen to be non-periodic such that the transmission and the control signal can be matched in terms of signal changes.

time is stated as 20 ns with typical rise and fall times of 5 ns and is, therefore, negligible in this context. The delay between the recorded control signal and the actual control output is unknown but likely to be in the order of a few milliseconds. This delay arises since the digital control signal, obtained from the manual remote control, is recorded, while the RF switch is connected to an analog relay switch output of the flight controller.

4.5 Chapter Summary

A setup for conducting coherent field measurements using a UAV has been presented in this chapter. It has been outlined that the setup consists of two parts, the flight part and the RF part, which can be examined separately to a certain degree while they also interact with each other. The main components of both parts have been described together with their mutual interaction. Additionally, the different coordinate systems of the measurement setup have been discussed which arise from the usage of several originally independent position measurement systems, on the one hand, and an NFFFT, on the other hand. Eventually, different approaches for the synchronization of the field and position data have been presented, where an RF switch can be employed for the cases in which a globally synchronized GPS timestamp is not feasible.

Chapter 5

Measurement Results

Both parts of the measurement setup, described in Chapter 4, have been tested separately. The RF part of the setup has been used for manual measurements where an operator person moved the probing antenna in the NF of the AUT. The results have been published in [Faul et al. 2020]. The flight performance and overall optimization of the UAV was tuned in many iterations. However, there are still some details which can be further optimized as will be outlined in Chapter 9.

Bringing all together, coherent UAV-based NF measurements have been performed at the sports campus of the TUM in Munich, Germany. Besides the measurement results, methods for the evaluation of the correctness of the measurement data are discussed in the following.

5.1 Planar Measurement Geometry

A planar measurement surface can be easily realized regarding the flight path of a UAV, since the UAV only needs to fly left and right while changing its altitude. In addition, a planar measurement geometry is also beneficial for the use of a laser tracker within the measurement setup since the prism reflector target can be mounted on the side of the UAV, maintaining an uninterrupted line-of-sight during the whole measurement. Therefore, planar UAV-based NF measurements were performed at first where the double-ridged horn antenna HF906 [R&S 2022b] was employed as AUT. It was placed on a stand about 3 m above ground, while the laser tracker was placed about 10 m to the side of the AUT. The probing antenna on the front of the UAV was a Vivaldi antenna realized as printed circuit board (PCB). Within the measurements, the polarization of the AUT was linear in vertical direction and coinciding with the vertical w-axis of the measurement coordinate system. Similarly, the polarization of the field probe was vertical but changed to horizontal for some measurement flights to also collect field data of the cross-polarized field component. For this, the field probe was substituted with a second identical Vivaldi antenna, mounted to a different holding structure as this simplified the exchange of the antennas and improved the position accuracy of the mounting procedure. The AUT together with the UAV and the horizontally polarized field probe are depicted in Fig. 5.1, while the UAV has been shown in Fig. 4.2 with the vertical field probe mounted at the front.

The AUT and the field probe were connected to a VNA of type R&S ZVL [R&S 2022f] that was placed on the ground and capable of recording the complex transmission parameter between the two antennas. As described before, the field probe was connected by a commercial RF-over-fiber link [ViaLiteHD 2020] and transmitting during the measurements. The measurements were conducted at a frequency of 2.45 GHz, while the source power and measurement bandwidth of the VNA were chosen to 0 dBm and 10 kHz, respectively. Additionally, an amplifier on the UAV boosted the signal about 20 dB. The UAV was covering the planar measurement surface in horizontal lines which are not exactly straight and

Figure 5.1: Picture of the AUT and the UAV during the planar in-situ measurement. The horizontally polarized field probe is depicted which is connected to the measurement receiver at the ground via an RF-over-fiber link.

horizontal due to wind and environmental effects. The maximum flight speed of the UAV was set to $2\,\mathrm{m\,s^{-1}}$, with 1 s wait time on each side of the measurement plane such that the UAV was able to realign itself before starting the flight back to the other side of the plane. These flight parameters have been found in several flight tests, regarding a stable and almost constant orientation of the UAV, respectively the field probe, on large parts of the measurement surface. Therefore, the field parts at the left and right edges of the measurement plane were cut out in the post-processing making the probe orientation much more homogeneous for the remaining field. The measurement coordinate system has been defined by the measurement of the aperture of the AUT as described in Section 4.3.

The magnitude of the measured but truncated NF is shown in Fig. 5.2 (a) and (b) for the vertical and horizontal polarization, i.e., the co- and cross-polarized field components, respectively. The horizontal lines of the flight paths can be easily seen in the figures. As a result of the high sample rate and the flight direction, the density of the field samples is much higher in horizontal than in vertical direction. However, the sampling theorem is fulfilled everywhere since the largest distance between two adjacent samples in vertical direction is about 20 cm. Figure 5.2 (a) also clearly shows the aperture of the AUT while the field diminishes to about $-35\,\mathrm{dB}$ to $-40\,\mathrm{dB}$ at the edges of the truncated scan plane. The phase of the measured field is depicted in Figs. 5.2 (c) and (d). According to simulations and planar measurements within anechoic chambers, one would expect rings of equal phase values within the planar measurement surface. However, the measurement surface is highly irregular and not quite a plane as the UAV changes its distance to the AUT during flight, which is due to environmental effects and can easily vary in the order of one or two wavelengths regarding the measurement frequency. The measured NF is transformed to the FF with the help of the FIAFTA. Looking carefully at the NF in Figs. 5.2 (a) and (b) reveals that there are some field samples with lower values than the surrounding field. This is due to the orientation change of the UAV during flight and is taken into account by the probe correction within the NFFFT. The main cuts of the resulting FF pattern at $\vartheta = 90°$ and $\varphi = 0°$ are shown in Figs. 5.3 (a) and (b), where the valid angles are marked according to (2.24) and (2.25). The transformed FF is compared to a reference measurement that has been performed using the spherical NF range in the anechoic chamber of the TUM. Furthermore, the error of the field from the UAV-based measurement E_{meas} is calculated with respect to the field of the reference measurement E_{ref}, according to (2.31). The

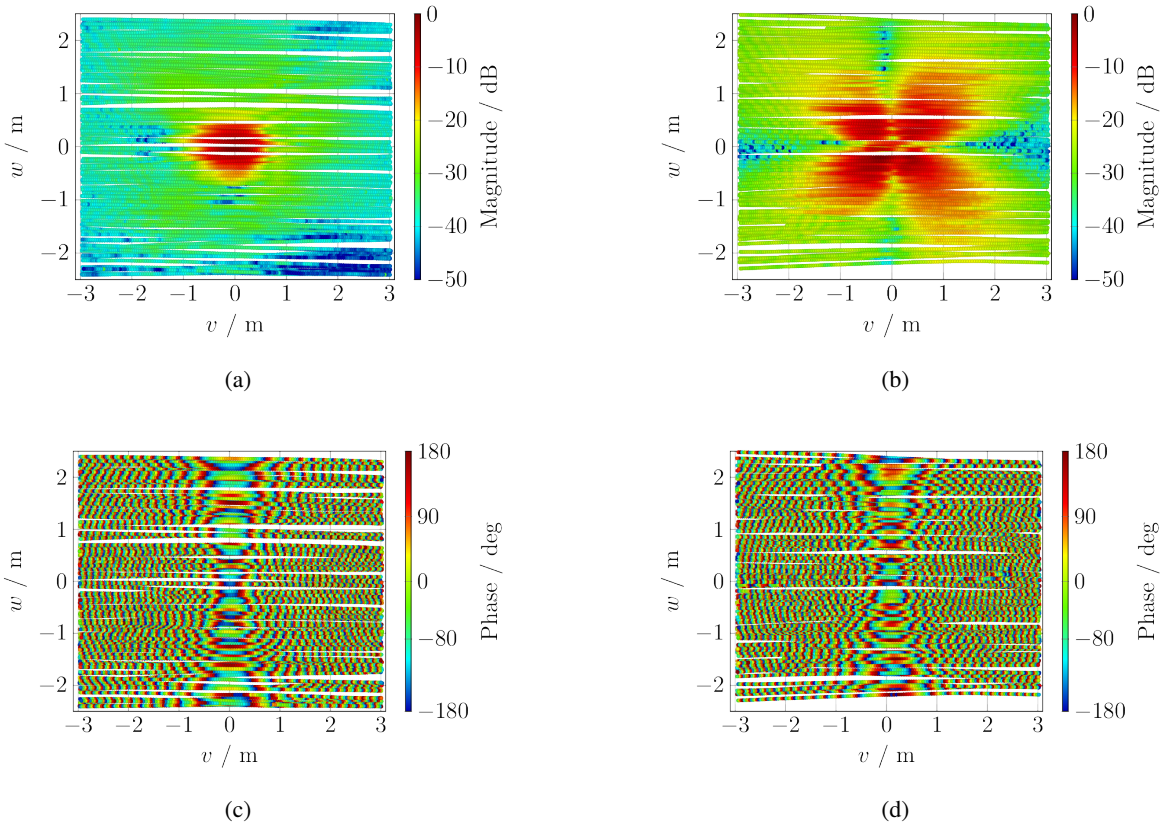

Figure 5.2: Two dimensional plots of the measured field resulting from the planar UAV-based antenna measurement. The magnitude of the vertical co-polar (a) and the horizontal cross-polar (b) components are depicted, while (c) and (d) show the phase of the vertical and horizontal field components, respectively.

maximum error within the valid angles is −17.7 dB in the ϑ- and −21 dB in the φ-cut of the FF. However, it can be easily seen that the error in the ϑ-cut, in Fig. 5.3 (a), is much larger than that in the φ-cut, in Fig. 5.3 (b), where the error is low in large parts. This is likely to be an effect of the used field probe whose phase pattern is more smooth in vertical than in horizontal direction, while the incident angle of the measured field on the field probe increases significantly to the edges of the scan plane. Also, the valid angles in φ are small as a result of the planar measurement, where especially those field samples at the edges of the scan plane that are prone to larger errors have a similar contribution within the NFFFT as no special pre-conditioning of the measured field is performed. The full FF error is depicted as 2D plot in Fig. 5.4, while, again, the valid angles are marked. The plot reveals that the FF error is not at all homogeneously distributed. The maximum error has a value of −9.56 dB and occurs at $\varphi = 68°$ and $\vartheta = 52°$. This is expected regarding the FF cuts in Fig. 5.3 as this maximum error occurs at the edge of the scan plane.

5.2 Cylindrical Measurement Geometry

The large error, especially in φ-direction of the FF, i.e., the ϑ-main cut, is supposed to be mainly due to the angular misalignment of the AUT and field probe, especially at the borders of the scan plane. Therefore, starting from the planar measurement geometry, the UAV has been programmed to always

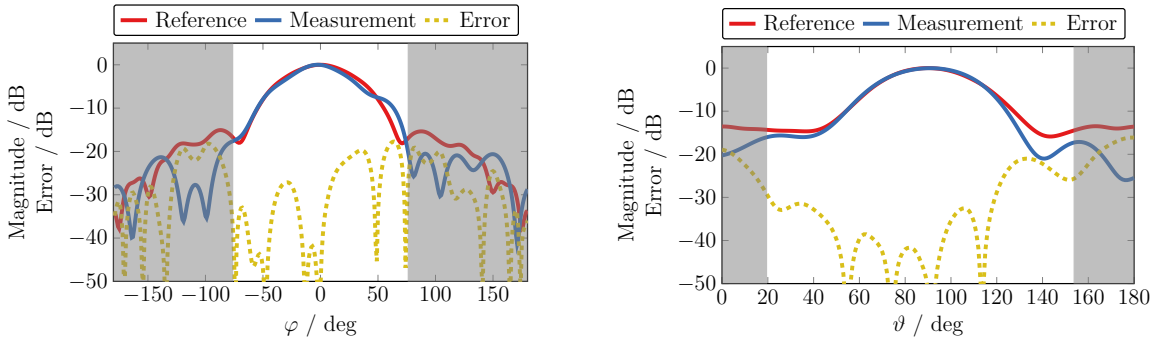

Figure 5.3: Main cuts of the FF at $\vartheta = 90°$ (a) and $\varphi = 0°$ (b) from the planar in-situ measurement. The valid angles are marked where the field beyond is grayed out.

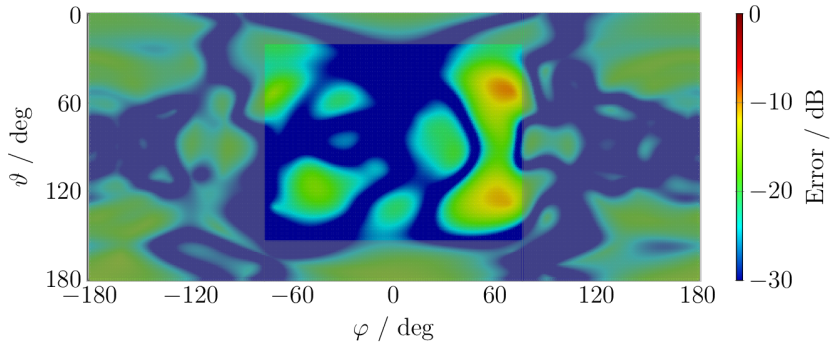

Figure 5.4: Two-dimensional plot of the FF error of the planar UAV-based measurement with respect to a reference measurement. The valid angles are marked according to the measured field.

point the field probe to the AUT. However, since the field probe is mounted to the UAV in a fixed manner, the UAV itself has to rotate during flight which, in turn, has an impact on the flight path itself as a consequence of the working principle of a hexacopter. Rotating the UAV during a planar flight resulted in an eight-shaped flight path with a comparably unstable orientation in several tests. Additionally, there was an occasional interruption of the required line of sight between the laser tracker and its reflector target that is mounted close to the field probe on the UAV, making it impossible to utilize the resulting flight path for real field measurements. Instead, a cylindrical measurement geometry was realized since a cylindrical flight has been found to be more stable than the “rotating” planar flight described before. The measurement setup was similar as for the planar measurement including the same AUT, while, this time, the laser tracker was placed underneath the AUT with a vertical distance of 1.6 m. The reflector target was placed underneath the field probe, realizing a stable line of sight to the laser tracker at all parts of the cylindrical scan surface, and circumventing the need to use a gimbal for the alignment of the reflector target which, in fact, would be too heavy for the employed hexacopter. Figure 5.5 shows a picture of the cylindrical measurement setup where even the RF-over-fiber link can be seen that connects the field probe with the VNA. The measurement frequency was 2.45 GHz, the source power of the VNA 0 dBm and the measurement bandwidth 10 kHz. As mentioned before, no gimbal was used to rotate the reflector target towards the laser tracker, since the payload and, therefore, the overall weight of the UAV was already pushed to its limits and adding more mass was not possible. Instead, two different tilt angles of the reflector target were realized which could be manually changed between flights. As

Figure 5.5: Picture of the cylindrical measurement setup. The laser tracker was placed under the AUT, maintaining a stable line-of-sight to the reflector target underneath the field probe at the front of the UAV.

a consequence, two different radiation patterns of the field probe including the UAV were used for the probe correction within the NFFFT, with the only difference of the tilt angle of the reflector target. In the measurement, the AUT was vertically polarized and only the co-polar, vertical, polarization was measured. The magnitude and phase of the measured field is depicted as 2D plot in Fig. 5.6, where the axes are given in cylindrical coordinates with $r = \sqrt{u^2 + v^2}$ and $\rho = \arctan(v/u)$. The plot of the magnitude in Fig. 5.6 (a) clearly shows the aperture of the antenna while also the single lines of the horizontal flight path are visible. The average radius of the scan cylinder was about 1.9 m though field parts close to the bottom could not be measured since the probe antenna interrupted the line of sight between the laser tracker and the reflector target. Similar as in the planar measurement, the field was significantly oversampled according to the sampling theorem to enable an averaging of the NF and, especially, to lower the influence of single erroneous field samples. The plot does also reveal very prominently that the horizontal lines of the flight path are in no way perfect horizontal. There is always a variation in altitude of the UAV during flight due to weather changes since the control of the altitude mainly relies on a barometer which is sensitive to temperature and wind gusts. The phase in Fig. 5.6 (b) does not exhibit a clear structure and seems to be mostly random. This is in part a consequence of orientation change of the probe but, primarily, due to the variation of the distance between AUT and field probe. In fact, the NFFFT proves that the phase is by no means random. The main cuts of the resulting FF at $\vartheta = 90°$ and $\varphi = 0°$ are shown in Fig. 5.7. Similar as for the planar case, the transformed FF is plotted against a reference measurement from the anechoic chamber, where the error is, again, calculated according to (2.31). As expected, the error of the measured field is significantly lower than for the planar case. The maximum error in the ϑ-cut is -32 dB within the valid angles, while it is even lower in the φ-cut. A comparison with the FF of the planar case confirms that the valid angles are larger in φ but smaller in ϑ which is due to the extend of the measured NF. This becomes even more clear in the 2D error plot, depicted in Fig. 5.8, where the area inside the valid angles is marked. This 2D plot reveals that the resulting FF error from the cylindrical UAV-based measurement is, for large parts of φ

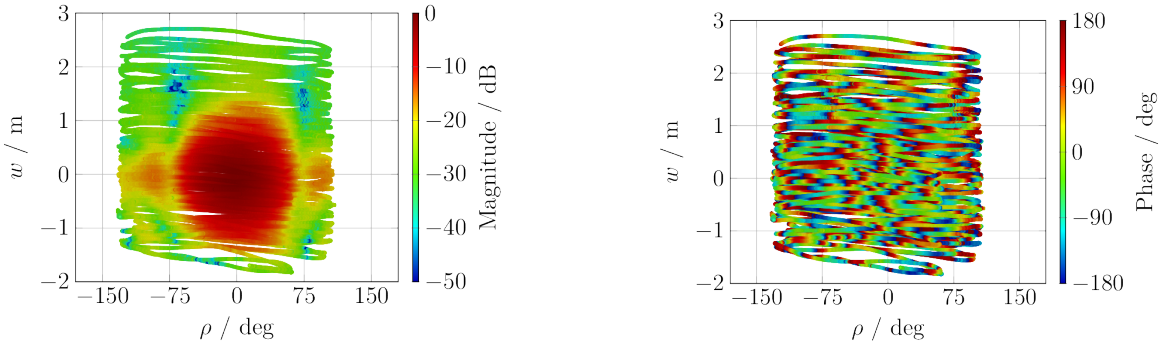

Figure 5.6: Two-dimensional plots of the magnitude (a) and phase (b) of the NF obtained from the cylindrical UAV-based antenna measurement. The plots are shown in cylindrical coordinates (r, ρ, w).

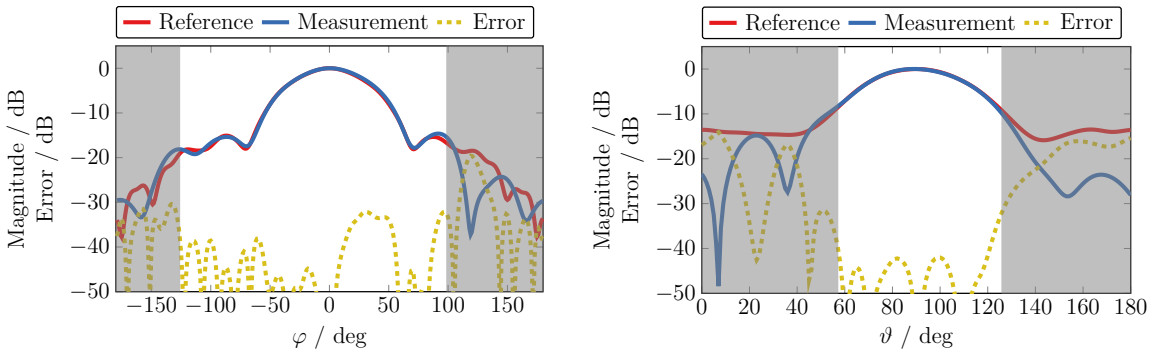

Figure 5.7: Main cuts of the FF from the cylindrical in-situ measurement at $\vartheta = 90°$ (a) and $\varphi = 0°$ (b). The valid angles are marked where the field beyond is grayed out.

and even outside the valid angles, less than −30 dB. The global maximum error of the FF is −21.3 dB at $\varphi = 51°$ and $\vartheta = 58°$, while overall a successful UAV-based NF measurement was performed with an error level better than −30 dB.

5.3 Verification of the Measured Field

Every measurement is prone to errors and uncertainties, which may change the measurement results in an undesired way. The most important sources for measurement errors occurring in UAV-based antenna measurements are discussed in Chapter 6. However, besides the knowledge of the different error sources and their general impact on the measurement accuracy, it is important to know how precise the field data in a specific measurement scenario is. Therefore, in the following, two methods for the verification and analysis of measured field data are discussed.

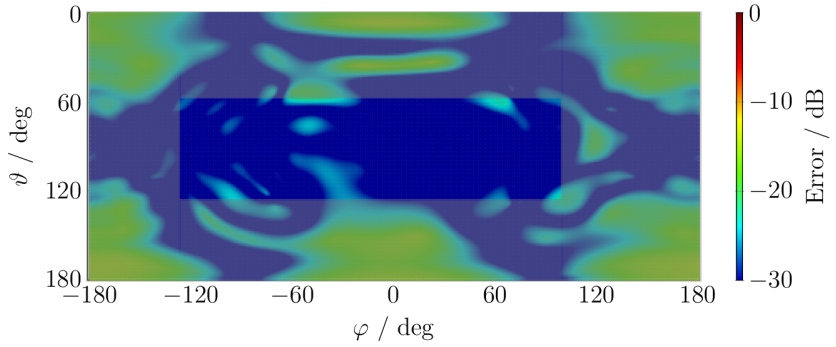

Figure 5.8: Two-dimensional plot of the FF error of the cylindrical UAV-based measurement with respect to a reference measurement. The valid angles are marked according to the measured field.

5.3.1 Analytical Calculation according to the Friis Equation

The transmission between two antennas is approximately described by the Friis transmission equation. However, as discussed in Section 2.3, the Friis transmission equation is only valid under FF conditions since plane waves are assumed to be incident on the antennas. Still, the equation also provides an approximation for the NF and, therefore, can be used to check if the measured field data are plausible. For this, the radiation pattern of the AUT and the field probe are used within the Friis transmission equation, which has been given in Section 2.3 as

$$P_\mathrm{r} = \left|1-\Gamma_\mathrm{r}\right|\left|1-\Gamma_\mathrm{t}\right|\left|\cos\psi\right|\left(\frac{\lambda}{4\pi r}\right)^2 G_\mathrm{r}(\vartheta_\mathrm{r},\varphi_\mathrm{r})G_\mathrm{t}(\vartheta_\mathrm{t},\varphi_\mathrm{t})P_\mathrm{t}\,. \tag{5.1}$$

Here, Γ_r and Γ_t are the reflection coefficients of the antennas due to impedance matching and ψ is the polarization-mismatch angle between the two antennas. Since the exact reflection coefficients of the antennas might be unknown, or at least the reflection coefficient of the AUT, Γ_r and Γ_t are both assumed to be zero. Further, the gains G of the antennas can be substituted by their directivities D, which, despite being a loss of information, can be justified as the theoretically calculated and the real measured fields are usually both normalized before comparison. The theoretical field at the different measurement locations r can be calculated by assuming an arbitrary transmitted power P_t, e.g., 0 dBm, and by the calculation of the corresponding angles ϑ_r and φ_r, regarding the underlying coordinate system and the instantaneous orientation of the field probe. All of these assumptions result in a changed Friis equation which denotes to

$$P_\mathrm{r} = \left|\cos\psi\right|\left(\frac{\lambda}{4\pi r}\right)^2 D_\mathrm{r}(\vartheta_\mathrm{r},\varphi_\mathrm{r})D_\mathrm{t}(\vartheta_\mathrm{t},\varphi_\mathrm{t})P_\mathrm{t}\,. \tag{5.2}$$

However, it becomes clear that the approach to use the Friis transmission equation for a first verification of the measured field data can only be used if the radiation pattern of the AUT is known or, at least, if it is approximately known as, e.g., in in-situ operational checks or in a recurring verification of the AUT. Moreover, the pattern of the field probe is, of course, assumed to be known, also with respect to the probe correction within the NFFFT. The continuous orientation change of the UAV is taken into account regarding the angles ϑ and φ of the AUT and probe patterns. Furthermore, the polarization mismatch is taken into account in (5.2), where ψ is equivalent to the roll angle χ of the UAV assuming that the vertical axis of the AUT coordinate system coincides with the altitude axis of the GPS coordinates. However, regarding the non-ideal suppression of the cross-polar (xp) components of the involved antennas in co-polar (cp) measurements, further terms must be introduced into (5.2), to account for the different cp-xp

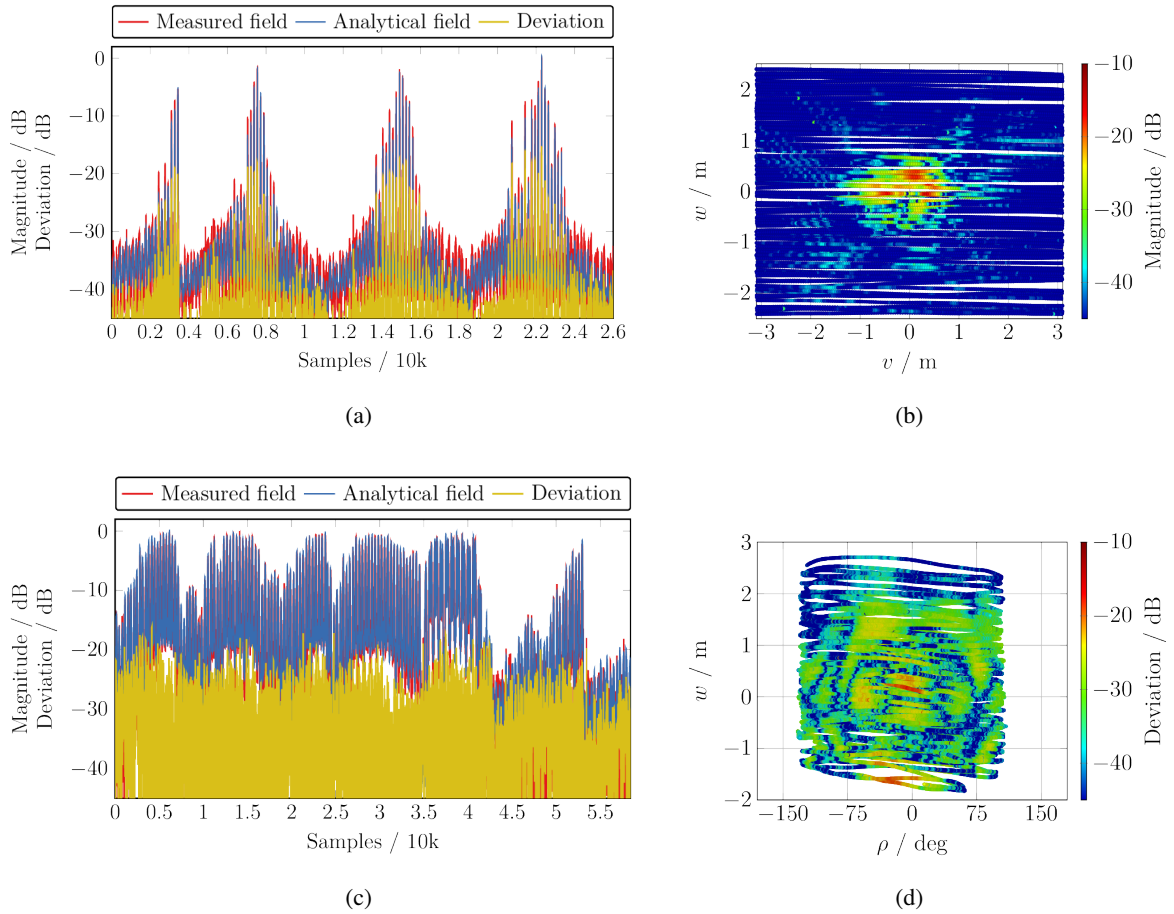

Figure 5.9: Deviation between the measured and the analytically calculated fields for the planar (a)/(b) and the cylindrical (c)/(d) measurement geometry. The deviation is plotted for every individual field sample in (a) and (c), while (b) and (d) show the spatial distribution of the magnitude of the deviation.

combinations. The total voltage U_r that would be seen by a measurement receiver is given by

$$U_\mathrm{r} = \sqrt{Z_0 P_{\mathrm{r},(\mathrm{cp,cp})}}\cos(\chi) + \sqrt{Z_0 P_{\mathrm{r},(\mathrm{xp,cp})}}\sin(\chi) + \sqrt{Z_0 P_{\mathrm{r},(\mathrm{cp,xp})}}\sin(\chi) + \sqrt{Z_0 P_{\mathrm{r},(\mathrm{xp,xp})}}\cos(\chi) \quad (5.3)$$

where Z_0 is the wave impedance of free space and χ the roll angle of the UAV and also the polarization mismatch between the AUT and field probe. The signs of the terms are determined with respect to the phase patterns of the involved antennas, while the power within the single terms is given by

$$P_{\mathrm{r},(i,j)} = \left(\frac{\lambda}{4\pi r}\right)^2 D_{\mathrm{r},i}(\vartheta_\mathrm{r}, \varphi_\mathrm{r}) D_{\mathrm{t},j}(\vartheta_\mathrm{t}, \varphi_\mathrm{t}) P_\mathrm{t}\,. \quad (5.4)$$

The field has been calculated according to (5.3) and (5.4) for the planar and cylindrical measurements discussed before. The deviations, together with the measured and the analytically calculated fields, are depicted in Fig. 5.9. Figure 5.9 (a) shows the magnitudes of the fields together with the magnitude of the deviation for every individual field sample. The measured and the calculated fields exhibit three mountain-like regions of larger field magnitude. Considering the planar measurement, these are the field regions in the main beam of the AUT from consecutive measurements. The deviation between the measured and the calculated field occurs in the same regions of the main beam where the measured and analytically calculated fields exhibit the largest magnitude values. Here, it shall be noted that both,

the measured and analytically calculated, fields are normalized in the plots while the deviation has been calculated according to (2.31). The maximum deviation is about −15 dB, while the deviation is smaller than −20 dB in large parts of the field. Figure 5.9 (b) shows the 2D spatial distribution of the deviation on the measurement plane, which confirms that the largest deviation occurs in the main beam of the AUT. Similar observations can be made regarding the cylindrical UAV-based measurement. The deviation between the measured and the analytically calculated field is depicted in Fig. 5.9 (c). Here, the maximum deviation is about −16 dB, while the deviation is again lower than −20 dB in large parts of the field. Similarly, the 2D plot in Fig. 5.9 (d) reveals that the largest deviation occurs in or close to the main beam of the AUT.

Both measurements exemplify that no exact agreement between the measured and the analytically calculated field can be expected. Though, the analytical calculation of the approximately measured field is a valuable approach for the verification of the measured field. Moreover, the calculation can be performed without the knowledge of the full NF and can, therefore, be executed on-line during the acquisition of the field data. Still, the method is only useful for plausibility checks since many assumptions are made and also the underlying FF condition might not be fulfilled in most measurement scenarios.

5.3.2 Recalculation of Field from the Equivalent Sources

An advanced method for the verification of the measured field makes use of the operation principle of the NFFFT. Within the NFFFT, equivalent sources are calculated from the measured NF data at or close to the position of the AUT. As described in Section 2.5, the FF is calculated from these equivalent sources, while the field can also be calculated at any other position in space. For the evaluation of the planar and cylindrical UAV-based measurements, electric and magnetic current densities on a triangular mesh that surrounds the AUT have been used as equivalent sources. These current densities are arranged in such a way that they represent the NF at the measurement positions as accurately as possible. However, the current distribution is often unable to ideally represent all NF samples due to manifold reasons such as erroneous measurement samples, limited computation time or the arrangement of the equivalent sources. The derived current distribution is, therefore, an approximation which results in the fact that the real measured field and the field recalculated from the equivalent currents does not exactly match. The deviation between the measured and the recalculated field is a measure of how good the measured field data can be represented by electric and magnetic currents on the AUT. Similarly, it is also a measure of how good the recorded field is, i.e., how much the ideal field of the AUT is disturbed by measurement uncertainties and noise.

Even if the measured NF can be analyzed by recalculating the field at the original measurement positions, it is difficult to detect the field parts that cannot be properly represented by the equivalent sources and are likely to be superimposed by errors. However, the recalculation procedure still allows to quantify how well the measured field as a whole can be represented by the equivalent sources. The deviation between the measured and the reconstructed field for the ith measurement position is given by

$$\epsilon_{\mathrm{NF},i} = \frac{\overset{*}{\boldsymbol{E}}_{\mathrm{meas},i} - \overset{*}{\boldsymbol{E}}_{\mathrm{rec},i}}{\sqrt{\frac{\sum_{k=1}^{N} \left| \overset{*}{\boldsymbol{E}}^{2}_{\mathrm{meas},k} \right|}{N}}}\,, \tag{5.5}$$

where $\overset{*}{\boldsymbol{E}}_{\mathrm{meas},i}$ and $\overset{*}{\boldsymbol{E}}_{\mathrm{rec},i}$ are the measured and reconstructed fields, while the asterisk indicates that the fields are normalized to their respective maxima. Further, N is the total number of measurement

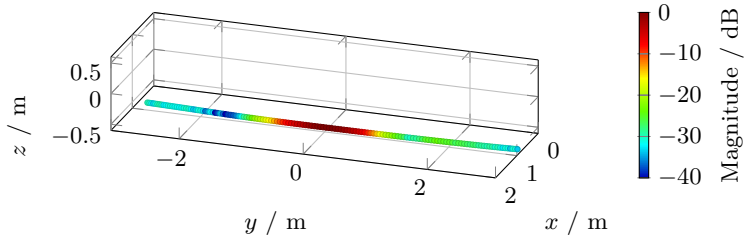

Figure 5.10: Magnitude of a single horizontal field line from the planar UAV-based field measurement and through the main beam of the antenna.

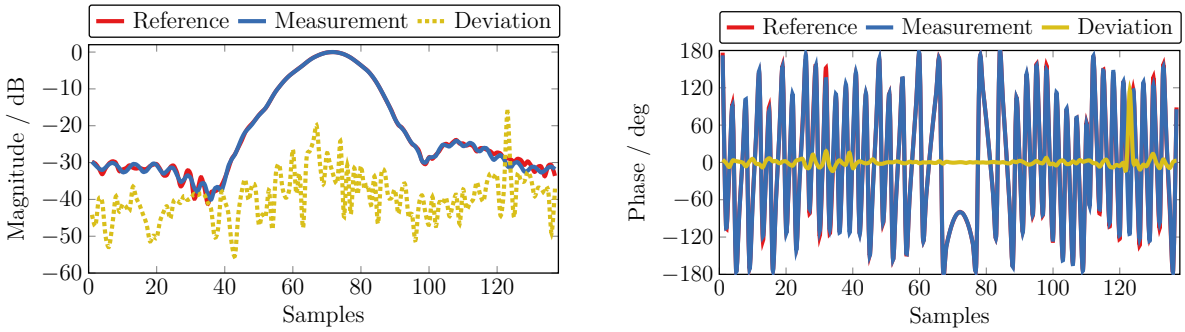

Figure 5.11: Comparison of the measured field and the field that has been reconstructed from the equivalent sources. Both fields have been normalized to their maxima. The field and deviation are shown individually for the single measurement positions of the chosen horizontal field line of the planar measurement.

positions. The overall deviation of the fields is eventually given by

$$\epsilon_{\mathrm{NF,all}} = \sqrt{\frac{\sum_{i=1}^{N} |\epsilon_{\mathrm{NF},i}|}{N}}\,. \tag{5.6}$$

For a detailed analysis, it is useful to extract single lines from the measured NF data and transform them independently from the rest of the field. The resulting FF is, of course, not meaningful but the deviation of the recalculated from the measured field reveals the most erroneous measurement positions, while care must be taken when field values are close to the noise floor of the measurement. A single horizontal field line through the middle of the main beam of the AUT from the planar UAV-based measurement is depicted in Fig. 5.10. In general, it is useful to select a field line which includes parts of the main beam since these are usually the field parts with the largest magnitudes within the whole measured NF. If the reconstruction of the field fails for those positions, it is very likely that there are more serious errors within the measurement or its evaluation. A first indication how well the measured NF can be reconstructed is the overall deviation according to (5.6). It is $\epsilon_{\mathrm{NF,all}} = 0.0146$, which is equal to $-36.7\,\mathrm{dB}$, for the horizontal field line of Fig. 5.10. The reconstructed field, together with the deviation of the measured field is shown in Fig. 5.11 for magnitude and phase. The plot in Fig. 5.11 (a) clearly shows that the deviation in magnitude between the originally measured and the recalculated field is in the range of $-30\,\mathrm{dB}$ to $-40\,\mathrm{dB}$ with some occasional higher values. For example, a single spike in the shown deviation curve goes up to $-15\,\mathrm{dB}$ for a field sample outside the main beam. This is an indication

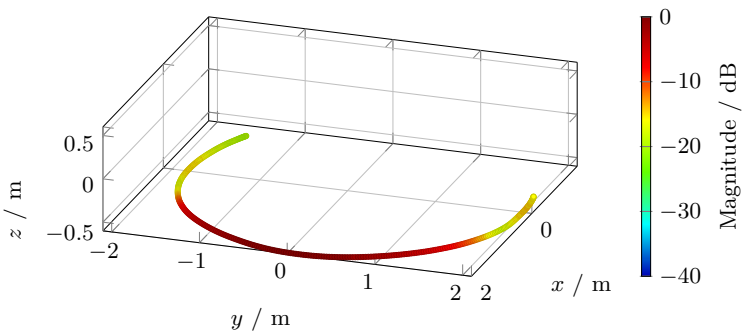

Figure 5.12: Measured probe magnitude along a single horizontal curve from the cylindrical UAV-based field measurement and through the main beam of the antenna.

that the field measurement at this position is erroneous and cannot be reconstructed. The deviation of the phase in Fig. 5.11 (b) supports this assumption. Here, the deviation is small for all positions, except for the same erroneous field value outside the main beam. It shall be noted that the phase deviation is generally larger for low magnitude values which is also reflected in Fig. 5.11 (b). Another deviation spike in the magnitude curve can be observed within the main beam. It goes up to $-20\,\mathrm{dB}$ while, for this sample, the phase deviation is found to be low. Looking at the underlying position and orientation data nothing conspicuous can be found for the respective field sample. However, regarding the low data rate of the orientation, it is still possible that the erroneous sample is due to a rapid orientation change which is not reflected in the data. It could also be an effect of the movement of the optical fiber that transmits the measured RF signal. As the UAV was flying on horizontal lines in front of the AUT, the maximum speed was reached within the main beam which implies that the fiber movement was highest there.

Analog to the planar measurement, the error analysis using the recalculation of the field samples from the equivalent sources is also performed for the cylindrical measurement. A single horizontal field line, again selected such that it includes parts of the main beam, is depicted in Fig. 5.12. Similar as before and according to (5.6), the overall error of the NF reconstruction of the horizontal field line is calculated to $\epsilon_{\mathrm{NF,all}} = 0.0198$, which is equal to $-34.1\,\mathrm{dB}$. The deviation between the measured and the reconstructed fields for the single positions is depicted in Fig. 5.13. The errors for the displayed horizontal field lines of the planar and the cylindrical measurement cases are almost similar. Therefore, it is expected that the field deviation is also similar. However, comparing the deviation in magnitude in Figs. 5.11 (a) and 5.13 (a) reveals that the average deviation is larger for the cylindrical case. Even if this is the case regarding the magnitude, the contrary is true when comparing the deviations in phase in Figs. 5.11 (b) and 5.13 (b). The phase deviation is very small while there are no significant spikes as for the planar case. This smaller phase deviation is likely to be an effect of the reduced influence of the field probe on the measurement data in the cylindrical case, which simultaneously also limits the influence of the imprecise orientation. Moreover, the measurement distance was larger in the cylindrical in comparison to the planar measurement. As a consequence of atmospheric attenuation, a larger distance between the AUT and the field probe results in lower field values which are closer to the noise floor. Therefore, the analysis from the reconstruction of the field of the planar and cylindrical measurement scenarios cannot be directly compared but at least confirm the assumption that the phase is more stable in a cylindrical measurement than in a planar one.

While providing more insights regarding the errors and quality of the measured field, the reconstruction of the field from the equivalent sources requires the knowledge of the full, or at least of large parts, of the NF for a detailed analysis. This is why this approach for error analysis cannot be performed in real-

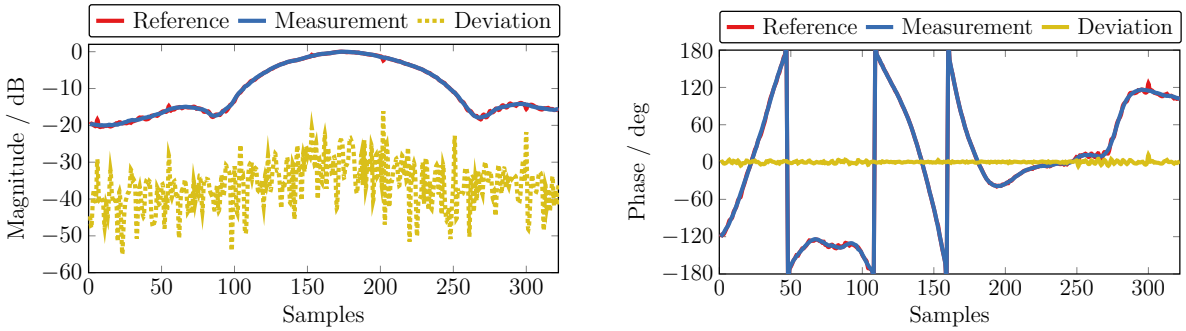

(a) (b)

Figure 5.13: Comparison of the measured field and the field that has been reconstructed from the equivalent sources. Both fields have been normalized to their maxima. The field and deviation are shown individually for the single measurement positions of the chosen horizontal field line of the cylindrical measurement.

time during the measurement of the field and, thus, remains a post-processing analysis. However, the combination with the analytically calculated field is very powerful, as a quick real-time check becomes possible using this method, while the errors in the measured field data can be analyzed in detail in the post-processing using the reconstruction approach.

5.4 Chapter Summary

UAV-based NF measurements have been presented using a planar and a cylindrical measurement setup. Furthermore, two different methods for the analysis of the measurement error have been discussed where it has been outlined that the analytical approach based on the Friis transmission equation can only be used for plausibility checks. The reconstruction of the field at the measurement positions allows a more detailed and accurate analysis, while large parts of the field are necessary which means that it can be better used during post-processing. The comparison of planar and cylindrical measurements showed that the error influence is lower for the latter, which is a consequence of the lower probe influence. Furthermore, it was also pointed out that planar UAV-based field measurements are easier to implement compared to their cylindrical counterparts because the trajectory is simpler and the measurement setup can also be implemented in a straightforward manner. However, the improvement in data quality in a cylindrical measurement outweighs the simplicity of a planar measurement geometry, making a cylindrical scan grid the preferred measurement geometry for UAV-based NF measurements.

Chapter 6

Uncertainties and Error Sources

Every measurement includes multiple sources for measurement uncertainties and errors. Understanding the error contribution of each component is the essential preliminary work that must be done to improve the accuracy of the measurement results. Furthermore, these insights can also indicate possible critical areas in terms of error contribution that require closer examination. In the literature, uncertainties and errors are sometimes differentiated. There, uncertainties are changes in measured or determined values which are not known and can, thus, not be compensated. However, results from multiple measurements can reveal an estimation of these uncertainties and with that an estimation of their impact within the measurement. Examples of measurement uncertainties include thermal noise and phase drifts. In contrast, errors are systematic changes of measurements or determined values which can be measured and compensated. Examples include the misalignment of antennas or an inaccurate field offset due to faulty calibration of the measurement receiver. Throughout this thesis, the terms *uncertainties* and *errors* are used interchangeably. Still, it is important to understand that there is a difference between uncertainties or random errors and systematic errors.

There are many sources of measurement errors within the field of NF antenna testing. Over the last decades, several estimations and investigations have been performed which can be found in the literature [Yaghjian 1975; Newell 1988; Slater 1991; Hansen 2008; IEEE 2012; Qureshi et al. 2013c; Parini et al. 2020b]. Most of these investigations can be traced back to an error classification into 18 terms which was first described by Newell [1988] and is nowadays known as the National Institute of Standards and Technology (NIST) 18 term error model for NF measurements. The different error sources are listed in Table 6.1. While this list of measurement errors is very detailed, Newell also considers a classification of the different errors into two broader categories: uncertainties in probe parameters and errors in the calculated spectrum of the NFFFT arising from the measured data [Newell 1988]. Since its presentation, the 18 term error model has been adapted while its applicability to cylindrical [Newell and Lee 2000] and spherical measurement geometries [Hindman and Newell 2006] has also been shown. However, the error analysis of NF measurements becomes much more complex when the NFFFT is considered which is needed to transform the measured NF to the FF. This is because there are NFFFT algorithms of various types with different prerequisites and, hence, different error behavior. Usually, these NFFFTs are cordial against small errors and may even improve the measured field data which is known as the processing gain of an NFFFT. For the transformation of the simulations and measurements in this thesis, the FIAFTA is employed. An error analysis of this NFFFT algorithm can be found in Paulus [2016].

As already outlined in Chapter 4, the UAV-based measurement setup is different from a setup used for traditional NF measurements in anechoic chambers. Besides the different connection type between the field probe and the measurement receiver, there is a conceptual difference especially regarding the positioning of the field probe. A general overview of the most common error sources within UAV-based NF measurements is given in Table 6.2 where the UAV-based measurement setup of Chapter 4

Table 6.1: Overview of the different error sources within NF measurements of antennas as described and classified by the NIST 18 term error model.

No.	Source of Error	No.	Source of Error
1)	Probe relative pattern	12)	Multiple reflections (probe / AUT)
2)	Probe polarization ratio	13)	Receiver amplitude nonlinearity
3)	Probe gain measurement	14)	System phase error due to:
4)	Probe alignment error		Receiver phase errors
5)	Normalization constant		Flexing cables / rotary joints
6)	Impedance mismatch factor		Temperature effects
7)	AUT alignment error	15)	Receiver dynamic range
8)	Data point spacing (aliasing)	16)	Room scattering
9)	Measurement area truncation	17)	Leakage and crosstalk
10)	Probe x, y-position errors	18)	Random errors in amplitude / phase
11)	Probe z-position errors		

is examined. To each of the identified error sources listed in Table 6.2, also the corresponding number of the 18 term error model is given. Here, it shall be noted that Table 6.2 lists only the errors which are either specific to and occur only in UAV-based measurements or have a different nature to the ones in chamber measurements due to the involved components. The table must be seen as an extension or refinement of the NIST errors rather than a replacement, i.e., the error terms which are only noted in Table 6.1 do still occur in UAV-based NF measurements, like the probe polarization ratio or leakage and crosstalk. In general, the error sources of UAV-based field measurement setups can be classified into three categories: errors in position and orientation, errors in the RF setup and other errors which do not easily fit into one of the aforementioned categories. Errors in position and orientation of the AUT and field probe are mostly related to how the positions and orientations of the two antennas are measured. As already mentioned, one of the major differences between NF measurements with UAVs and those in anechoic chambers is the positioning. While the AUT and field probe are precisely positioned within measurements in anechoic chambers, the actual position of the two antennas and their mutual distance is determined within UAV-based NF measurements using an external position measurement system. The precision of this position measurement system is crucial while also the exact execution of the position measurement is of importance, e.g., whether the position of the UAV or the attached field probe is measured and how the position of a possibly unknown AUT is determined. Furthermore, it has to be taken into account that the accuracy of the orientation has an influence on the position since the orientation of the UAV permanently changes during measurement. This becomes especially important when offsets are to be determined, e.g., from the center of the UAV to the field probe. The errors in the RF setup are mainly due to the changed measurement setup in a non-controlled environment. Most prominent in that sense is the reflection from the ground as well as external scatterers which may occur. However, also the UAV itself has an influence on the measurement as it changes the radiation pattern of the isolated field probe. While some error sources are introduced by additional components, like the RF-over-fiber link, others are similar and do also occur in traditional NF measurements, e.g., the field truncation which inevitably is almost always present in UAV-based field measurements as the field cannot be measured on a full sphere. Moreover, there are other error sources which are specific to in-situ measurements and do not clearly fit into the categories of position or RF errors but, most often, have an influence on both. Examples are the influence of the UAV performance in terms of flight speed and orientation due to wind and unstable weather conditions or, also, the synchronization of the different

Table 6.2: Error sources within UAV-based antenna measurements, where the corresponding number according to the NIST classification in Table 6.1 is given for the single entries. Only errors that are specific to the UAV-based measurement setup are listed.

Category	Source of Error	Component in Setup	No.
Position / Orientation	Position / Alignment of AUT	Positioning system	7
	Position of probe	Positioning system	4,10,11
	Orientation of probe	IMU	4,10,11
RF Setup	Probe pattern	Field probe / UAV	1,2,3
	Rotor influence	UAV	1
	Ground reflection	AUT mounting	16
	External scatterers	Measurement location	16
	Field truncation	Measurement geometry	9
	VNA noise	VNA	14,15
	Probe connection	RF-over-fiber link	14
	Electromagnetic Interference	UAV and other equipment	18
Other Errors	Measurement time	VNA	
	Synchronization of VNA / LT / UAV	Trigger / Device control	

measurement devices in the distributed UAV-based setup, especially between the flying part and the ground station.

In the following, the precision and accuracy of the single components of the measurement setup is evaluated as the knowledge of the error bounds is fundamental for the analysis and validation of the measured field data. However, only error sources that are specific to UAV-based or in-situ measurements are discussed or those which are different or additional to traditional NF measurements in anechoic chambers. Eventually, the impact of the different error sources is investigated by numerical simulations before approaches for their treatment are discussed.

6.1 Errors in Position and Orientation

Within NF antenna measurements, the electromagnetic radiation of an AUT is measured at different positions in the vicinity of the AUT. In the UAV-based measurement setup, a laser tracker or, depending on the measurement frequency, a GNSS is employed for the determination of the actual measurement position, as presented in Chapter 4. The accuracy of the measurement positions has a large impact on the accuracy of the NFFFT and is, thus, crucial for the accuracy of the resulting FF radiation pattern.

6.1.1 Laser Tracker

The UAV-based measurement setup, described in Chapter 4, employs a laser tracker for the determination of the UAV position. The laser tracker is of type FARO Vantage [FARO 2016] and consists of a measurement head and a control unit. The laser tracker is mobile and capable of measuring the angular position and distance range of a spherically mounted retroreflector (SMR), its target. The manual [FARO 2016] and data sheet [FARO 2013] state a typical accuracy of 39 µm for point-to-point and 297 µm for horizontal measurements of a scale bar. However, the exact accuracy of the position measurement de-

pends on the used SMR and also on the weather conditions of the operation environment.

The precision of the laser tracker in static conditions has been measured in an office environment over 2.4 h. For this, the SMR was placed on a stand and not moved or touched during the measurement, where the maximum variation in the position was about 40 µm. In another test, the SMR was rotated around its optical center which resulted in a maximum position change of about 90 µm. These investigations have been carried out using the SMR which has been shipped with the laser tracker. The SMR is made of steel and uses a magnetic holder which is detrimental for the use on a UAV as it can influence the performance of the magnetic compass. Therefore, in the actual UAV-based field measurements, a different prism reflector target was used that is smaller and lighter. Similar as before, the prism reflector target was rotated around its supposed optical center, as no documentation was available for the specific reflector target. The maximum deviation was about 1.54 mm during the test. Even if this is significantly more than for the SMR, it is still sufficient for NF measurements in the S-band.

6.1.2 Global Navigation Satellite System

The UAV of the measurement setup uses multiple GNSS receivers for flight navigation which can also be used to determine the measurement positions, especially at lower frequencies. As described in Section 3.3, the precision of the GNSS position depends on the number of satellites whose signals can be used by the receiver. However, there are some major differences in the precision of standard single and dual band GNSS receivers and that of RTK GNSS systems.

The standard GNSS receiver of the employed UAV is of type u-blox NEO-M8N [ublox 2021a]. It is a single-band GNSS receiver and uses only the higher frequency bands around 1.57 GHz of the different satellite navigation systems. It can simultaneously use three concurrent systems out of GPS, GLONASS, BDS and Galileo. The precision of the position has been determined in a static measurement setup in which the GNSS receiver and its antenna were fixed on a table with clear sky above and no relevant obstacles nearby. The position has been recorded for 30 min as depicted in Fig. 6.1 (a). As shown in the plot, the maximum deviation from the mean value of the position was 3.05 m in horizontal and 6.95 m in vertical direction in the measurement, which are typical values for this kind of GNSS receiver and are also in accordance with the numbers given by the manufacturer in the data sheet [ublox 2021a]. The standard deviation has been calculated to 0.63 m for the horizontal and 2.35 m for the vertical direction, where, according to the Chebyshev inequality [Papoulis and Pillai 2002], at least 75 % of the position values fall into the range of two standard deviations around the mean value $\bar{r} \pm 2\sigma$. This means that for the horizontal position, an inaccuracy of about 2.35 m with some occasional deviations of about 3.6 m must be expected, while the position accuracy in vertical direction is even worse. In comparison, a multi-band GNSS receiver of type u-blox ZED-F9P [ublox 2021b] was evaluated. It is a receiver that is capable of using all accessible frequency bands of the different GNSSs, resulting in a better position accuracy. Indeed, the multi-band feature of the GNSS receiver improves the position accuracy as can be seen in the measurement in Fig. 6.1 (b). The maximum deviations from the mean position are 449.43 mm in horizontal and 750.95 mm in vertical direction, which is about six times less than for the single-band case. The same behavior can be observed for the standard deviation which is 102.21 mm in vertical and 342.41 mm in horizontal direction. As already described in Section 3.3.3, a further improvement of the GNSS position can be achieved by the employment of an RTK system. However, for the realization of an RTK system, special GNSS receivers are necessary that are capable of accepting correction data for the enhancement of the GNSS position. From the aforementioned receivers, the M8N is not capable of handling such RTK correction data, while the F9P receiver can do so. To compare the impact of the multi-band usage over the single-band case also within an RTK system, two measurements with a fully working RTK system have been performed. The only difference between the measurements was that the F9P receiver has been configured to use only single-band satellite data in the first and to

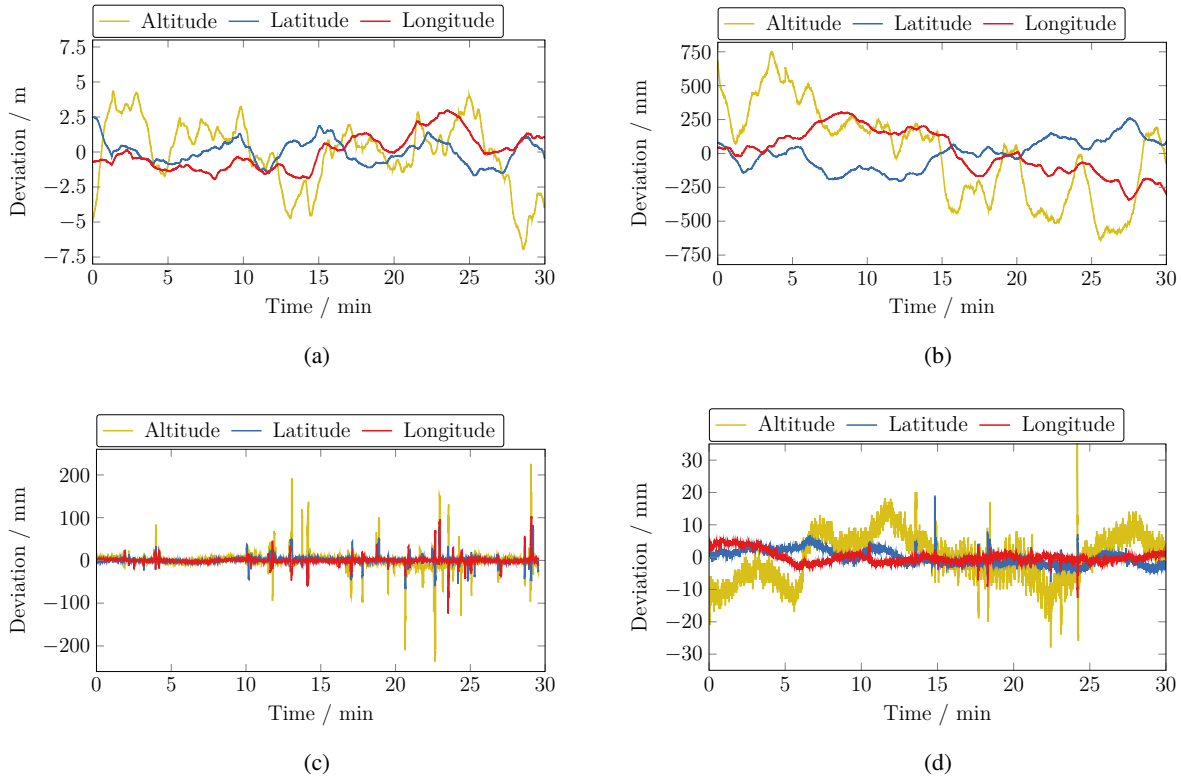

Figure 6.1: Deviation in position during static measurements from different GNSS receivers over time. Measurements with a single-band (a) and a multi-band (b) receiver have been performed, while additional measurements show the position change of a single-band (c) and a multi-band (d) real-time kinematic configuration. Note that the scale of the vertical axis is different for the single plots to account for the large differences in the position deviations.

use all available frequency bands of GNSS in the second measurement. The plots in Figs. 6.1 (c) and (d) show the position change within a 30 min recording for the single-band and the multi-band RTK setup. The measurements clearly show that the precision of the position is much better when an RTK system is used, where the maximum deviation from the mean in the single-band case is only 128.78 mm and 225.92 mm in horizontal and vertical directions, respectively. However, as expected, the position accuracy is again better for the multi-band RTK setup with a maximum deviation of only 18.79 mm and 40.07 mm, while also the standard deviation is lowest in comparison to all other configurations. An overview of the maximum and standard deviations for the tested cases are given in Table 6.3. Overall, it shall be mentioned that the presented values for the position accuracy are results of static measurements in which the GNSSs receivers were not moving. However, even if the accuracy is smaller in dynamic scenarios, it can be expected that it is in a similar order and not too far off from the static case regarding a comparison to the laser tracker position and with respect to the literature [Nguyen et al. 2021; Hohensinn et al. 2022; Nguyen and Cho 2023].

6.1.3 Accuracy of the UAV Orientation

The probe antenna is mounted to the front of the UAV in a fixed manner which implies that the orientation of the UAV is always similar to the orientation of the field probe. As described before, the flight controller provides the rotation around the three principal axis, roll, pitch and yaw, which are used within

Table 6.3: Precision of the different GNSS receivers and configurations used by the UAV of the measurement setup. The comparison includes single-band (SB) and multi-band (MB) receiver types, as well as a real-time kinematic (RTK) system.

GNSS Receiver		Max. deviation		Std. deviation (σ)	
Model	Type	horz.	vert	horz.	vert.
u-blox M8N	SB	3.05 m	6.95 m	0.628 m	2.353 m
u-blox F9P	MB	449.43 mm	750.95 mm	102.21 mm	342.41 mm
u-blox F9P RTK	SB	128.78 mm	225.92 mm	12.45 mm	23.72 mm
u-blox F9P RTK	MB	18.79 mm	40.07 mm	1.48 mm	7.22 mm

Table 6.4: Standard deviation of the rotation around the principle axis of a UAV. The data were obtained from measurements in which the hexacopter was statically placed on the ground and did not move during recording.

	Roll	Pitch	Yaw
Std. Deviation σ	0.0376°	0.0521°	0.1027°

the NFFFT as rotation angles for the field probe, while offsets due to the measurement setup have to be considered. The roll and pitch angles provided by the flight controller are calculated from the fusion of several gyroscopes and accelerometers, where the yaw angle, in contrast, is retrieved from an external magnetometer or compass. The UAV uses a compass that is based on the RM3100 chip [PNI 2022] which works as magneto-inductive sensor and is stated to have an higher accuracy than sensors based on the Hall effect [Regoli et al. 2018].

The precision of the provided orientation angles have been evaluated in different measurements. First, the long-time stability and drift of roll and pitch was measured over 3 h where the UAV was placed on an office desk and did not move. The yaw axis was evaluated in a similar manner where the UAV was placed on the ground away from any building for about 14 min. The resulting standard deviations from the mean values for all three principal axes are given in Table 6.4.

In addition, also dynamic measurements have been performed, to determine the precision of the roll and pitch angles in motion. For this, the UAV was mounted to the spherical positioner of the anechoic NF chamber at the TUM. The positioner is used as reference since the manufacturer states a step resolution of 0.01° and a position repeatability of 0.03° according to the data sheet [NSI 2011]. Rotations of the UAV to the desired orientation angles were performed with respect to the positioner values. There was a wait time of 20 s between two subsequent rotations, during which the minimum and maximum angles were determined. Figure 6.2 (a) shows the deviation between the measured roll and pitch angles and the desired positioner angles where the error bars indicate the minimum and maximum angles for each position. According to the plot, it seems that the deviation is highest for the large rotation angles. This is in part due to the fact that a static offset was minimized for a rotation angle of 0°. Still, the measurements show that the deviation changes with the orientation angle where the maximum deviation is about 0.56°. The plot also reveals that the deviation was different for the rotation around the roll and the pitch axes. Another measurement was performed for the investigation of the repeatability of the roll and pitch angles. Therefore, the UAV was rotated left and right, respectively forth and back, always to 0° where the minimum and maximum values have been determined during a measurement time of 20 s. Figure 6.2 (b) shows the repeatability at 0° where the maximum deviation is about 0.3°. Regarding the errors in the orientation angles, it must be considered that an inaccurate orientation is likely to result in

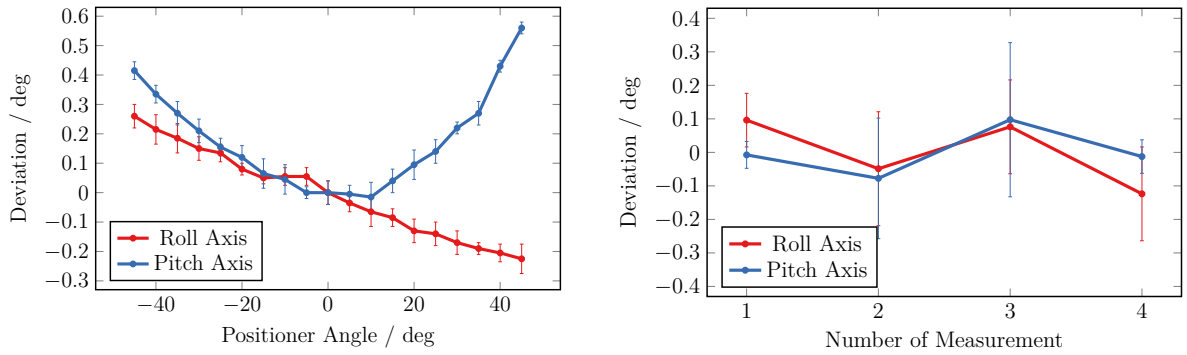

(a) (b)

Figure 6.2: The accuracy (a) and the repeatability (b) of the orientation angles, provided by the UAV with respect to the rotation angle of a sophisticated spherical positioner, have been measured in an anechoic chamber. The repeatability has been measured at a rotation angle of 0°.

a wrong position as there is some distance between the laser tracker reflector target and the phase center of the field probe which needs to be corrected in the post-processing. However, this distance depends on the chosen field probe and the actual UAV.

6.2 Errors in the RF Setup

Besides the degradation of the accuracy of the FF radiation pattern due to errors in position and orientation, obviously, the accuracy of the RF part of the measurement setup needs to be evaluated. Aside from the measurement receiver itself, the field probe is certainly the component in the measurement setup that has the largest influence on the measured field data, where it becomes even more important in UAV-based field measurements as the UAV itself must be considered as part of the field probe. Furthermore, while high-frequency cables are usually quite robust and their influence is almost negligible, the situation is different for coherent UAV-based measurements since the field probe is connected via an optical RF-over-fiber link to the measurement receiver.

6.2.1 Impact of the Chosen Field Probe

The impact of the field probe on the measured field data depends on the chosen measurement geometry where, e.g, it is largest for planar and, in comparison, low for spherical measurement geometries. This is a consequence of the fact that the radiation pattern of the field probe influences the measured field values, as described in Section 2. The influence of the field probe on the measured field values has been extensively studied in the literature [Hansen 2008; Parini et al. 2020a,b] for classical NF antenna measurements and different scan geometries. However, the impact of the field probe is even more complicated in UAV-based NF measurements as the probe is usually mounted quite close to the UAV body and the rotors. This is often due to the fact that the flight performance of a multicopter increases when the mass of the UAV is evenly distributed over the same and the center of gravity is in the middle of the UAV. As a result of the insufficient spacing between the field probe and the UAV body, both components will couple depending on the actual distance and materials. Therefore, the real field probe has to be considered as a combination of the actual probe antenna and the body or frame of the UAV. Given the PCB-fabricated Vivaldi antenna and the copter described in Section 4, a comparison of numerical simulations of the FF radiation pattern of the isolated field probe and the field probe mounted to the UAV

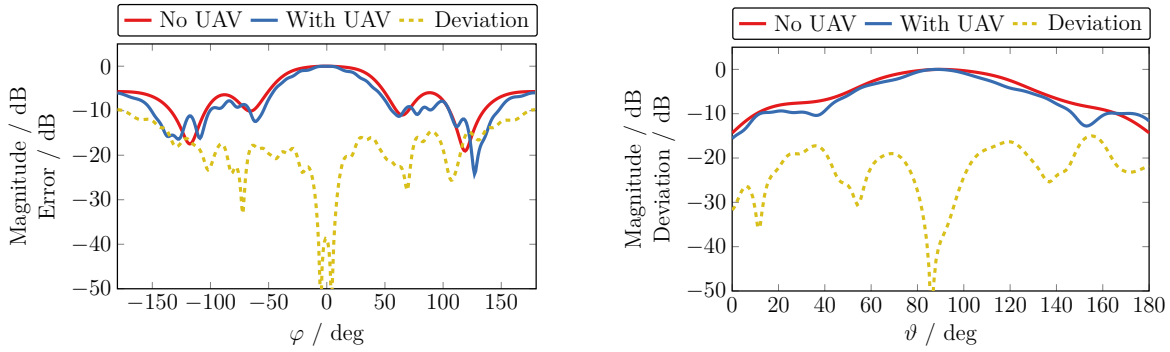

(a) (b)

Figure 6.3: Comparison of the FF main cuts at $\vartheta = 90°$ (a) and $\varphi = 0°$ (b) for the isolated radiation pattern of the field probe and the combined pattern when the field probe is mounted to the front of the UAV.

is shown in Fig. 6.3 in terms of the FF main cuts at $\vartheta = 90°$ and $\varphi = 0°$ for a frequency of 2.45 GHz. As found from the graphs, the pattern cuts of the field probe are significantly different with and without the UAV body being present. The field deviation is about -20 dB for the normalized patterns according to the complex error measure of (2.32). This large difference of the radiation patterns gains even more importance considering that the UAV frame is largely made out of some non-conducting plastic material, where other UAV frames are made of conducting carbon-fiber material and are, therefore, likely to have an even larger impact on the field probe pattern. Therefore, it is important to consider the pattern of the field probe including the UAV for the probe correction within the NFFFT.

6.2.2 Influence of the Rotor Blade Rotation on the Measured Field

The UAV frame has to be considered as part of the field probe within UAV-based NF measurements as already mentioned. However, this implies that the field probe is not static anymore and contains moving parts regarding the spinning rotors of the UAV. Depending on the UAV and the actual measurement setup, the situation can be even worse as the probing antenna might be mounted quite close to the rotors, e.g., for reasons of flight stability. Therefore, one can assume that there is some coupling between the antenna and the UAV body. This assumption is also backed by the numerous publications discussing the influence of the spinning UAV-rotors on the electromagnetic field of a radio detection and ranging (RADAR) system [Ritchie et al. 2015; Rizwan et al. 2017; Khristenko et al. 2018]. In fact, the rotation of the rotor blades creates modulation patterns in the RADAR signal that can be treated as kind of “fingerprints" as each of them belongs to a certain type of UAV with a specific number of rotors [Chen et al. 2006; Wit et al. 2012; Klaer et al. 2020; Zhao and Su 2020]. Taking this approach further, there are publications which discuss how these fingerprints can be used to distinguish UAVs from birds [Torvik et al. 2016; Rahman and Robertson 2018]. Still, all of these investigations are specific to RADAR while, interestingly, more general investigations on the impact of the rotating UAV-rotors on the electromagnetic field of an antenna are not covered well in the literature, except for some brief observations [Paonessa et al. 2020; Virone et al. 2021]. This might be due to the fact that a general analysis of the rotor impact is most relevant when it comes to antenna field measurements, where the interest in in-situ, and especially UAV-based, field measurements increased just recently.

In this chapter, measurements are discussed that have been performed to analyze the impact of the rotating rotor blades of the UAV on the recorded field data. All measurement results have been published

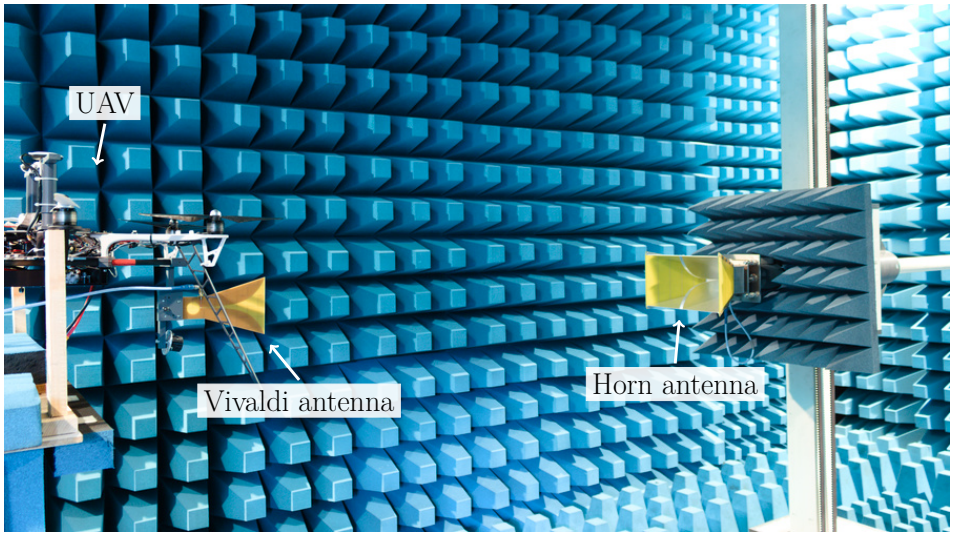

(a)

(b)

Figure 6.4: Measurement setup in the anechoic chamber (a) and as schematic showing the connections of the single devices (b). The UAV was mounted on a wooden holder and connected to a signal generator. The probing horn antenna was mounted on a vertical linear stage and connected to different measurement receivers. Both antennas were facing each other. (a) © 2021 IEEE, [Faul et al. 2021b]

in Faul et al. [2021b] and Faul et al. [2021c], where this section is a reproduction of these publications from which also most of the figures are taken.

Measurement Setup

Measurements regarding the influence of the rotating rotor blades have been performed in an anechoic chamber at the TUM since this controlled environment ensures that the measured field is only influenced by the UAV and its related parts, while external scatterers are dismissed. For the measurements, the same UAV and the PCB-fabricated Vivaldi antenna as for the in-situ measurements of Chapter 5 have been used, including all parts except for the battery since the UAV was powered with an external power supply. Before the actual usage, the power supply has been measured in an isolated manner to ensure that it does not emit electromagnetic fields which superimpose the actual rotor effects and lead to wrong conclusions. The UAV was mounted on a wooden holder that is non-conducting and stable enough to keep the UAV in place, even for higher thrust of the motors. A double-ridged waveguide horn antenna of type R&S HF906 [R&S 2022b] was mounted on a vertical linear stage opposite of the Vivaldi antenna and the UAV with a distance of about 1.1 m. The setup is shown in Fig. 6.4 (a). Beside the arrangement of the UAV and the horn antenna, the figure also shows that the tips of the pyramid absorbers in the anechoic chamber are cut at a certain length. This obviously limits the operation frequency range of the absorbers but is a trade off with respect to a compact footprint. Still, the cut pyramid absorbers and the

measurement chamber in total are used within their operation frequency range. The Vivaldi antenna at the front of the UAV was connected to and fed from a signal generator of type R&S SMIQ [R&S 2022d]. On the other side of the signal flow, a signal analyzer of type R&S FSIQ [R&S 2022a] and a network analyzer of type R&S ZVL [R&S 2022f] were used as test receivers in different measurement scenarios, the latter also in its spectrum analyzer mode. The receivers have been connected to the horn antenna which served as field probe in this measurement setup. A schematic of the measurement setup is depicted in Fig. 6.4 (b). It can be seen that the single measurement devices were linked by a common reference signal. However, it shall be noted that even if the measurement receiver was linked to the signal generator in terms of reference frequency, the actual measured field values are still scalar as they do not contain any phase information. The UAV motors were controlled remotely by a PC from outside the measurement chamber. For this, an Ethernet-over-fiber link was employed which connected the PC with the RPi on the UAV, similar to the setup used for in-situ measurements and described in Chapter 4. Similar as for the power supply, electromagnetic compatibility (EMC) measurements have been performed for all other electronic components of the UAV, including the RPi and the Ethernet-over-fiber link to ensure that these components do not contribute to and disturb the measurements.

Figure 6.4 (a) shows both antennas, the Vivaldi and the horn antenna, in vertical polarization. In addition to this configuration, measurements with horizontal polarization have also been performed. For this, both antennas were rotated about 90° such that their polarization matched again. The UAV contains a total of six rotors, where only the two rotors at the front were spinning during the measurements. One of the reasons for the operation of only two rotors is the available current from the power supply while batteries do not allow to perform measurements with spinning rotors over several hours. Nevertheless, measurements were performed with all six rotors spinning to ensure the suitability of the measurement approach. The comparison of the measurements with two and six rotors revealed no significant difference and it can, therefore, be concluded that the influence of the rear rotors is negligible in the investigated combination of UAV and probe antenna. The front rotors are dominant in terms of impact on the field of the Vivaldi antenna as they are closest to it.

Rotor Influence in Frequency Domain

Following the theory of the micro-Doppler effect, a modulation of the electromagnetic field of the Vivaldi antenna caused by the rotating rotor blades can be anticipated. Therefore, measurements in the frequency domain were performed using the FSIQ signal analyzer. Within those measurements, the full spectrum has been acquired while the front rotors of the UAV were spinning with constant speed. The FSIQ was connected to the probing horn antenna, while its resolution bandwidth (RBW) was chosen to 10 Hz. As described before, the Vivaldi antenna on the UAV was fed from a signal generator that was tuned to a frequency of 2.45 GHz. The average noise level of the measurement setup was determined to about -130 dBm in a static measurement with non-spinning rotors and deactivated power source of the signal generator. The rotor speed during these frequency-domain measurements was 2044 rpm which is equal to $34\,\mathrm{s}^{-1}$. Measurements were performed with different rotor materials which shall reflect the different use cases since there is not one single material that is used for all available rotors on the market. Commonly, smaller UAVs use plastic rotors whose stability is often enhanced with a glass-fiber structure. However, their explicit structure and often even the exact material is not known. Still, the rotors are dielectric and are, therefore, treated and named as such during the measurements. In comparison, larger UAVs commonly use rotors made of carbon fiber material. Again, the exact length and arrangement of the individual fibers are not known, but they strongly influence the conductivity of the rotor material. Therefore, the worst case scenario of fully conducting rotors was included in the measurements for which dielectric plastic rotors were covered with conducting copper tape.

The measured frequency spectrum for the case of vertical polarization of the antennas is depicted in

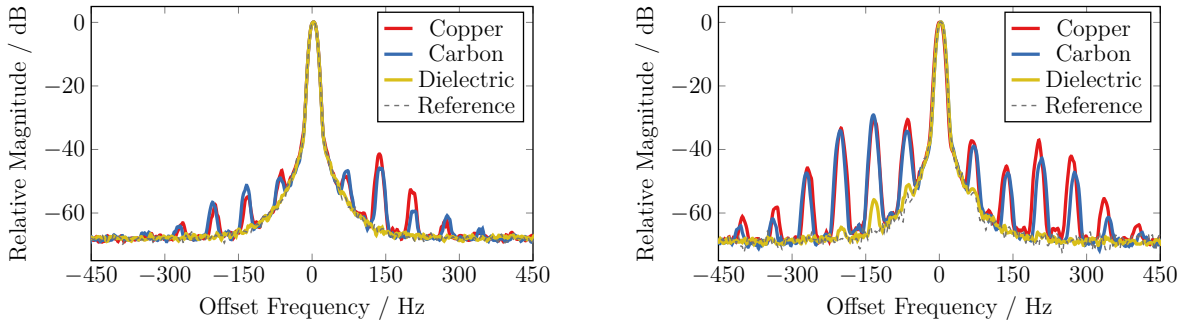

Figure 6.5: Normalized frequency spectra, measured for spinning rotors and using copper, carbon-fiber and dielectric rotors. The case of static, non-spinning rotors is included as reference. The measurements have been performed for the cases of vertical (a) and horizontal (b) polarization of the antennas. The horizontal frequency axis in the plots shows the frequency offset relative to the carrier frequency of 2.45 GHz. © 2021 IEEE, [Faul et al. 2021b]

Fig. 6.5 (a) where each spectrum is an average of 15 subsequent measurements. The reference frequency spectrum has been measured for the case where the rotors are not spinning and, therefore, it contains only the peak at the carrier frequency. Here, it shall be noted that the horizontal axis is given as frequency offset from the carrier frequency of 2.45 GHz while the plotted spectra are, additionally, normalized to the magnitude at the carrier frequency. Figure 6.5 (a) shows that higher and lower sideband frequencies arise in the measured frequency spectra for the cases of the spinning carbon-fiber and copper rotors. These sideband frequency peaks describe a modulation of the electromagnetic field, where, in both cases, the modulation peaks occur at almost the same frequencies while their magnitude is also similar. This is an indication that the carbon-fiber rotors are indeed conductive and that their behavior in terms of electrical characteristics and impact on the electromagnetic field is similar to the copper-coated rotors. Furthermore, the plot reveals that the impact of the dielectric rotors on the vertically polarized field of the Vivaldi antenna is negligible since the corresponding spectrum is almost identical to the reference. The first upper and lower sideband frequencies of copper and carbon-fiber measurements occur at 68 Hz, while all higher frequency peaks occur at multiples thereof with a maximum deviation from these frequencies of ±5 Hz. This deviation is mainly due to the RBW of the signal analyzer which was 10 Hz for these measurements. The basic modulation frequency of 68 Hz is equal to twice the rotation speed, which in turn is a consequence of the fact that a single rotor consists of two rotor blades. Figure 6.5 (b) shows the measured frequency spectra for the horizontal polarization of the antennas for the different rotor types. In direct comparison, the spectra for the case of vertical polarization of the antennas are similar with respect to the occurring modulation frequencies, although the magnitudes of the single sideband frequency peaks are significantly different. This is especially noticeable for the measurements with the copper and carbon-fiber rotors, where the magnitude difference between the highest sideband peak and the carrier is only 29 dB, while it is about 42 dB for the vertical polarization. In addition, an impact of the dielectric rotors is found for the case of horizontal polarization but it is still negligible in comparison to the impact of the other rotor materials.

The preceding measurements reveal that there is an influence of the spinning rotors on the electromagnetic field of the Vivaldi antenna mounted to the UAV. However, they also show that the rotor influence depends on the polarization of the antenna and, therefore, on the mutual orientation between the antenna and the rotors. An extreme setting is the measurement through the rotor plane, i.e., the case where one antenna is above and one antenna is below the rotor plane such that the rotor blades occasionally block

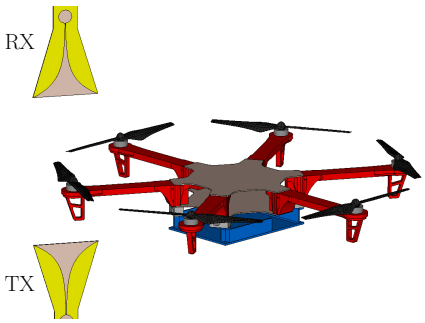

Figure 6.6: Schematic measurement setup for the measurements where the rotating rotor blades occasionally block the main beam of the antennas which are arranged in an opposite manner above and below the rotor plane. © 2021 IEEE, [Faul et al. 2021b]

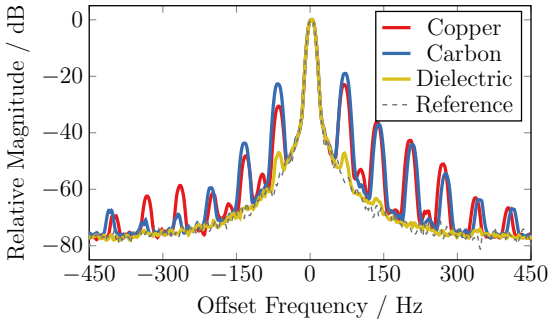

Figure 6.7: Normalized frequency spectra from measurements with the different rotor types and the setup where one rotor occasionally blocks the main beam of the antennas. The horizontal frequency axis shows the frequency offset relative to the carrier frequency of 2.45 GHz. © 2021 IEEE, [Faul et al. 2021b]

the antenna beams. Such a measurement setup was realized using two Vivaldi antennas. A schematic of the setup is shown in Fig. 6.6. As intended, the setup was arranged in a way that the main beam was blocked with every rotation of the rotor blade. To dismiss changing reflection and an impact of the other rotors, only one rotor was spinning. Analogous to the measurements before, the full frequency spectrum was acquired by the signal analyzer with a center frequency of 2.45 GHz, where the measurement was repeated using all three rotor types. The corresponding normalized frequency spectra are depicted in Fig. 6.7. Similar as for the measurements in Fig. 6.5, frequency peaks arise at frequencies which are equal to twice the rotation speed of the rotor blades, while the impact of the copper and carbon-fiber rotor is again almost similar. However, for this configuration, where the field is measured “through" the rotor, the difference between the highest sideband peaks and the carrier is only about 20 dB and, therefore, even smaller than for the case of horizontal polarization. The differences for the employed rotor materials are significant, where the plastic rotors exhibit, again, some modulation peaks but at a magnitude level that is still negligible for actual NF measurements with UAVs.

One drawback of these frequency spectrum measurements is that the modulation signal, caused by the spinning rotors, cannot be fully characterized since the frequency spectrum is magnitude-only and lacks information about the phase. However, additional measurements with an oscilloscope and also using the demodulation function of the FSIQ lead to the conclusion that the rotor-caused modulation is a superposition of an amplitude modulation (AM) and a phase modulation (PM), where the AM seems to be dominant. These findings explain the observation that the sideband peaks close to the carrier are higher in Fig. 6.7 in comparison to the measurements in Figs. 6.5. This is due to the fact that the AM

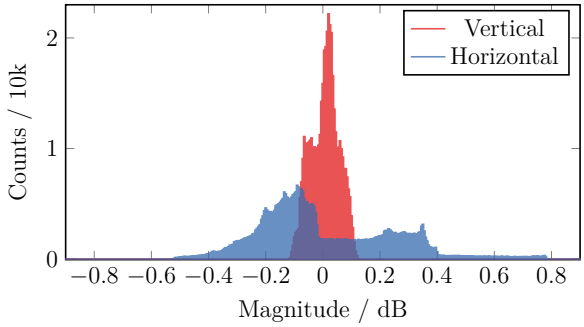

Figure 6.8: Histogram showing the deviation in magnitude from the mean value of zerospan measurements at a frequency of 2.45 GHz. The measurements have been performed for vertical and horizontal polarization of the Vivaldi antenna. © 2021 IEEE, [Faul et al. 2021b]

component increases when the beam of the antennas is directly blocked by the rotor blades, similar to an optical shutter. However, at the same time, the rotating rotor blades cause a PM as a consequence of the Doppler effect which is equal to a phase change [Neipp et al. 2003]. Therefore, it is reasonable that the phase modulation is higher for horizontal polarization of the antennas since the rotation plane and the polarization are aligned in this case. In principle, the PM is present in all rotor measurements as the single rotor blades are curved and not flat.

Overall, it is difficult to clearly characterize the modulation signal that is caused by the rotating rotor blades. The modulation signal changes for different rotors of different materials, or also for rotor types of different shape. The effect of the modulation is specific to a certain type of UAV and also to the mutual arrangement of the UAV and the antenna. However, an exact characterization of the modulation signal is not only very complicated, but also not necessary. In the first place, the influence of the spinning rotors – or any other part of the UAV – on the probing antenna shall always be minimized. Further, it is worth to measure the resulting rotor influence, while it is irrelevant which temporal form the overall signal has as long as the rotor-induced modulation signal is not fully characterized for all possible cases, i.e., for every possible rotor position, and the actual measurement of the field is synchronized with the modulation.

Since the exact knowledge of the rotor-induced modulation signal is a less realistic case due to the large number of possible rotor constellations, a statistical characterization of the modulation signal is preferred. For this, zerospan measurements have been performed at a frequency of 2.45 GHz using the spectrum analyzer mode of the ZVL VNA. Within a zerospan measurement, the frequency span is set to 0 Hz where the field is repeatedly measured at the center frequency according to the number of measurement samples N. The resulting signal is effectively a time signal which represents a demodulation of the RF signal with the center frequency. The time base of this resulting time signal is defined by the sweep time and RBW of the spectrum analyzer which was chosen to 10 s and 3 kHz, respectively. The magnitude distribution of zerospan measurements for the cases of vertical and horizontal polarization and for the setup in which both antennas face each other is depicted in Fig. 6.8. In the histogram, the horizontal axis shows the deviation of the magnitude from the mean value while the vertical axis represents the number of occurrences. It can be easily seen that the magnitude values are more spread for horizontal polarization in comparison to the vertical polarization of the antennas. This is also reflected in the standard deviation for both cases, where the standard deviation for the horizontal polarization $\sigma_{\text{horz}} = 0.23\,\text{dB}$ is more than four times that of the standard deviation for the vertical case $\sigma_{\text{vert}} = 0.049\,\text{dB}$. This difference has a significant impact as the Chebyshev inequality states that at least 75 % of the magnitudes fall within the range of $\overline{x} \pm 2\sigma$, where $\overline{x}$ is the mean value of the zerospan measurement. Therefore, magnitude deviations of about 0.46 dB must be expected in the given configuration of the measurement

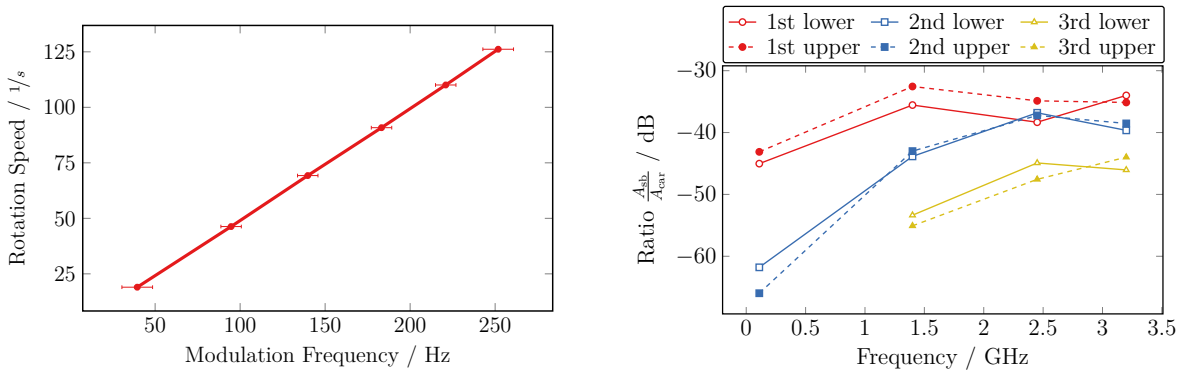

(a) (b)

Figure 6.9: Influence of the rotation speed of the rotor blades (a) and the carrier frequency (b) on the modulation content. The frequency of the first modulation peak has been evaluated for a carrier frequency of 2.45 GHz in (a) while, in (b), the influence of the different carrier frequencies is given in terms of the sideband ratio for a rotation speed of 2044 rpm. © 2021 IEEE, [Faul et al. 2021b]

setup.

Characteristics of the Rotor Influence

Besides the characterization of the rotor-induced modulation effect, questions arise about the dependence of the modulation on the measurement setup and its parameters. It has already been mentioned that the first sideband frequencies relative to the carrier, i.e., the peaks to lower and higher frequencies that are closest to the carrier peak in Fig. 6.5, occur at frequencies which are equal to twice the rotation speed of the UAV rotors. The double rotation speed can be explained by the fact that each rotor comprises two rotor blades. It has also been found that all higher modulation peaks are harmonics and occur at multiples of the first sideband frequency. However, since the modulation frequency matches that well with the rotation speed in all preceding measurements, the question arises whether there is a true link between both quantities or the findings were just a coincidence. Therefore, measurements of the frequency spectrum, similar as before, have been performed for different rotation speeds of the rotors. Since the impact of the carbon-fiber rotors has been found to be similar to the copper rotors and they represent a realistic use case, only this type of rotors was used within these measurements. Additionally, this has also been the case for all further measurements where not stated differently. The link between the frequency of the first upper sideband peak and the rotation speed is shown in Fig. 6.9 (a). The plot reveals that the modulation frequency scales with the rotation speed and is always twice its value. To reach a certain level of confidence, several subsequent measurements were made with error bars showing the spread in the modulation frequencies that have been determined from the individual frequency spectra. The maximum frequency spread for a single rotation speed is about 9 Hz, which is within the limits what can be expected from the measurement since the RBW of the signal analyzer was chosen to 10 Hz in these measurements. Still, another reason for the spread of the modulation frequency may be the accuracy of the rotation speed which has been determined with a consumer-grade handheld meter for every single measurement.

Equally important as the dependence of the rotor-caused modulation on the rotation speed is its dependence on the carrier frequency. The carrier frequency is the frequency that the signal generator is tuned to and which is also chosen as center frequency of the signal analyzer. To reveal the impact of the carrier frequency on the arising modulation, full spectral measurements were performed for different carrier

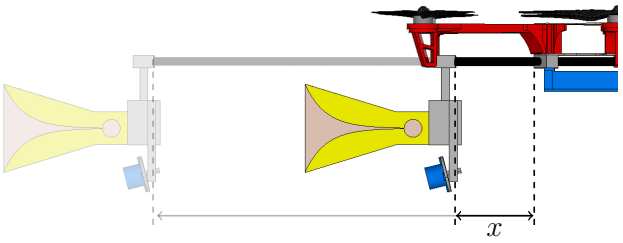

Figure 6.10: Mounting of Vivaldi probe antenna at the front of the UAV. The distance x between the back of the antenna holder and the front of the UAV body has been changed between subsequent measurements. © 2021 IEEE, [Faul et al. 2021b]

frequencies. To enable a comparison of the different measured spectra, the ratio of the magnitude of the sideband peak to the magnitude of the carrier peak was calculated for the individual measurements. This sideband ratio (SBR) denotes to

$$SBR = \frac{A_{\mathrm{sb}}}{A_{\mathrm{car}}}, \tag{6.1}$$

where A_{sb} and A_{car} are the linear magnitudes of the sideband peaks and the carrier peak, respectively. Figure 6.9 (b) shows the SBRs for the first three upper and lower sideband frequency peaks over different carrier frequencies. From the figure it is found that for measurements above 1 GHz the SBR for the first two sideband peaks remains on a similar level, while the magnitude of the third sideband peak seems to increase for higher carrier frequencies. Here, it is important to note that the measurements at 1.4 GHz and above were performed using the Vivaldi antenna, i.e., the UAV setup described in Chapter 4 was used. For the measurement at 110 MHz a folded dipole ring antenna has been employed since the Vivaldi antenna does not work for such low frequencies anymore. It was attached in a similar manner at the front of the UAV. The ring antenna has a diameter of about 0.55 m and is horizontally polarized. Therefore, the increase of the SBR from 110 MHz to 1.4 GHz, in Fig. 6.9 (b), is, at least partially, due to the fact that the antenna was changed where the ring dipole was much closer to the UAV in terms of wavelength, being about 2.7 m for 110 MHz. Furthermore, at such long wavelengths, the rotors are much smaller than the wavelength, while they are at least in the same order of magnitude for measurements at higher frequencies. Regarding the fact that the sideband frequency peaks were located and measured at the same frequencies in the spectrum, these measurements also reveal that the rotor-induced modulation effect and the actual modulation frequency are independent of the chosen carrier frequency.

In addition to the dependence of the modulation signal on the rotation speed and the carrier frequency, the spatial distribution of the rotor-caused modulation has been investigated. During the construction of the UAV-based field measurement system in Chapter 4, it has been assumed that the amount of mutual coupling between the Vivaldi antenna and the UAV body depends on their distance of separation. To prove this assumption and to quantify the influence, measurements have been performed with different distances between the Vivaldi antenna and the UAV body where the carrier frequency was again 2.45 GHz. Figure 6.10 shows the model of the UAV together with the Vivaldi antenna at the front which can be moved along the carbon fiber tube holder. Similar as before, the SBR values have been calculated for the first three sideband frequencies at different distances x between the antenna holder and the front of the UAV body. The results are depicted in Fig. 6.11, where each curve is a result of averaging six subsequent measurements. It can be easily seen that the SBR decreases for larger distances x. From the underlying spectral data it is found that the decrease of the SBR is a consequence of lower magnitudes of sideband peaks in comparison to the carrier peak with increasing x, i.e., the rotor-caused influence on the electromagnetic field decreases for larger distances between the antenna and the UAV body. This is an important finding for the mounting of any antenna to a UAV as, in principle, bringing the antenna several

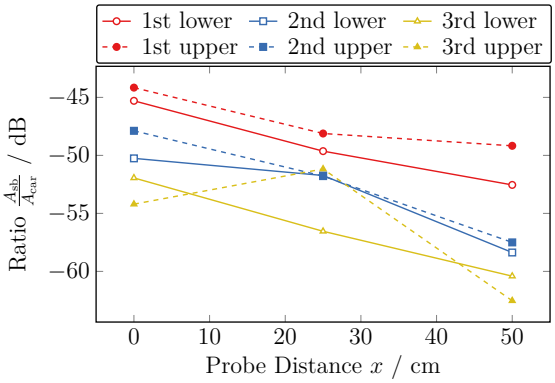

Figure 6.11: Sideband-ratios of the first three modulation frequency peaks for different distances x between the Vivaldi probe antenna and the UAV body. © 2021 IEEE, [Faul et al. 2021b]

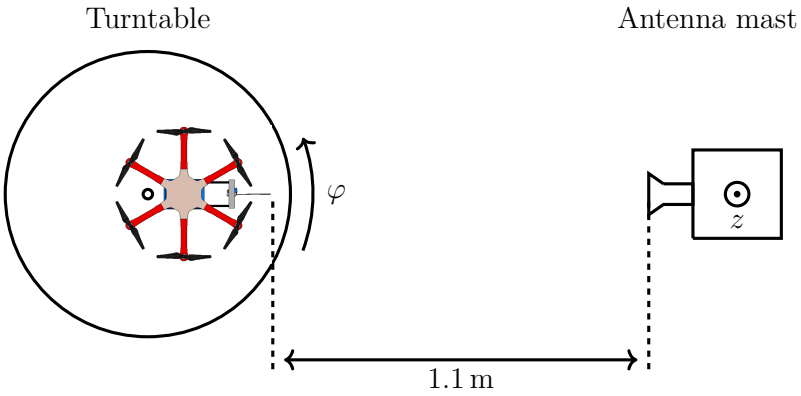

Figure 6.12: Schematic of the cylindrical measurement setup in the anechoic chamber for the analysis of the spatial dependence of the rotor-caused modulation. © 2021 IEEE, [Faul et al. 2021b]

wavelengths away from the UAV body would indeed dismiss most effects of mutual coupling between both components and, therefore, also the rotor-caused field modulation. However, the mounting of an antenna to a UAV remains a trade-off between the coupling with UAV parts and flight stability which asks for bringing all mass to the center of gravity of the UAV [Kemper and Fatikow 2006; Magnussen et al. 2014].

Moreover, the field of any antenna is usually different for different spatial directions. In the specific case, the FF radiation pattern of the Vivaldi antenna changes when it is mounted to the UAV as discussed in Section 6.2.1. With that in mind, it can also be assumed that the rotor-induced modulation effect is different for different spatial directions. Consequently, measurements have been performed where the UAV, together with the Vivaldi antenna and the wooden holder, has been placed on a turntable within the anechoic chamber. The probing horn antenna was mounted on a linear stage which could be moved vertically where the distance between the Vivaldi and the horn antenna was about 1.1 m. A schematic of the measurement setup is depicted in Fig. 6.12. With the help of this setup, the field can be measured on a cylindrical surface. Hence, the modulation content was measured in the two main cuts of the cylinder, i.e., variable φ for $z = 0\,\mathrm{m}$ and variable z for $\varphi = 0°$, while the antennas were always aligned facing each other for $(\varphi, z) = (0°, 0\,\mathrm{m})$. The modulation content was again represented by the SBR which means that the full spectra were measured for the single positions and a center frequency of 2.45 GHz. The SBRs of both cylindrical main cuts are depicted in Figs. 6.13 (a) and (b), where all curves are

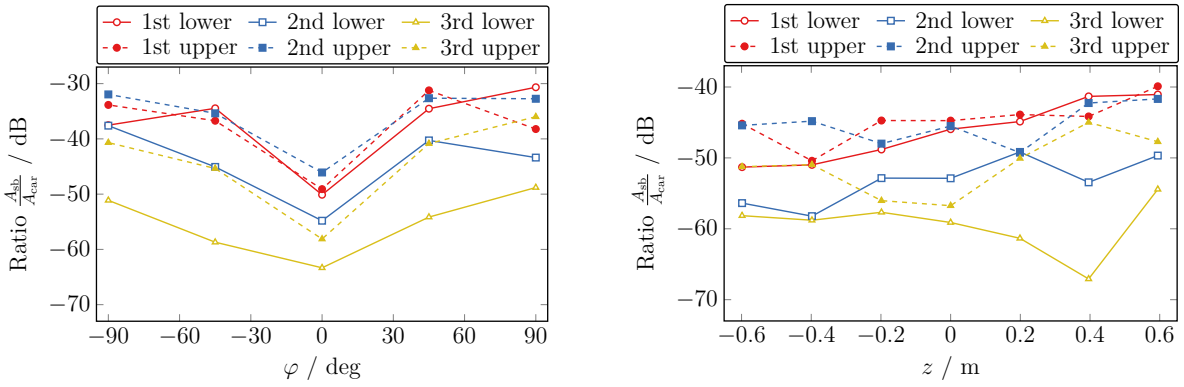

Figure 6.13: Spatial dependence of the rotor-caused modulation content. The sideband-ratios have been measured along the horizontal (a) and the vertical (b) main cut of a cylindrical measurement surface for $z = 0\,\text{m}$ and $\varphi = 0°$, respectively. © 2021 IEEE, [Faul et al. 2021b]

averages from three subsequent measurements. It can be seen from Fig. 6.13 (a) that the SBR increases for angles φ different from zero, i.e., when the table is turned to either direction. To recall, an increase of the SBR value means that the magnitude of the sideband frequency peaks increases in relation to the carrier peak. In fact, the actual measured spectral data reveal that the carrier peak decreases while the sideband peaks which represent the modulation remain almost constant when the table is turned. This important finding clearly states that the field of a prospective AUT shall be measured using the main beam of the UAV-mounted field probe. Regarding the vertical main cut in Fig. 6.13 (b), it can be found that the SBR increases with higher values of z. Theoretically, moving the probing horn antenna to $z = \infty$ would result in the case of the measurement through the rotor plane as discussed before and depicted in Fig. 6.7. Therefore, an increase of the SBR values for larger z is expected. Still, the increase of the SBR is less significant for changes in z than for changes in φ-direction.

Rotor Influence on Transmission Measurements

So far, the modulation that is caused by the rotating rotor blades has been investigated by conducting full spectrum measurements and evaluating the single spectral lines. In contrast, classical antenna measurements rely on transmission measurements between the AUT and a known field probe. To cover this realistic measurement scenario, transmission measurements have been performed. In principle the same setup as in Fig. 6.4 (a) was used where the UAV, including the Vivaldi antenna, was mounted on the wooden holder with the probing horn antenna opposite such that both antennas face each other. The only difference was regarding the used measurement devices as neither a signal generator nor a signal analyzer was employed. Instead, both antennas were connected to a VNA of type R&S ZVL [R&S 2022f], enabling complex transmission measurements between both antennas. Here, the Vivaldi antenna on the UAV was transmitting. Measurements were performed in a pseudo-zerospan mode, i.e., the measurements of the single samples were performed at almost the same frequency of 2.45 GHz. In contrast to the spectrum analyzer mode of the ZVL, the network analyzer mode does not support a real zerospan-measurement with a frequency span of 0 Hz. Therefore, the frequency span was set to the lowest possible value of 2 Hz. This frequency span can be neglected regarding the center frequency of 2.45 GHz which is effectively not changed throughout a measurement sweep. Within one sweep 2000 field samples were recorded. Figure 6.14 shows the deviation of the measured magnitude from the mean value for different RBWs. Within these measurements, the rotors were not spinning but the UAV and all other components

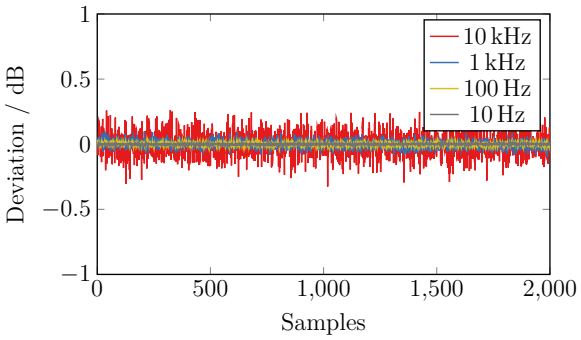

Figure 6.14: Deviation of the magnitude from its mean value as a result of pseudo-zerospan transmission measurements between the Vivaldi antenna and the probing horn antenna without spinning rotors. The measurements have been performed for different measurement bandwidths of the VNA. © 2021 IEEE, [Faul et al. 2021b]

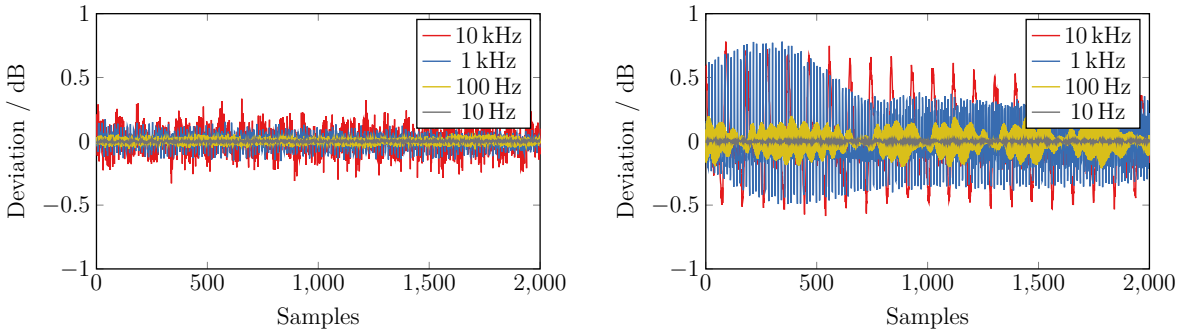

Figure 6.15: Deviation of the magnitude from its mean value as a result of pseudo-zerospan transmission measurements between the Vivaldi antenna and the probing horn antenna with spinning rotors. The measurements have been performed for vertical (a) and horizontal (b) polarization of the antennas and for different measurement bandwidths of the VNA. © 2021 IEEE, [Faul et al. 2021b]

were powered. Therefore, the measurement serves as a reference for the following ones. It can be easily seen that the magnitude deviation increases for higher RBWs which is expected from theory as this also increases the noise level of the measurement. The deviation in magnitude increases even more when the rotors are spinning. Measurements have been performed with the same rotation speed of the front rotors as for the spectral measurements, which was 2044 rpm. Also to enable a comparison, the carbon-fiber rotors were used. The deviation in magnitude for the vertical and horizontal polarization of the antennas is depicted in Figs. 6.15 (a) and (b), respectively. Note that also here both antennas were rotated such that the polarization between them always matched. As depicted in Fig. 6.15 (a), the magnitude deviation from the mean for vertical polarization and with spinning rotors is slightly higher than for the case without spinning rotors, except for an RBW of 10 Hz where it is similar to the static case. The measurements with the horizontal polarization and spinning rotors draw a different picture. Here, the deviation is significantly larger as can be easily seen in Fig. 6.15 (b). However, to enable a comparison between the different measurements, the maximum deviation of the magnitude from the mean together with the maximum phase deviation for the different measurement cases is given in Table 6.5. Looking at the table, the rotor influence is negligible for an RBW of 10 Hz for both polarizations. The reason that these values are similar to the static case is the integration time of the measurement receiver which

Table 6.5: Maxmimum deviation in magnitude and phase from their respective mean value as result from several zerospan transmission measurements. The measurements have been performed for different scenarios with and without spinning rotors and with different arrangements, where the antennas face each other (face-to-face) and also where the main beam is occasionally blocked by the rotors (through). In addition, the resolution bandwidth was changed between the measurements to reveal the impact of this important parameter.

RBW	static rotors	spinning rotors		
		face-to-face		through
		vertical	horizontal	
10 Hz	0.0132 dB ∠ 0.512°	0.0182 dB ∠ 0.499°	0.0194 dB ∠ 0.538°	⁄
100 Hz	0.0357 dB ∠ 0.640°	0.0635 dB ∠ 0.806°	0.2112 dB ∠ 1.218°	0.8727 dB ∠ 3.886°
1 kHz	0.0978 dB ∠ 0.909°	0.1730 dB ∠ 1.562°	0.7810 dB ∠ 3.811°	1.4924 dB ∠ 7.844°
10 kHz	0.3247 dB ∠ 2.966°	0.4104 dB ∠ 3.877°	0.7809 dB ∠ 4.882°	1.4905 dB ∠ 9.378°

is $1/10\,\mathrm{Hz} = 100\,\mathrm{ms}$ and, therefore, significantly longer than a period of the modulation which is only $T_{\mathrm{mod}} = 1/68\,\mathrm{Hz} = 14.7\,\mathrm{ms}$. However, the situation is different for the other RBWs. The highest deviation is found for 1 kHz and 10 kHz with values of about 0.78 dB magnitude and almost 5° phase deviation. However, experience shows that in NF measurements a phase error of 7° leads to a measurement error of about −50 dB. In agreement to the full spectrum measurements, it is found that the deviation is larger for horizontal than for vertical polarization of the antennas. It can also be observed that the deviation in magnitude and phase is even larger for the case where the field is measured through the rotor plane as in Fig. 6.7 which, however, is expected.

As described before, zerospan measurements can also be seen as time measurements of the demodulated carrier signal. This is not fully correct for the performed pseudo-zerospan measurements. Still, neglecting the fact that the frequency span in the measurement was 2 Hz and with the assumption that the measurement of the single field values takes only the time defined by the RBW, the total measurement time $T_{\mathrm{meas,tot}}$ for a sweep of $N = 2000$ samples is given by

$$T_{\mathrm{meas,tot}} = N\frac{1}{RBW} = 2000\frac{1}{10\,\mathrm{kHz}} = 200\,\mathrm{ms}\,. \tag{6.2}$$

Following this approach, the period of the modulation signal in Fig. 6.15 (b) can be determined to about 15 ms for $RBW = 10\,\mathrm{kHz}$. This almost fits with the periodicity of the modulation signal of 68 Hz which has been observed before. Nevertheless, there is some uncertainty regarding the exact acquisition time and also of the exact modulation frequency in the spectral measurements even if the frequency was found from an average of 15 subsequent measurements.

Dependence of Modulation on Antenna

Throughout these investigations, it has been partially found that the rotor-caused modulation depends on the spatial direction of the measurement and, therefore, on the radiation pattern of the Vivaldi antenna. As a consequence, it is expected that the rotor-caused modulation is different for a different antenna. For this, measurements with an antenna were performed that has been designed for the operation on a UAV [Azhar and Eibert 2021]. The antenna is a Vivaldi structure, made of aluminum to provide a better mechanical stability than the PCB antenna. It has a comparably low weight and also a low wind load. Further, the antenna comprises two polarizations while its backlobe has been minimized with

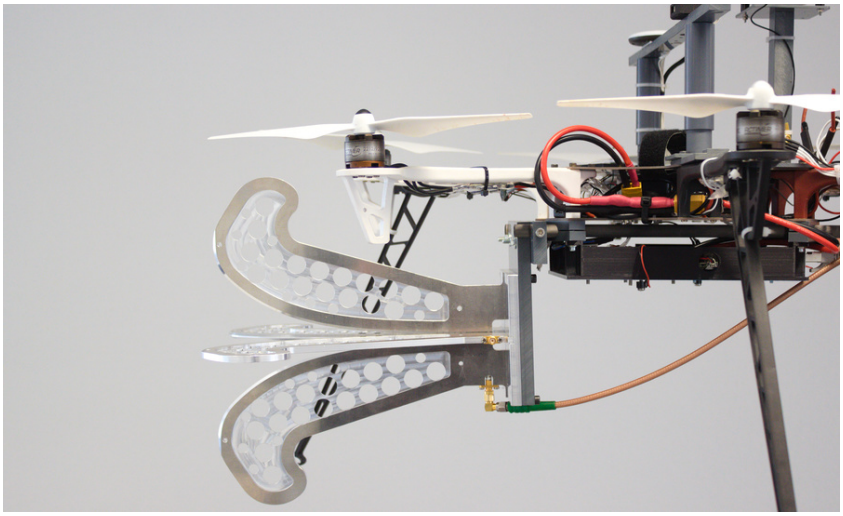

Figure 6.16: The aluminum Vivaldi antenna has been mounted at the front of the UAV to reveal the impact of the antenna itself on the modulation content. Due to its size, parts of the antenna are beneath the rotor blades. © 2021 IEEE, [Faul et al. 2021b]

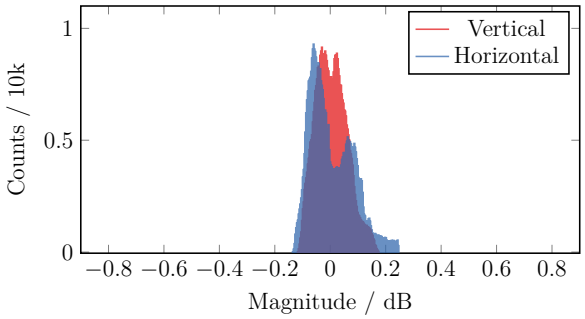

Figure 6.17: Histogram showing the deviation in magnitude from the mean value as a result of zerospan measurements at a frequency of 2.45 GHz. The measurements have been performed for the vertical and horizontal polarization of the aluminum Vivaldi antenna where the antenna was not rotated between the measurements. © 2021 IEEE, [Faul et al. 2021b]

the intention to reduce the mutual coupling with the UAV. The antenna was mounted to the front of the UAV as depicted in Fig. 6.16. Again, measurements of the full spectrum were performed for both polarizations while, also here, the polarization of the Vivaldi antenna and the horn antenna matched. From the measurements it is found that the sideband peaks occur at similar frequencies as for the PCB Vivaldi antenna, whereas the modulation is higher for the horizontal polarization in comparison to the vertical one. However, the difference between the two polarizations is not as significant as for the PCB Vivaldi antenna. This can also be seen in the histogram in Fig. 6.17 which shows the deviation in magnitude from the mean value and originates from zerospan measurements with the spectrum analyzer. The smaller difference between the two polarizations is also reflected in the standard deviation σ which is 0.056 dB for the vertical and 0.078 dB for the horizontal polarization. While the standard deviation for the vertical polarization is somehow similar to the one of the PCB Vivaldi antenna, it is significantly smaller for the aluminum antenna regarding the horizontal polarization.

6.2.3 Stability of the RF-over-fiber Link

Within the measurement setup, the field probe on the UAV is connected to the VNA on the ground via an RF-over-fiber link from ViaLiteHD [ViaLiteHD 2020]. The fiber link has a frequency range from 10 MHz to 3 GHz and works by modulating a near-infrared laser with the RF signal. The manufacturer specifies the total link gain as 0 dB, where the transmitter lowers the signal level by 15 dB and the receiver amplifies it by the same amount. However, the total gain of the link that is actually seen in measurements also depends on the used fiber and, in particular, on the cleanliness of the optical connectors which could be observed during many measurement campaigns. Also, important for the NF measurements is the noise figure of the fiber link as it reduces the dynamic range of the overall RF setup, especially for the case where the field probe on the UAV is receiving. The noise figure is specified as 23.5 dB and increases with increasing optical loss. Even if values for the gain stability of the fiber link are given by the manufacturer in the data sheet, measurements have been performed to evaluate the RF-over-fiber link with the used optical fibers.

First, the long-time stability of the fiber link has been tested in an air-conditioned measurement lab. For this, the complex transmission of two independent but similar fiber links was recorded over 20 h during which the fibers were not moved or even touched. The measurement was conducted using a VNA of type R&S ZVA24 [R&S 2022e] at a frequency of 2.45 GHz in accordance to the UAV-based measurements in Chapter 5. Figures 6.18 (a) and (b) show the magnitude and phase of two independent RF-over-fiber links of this long-time measurement. Looking at the plots, a very prominent periodic fluctuation of the magnitude and also the phase can be observed. The period of this fluctuation is about 50 min. For the reason that the fibers were not touched during the measurement, it is very likely that this fluctuation is caused by the air-conditioning of the lab. It has been found with a consumer-grade weather logger that the temperature and humidity in the lab changes with about the same period while all other conditions are kept as stable as possible. It is also unlikely that this fluctuation is caused by the power supply, as no change of the transmission parameter could be observed in a separate test where the voltage was intentionally adjusted within the input voltage range of the fiber converters. Furthermore, it has been observed in additional tests that manually heating the fiber and/or the fiber converters changes the magnitude and phase of the transmission significantly, while the phase is more sensitive to external influence. The same long-time test as in Fig. 6.18 has been carried out multiple times with different lengths of the optical fibers. From all of these measurements, no clear behavior of the fiber links could be derived since the drift, and even the periodic fluctuation, is different in each measurement and for different fiber lengths. However, longer fibers show a larger drift in magnitude and phase in compari-

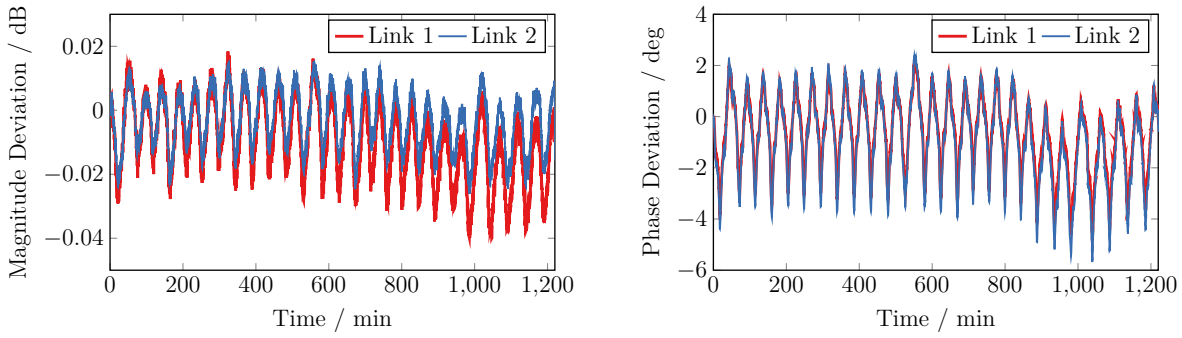

Figure 6.18: Long-time stability of the complex transmission of an RF-over-fiber link in magnitude (a) and phase (b). The measurements have been performed in an air-conditioned lab using a VNA.

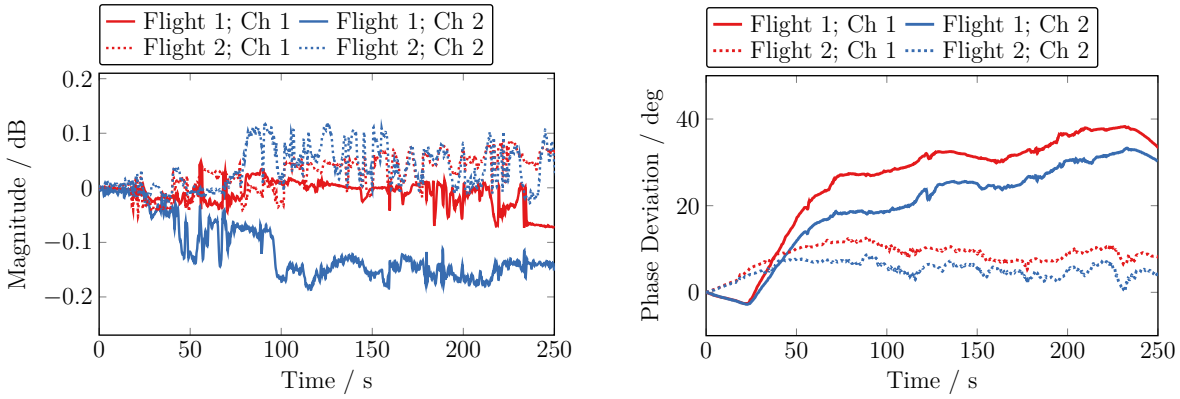

Figure 6.19: Stability of the complex transmission of an RF-over-fiber link in magnitude (a) and phase (b) during flight. The measurements have been performed outside using a VNA. The figures show two measurements during which two fiber links have been measured, each.

son to their shorter counterparts. The comparison of the different fiber links does also reveal that two independent but similar links do most likely not behave in the same way, even if they are exposed to the same environmental conditions. This finding is especially important if multiple RF-over-fiber links are used within one measurement setup, e.g., to simultaneously measure the co- and cross-polarization of the field or for measurements with several field probes.

In addition and besides the long-time stability, the behavior of the fiber link regarding moving and bending is of interest since the fiber is constantly exposed to such effects during flight in UAV-based field measurements. For such an investigation, the same measurement setup as before has been used. In a first test, the fibers were randomly moved and bent during the measurement which, still, took place in the lab. The change of the transmission parameter of the fiber during these dynamic measurements was found to be about 0.04 dB in magnitude and 4° in phase which is far less in comparison to the change in the long-time measurement. However, even if the impact of the fiber movement is small, it is the result of a lab test. Therefore, another measurement was performed under real in-situ conditions. Similar as before, the transmission parameters of two independent fiber links were recorded with the ZVA. All fiber converters, transmitters and receivers, were placed next to the VNA while being connected to it. Moreover, the fibers were tight to the UAV which was flying a random path, i.e., only the fibers experienced influences of the UAV flight while the connectors were protected from additional forces. The resulting changes in magnitude and phase for both fiber links and from two different measurements are depicted in Figs. 6.19 (a) and (b). The comparison of Figs. 6.18 (a) and 6.19 (a) clearly shows that the magnitude change is about one order of magnitude larger in the dynamic flight measurement scenario, where the identical optical fibers with same length were used in both measurements. It can also be seen that the magnitude of the transmission parameter behaves differently for different measurements and even for the different fiber links within the same measurement. However, the magnitude change is still within the specification of the manufacturer which is given in the datasheet as 0.25 dB [ViaLiteHD 2020]. Regarding the phase change of the UAV measurement in Fig. 6.19 (b), the situation is different. On the one hand, the change of the phase from both fiber links behaves in a similar manner even if there is an offset between the two links. On the other hand, the phase change is very different for different measurements while the variation in absolute numbers is too large for precise NF measurements. The plot in Fig. 6.19 (b) shows two measurements where the absolute phase change in one measurement is about 15° and in the other about 40°. Other additional measurements have even shown values of about

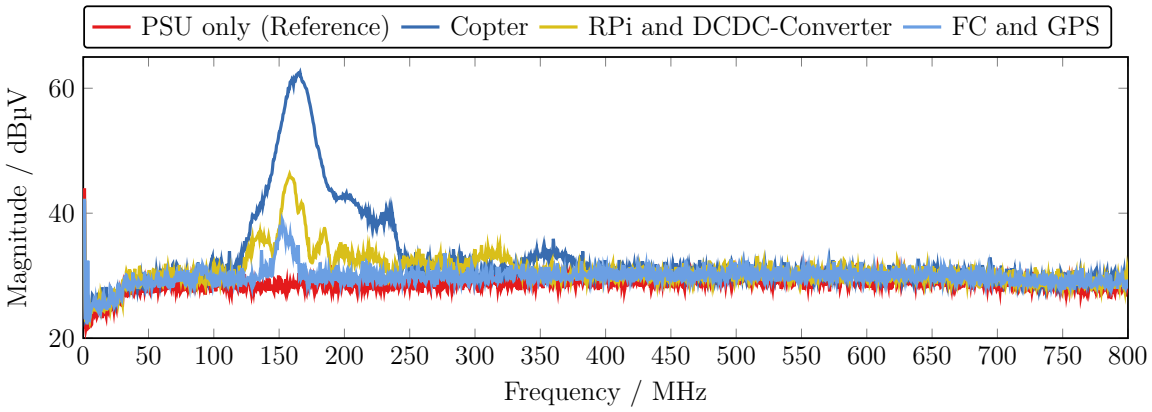

Figure 6.20: Frequency spectra showing the RF emission of the complete UAV, the flight controller (FC) together with the GNSS receiver board and the RPi. The measurement of the isolated power supply unit (PSU) is shown as reference.

80°. Overall, the measurements reveal that the phase change during flight and during measurement is a critical point within a measurement setup relying on an RF-over-fiber link for the connection of the field probe to the measurement receiver. Therefore, strategies for the compensation or, at least, characterization are needed.

6.2.4 Electromagnetic Interference

In addition to the errors in the measurement setup, it is important to characterize the electromagnetic interference (EMI) of the UAV as any emission from the UAV has the potential to disturb the field data of the NF measurements while also external RF sources can have an influence on the UAV performance.

To characterize the emission from the UAV and its single components, the UAV has been mounted in an EMC measurement chamber using the same wooden holder as for the rotor influence measurements in Section 6.2.2. A logarithmic periodic antenna of type R&S HL562 has been used as probing antenna. It was placed about 2 m away from the UAV and connected to an EMC measurement receiver of type R&S ESCS30, situated outside of the measurement chamber. The UAV was powered by a 10 A power supply unit (PSU) during the measurements since batteries could not provide enough energy for measurements over a longer time. To ensure that all recorded emission is solely caused by the UAV, the emission of the isolated power supply was measured at first, i.e., the UAV was not powered. The corresponding frequency spectrum in the frequency range from 1 MHz to 800 MHz is shown in Fig. 6.20 as reference where the spectrum was measured with an RBW of 1 MHz. The spectrum exhibits a noise level that is almost constant over the full frequency range, while no emission from the used PSU was found. In contrast, the measured spectrum of the UAV, including all components and with active motors, shows dominant emission between 100 MHz and 400 MHz with a frequency peak of 62 dBµV at 164 MHz. To identify the contribution of the single components of the UAV, measurements have been performed in which only specific components were active. In one of these measurements only the flight controller and the used GNSS receiver board was powered via an Universal Serial Bus (USB) cable. The corresponding frequency spectrum is also shown in Fig. 6.20. Here, a frequency peak can be observed at 152 MHz that is, however, much lower in magnitude than the one for the complete UAV. Another measurement was performed in which only the RPi was powered using a DC/DC converter via the PSU. This measurement shows a dominant emission around 158 MHz where the magnitude peak is 46.2 dBµV which is equal to −60.8 dBm. A similar measurement in which the RPi was powered using the original RPi PSU, that

did not show any emission when testing on its own, revealed that the observed emission is caused by the DC/DC converter. This observation was verified in additional measurements since several DC/DC converters of the same type were used. Beside the shown frequency range, measurements have been performed at higher frequencies up to 2.75 GHz while no emission higher than 800 MHz could be observed from the UAV and its components. Since the UAV-based measurements, described in Chapter 5, were performed at a frequency of 2.45 GHz with an RBW of 1 kHz and 10 kHz the observed emission from the UAV components are negligible. Still coherent transmission measurements have been performed inside the chamber using the same measurement setup as in the actual measurements where no impact of the RF emission on the measured field value was found. These transmission measurements have been conducted for a frequency of 2.45 GHz as well as for 110 MHz in view of measurements of air navigation systems.

Besides the measurements regarding the emission from the UAV, also tests have been conducted to reveal the impact that external RF sources can have on the UAV. For this, the same measurement setup as above was used with the only difference that the logarithmic periodic antenna was fed by a signal generator. The generator was tuned to different frequencies and output powers, eventually similar to what occurs in UAV-based measurements of air navigation systems. At the same time, the UAV was powered with spinning motors while the output of the UAV sensor measurements was observed. During this test no anomaly was found which led to the conclusion that the operation of the UAV in the scope of this thesis is safe.

6.3 Other Uncertainties and Error Sources

6.3.1 Measurement Time

One of the characteristics of UAV-based antenna measurements is that the field probe is constantly moving, even during data acquisition. This is an implication of the fact that the field probe is carried by a UAV, which is not able to precisely hover at a specific position for a longer time due to multiple reasons, such as wind gusts and the precision of the GNSS navigation data. Therefore, the measurement or data acquisition time T_{meas} is of great importance since it has a direct impact on the precision of the measurement position. If a VNA is used as measurement receiver, the measurement time depends on the RBW of the VNA. The relation is given by

$$T_{\text{meas}} = \frac{1}{RBW}. \tag{6.3}$$

If a UAV is flying with an airspeed of $1\,\mathrm{m\,s^{-1}}$ and the field is measured with an $RBW = 1\,\mathrm{kHz}$, i.e., a measurement time of 1 ms according to (6.3), then the UAV travels 1 mm within a single field measurement. This is within the allowed position accuracy regarding the rule of thumb where a position accuracy of $\lambda/50$ results in an error level of $-50\,\mathrm{dB}$. Taking the field measurements described before, $\lambda/50$ are 2.45 mm for a measurement frequency of 2.45 GHz. However, if the RBW is reduced to 100 Hz while maintaining the speed of the UAV, the UAV already travels 10 mm within a single measurement, which is significantly more than what is required for a low measurement error of $-50\,\mathrm{dB}$.

6.3.2 Data Synchronization

The field, position and orientation data are obtained from different measurement devices. This requires a synchronization of the measurement data which can be either realized by common timestamps or by the matching of, e.g., position data in the post-processing, where different methods have been described in Section 4.4. Still, an exact matching of the measurement data is not possible with the presented ap-

Table 6.6: The impact of the NF errors was evaluated for different frequencies and measurement distances, respectively radii, of the cylindrical geometry.

Frequency	Wavelength	Measurement Distance / Radius r			
f	λ	7.5λ	10λ	12.5λ	15λ
1 GHz	0.3 m	2.25 m	3 m	3.75 m	4.5 m
2 GHz	0.15 m	1.125 m	1.5 m	1.875 m	2.25 m
3 GHz	0.1 m	0.75 m	1 m	1.25 m	1.5 m

proaches and, eventually, a small but unknown time delay will remain. A present time delay results in either a mismatch of the orientation data in comparison to position and field, e.g., as for the measurements presented in Chapter 5, or in a mismatch of position and orientation in comparison to the field data for measurements at lower frequencies where no laser tracker is employed for the acquisition of the measurement positions. To lower the influence of the orientation errors resulting from the synchronization mismatch, the flight path is usually chosen such that the orientation is almost constant over large parts of the measurement surface. However, this is not sufficient for measurements where also the position data depends on the time synchronization of the measurement devices as for the case where RTK position data is used.

6.4 Impact of the Error Contributions

Numerical simulations have been performed to judge the impact of the different NF errors on the FF. For this, the simulated NF data was perturbed with random offsets that were chosen to be within specific intervals according to the characterization of the single components in this chapter. In general, one can also think about an analytical analysis of the impact of the NF errors. However, the FIAFTA, which was employed as NFFFT, processes the measured NF data in a way that makes it hard to analytically track errors as the algorithm is reluctant against outer disturbances to a certain degree. Furthermore, it has to be noted that the following numerical investigations are specific to the combination of the used antenna, the measurement geometry and the NFFFT algorithm. Still, they will be similar for other setups even if they are not universally applicable. In principle, such investigations need to be performed for every change in the measurement setup or even for changes in the NFFFT parameters. However, the purpose of these error investigations is rather the exact characterization of the errors and more to reveal the impact of the different sources and to unveil those which are most critical. This allows to tackle and reduce the error sources with the largest impact in another step, following the simulation results and improving the measurement setup.

6.4.1 Simulation Model

A model of the DRH400 horn antenna [RFSpin 2013] served as AUT within the simulations which were made in a time-harmonic, single frequency manner. The horn antenna was modeled in Altair FEKO [Altair 2022] which works with the method of moments (MoM) technique to calculate the NF data. Also, the FF was calculated as reference in FEKO. A cylindrical measurement geometry was chosen for the NF since most UAV-based NF measurements use cylindrical geometries. The height of the measurement cylinder was 10 m while its radius r was chosen in dependence of the measurement frequency f as simulations have been performed for multiple frequencies. An overview of the measurement frequencies and the corresponding radii in dependence on the wavelength λ is given in Table 6.6. The vertical

sampling of the cylindrical measurement geometry was always chosen to $\Delta z = \lambda/3$ which means that the actual value varied with the wavelength. Similarly, the sampling in horizontal direction was chosen to $\Delta\varphi = \lambda/10$ with respect to the minimum sphere of radius 0.5 m, enclosing the AUT. The choice of Δz and $\Delta\varphi$ clearly implies an oversampling in vertical and horizontal direction. This is intended as the field is very likely to be oversampled within UAV-based field measurements as the field is continuously measured during flight.

For the analysis itself, offsets were added to the single field and position data before the transformation to the FF, unless otherwise stated. The offsets are uniformly distributed random numbers within an interval $[-a, a]$. Even if all parameters are influenced at the same time in real measurements, only one parameter was disturbed at a time within the simulations. This approach has been chosen to reveal the differences in the impact of the single parameters.

6.4.2 Errors in Position and Orientation

Following the categorization of the uncertainties in this chapter, the impact of the position and orientation has been investigated at first. For this, the position of every single NF sample was disturbed by a random offset that is within the interval $\left[-\lambda/10, \lambda/10\right]$, where λ is the wavelength of the electromagnetic field. A different offset within the interval was added to the three components of the position as the NF position is given in Cartesian coordinates. Figure 6.21 (a) shows the maximum error of the horizontal FF main cut at $\vartheta = 90°$ and for a measurement radius of $r = 10\lambda$. The error is plotted over the position uncertainty and for different frequencies, while the choice of the horizontal main cut has been made for clarity and has no implication on the generality of the results. The single curves of the graph are an average of five simulations with random offsets inside the same interval. In addition, the error curves have been smoothed by a moving average filter to suppress noise. The resulting graph shows clearly that the FF error increases with increasing position uncertainty. This is well known and the reason why highly sophisticated positioners are employed for NF measurements of antennas in anechoic chambers. The graph also reveals that the error behavior is independent of the measurement frequency. The curve for a frequency of 3 GHz shows a static offset which may be due to the slightly different behavior of the antenna for different frequencies and the resulting change in the amount of energy that is covered by the cylindrical geometry. Still, the underlying trend is similar for all frequencies. In an analogous way, Fig. 6.21 (b) shows the simulations for variable measurement radii r but a fixed frequency of 2 GHz. Also here, it is found that the FF depends only on the position uncertainty and not on the actual radius. However, the radius has a significant influence on the valid angles of a cylindrical measurement which is not reflected in the shown curves. The comparison of both graphs, Figs. 6.21 (a) and (b), reveals that the FF error is below -40 dB for an uncertainty in position of $0.02\lambda = \lambda/50$. Regarding the different position measurement systems used in NF measurements, discussed in Section 6.1, it must be taken care that the position accuracy of the chosen system is sufficiently high with respect to the desired measurement frequency and the sampling theorem, which can become easily challenging for frequencies in the S-band and above.

Closely related to position errors are uncertainties in the orientation of the field probe. Similar as before, the numerically simulated ideal NF data is transformed where only the elevation angle is blurred by adding random numbers within the interval $[-3°, 3°]$. The resulting plots of the maximum errors of the horizontal FF main cut are shown in Figs. 6.21 (c) and (d) for different frequencies at $r = 10\lambda$ and different radii at 2 GHz, respectively. It can be easily seen that the error curves increase about 10 dB for an elevation uncertainty of $\pm 3°$ in both plots where the low overall error level must be taken into account. Also, it must be mentioned that an uncertainty of 3° in elevation is significantly larger than what has been found in terms of precision and repeatability of the IMU of the UAV in Section 6.1.3. There, the maximum deviation has been found to be 0.56° where the impact of the elevation uncertainty

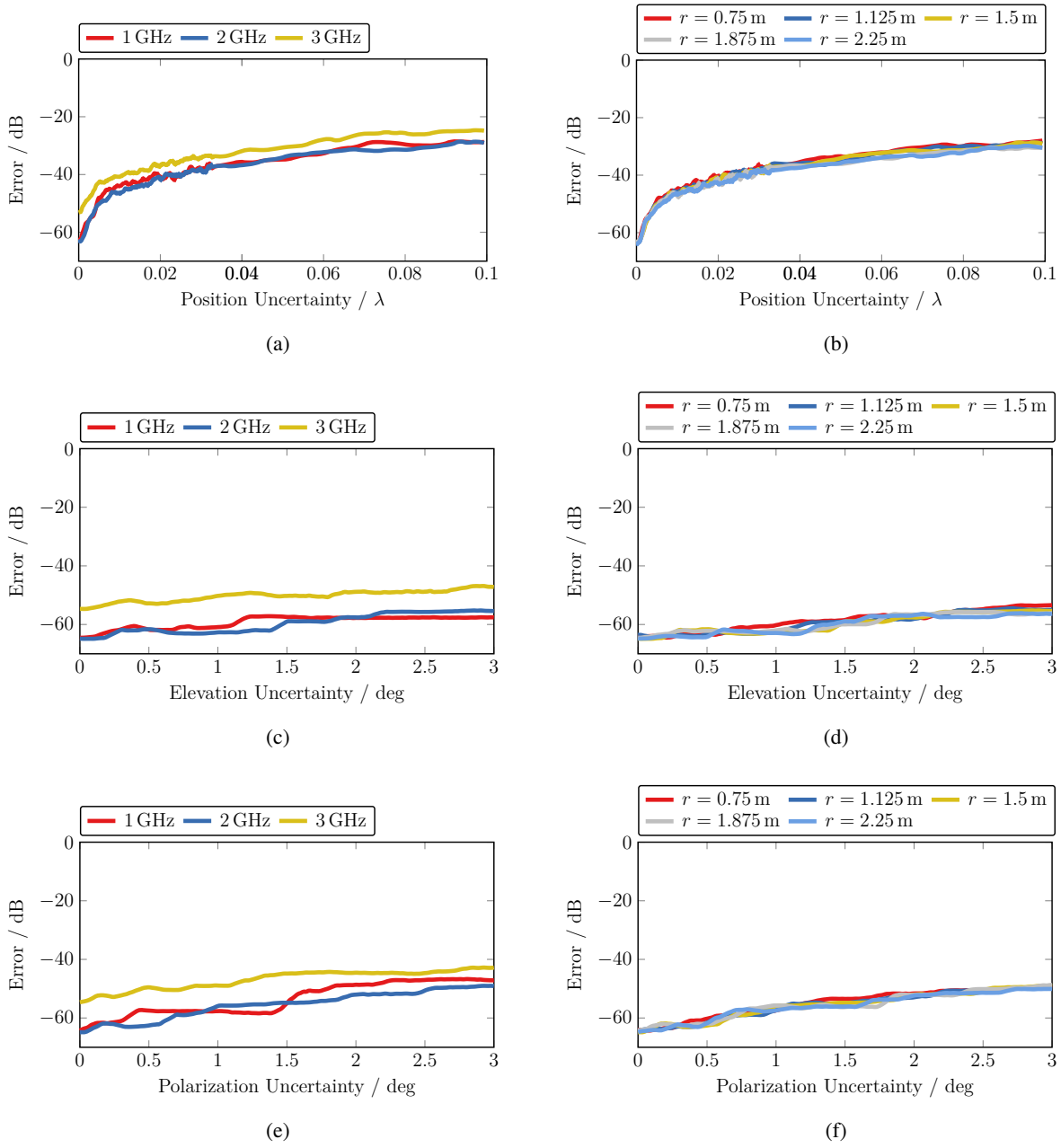

Figure 6.21: Maximum error of the horizontal FF main cut at $\vartheta = 90°$ for different uncertainty values in position, (a) and (b), elevation, (c) and (d), and polarization, (e) and (f). The graphs show simulations for a variable frequency and fixed radius $r = 10\lambda$, as well as for a frequency of 2 GHz and various radii of the cylindrical measurement geometry.

is sufficiently low for these values.

Regarding the uncertainty of the polarization, a similar picture can be drawn as for the elevation. Also here random numbers in the interval $[-3°, 3°]$ have been added to the correct polarization angles of the different measurement positions. Figures 6.21 (e) and (f) reveal that the FF error increases by about 15 dB for a polarization uncertainty of $\pm 3°$ while, again, the impact for the measured maximum deviation of the angles derived from the IMU is still negligible, regarding the overall low error level. However,

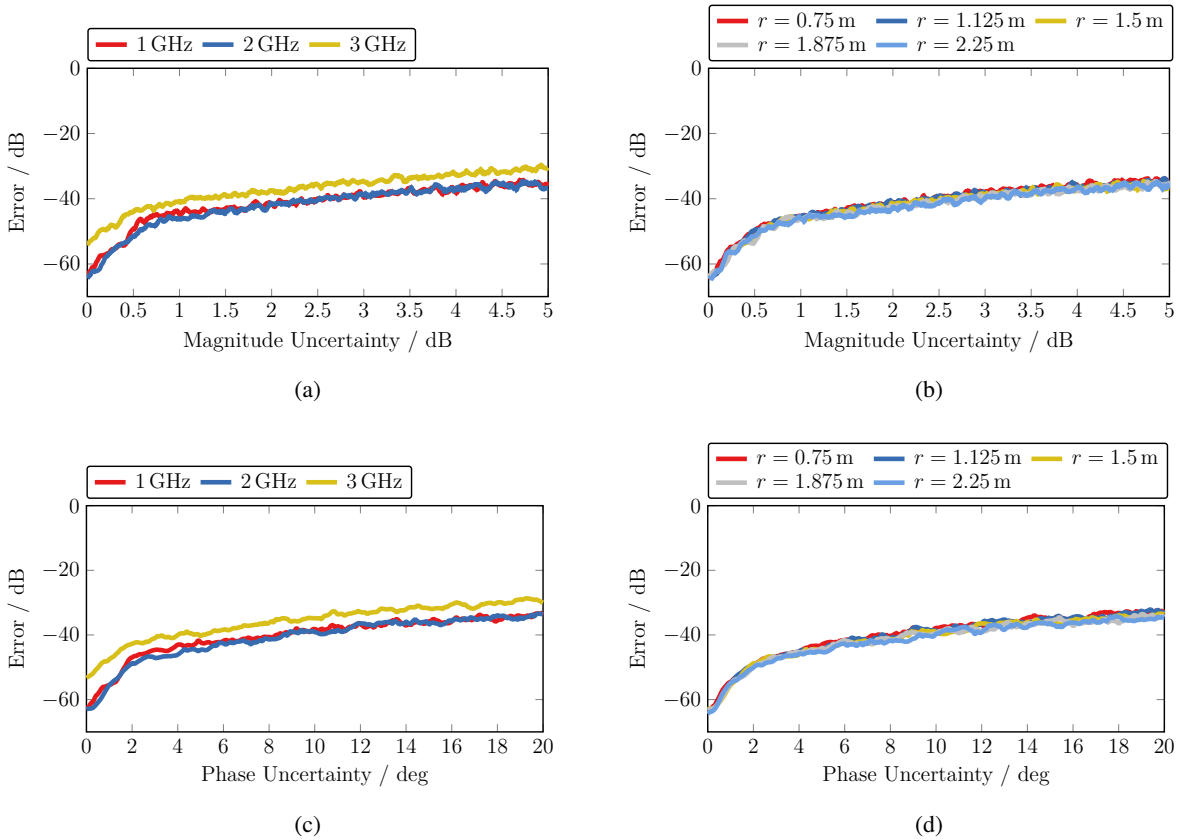

Figure 6.22: Maximum error of the horizontal FF main cut at $\vartheta = 90°$ for different uncertainty values in magnitude, (a) and (b), and phase, (c) and (d). The graphs show simulations for a variable frequency and fixed radius $r = 10\lambda$, as well as for a frequency of 2 GHz and various radii of the cylindrical measurement geometry.

even if the simulations reveal that small uncertainties in elevation and polarization are unimportant in comparison to uncertainties in the actual measurement position, it is important to note that the simulations are only valid for one specific combination of AUT and field probe where other combinations may lead to different results. Still, the trend of the position having a larger influence on the FF error than the orientation angles is likely to be the same within the considered uncertainty intervals. In addition, it shall also be recalled that an uncertainty in the orientation may have a direct impact on the accuracy of the position depending on the offset between the measured position and the actual field probe.

6.4.3 Errors of the Field Data

Besides the simulations regarding the influence of the position errors, also the uncertainty in the field values needs to be investigated. Following the same approach as before, uncertainties in magnitude have been added to the otherwise ideal NF values. The random uncertainty values are in the interval of $[-5\,\mathrm{dB}, 5\,\mathrm{dB}]$ while the corresponding plots are given in Figs. 6.22 (a) and (b) for different frequencies at $r = 10\lambda$ and for variable radii at 2 GHz, respectively. Within the graphs the curves for the different frequencies and radii of the measurement cylinder are almost identical, except for the 3 GHz curve which has an offset, similar as before. However, all curves exhibit a rapid increase of the FF error for uncertainty values in magnitude up to about 0.5 dB while the curve flattens and increases much slower with increasing uncertainty above this value. Regarding the measurements in this chapter, the

uncertainties in magnitude are mostly caused by the rotor influence and fiber drift. However, the largest realistic magnitude uncertainties are about $\pm 0.8\,\mathrm{dB}$ which lead to a FF error of about $-46\,\mathrm{dB}$ in the simulations. This appears to be an increase of about 21 dB from the error level of the undisturbed simulation which is $-65\,\mathrm{dB}$.

Moreover, the field values cannot only be disturbed in magnitude but also in phase which is commonly the more critical parameter within coherent NF measurements. Therefore, in an analogous manner as before, the field values have been disturbed in phase by adding random values in the interval of $[-20°, 20°]$ to the single field values. The resulting graphs are depicted in Fig. 6.22 (c) for different frequencies at $r = 10\lambda$ and in Fig. 6.22 (d) for variable radii at 2 GHz. Again, the different frequencies and radii do not seem to influence the FF error while the phase uncertainty clearly does. The error curves increase quickly for phase uncertainties up to 2° and increase with a much flatter ramp up until 20° where the simulation ended. Regarding this phase error of 20°, the corresponding FF error is about 25 dB higher in comparison to the ideal undisturbed field data. Yet, it must be taken into account that phase errors in the order of 40° can be easily observed regarding the characterization of the different components, especially regarding the measurements of the RF-over-fiber link. Taking this into account, the simulations of Fig. 6.22 (c) and (d) reveal that the impact of the phase uncertainty of the FF error is crucial.

Considering all simulation results, one comes to the conclusion that the position and phase of the field are the most critical parameters as they have the largest impact on the FF error. However, it must also be considered that the actual measurement errors are likely to be larger as suggested by the simulations as the actual errors and uncertainties in real measurements will always be a combination of the different sources while, here, only the isolated parameters have been investigated. Furthermore, the results are, strictly speaking, only valid for the specific case that has been simulated. Still, the simulations provide a starting point for the identification and treatment of the most demanding error sources.

6.5 Treatment and Compensation of the Error Sources

The investigations in this chapter showed that there are multiple sources for errors and uncertainties in UAV-based field measurements, where some of them are more demanding and others are almost negligible. The simulations in Section 6.4 revealed that uncertainties in the position and phase have the highest impact on the FF error, considering the values of the uncertainties that have been observed in the measurements in Sections 6.1 to 6.3.

In the discussed setup, the measurement positions are determined by a GNSS receiver and/or a laser-tracker. Since both systems are not directly related to the AUT, the measured position data is threatened by misalignment and wrong coordinate transformations and care must be taken. Even if these errors are basically static offsets, they can become more complex if the orientation of the UAV is taken into account. This is because the orientation changes all the time which influences the position information, depending on the offset between the location of the measured position on the UAV to the location of the field probe. To prevent this behavior, at first, it is beneficial to jointly measure the position and orientation information in terms of a six-dimensional (6D) positioning system. If such a 6D measurement system is not available, it is favorable to measure the position of the UAV in the origin of the local UAV coordinate system while the field probe is brought to this point as close as possible. Overall, it is important that the accuracy of the chosen position measurement system is sufficient with respect to the measurement frequency. Moreover, the fusion of multiple sensors can improve the accuracy significantly which is, therefore, largely implemented for position and orientation measurement systems.

While errors in phase may theoretically be caused by any component in the RF part of the setup, the characterization of the single components revealed that the RF-over-fiber link and the influence of the

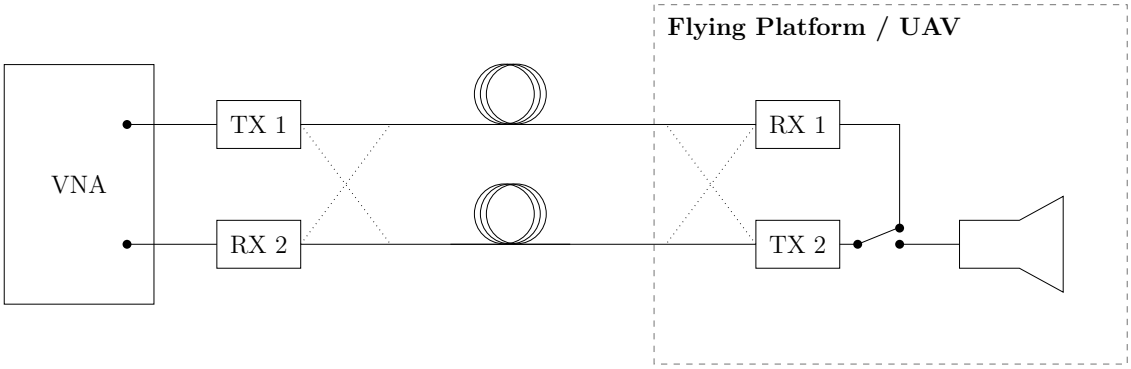

Figure 6.23: Setup for the calibration of the optical fiber link in question TX2-RX2. A switch is used to connect the fiber link to a second fiber link TX1-RX1 which allows to close the RF loop to the ground. Optical switches allow the exchange of the used fibers between the two links.

rotating rotor blades have the highest impact on the measured field values. The behavior of the RF-over-fiber link has been found to be unstable as it seems to be sensitive to environmental conditions. This can result in large drifts of the phase of the transmission parameter which is crucial for measurements with the setup presented in Chapter 4. Accordingly, a calibration of the fiber link is necessary that has to be constantly repeated during flight as the phase of the transmission parameter is likely to change between and also during measurements. One possible implementation of a calibration may involve a second fiber link which is used in reverse direction to the first one. This closes the RF loop containing two optical fiber links, i.e., involving the link to the UAV which is normally used for field measurements. In combination with optical switches, the fibers, working in ground-UAV direction and vice versa, can be exchanged which allows for the determination of the transmission parameter of the single fibers if the antenna signal is additionally taken into account. A schematic drawing of the calibration setup is depicted in Fig. 6.23. In contrast to a calibration, also a tracking of the fiber link parameters is conceivable. For this, a model of the RF-over-fiber link can be used to predict the next parameter values while the model is updated by actual measurements. A third approach for calibration of the RF-over-fiber link is the employment of an independent RF source on the UAV which is occasionally connected to the fiber link as reference. Here, it is important that the RF source is stable in magnitude and phase over the time of the whole measurement.

Besides the RF-over-fiber link, the influence of the rotating rotor blades has been found to be critical in terms of impact on the phase of the measured field signal regarding accurate measurements. The foundation of this error source is the field pattern of the probe that changes for different arrangements of the rotor blades. To quantify and with respect to calibration procedure, the change of the radiation pattern of the field probe can be either measured, simulated or analytically calculated, where the latter seems to be the most complicated approach. Given that the field probe pattern is available for any rotor arrangement, the actual rotor arrangement can be determined by, e.g., a high-speed camera for the single measurements. Alternatively, the rotation speed of the rotor blades can be measured using a laser or other optical system while the actual rotor arrangement during the measurement is eventually calculated. Similar to this approach is the usage of the motor control signals to determine the rotor arrangement since they are related to the rotation speed of the rotors. More advanced UAV motors do even provide messages in a feedback channel which contain information such as the rotation speed of the rotor blades. However, alongside these very effortful approaches of determining the rotor arrangement, there are some steps that could be implemented into the measurement before. The measurements in Fig. 6.13 show, that the impact of the rotor modulation effect can be minimized when the field is measured with the main

beam of the antenna. Therefore, a cylindrical, or even spherical, measurement geometry shall be used in UAV-based antenna measurements, where the latter requires a gimbal to decouple the orientation of the field probe from that of the UAV. Furthermore and before everything else, the field probe is to be separated as much as possible from the UAV body since larger distances between both components reduce the rotor modulation significantly as shown in Fig. 6.11.

6.6 Chapter Summary

In this chapter, the different error sources of a UAV-based field measurement setup have been investigated. After reviewing the NIST 18 term error model that is commonly used in NF antenna measurements, the most demanding additional error sources in the considered coherent UAV-based measurements setup have been listed. It was outlined that the errors can basically be separated into positional errors and into errors within the RF part. After the characterization of the single components of the measurement setup, numerical simulations were performed to judge on the significance of the error contribution of the single components. Therefore, the error bounds that have been found from the measurements were used as input for the simulations. As expected, the simulations revealed that the position of the measured field is critical, while the position measurement system that is actually employed has to be chosen appropriately regarding the measurement frequency. Concerning the RF part of the measurement setup, it has been found that the mutual coupling between the probe antenna and the UAV, especially with the rotors of the UAV, can disturb the measured field values substantially. Moreover, the used RF-over-fiber link has been identified as crucial and very delicate component which can cause errors in magnitude and phase of the measured field that are far from what is acceptable in NF measurements as backed by the simulations. Therefore, different approaches for calibration of the RF-over-fiber link and the treatment of the other error sources have been briefly described.

Part III

Measurement of Modulated Fields

Chapter 7

Measurement of Continuously Modulated Fields

The realization of in-situ antenna measurements with UAVs enables the characterization of antennas in their real operating environment, as discussed in Part II of this thesis. While most AUTs might be fully accessible for characterization, like for example large reflector antennas [Punzet et al. 2022] and mobile base stations [García-Fernández et al. 2018b], some antennas are not. In these cases it is not possible to feed the AUT with a specifically tailored test signal, but there may also be situations in which the feeding of a test signal is not desired, e.g., when antennas have to be measured during their normal operation or when the transmitted signals are to be verified. In those scenarios, there is a need to deal with modulated field signals within the NF measurement of antennas. As described in Chapter 2, NF measurements are commonly performed in a single-frequency time-harmonic manner where the transmission between the AUT and the field probe is measured. So far, UAV-based antenna measurements are based on the same technique and have almost exclusively been demonstrated for single-frequency measurements. Regarding the treatment of possible modulated field signals in in-situ measurements, there are NFFFT algorithms that work in the time domain and can deal with such fields [Hansen and Yaghjian 1995; Oetting and Klinkenbusch 2005]. However, in contrast, most NFFFTs work in the frequency domain and are usually faster and more efficient than their time-domain counterparts. Furthermore, advanced frequency-domain NFFFT algorithms, e.g., the FIAFTA, offer additional features, like the consideration of ground or nearby scatterers, which are useful to treat in-situ measurement environments appropriately. The usage of a frequency-domain NFFFT algorithm within in-situ measurements of modulated field signals requires a method to convert the modulated fields to time-harmonic equivalents that can be transformed to the FF. In Faul et al. [2019], two methods for the measurement of continuously modulated fields have been proposed, i.e., a long-time measurement (LTM) and a short-time measurement (STM) approach. Although the restriction to continuously modulated fields is a limitation of generality, the methods are applicable to specific but valuable scenarios. They have been developed with the verification of ground based navigational aids (NAVAIDs) for aviation in mind, like the Doppler VHF Omnidirectional Radio Range (DVOR) or the Instrument Landing System (ILS). Those NAVAIDs work with basic analog amplitude and frequency modulation schemes. However, an extension of the measurement methods to other non-continuous modulation schemes may be possible.

This chapter is based on [Faul et al. 2019, 2021a; Faul and Eibert 2021; Faul et al. 2023] and describes the general concept of both measurement approaches, while also an analytical description is given. Moreover, the applicability of the measurement approaches are demonstrated by numerical simulations and measurements, before distance and time constraints of the short-time measurement approach are discussed.

7.1 Theoretical Background

This section gives an overview of basics from the field of signal theory, which are assumed in the following chapter. Further knowledge of signal description in the time and spectral frequency domain is also assumed, as well as the basics of electromagnetics. This theoretical background can also be found in the literature, e.g., in Rupprecht [1993], Hoffmann [2005] and Balanis [2012].

7.1.1 Measurement of Signals

A time-varying signal is described by its amplitude change over time, where the amplitude can be either real-valued or complex. However, any signal can also be described by its spectral content that is revealed, e.g., with the help of the Fourier transform where also other transformations exist. The Fourier transform is a mathematical operation that allows for the decomposition of a signal. For example, a signal which originally depends on time is transformed into a signal which depends on temporal frequencies. The time- and the frequency-domains, the latter is also known as spectral domain, allow for a simplified description of certain signal characteristics. The continuous Fourier transform of a continuous signal $x(t)$ is given by

$$\mathcal{F}\{x(t)\} = X(\omega) = \int_{-\infty}^{\infty} x(t)\, \mathrm{e}^{-\mathrm{j}\omega t}\, \mathrm{d}t\,. \tag{7.1}$$

The transformation result $X(\omega)$ is the corresponding spectral function to $x(t)$, where $\omega = 2\pi f$ describes the angular and f the temporal frequency. This interpretation is used for the transformation result of time signals but others are also possible when, e.g., spatial distributions are transformed and spatial frequencies are considered. The inverse of the continuous Fourier transform in (7.1) denotes to

$$\mathcal{F}^{-1}\{X(\omega)\} = x(t) = \frac{1}{2\pi} \int_{-\infty}^{\infty} X(\omega)\, \mathrm{e}^{\mathrm{j}\omega t}\, \mathrm{d}\omega\,. \tag{7.2}$$

As stated by the limits of the integrals in (7.1) and (7.2), the Fourier transform is calculated for times and frequencies in the range from negative to positive infinity. However, practical signals usually have a defined start and end time which means that, in reality, the integral limits of the Fourier transform are defined by the signals themselves. Regarding the measurement of a signal, the integral limits are not only defined by the signal itself but also by the measurement time. This can be accounted for with the introduction of a window function $w(t)$, which changes (7.1) to

$$X(\tau, \omega) = \int_{-\infty}^{\infty} x(t) w(t-\tau)\, \mathrm{e}^{-\mathrm{j}\omega t}\, \mathrm{d}t\,. \tag{7.3}$$

The window function can be of various form, e.g., a simple form of $w(t)$ is a rectangular function that is equal to one for all times inside the measurement interval T_{meas} and zero elsewhere. Following this notation, the time offset τ is changed to measure and derive the frequency content of different parts of the signal as illustrated in Fig. 7.1. Equation (7.3) is commonly known as the short-time Fourier transform (STFT) [Allen 1977]. The change of the spectral frequency components of a signal over time can be visualized in form of a spectrogram, where the frequency is plotted over time. An example of the spectrogram of a linear chirp signal from 0 Hz to 450 Hz is depicted in Fig. 7.2 (a). The plot shows that the frequency increases with time. However, the single frequencies are not clearly resolved while the measurement time is also not precise. This is a consequence of the uncertainty principle. Limiting a signal in time has direct consequences on its corresponding frequency spectrum, since, in general, time-limited signals have an infinite frequency spectrum while bandlimited signals are infinite in time. The uncertainty principle of communication, also known as Küpfmüller's uncertainty principle [Peters 1967; Hoffmann 2005], describes the relationship between the temporal extent of a signal, its duration

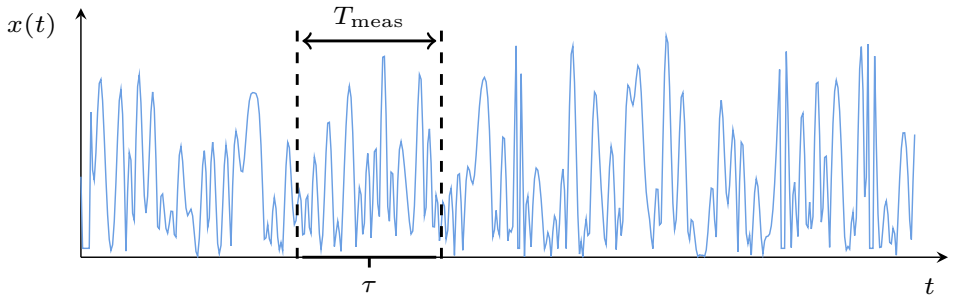

Figure 7.1: Temporal length T_{meas} of a window function $w(t)$ which allows for the analysis of the spectral content for different parts of the time signal. The temporal "position" of the window function depends on the parameter τ.

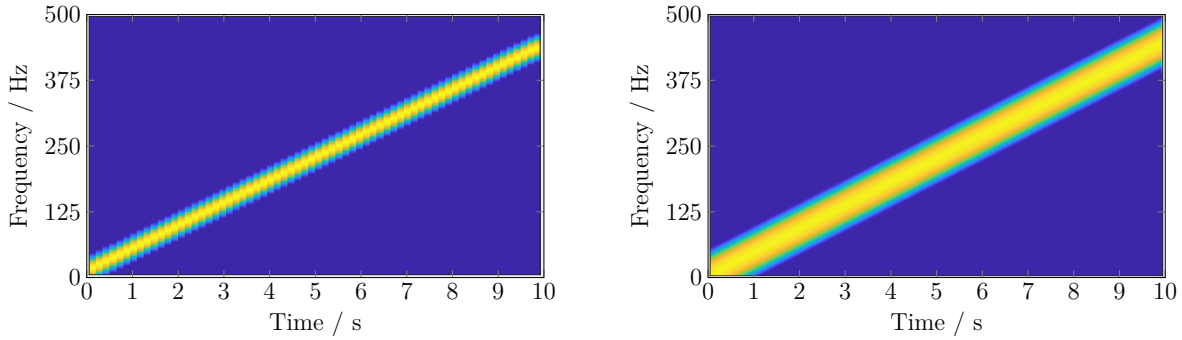

Figure 7.2: Spectrogram of a linear chirp signal with a frequency sweep from 0 Hz to 450 Hz. The measurement time of the short-time Fourier transform has been chosen to 600 ms (a) and 150 ms (b).

T, and the frequency resolution Δf, i.e., the minimum difference in frequency that can be distinguished. It denotes to

$$T \geq \frac{1}{\Delta f}\,. \tag{7.4}$$

The spectrogram in Fig. 7.2 (a) was calculated with a measurement time, respectively opening time of the window, of 600 ms. If the time is to be resolved with higher precision, the measurement time can be shortened while, as a consequence, the frequency will be more blurred. For illustration, the spectrogram of the same chirp for a measurement time of 150 ms is depicted in Fig. 7.2 (b).

7.1.2 Analytic Signal and Complex Baseband

Since the Fourier transform is inevitably dependent on the time signal, some rules apply, e.g., the magnitude spectrum of a real-valued time signal is symmetric, containing positive and negative frequency components, where multiple frequencies close to each other are called frequency bands. An example of such a spectrum is schematically shown in Fig. 7.3. However, the information content is equal for the positive and negative frequency bands, as they are mirror frequencies. As a consequence, often only one sideband is transmitted in radio communication. Such a single-sideband signal is also known as analytic signal.

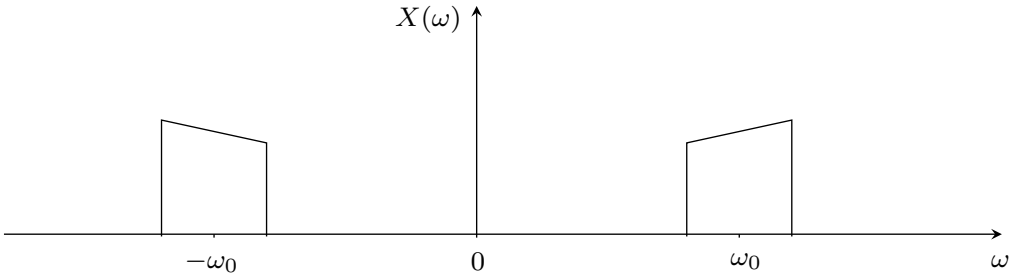

Figure 7.3: Magnitude of the spectral content of a real-valued time signal. The spectrum is symmetric regarding positive and negative frequencies while both bands contain the same information.

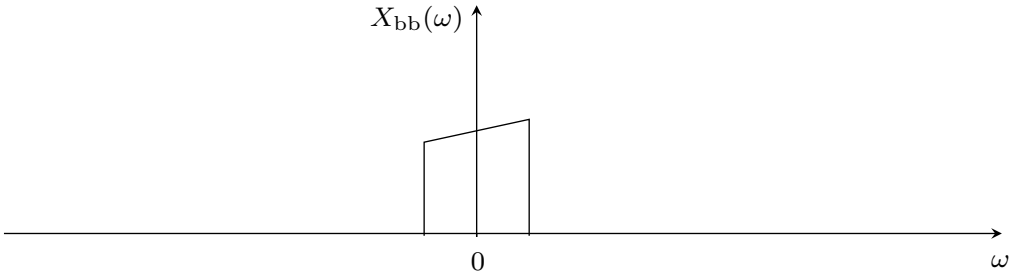

Figure 7.4: Frequency spectrum of a baseband signal. The frequency content is centered around 0 Hz which implies a complex time signal in case of no symmetry.

Due to the symmetry rules of the Fourier transform, an analytic signal is always complex in time-domain. Its real and imaginary parts are related to each other by the Hilbert transform[1]. Therefore, the analytic signal $s_{\mathrm{a}}(t)$ can be calculated from the real-valued signal $s(t)$ by

$$s_{\mathrm{a}}(t) = s(t) + \mathrm{j}\hat{s}(t)\,, \tag{7.5}$$

where $\hat{s}(t) = \mathcal{H}\{s(t)\}$ is the Hilbert transform of $s(t)$. However, the analytic signal is not only important when it comes to single-sideband modulation, but also for baseband signals. Baseband signals, in contrast to modulation signals, are signals whose spectrum is located around the origin of the frequency axis, as schematically depicted in Fig. 7.4. It is useful to analyze signals in the baseband since the highest frequency present is lowered and with that the sampling theorem is relaxed. Regarding $s_{\mathrm{a}}(t)$, the corresponding complex baseband signal $s_{\mathrm{bb}}(t)$ can be determined by

$$s_{\mathrm{bb}}(t) = s_{\mathrm{a}}(t)\,\mathrm{e}^{-\mathrm{j}\omega_0 t}\,, \tag{7.6}$$

where ω_0 is an arbitrary but fixed frequency. For modulated signals, ω_0 is usually the carrier frequency.

[1]The Hilbert transform is a linear integral transformation. It is given for a real function $s(t)$ with time t by

$$\mathcal{H}\{s(t)\} = \hat{s}(t) = \frac{1}{\pi}\int_{-\infty}^{+\infty}\frac{s(\tau)}{t-\tau}\,\mathrm{d}\tau = s(t) * \frac{1}{\pi t}\,,$$

which describes a convolution (symbol $*$) in time-domain. The Fourier transform of $(\pi t)^{-1}$ is the signum function multiplied by the imaginary unit j.

7.2 Measurement Approaches

In general, a time-harmonic electromagnetic field $\underline{\boldsymbol{E}}(\boldsymbol{r}, t)$ at position $\boldsymbol{r}$ and time t can be described by

$$\underline{\boldsymbol{E}}(\boldsymbol{r}, t) = \boldsymbol{E}(\boldsymbol{r})\, \mathrm{e}^{\mathrm{j}\omega t}\,, \tag{7.7}$$

where $\boldsymbol{E}(\boldsymbol{r})$ is a complex vector field and ω the frequency of the field. Regarding the time-harmonic property of the field, $\boldsymbol{E}(\boldsymbol{r})$ is also called phasor which is commonly independent of time. To differentiate whether a complex field E includes the time dependency $\mathrm{e}^{\mathrm{j}\omega t}$ or not, the following convention is introduced: time-harmonic fields which do not depend on time are written in latin letters, e.g., $\boldsymbol{E}(\boldsymbol{r})$, while fields which include the time dependency are additionally underlined, e.g., $\underline{\boldsymbol{E}}(\boldsymbol{r}, t)$. In general, the complex form of the field is only a mathematical description, which simplifies calculations. Still, the instantaneous measurable field $\boldsymbol{\mathcal{E}}(\boldsymbol{r}, t)$ is given by

$$\boldsymbol{\mathcal{E}}(\boldsymbol{r}, t) = \Re\left[2\pi \underline{\boldsymbol{E}}(\boldsymbol{r}, t)\right] = \Re\left[2\pi \boldsymbol{E}(\boldsymbol{r})\, \mathrm{e}^{\mathrm{j}\omega t}\right]\,, \tag{7.8}$$

where $\Re\left[\ldots\right]$ is the real part operator. Here, it shall be noted that the usage of the real part is only a convention which has been chosen in accordance with Balanis [2012] and will be followed throughout the succeeding chapters. Regarding the complex form in (7.7), a continuously modulated field signal is described by the introduction of a continuous complex modulation function $m(\boldsymbol{r}, t)$ that depends on position $\boldsymbol{r}$ and time t. The modulated field signal denotes to

$$\underline{\boldsymbol{E}}_{\mathrm{mod}}(\boldsymbol{r}, t) = m(\boldsymbol{r}, t)\boldsymbol{E}(\boldsymbol{r})\, \mathrm{e}^{\mathrm{j}\omega_0 t}\,, \tag{7.9}$$

where $\boldsymbol{E}(\boldsymbol{r})$ is again a complex time-harmonic vector field and ω_0 the angular frequency of the time-harmonic carrier. Here, a continuous modulation means that the modulation signal is continuously varying, depending on position and time, with a certain periodicity and without abrupt changes in magnitude or phase. The measurement of such a field signal in frequency domain can be described by the STFT as described in Section 7.1.1. The STFT of a field signal denotes to

$$\boldsymbol{E}(\boldsymbol{r}, \tau, \omega) = \int_{-\infty}^{\infty} \underline{\boldsymbol{E}}(\boldsymbol{r}, t) w(t - \tau)\, \mathrm{e}^{-\mathrm{j}\omega t}\, \mathrm{d}t\,, \tag{7.10}$$

where $w(t)$ is a window function, $\underline{\boldsymbol{E}}(\boldsymbol{r}, t)$ the complex time-domain field signal, and $\boldsymbol{E}(\boldsymbol{r}, \tau, \omega)$ its corresponding spectrum in the frequency domain, in dependence on the time offset τ. The window function is only non-zero during the measurement and its length is, therefore, directly linked to the measurement time T_{meas}. The measurement time is defined by the desired frequency resolution Δf where the relation between T_{meas} and Δf is again a consequence of Küpfmüller's uncertainty principle in (7.4).

In the following, for simplicity, it is assumed that the modulation signal is independent of position and does only depend on time. Therefore, (7.9) changes to

$$\underline{\boldsymbol{E}}_{\mathrm{mod}}(\boldsymbol{r}, t) = m(t)\boldsymbol{E}(\boldsymbol{r})\, \mathrm{e}^{\mathrm{j}\omega_0 t}\,. \tag{7.11}$$

One approach for the NFFFT of such a modulated field is the transformation of the single frequency components. For this purpose, T_{meas} is chosen to be long enough such that all relevant frequency components can be properly resolved and distinguished. Here, the lowest frequency component of the field signal determines the measurement time that can become quite long if low frequencies, e.g., in the order of a few ten Hertz, are present in the signal. This approach is, therefore, called long-time measurement (LTM) in the following. Within the LTM, the measurement and Fourier transform is performed for every measurement position, resulting in a full frequency spectrum per position. Extracting one frequency component from each of the measurement spectra at the different measurement positions forms a set

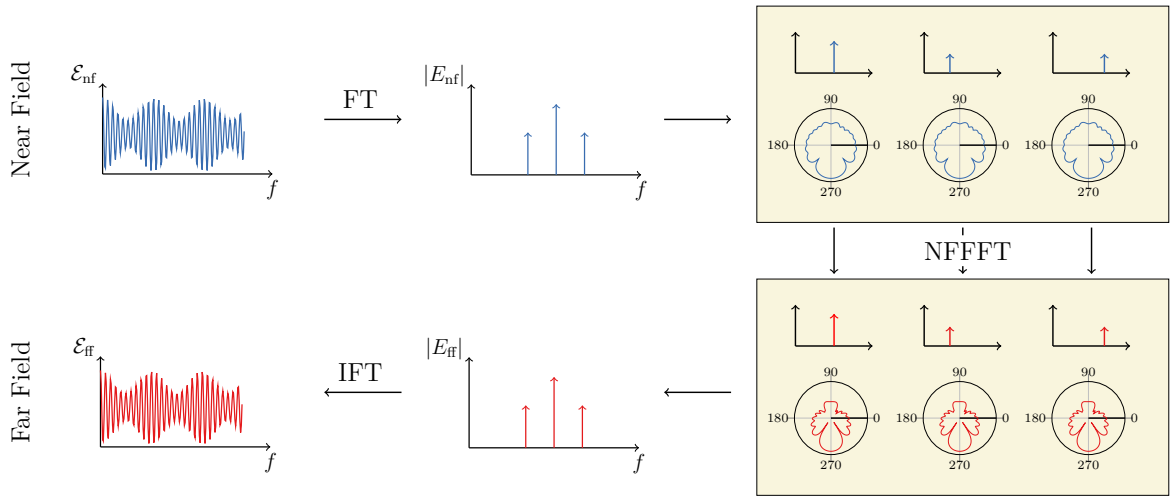

Figure 7.5: The different steps of the LTM approach. A Fourier transform (FT) of the NF time signal reveals the spectral content where the single frequencies are transformed independently to the FF. There, the spectrum is composed again using the resulting field from the NFFFTs. The FF time signal can eventually be calculated by an inverse Fourier transform (IFT).

of NF data that can be transformed to the FF using the time-harmonic NFFFT. This transformation is repeated for all individual frequency components of the spectrum, i.e., one frequency of all spectra at the different positions is transformed simultaneously to the FF. Then in the FF, the frequency spectrum can be composed with the different spectral components that have been transformed by the NFFFT. Eventually, a subsequent inverse Fourier transform delivers the time signal in the FF, respectively the time-varying FF radiation pattern. In total, the measurement approach comprises six steps which are illustrated in Fig. 7.5. As stated, the main drawback of the LTM is the measurement time which can become comparably long if low frequency components are present in the field signal and therefore a fine frequency resolution is necessary. Still, the LTM approach works perfectly if the field is measured at static positions, i.e., the field probe does not move during single field measurements. In contrast, the approach blurs the measurement position if the field probe is constantly moving. Depending on the movement speed, the measurement time and the measurement frequency, the LTM approach can have a significant impact on the accuracy of the field measurement.

If the measurement time T_{meas} is chosen to be shorter than required by (7.4), the single frequency components cannot be separated anymore. Still, if the measurement time is further reduced to such an extent that the modulation signal appears to be constant during the single measurements, effectively only the carrier of the signal is measured as depicted in Fig. 7.6. With such a short measurement time, (7.11) changes to

$$\underline{\boldsymbol{E}}_{\mathrm{mod}}(\boldsymbol{r}, t_i) = m_i \boldsymbol{E}(\boldsymbol{r})\, \mathrm{e}^{\mathrm{j}\omega_0 t}\,, \tag{7.12}$$

where $m_i = m(t_i)$ is the instantaneous modulation state at time t_i. This means that the envelope of the modulated field signal is sampled by every measurement where the measured field value is the time-harmonic carrier of the signal, weighted with the constant factor m_i. If the whole time-varying NF is sampled in this way, all measured samples with the same modulation state m_i are combined to a set of NF data. Each of these data sets can be transformed to the FF using the time-harmonic NFFFT. The resulting FF will also be weighted with the same constant modulation state m_i due to the linearity of the field transformation. The consecutive measurement and transformation of the NF data sets results in the direct reconstruction of the modulation signal in the FF. Due to the short measurement time that is required for the actual field acquisition, at least in comparison to the LTM approach, this measurement

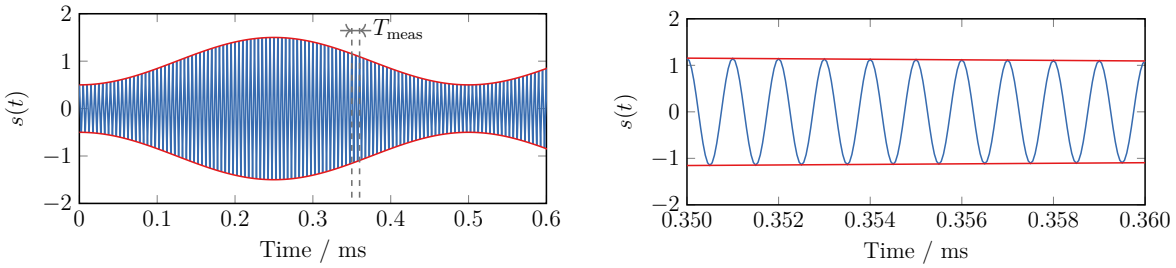

Figure 7.6: Schematic principle of the STM approach where the measurement time T_{meas} is such short (a) that the modulation can be treated as constant and effectively only the carrier is measured (b). [Faul et al. 2019]

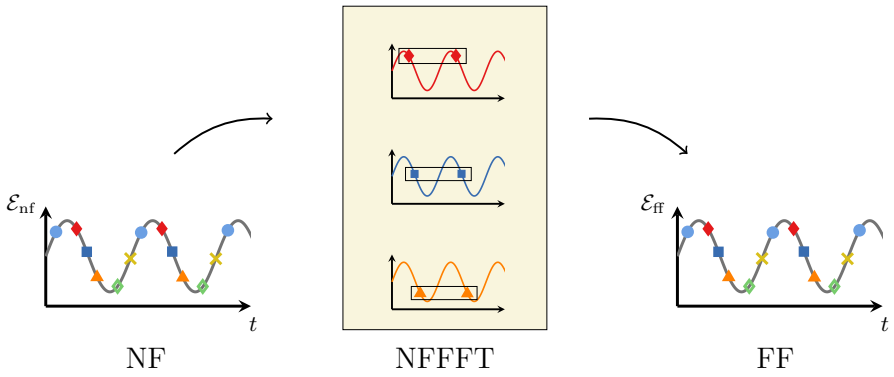

Figure 7.7: Schematic of the principle of the STM approach. Samples with equal modulation states are transformed together by a time-harmonic NFFFT. In the FF, the order of the samples is adjusted according to their order in the NF signal. [Faul et al. 2019]

approach is called short-time measurement (STM) in the following. The principle of the STM method is illustrated in Fig. 7.7. The main advantage of the STM over the LTM approach is the substantially shorter measurement time at the different measurement positions, which is especially beneficial when it comes to UAV-based antenna measurements with a constantly moving field probe. However, it is assumed in the STM that the position change of an employed UAV is negligible and that the modulation signal does not change significantly during the measurement interval. These assumptions are discussed in Section 7.6. Regarding the more general version of the modulation signal $m(\boldsymbol{r}, t)$ which depends on position and time, the transformable data sets within the STM are given in an analogous way by similar modulation states $m_{ij} = m(\boldsymbol{r}_i, t_j)$ which also implies similar positions $\boldsymbol{r}_i$ in this case. In addition, there are several prerequisites for the application of both measurement methods:

Periodicity Both approaches, LTM and STM, work only if the underlying modulated field signal is periodic. This is due to the fact that, e.g., within the STM, samples of the same modulation state are combined to data sets that can be transformed to the FF. If the field signal would not be periodic, finding samples of the same modulation state may be possible, but they do not have a meaning when put together. Furthermore, it is important for the STM that the period of the modulation signal is much longer than the period of the carrier, i.e., the carrier frequency has to be much larger than the modulation frequency. This is a consequence of the assumption that the modulation signal remains constant during the single

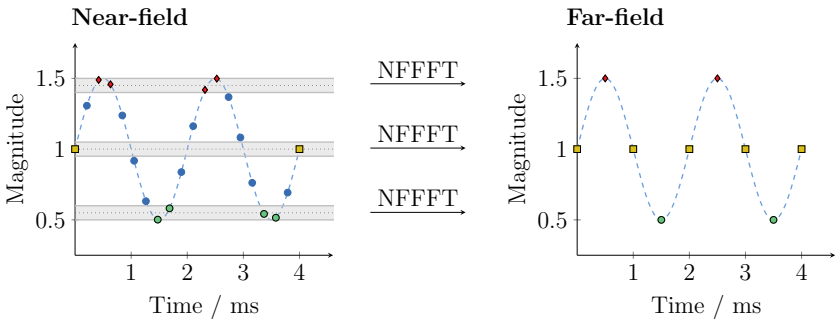

Figure 7.8: Principle of the STM approach showing the interval in which the values are treated as equal. The FF signal is composed regarding the relative time-position of the samples within the modulation period. [Faul et al. 2023]

measurements while the time-varying carrier is measured.

Sampling The STM approach is effectively a sampling of the envelope of the modulated field signal. Therefore, the sampling theorem with respect to the modulation signal must be fulfilled for its reconstruction. The sampling theorem is given by

$$\Delta T < \frac{1}{2 f_m}, \tag{7.13}$$

where ΔT is the time between two consecutive measurements and f_m is the modulation frequency or, if the modulation signal consists of multiple frequencies, the largest frequency present in the modulation signal.

Synchronization To combine the measured field samples that share the same modulation state, some sort of synchronization between the modulation signal and the measurement is necessary. One possibility is to measure the field with the periodicity of the modulation signal, i.e., the modulation signal is always sampled at the exact same temporal position in the signal period. Starting measurements for different modulation states will result in the sampling of the full modulation signal. However, the frequency stability over long time is critical within this approach as any drift in the measurement frequency or, also, in the modulation frequency results in the measurement of slightly different modulation states. As a consequence, the different and, in this sense, wrong modulation states will be combined in a data set which is processed by the NFFFT leading inevitably to erroneous results. Another problem which needs to be considered using this approach, is that the modulation signal can often not be accessed in practical situations. In this case, a complicated but robust extraction of the modulation signal has to be performed from a reference antenna to be used as trigger signal, while no frequency drift between the local oscillators (LOs) of the involved RF equipment must occur.

Another approach for the realization of the synchronization between the modulation signal and the measurement is the self-comparison of the modulation signal. For example, an AM signal which is sampled with a high data rate allows to treat all modulation states within a certain interval $m_i \pm \epsilon$ as equal. Here, ϵ is the witdh of the interval and has to be chosen carefully and with respect to the absolute amplitude of the modulation signal. This principle is visualized in Fig. 7.8, where the figure shows the NF signal of a single position. The measured field samples are combined according to their instantaneous amplitudes, i.e., their modulation states, and are transferred together to the FF where the samples are arranged to form the modulated FF signal, using the knowledge of the relative time-position within a modulation period. Regarding the figure, it becomes clear that the more samples are measured within one modula-

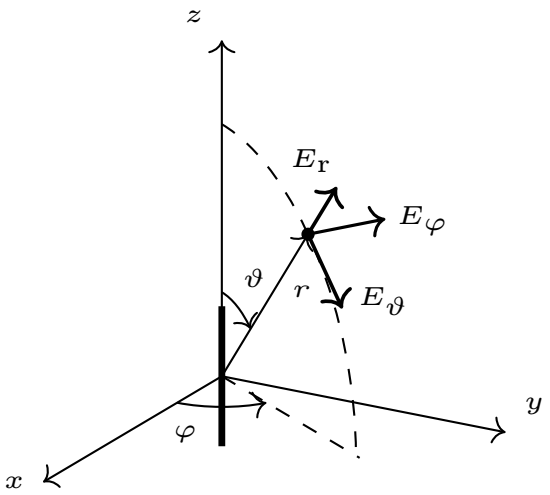

Figure 7.9: Orientation of a single Hertzian dipole within a Cartesian coordinate system. The single components of the electric field are depicted in spherical coordinates which are commonly used for the description of the FF.

tion period, the smaller the interval 2ϵ can be chosen which reduces time uncertainty within the period and, therefore, noise within the transformed FF signal.

Wavelength The wavelength of the modulation signal must be much larger than the NF measurement distance and also larger than the distance between any two measurement positions. This is important since it is assumed that the modulation signal has the same influence at all measurement positions. A large wavelength with respect to the measurement distance ensures that the phase change of the modulation signal, which is caused by spatial variation, is negligible between the single measurements.

7.3 Analytical Description of the Measured Field

Following the principal description of the LTM and STM approaches in Section 7.2, an analytical formulation is given in this section. For this purpose, the example of a complex modulated current signal used to excite an infinitesimal linear wire dipole, a Hertzian dipole, is considered. Even if this is not a practical antenna which is materialized and used in real applications, the case of a Hertzian dipole has been chosen for simplicity and because of the fact that all antennas can be represented as a superposition of Hertzian dipoles with different excitations.

7.3.1 Electric Field of a Hertzian Dipole

An Hertzian dipole shall be placed symmetrically in the origin of a Cartesian coordinate system. It is oriented in *z*-direction as depicted in Figure 7.9, where also the corresponding electric field vectors are shown. As the length *l* of the dipole is infinitely small and its diameter shall also be negligible, the electrical current along the dipole is constant. According to Smith [1997], the transient electric field of

the considered dipole is given in time-domain by

$$\mathcal{E}_\vartheta(\boldsymbol{r},t) = \frac{l\sin\vartheta}{4\pi\varepsilon}\left[\frac{1}{r^3}\int_{-\infty}^{t-\frac{r}{c}} I(\tau)\,\mathrm{d}\tau + \frac{1}{cr^2}I\left(t-\frac{r}{c}\right) + \frac{1}{c^2 r}\frac{\partial}{\partial t}I\left(t-\frac{r}{c}\right)\right] \tag{7.14}$$

and

$$\mathcal{E}_\mathrm{r}(\boldsymbol{r},t) = \frac{l\cos\vartheta}{2\pi\varepsilon}\left[\frac{1}{r^3}\int_{-\infty}^{t-\frac{r}{c}} I(\tau)\,\mathrm{d}\tau + \frac{1}{cr^2}I\left(t-\frac{r}{c}\right)\right], \tag{7.15}$$

where $I(t)$ is the exciting time-varying electric current, r the radial distance of the observation point, $c = 1/\sqrt{\varepsilon\mu}$ the speed of light, ε and μ the electric permittivity and magnetic permeability and t the time vector. In addition, it shall be noted that the tangential component of the electric field in φ-direction is zero due to the orientation of the dipole in $\hat{z}$. It is therefore

$$\mathcal{E}_\varphi(\boldsymbol{r},t) = 0\,. \tag{7.16}$$

As mentioned earlier, electromagnetic fields are often of sinusoidal form which is commonly referred to as time-harmonic. The time-harmonic nature of fields allows for a simplification of the fields in terms of their mathematical description using complex notation. A time-harmonic current $I(\boldsymbol{r},t)$, that additionally depends on the position $\boldsymbol{r}$, is, for example, described by

$$\underline{I}(\boldsymbol{r},t) = I_0(\boldsymbol{r})\,\mathrm{e}^{\mathrm{j}\omega t}\,, \tag{7.17}$$

where $I_0(\boldsymbol{r})$ is a complex current that depends on the position but is independent of time. However, the dependence on position is not explicitly mentioned in the following and $I_0(\boldsymbol{r})$ will only be written as I_0 for reasons of clarity. I_0 is also known as the phasor of the time-harmonic field where ω is the angular frequency of the field. Considering (7.17) as excitation of a single Hertzian dipole leads to the description of its field for the time-harmonic case. Inserting (7.17) into (7.14) yields

$$\begin{aligned}\underline{\boldsymbol{E}}_\vartheta(\boldsymbol{r},t) &= \frac{l\sin\vartheta}{4\pi\varepsilon}\left[\frac{1}{r^3}\frac{1}{\mathrm{j}\omega}I_0\,\mathrm{e}^{\mathrm{j}\omega\left(t-\frac{r}{c}\right)} + \frac{1}{cr^2}I_0\,\mathrm{e}^{\mathrm{j}\omega\left(t-\frac{r}{c}\right)} + \frac{1}{c^2 r}\mathrm{j}\omega I_0\,\mathrm{e}^{\mathrm{j}\omega\left(t-\frac{r}{c}\right)}\right],\\ &= \mathrm{j}\frac{I_0 l\sin\vartheta}{4\pi r\varepsilon}\left[-\frac{1}{\omega r^2} + \frac{1}{\mathrm{j}cr} + \frac{\omega}{c^2}\right]\mathrm{e}^{\mathrm{j}\omega t}\,\mathrm{e}^{-\mathrm{j}\omega\frac{r}{c}}\,.\end{aligned} \tag{7.18}$$

With the introduction of the wave number $k = \omega/c$ and the wave impedance $\eta = \sqrt{\mu/\varepsilon}$, (7.18) changes to

$$\underline{\boldsymbol{E}}_\vartheta(\boldsymbol{r},t) = \mathrm{j}\eta\frac{kI_0 l\sin\vartheta}{4\pi r}\left[1 + \frac{1}{\mathrm{j}kr} - \frac{1}{(kr)^2}\right]\mathrm{e}^{-\mathrm{j}kr}\,\mathrm{e}^{\mathrm{j}\omega t}\,. \tag{7.19}$$

As described in Section 7.2, the exponential time-dependent term is supressed in the time-harmonic form. Therefore, (7.19) reduces to

$$\boldsymbol{E}_\vartheta(\boldsymbol{r},\omega) = \mathrm{j}\eta\frac{kI_0 l\sin\vartheta}{4\pi r}\left[1 + \frac{1}{\mathrm{j}kr} - \frac{1}{(kr)^2}\right]\mathrm{e}^{-\mathrm{j}kr}\,. \tag{7.20}$$

In an analogous manner, the time-harmonic form of the radial r-component of the electric field can be derived from (7.15). It denotes to

$$\boldsymbol{E}_\mathrm{r}(\boldsymbol{r},\omega) = \eta\frac{I_0 l\cos\vartheta}{2\pi r^2}\left[1 + \frac{1}{\mathrm{j}kr}\right]\mathrm{e}^{-\mathrm{j}kr}\,. \tag{7.21}$$

The equations of the field components in (7.20) and (7.21) can also be found in the literature [Balanis

2005], where often only the time-harmonic form is discussed.

7.3.2 Modulated Field of a Hertzian Dipole

In general, the time-harmonic form of the electric field of a Hertzian dipole is often used over its time-domain counterpart as it allows for a much easier calculation of the radiated field from a Hertzian dipole. However, it is only applicable when the excitation signal of the dipole is sinusoidal and mono-frequent. Still, for the case of a modulated excitation signal a similar description can be found regarding the formulas in Section 7.3.1. For the investigation, the excitation signal of (7.17) is extended with a modulation signal. Considering a complex single-sideband modulation, the current signal denotes to

$$\underline{I}(t) = \left[1 + M\,\mathrm{e}^{\mathrm{j}\omega_\mathrm{m} t}\right] I_0\,\mathrm{e}^{\mathrm{j}\omega_0 t}\,, \tag{7.22}$$

where M is the modulation index and ω_m and ω_0 are the angular frequencies of the modulation signal and the carrier, respectively. Inserting (7.22) into (7.14) yields

$$\begin{aligned}\underline{\boldsymbol{E}}_{\vartheta,\mathrm{mod}}(\boldsymbol{r},t) = \frac{l\sin\vartheta}{4\pi\varepsilon}\Bigg[\frac{1}{r^3} I_0\left(\frac{1}{\mathrm{j}\omega_0}\,\mathrm{e}^{\mathrm{j}\omega_0 t'} + \frac{M}{\mathrm{j}(\omega_0+\omega_\mathrm{m})}\,\mathrm{e}^{\mathrm{j}(\omega_0+\omega_\mathrm{m})t'}\right) + \frac{1}{cr^2}\left(1 + M\,\mathrm{e}^{\mathrm{j}\omega_\mathrm{m} t'}\right) I_0\,\mathrm{e}^{\mathrm{j}\omega_0 t'} \\ + \frac{1}{c^2 r}\left(\mathrm{j}\omega_0 + \mathrm{j}(\omega_0+\omega_\mathrm{m}) M\,\mathrm{e}^{\mathrm{j}\omega_\mathrm{m} t'}\right) I_0\,\mathrm{e}^{\mathrm{j}\omega_0 t'}\Bigg]\,,\end{aligned} \tag{7.23}$$

where the substitution $t' = t - {}^{r}/_{c}$ has been introduced. Next, the terms in (7.23) can be re-grouped and simplified which yields

$$\underline{\boldsymbol{E}}_{\vartheta,\mathrm{mod}}(\boldsymbol{r},t) = \frac{\mathrm{j} I_0 l\sin\vartheta}{4\pi r\varepsilon}\left[\frac{-1}{\omega_0 r^2} + \frac{1}{\mathrm{j}cr} + \frac{\omega_0}{c^2} + M\left(\frac{-1}{(\omega_0+\omega_\mathrm{m})r^2} + \frac{1}{\mathrm{j}cr} + \frac{(\omega_0+\omega_\mathrm{m})}{c^2}\right)\mathrm{e}^{\mathrm{j}\omega_\mathrm{m} t'}\right]\mathrm{e}^{\mathrm{j}\omega_0 t'}\,. \tag{7.24}$$

Introducing the wave impedance $\eta = \sqrt{{}^{\mu}/_{\varepsilon}}$, substituting $\omega_\mathrm{x} = \omega_0 + \omega_\mathrm{m}$, and with help of the wave number $k_i = {}^{\omega_i}/_{c}$, (7.24) can be rewritten and further simplified to

$$\underline{\boldsymbol{E}}_{\vartheta,\mathrm{mod}}(\boldsymbol{r},t) = \mathrm{j}\eta\frac{k_0 I_0 l\sin\vartheta}{4\pi r}\left(1 + \frac{1}{\mathrm{j}k_0 r} - \frac{1}{(k_0 r)^2}\right)\mathrm{e}^{-\mathrm{j}k_0 r}\,\mathrm{e}^{\mathrm{j}\omega_0 t} \tag{7.25}$$

$$+\,\mathrm{j}\eta\frac{k_\mathrm{x} I_0 l\sin\vartheta}{4\pi r} M\left(1 + \frac{1}{\mathrm{j}k_\mathrm{x} r} - \frac{1}{(k_\mathrm{x} r)^2}\right)\mathrm{e}^{-\mathrm{j}k_\mathrm{x} r}\,\mathrm{e}^{\mathrm{j}\omega_\mathrm{x} t}\,. \tag{7.26}$$

Eventually, comparing (7.26) with (7.19) reveals that the modulated field is a superposition of the time-harmonic fields of the single spectral frequencies of the modulation signal. This was also expected as the sum signal needs to consist of the single frequency components of the modulation signal. Therefore, the field, described in (7.26), can be written as

$$\underline{\boldsymbol{E}}_{\vartheta,\mathrm{mod}}(\boldsymbol{r},t) = \boldsymbol{E}_\vartheta(\boldsymbol{r},\omega_0)\,\mathrm{e}^{\mathrm{j}\omega_0 t} + M\,\boldsymbol{E}_\vartheta(\boldsymbol{r},\omega_0+\omega_\mathrm{m})\,\mathrm{e}^{\mathrm{j}(\omega_0+\omega_\mathrm{m})t}\,. \tag{7.27}$$

In a similar manner, the expression for the radial r-component of the electric field can be found. It denotes to

$$\underline{\boldsymbol{E}}_{\mathrm{r,mod}}(\boldsymbol{r},t) = \boldsymbol{E}_\mathrm{r}(\boldsymbol{r},\omega_0)\,\mathrm{e}^{\mathrm{j}\omega_0 t} + M\,\boldsymbol{E}_\mathrm{r}(\boldsymbol{r},\omega_0+\omega_\mathrm{m})\,\mathrm{e}^{\mathrm{j}(\omega_0+\omega_\mathrm{m})t}\,. \tag{7.28}$$

Especially the fact that the field of a Hertzian dipole for a continuously modulated excitation signal can be written as a superposition of time-harmonic fields, simplifies the calculation of such fields since no derivation of the excitation signal needs to be calculated in the complex form. This approach is also used in simulations in the following.

7.3.3 Short- and Long-Time Measurement Approaches

The expressions (7.27) and (7.28) describe the field of a Hertzian dipole as it would be measured in time domain following the LTM approach and with the assumption that the measurement time is indefinitely long. The corresponding measurement in the frequency-domain is given by the Fourier transform of (7.27) and (7.28) where the single frequency components are resolved and the field for the individual frequencies is given by (7.20) and (7.21). Strictly speaking, a finite measurement time can only be described by the introduction of a window function $w(t)$. The resulting field in time-domain can be written as

$$\underline{\breve{\boldsymbol{E}}}_{\vartheta}(\boldsymbol{r},t) = \underline{\boldsymbol{E}}_{\vartheta,\mathrm{mod}}(\boldsymbol{r},t) w\left(t-t_0\right)\,, \tag{7.29}$$

where the actual measurement parameters are defined by the parameters of the window function. The measurement time, or opening time in case of a rectangular function is T_{meas} and t_0 a time offset. With the assumption of a rectangular window function $w(t) = \mathrm{rect}(t)$, the Fourier transform of (7.29) denotes to

$$\begin{aligned}
\breve{\boldsymbol{E}}_{\vartheta}(\boldsymbol{r},\omega) &= \int_{-\infty}^{\infty} \underline{\breve{\boldsymbol{E}}}_{\vartheta}(\boldsymbol{r},t)\,\mathrm{e}^{-\mathrm{j}\omega t}\,\mathrm{d}t \\
&= \int_{-\infty}^{\infty} \underline{\boldsymbol{E}}_{\vartheta,\mathrm{mod}}(\boldsymbol{r},t)\,\mathrm{rect}\left(t-t_0\right)\,\mathrm{e}^{-\mathrm{j}\omega t}\,\mathrm{d}t \\
&= \int_{-\infty}^{\infty} \left[\boldsymbol{E}_{\vartheta}(\boldsymbol{r},\omega_0)\,\mathrm{e}^{\mathrm{j}\omega_0 t} + \boldsymbol{M}\,\boldsymbol{E}_{\vartheta}(\boldsymbol{r},\omega_0+\omega_{\mathrm{m}})\,\mathrm{e}^{\mathrm{j}(\omega_0+\omega_{\mathrm{m}})t}\right]\,\mathrm{rect}\left(t-t_0\right)\,\mathrm{e}^{-\mathrm{j}\omega t}\,\mathrm{d}t\,.
\end{aligned} \tag{7.30}$$

Considering and combining some basic Fourier transformation pairs [Bronstein et al. 2012], the Fourier transformation

$$\mathcal{F}\left\{\,\mathrm{rect}\left(t-t_0\right)\,\mathrm{e}^{\mathrm{j}\omega_0 t}\right\} = \mathrm{sinc}\left(\frac{T_{\mathrm{meas}}}{2}(\omega_0-\omega)\right)\,\mathrm{e}^{\mathrm{j}(\omega_0-\omega)t_0}\,, \tag{7.31}$$

can be found, where the rectangular function is defined as

$$\mathrm{rect}(x) = \begin{cases} \frac{1}{T_{\mathrm{meas}}} & \text{for } -\frac{T_{\mathrm{meas}}}{2} \le x \le \frac{T_{\mathrm{meas}}}{2} \\ 0 & \text{elsewhere} \end{cases} \tag{7.32}$$

and the sinc-function as

$$\mathrm{sinc}(x) = \frac{\sin(x)}{x}\,. \tag{7.33}$$

Considering (7.31), (7.30) can be written as

$$\begin{aligned}
\breve{\boldsymbol{E}}_{\vartheta}(\boldsymbol{r},\omega) &= \boldsymbol{E}_{\vartheta}(\boldsymbol{r},\omega_0)\,\mathrm{sinc}\left(\frac{T_{\mathrm{meas}}}{2}(\omega_0-\omega)\right)\,\mathrm{e}^{\mathrm{j}(\omega_0-\omega)t_0} \\
&\quad + \boldsymbol{M}\,\boldsymbol{E}_{\vartheta}(\boldsymbol{r},\omega_0+\omega_{\mathrm{m}})\,\mathrm{sinc}\left(\frac{T_{\mathrm{meas}}}{2}(\omega_0+\omega_{\mathrm{m}}-\omega)\right)\,\mathrm{e}^{\mathrm{j}(\omega_0+\omega_{\mathrm{m}}-\omega)t_0}\,,
\end{aligned} \tag{7.34}$$

which is a description of the spectral measurement with finite measurement time T_{meas} that represents the LTM and STM approaches, where the only difference is the measurement time.

Within the STM, the frequency of the measurement receiver is tuned to the carrier frequency ω_0. Therefore, (7.34) reduces to

$$\breve{\boldsymbol{E}}_{\vartheta}(\boldsymbol{r},\omega_0) = \boldsymbol{E}_{\vartheta}(\boldsymbol{r},\omega_0) + \boldsymbol{M}\,\boldsymbol{E}_{\vartheta}(\boldsymbol{r},\omega_0+\omega_{\mathrm{m}})\,\mathrm{sinc}\left(\frac{T_{\mathrm{meas}}\omega_{\mathrm{m}}}{2}\right)\,\mathrm{e}^{\mathrm{j}\omega_{\mathrm{m}}t_0}\,, \tag{7.35}$$

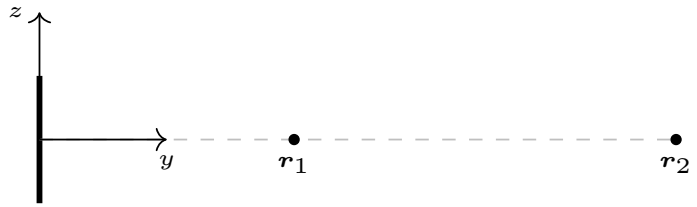

Figure 7.10: Arrangement of the Hertzian dipole and the observation positions $\boldsymbol{r_1}$ and $\boldsymbol{r_2}$ considered for the calculation of the field deviation.

where the argument of the sinc-function $(T_{\text{meas}}\omega_{\text{m}})/2$ is a measure for the error that is made regarding the measurement time T_{meas}, respectively the length of the measurement window. Within the STM, T_{meas} is a fraction of the period of the modulation signal T_{m}. Therefore, the sinc-argument can be written as

$$\frac{T_{\text{meas}}\omega_{\text{m}}}{2} = \frac{nT_{\text{m}}2\pi f_{\text{m}}}{2} = \frac{nT_{\text{m}}2\pi}{2T_{\text{m}}} = n\pi\,, \tag{7.36}$$

with $T_{\text{meas}} = nT_{\text{m}}$. For short measurement times T_{meas}, (7.35) reduces to

$$\breve{\boldsymbol{E}}_{\vartheta}(\boldsymbol{r},\omega_0) \approx \boldsymbol{E}_{\vartheta}(\boldsymbol{r},\omega_0) + M\,\boldsymbol{E}_{\vartheta}(\boldsymbol{r},\omega_0+\omega_{\text{m}})\,\mathrm{e}^{\mathrm{j}\omega_{\text{m}}t_0}\,, \tag{7.37}$$

since the sinc-function approaches unity as $\text{sinc}(0) = 1$. For long measurement times, the value of the sinc-function decreases with increasing measurement time until it approaches zero for very long measurement times which represents the case of the LTM approach.

7.3.4 Distance Error

The wave number

$$k = \frac{\omega}{c_0} = \frac{2\pi}{\lambda} \tag{7.38}$$

is an important parameter for the description of the propagation and spatial phase distribution of a time-harmonic electromagnetic wave, where ω is the angular frequency of the wave, λ its wavelength and c_0 the speed of light in free space, assuming the wave propagates in free space. Hence, it becomes clear that a modulation changes the field distribution in comparison to the case where only the time-harmonic wave at the carrier frequency is present. Given this relationship between the frequency and phase distribution, it can be assumed that a modulated field introduces errors into the measurement as the phase of the modulation signal might differ between two measurement positions. To investigate this, the field error between two positions $\boldsymbol{r_1}$ and $\boldsymbol{r_2}$ is calculated, where both positions are located on the same radial from the radiation source. For simplicity, a single Hertzian dipole is used as radiation source while it is assumed that all field values are measured at the same time t_0. The arrangement is depicted in Fig. 7.10.

In general, the deviation ϵ_{dist} between the field values at $\boldsymbol{r_1}$ and $\boldsymbol{r_2}$ is given by

$$\epsilon_{\text{dist}} = \frac{\underline{\boldsymbol{E}}_{\text{mod},\vartheta}(\boldsymbol{r_2},t_0)}{\underline{\boldsymbol{E}}_{\text{car},\vartheta}(\boldsymbol{r_2},t_0)} - \frac{\underline{\boldsymbol{E}}_{\text{mod},\vartheta}(\boldsymbol{r_1},t_0)}{\underline{\boldsymbol{E}}_{\text{car},\vartheta}(\boldsymbol{r_1},t_0)}\,, \tag{7.39}$$

where $\boldsymbol{E}_{\text{mod}}$ is the modulated field as described in (7.27) and $\boldsymbol{E}_{\text{car}}$ only the field at the carrier frequency

at ω_0. Rewriting (7.39) leads to

$$\begin{aligned}\epsilon_{\text{dist}} &= \frac{\boldsymbol{E}_\vartheta(\boldsymbol{r}_2,\omega_0)\,\mathrm{e}^{\mathrm{j}\omega_0 t_0} + \boldsymbol{M}\,\boldsymbol{E}_\vartheta(\boldsymbol{r}_2,\omega_0+\omega_\mathrm{m})\,\mathrm{e}^{\mathrm{j}(\omega_0+\omega_\mathrm{m})t_0}}{\boldsymbol{E}_\vartheta(\boldsymbol{r}_2,\omega_0)\,\mathrm{e}^{\mathrm{j}\omega_0 t_0}} - \frac{\boldsymbol{E}_\vartheta(\boldsymbol{r}_1,\omega_0)\,\mathrm{e}^{\mathrm{j}\omega_0 t_0} + \boldsymbol{M}\,\boldsymbol{E}_\vartheta(\boldsymbol{r}_1,\omega_0+\omega_\mathrm{m})\,\mathrm{e}^{\mathrm{j}(\omega_0+\omega_\mathrm{m})t_0}}{\boldsymbol{E}_\vartheta(\boldsymbol{r}_1,\omega_0)\,\mathrm{e}^{\mathrm{j}\omega_0 t_0}} \\ &= 1 + M\frac{\boldsymbol{E}_\vartheta(\boldsymbol{r}_2,\omega_0+\omega_\mathrm{m})}{\boldsymbol{E}_\vartheta(\boldsymbol{r}_2,\omega_0)}\,\mathrm{e}^{\mathrm{j}\omega_\mathrm{m}t_0} - 1 - M\frac{\boldsymbol{E}_\vartheta(\boldsymbol{r}_1,\omega_0+\omega_\mathrm{m})}{\boldsymbol{E}_\vartheta(\boldsymbol{r}_1,\omega_0)}\,\mathrm{e}^{\mathrm{j}\omega_\mathrm{m}t_0} \\ &= M\left[\frac{\boldsymbol{E}_\vartheta(\boldsymbol{r}_2,\omega_0+\omega_\mathrm{m})}{\boldsymbol{E}_\vartheta(\boldsymbol{r}_2,\omega_0)} - \frac{\boldsymbol{E}_\vartheta(\boldsymbol{r}_1,\omega_0+\omega_\mathrm{m})}{\boldsymbol{E}_\vartheta(\boldsymbol{r}_1,\omega_0)}\right]\mathrm{e}^{\mathrm{j}\omega_\mathrm{m}t_0}\,. \end{aligned} \tag{7.40}$$

Since the field difference between two field positions is calculated, all fields are normalized to the field values at $\boldsymbol{r_1}$ as it would be in the case where a reference antenna is placed at $\boldsymbol{r_1}$. This changes (7.40) to

$$\epsilon_{\text{dist}} = M\left[\frac{\boldsymbol{E}_\vartheta(\boldsymbol{r}_2,\omega_0+\omega_\mathrm{m})}{\boldsymbol{E}_\vartheta(\boldsymbol{r}_2,\omega_0)}\frac{\boldsymbol{E}_\vartheta(\boldsymbol{r}_1,\omega_0)}{\boldsymbol{E}_\vartheta(\boldsymbol{r}_1,\omega_0+\omega_\mathrm{m})} - \frac{\boldsymbol{E}_\vartheta(\boldsymbol{r}_1,\omega_0+\omega_\mathrm{m})}{\boldsymbol{E}_\vartheta(\boldsymbol{r}_1,\omega_0)}\frac{\boldsymbol{E}_\vartheta(\boldsymbol{r}_1,\omega_0)}{\boldsymbol{E}_\vartheta(\boldsymbol{r}_1,\omega_0+\omega_\mathrm{m})}\right]\mathrm{e}^{\mathrm{j}\omega_\mathrm{m}t_0} \tag{7.41}$$

$$= M\left[\frac{\boldsymbol{E}_\vartheta(\boldsymbol{r}_2,\omega_0+\omega_\mathrm{m})}{\boldsymbol{E}_\vartheta(\boldsymbol{r}_1,\omega_0+\omega_\mathrm{m})}\frac{\boldsymbol{E}_\vartheta(\boldsymbol{r}_1,\omega_0)}{\boldsymbol{E}_\vartheta(\boldsymbol{r}_2,\omega_0)} - 1\right]\mathrm{e}^{\mathrm{j}\omega_\mathrm{m}t_0}\,. \tag{7.42}$$

Inserting (7.20) and with the substitutions $\omega_\mathrm{x} = \omega_0 + \omega_\mathrm{m}$ and $k_\mathrm{x} = k_0 + k_\mathrm{m}$, (7.42) can be rewritten as

$$\epsilon_{\text{dist}} = M\left[\frac{\mathrm{j}\eta\frac{k_\mathrm{x}I_0 l\sin\vartheta}{4\pi r_2}\left(1+\frac{1}{\mathrm{j}k_\mathrm{x}r_2}-\frac{1}{(k_\mathrm{x}r_2)^2}\right)\mathrm{e}^{-\mathrm{j}k_\mathrm{x}r_2}}{\mathrm{j}\eta\frac{k_\mathrm{x}I_0 l\sin\vartheta}{4\pi r_1}\left(1+\frac{1}{\mathrm{j}k_\mathrm{x}r_1}-\frac{1}{(k_\mathrm{x}r_1)^2}\right)\mathrm{e}^{-\mathrm{j}k_\mathrm{x}r_1}}\frac{\mathrm{j}\eta\frac{k_0I_0 l\sin\vartheta}{4\pi r_1}\left(1+\frac{1}{\mathrm{j}k_0r_1}-\frac{1}{(k_0r_1)^2}\right)\mathrm{e}^{-\mathrm{j}k_0r_1}}{\mathrm{j}\eta\frac{k_0I_0 l\sin\vartheta}{4\pi r_2}\left(1+\frac{1}{\mathrm{j}k_0r_2}-\frac{1}{(k_0r_2)^2}\right)\mathrm{e}^{-\mathrm{j}k_0r_2}} - 1\right]\mathrm{e}^{\mathrm{j}\omega_\mathrm{m}t_0} \tag{7.43}$$

$$= M\left[\frac{1+\frac{1}{\mathrm{j}k_\mathrm{x}r_2}-\frac{1}{(k_\mathrm{x}r_2)^2}}{1+\frac{1}{\mathrm{j}k_\mathrm{x}r_1}-\frac{1}{(k_\mathrm{x}r_1)^2}}\mathrm{e}^{-\mathrm{j}k_\mathrm{x}(r_2-r_1)}\,\frac{1+\frac{1}{\mathrm{j}k_0r_1}-\frac{1}{(k_0r_1)^2}}{1+\frac{1}{\mathrm{j}k_0r_2}-\frac{1}{(k_0r_2)^2}}\mathrm{e}^{-\mathrm{j}k_0(r_1-r_2)} - 1\right]\mathrm{e}^{\mathrm{j}\omega_\mathrm{m}t_0} \tag{7.44}$$

$$= M\left[\frac{(k_\mathrm{x}r_2)^2-\mathrm{j}k_\mathrm{x}r_2-1}{(k_\mathrm{x}r_1)^2-\mathrm{j}k_\mathrm{x}r_1-1}\frac{(k_\mathrm{x}r_1)^2}{(k_\mathrm{x}r_2)^2}\,\frac{(k_0r_1)^2-\mathrm{j}k_0r_1-1}{(k_0r_2)^2-\mathrm{j}k_0r_2-1}\frac{(k_0r_2)^2}{(k_0r_1)^2}\mathrm{e}^{-\mathrm{j}(k_\mathrm{x}-k_0)(r_2-r_1)} - 1\right]\mathrm{e}^{\mathrm{j}\omega_\mathrm{m}t_0} \tag{7.45}$$

$$= M\left[\frac{(k_\mathrm{x}r_2)^2-\mathrm{j}k_\mathrm{x}r_2-1}{(k_\mathrm{x}r_1)^2-\mathrm{j}k_\mathrm{x}r_1-1}\,\frac{(k_0r_1)^2-\mathrm{j}k_0r_1-1}{(k_0r_2)^2-\mathrm{j}k_0r_2-1}\mathrm{e}^{-\mathrm{j}k_\mathrm{m}(r_2-r_1)} - 1\right]\mathrm{e}^{\mathrm{j}\omega_\mathrm{m}t_0}\,. \tag{7.46}$$

The field deviation described by (7.46) is shown in Fig. 7.11 as 2D plot in dependence on the measurement radius and the modulation frequency. The radius is the distance between two measurement positions $r = \left\|\boldsymbol{r}_2 - \boldsymbol{r}_1\right\|$, where the reference position $\boldsymbol{r}_1$ has been chosen to 0.1 m from the radiation source in these simulations. The carrier frequency f_m has been chosen to 3 GHz in the shown calculations, while other frequencies have also been tested. Investigating Fig. 7.11, it can be easily seen that the deviation is small for low modulation frequencies and for small distances. This is expected since the ratio of the measurement radius to the modulation wavelength is small in both cases. In contrast, the deviation increases with increasing ratio while it reaches a maximum when the radius is half the modulation wavelength. It is also found in Fig. 7.11 and further simulations that the deviation diminishes when the radius is a multiple of the modulation wavelength. This is a consequence of the periodicity of the sinusoidal modulation signal. In addition to the 2D plot, Fig. 7.12 shows the field deviation for fixed measurement radii, i.e., on horizontal lines in Fig. 7.11. It can be seen that the deviation increases with increasing radius while the periodicity of the modulation signal plays a crucial role as illustrated for $r = 3\,\mathrm{m}$.

While (7.46) describes the field deviation for infinite measurement times and, therefore, for the LTM

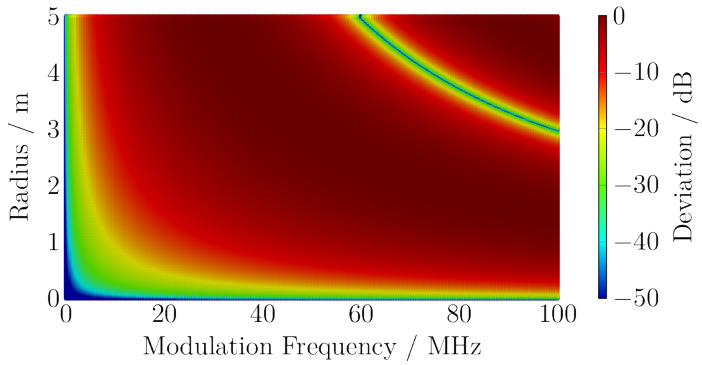

Figure 7.11: Deviation in the field values between two measurement positions as described in (7.46). The deviation is show in dependence on the measurement radius and the modulation frequency.

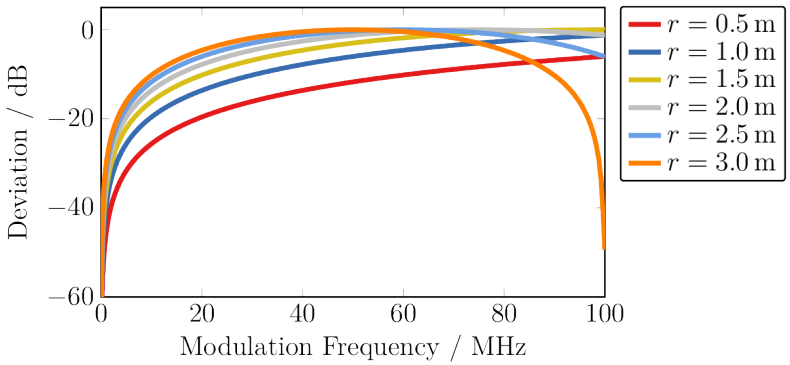

Figure 7.12: Deviation in the field values for fixed observation distances and varying modulation frequency. The single lines are identical to horizontal lines in Fig. 7.11.

approach, a similar formula can be found for the STM approach. Considering (7.35) as description of the modulated field, (7.46) changes to

$$\epsilon_{\mathrm{STM,dist}} = M \left[\frac{(k_\mathrm{x} r_2)^2 - \mathrm{j} k_\mathrm{x} r_2 - 1}{(k_\mathrm{x} r_1)^2 - \mathrm{j} k_\mathrm{x} r_1 - 1} \, \frac{(k_0 r_1)^2 - \mathrm{j} k_0 r_1 - 1}{(k_0 r_2)^2 - \mathrm{j} k_0 r_2 - 1} \, \mathrm{e}^{-\mathrm{j} k_\mathrm{m} (r_2 - r_1)} - 1 \right] \operatorname{sinc}\left(\frac{T_\mathrm{meas} \omega_\mathrm{m}}{2} \right) \mathrm{e}^{\mathrm{j} \omega_\mathrm{m} t_0} \,, \tag{7.47}$$

where T_meas is the measurement time. Fig. 7.13 shows a 2D plot of (7.47) where T_meas has been chosen to 25 ns. Similar as before, it is found that the deviation is small for small observation radii and low modulation frequencies. Furthermore, the deviation diminishes when the radius is equal or close to a multiple of the modulation wavelength. It is found that the deviation diminishes for 40 MHz and 80 MHz which is clearly an artifact of the measurement time since $1/25\,\mathrm{ns} = 40\,\mathrm{MHz}$. In the specific case of Fig. 7.13, the sampling theorem given in (7.13) is violated for modulation frequencies above 20 MHz which results in a periodic pattern. At the same time, the comparison of Fig. 7.13 and Fig. 7.11 reveals that the deviation is the same for modulation frequencies up to 20 MHz.

The visualizations of the analytical field deviation support the assumptions made in Section 7.2. While the sampling theorem has to be fulfilled for the modulation frequency when employing the STM approach, also restrictions on the ratio of the measurement radius to the modulation wavelength apply. Theoretically, the field can be measured at various distances from the radiation source as the field deviation diminishes periodically with the modulation signal's periodicity. However, in this case it is crucial that all field positions are within the same period since the time delay, respectively phase, of the modula-

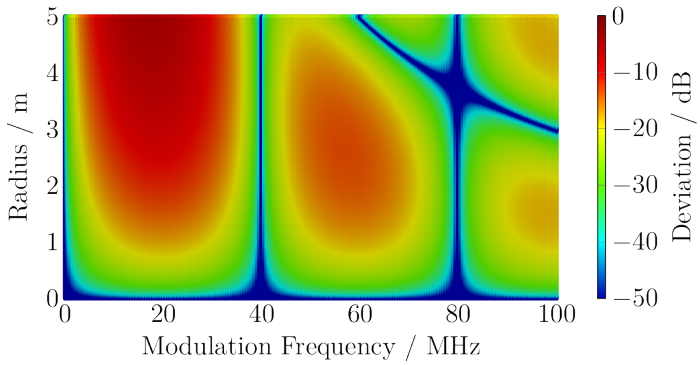

Figure 7.13: Deviation in the field values between two measurement positions and for the STM approach as described in (7.47). The deviation is show in dependence on the measurement radius and the modulation frequency, while the measurement time has been chosen to $T_{\text{meas}} = 25\,\text{ns}$.

tion signal will differ more than 360° otherwise. Hence, it remains a practical rule that the measurement radius shall be much smaller than the wavelength of the modulation signal.

7.4 Verification by Simulation

In addition to the conceptual and analytical description of the LTM and STM approaches, their practical applicability is demonstrated by numerical simulations in the following.

7.4.1 Simulation Model

The simulations were carried out in MathWorks MATLAB [MathWorks 2022] using a horn antenna as AUT that was modeled by 2232 Hertzian dipoles within the simulations. This is, in fact, a representation of the horn by equivalent sources as described for the NFFFT. For the simulations, the Hertzian dipole representation has the advantage over, e.g., full-wave simulations that the field at various positions can be calculated in a fast and simple manner by programming languages like MATLAB, which are versatile and often used in development. The NF data is generated synthetically from the dipoles while their excitation was obtained by discretizing the surface currents resulting from time-harmonic full-wave simulations of the horn antenna which have to be performed once per frequency. These full-wave simulations were performed in CST Microwave Studio [CST 2020] at a frequency of 3 GHz. Figure 7.14 shows the arrangement of the Hertzian dipoles. In the simulations, the horn antenna is transmitting an amplitude modulated field signal as described by (7.11), while $m(t)$ denotes to

$$m(t) = 1 + M \cos\left(\omega_{\text{m}} t + \varphi_{\text{m}}\right) . \tag{7.48}$$

Here, $M = 0.5$ is the modulation index and $\omega_{\text{m}} = 2\pi 500\,\text{Hz}$ the angular modulation frequency. Both values have been chosen by convenience and close to what is realistic in prospective application fields of the measurement approaches. However, this implies no restriction on generality as will be pointed out in the following sections. Other values have also been tested but are not shown in the following for reasons of clarity. Similar to the other values, the modulation phase offset has been chosen to $\varphi_{\text{m}} = 0°$ for the presented simulations while, again, further simulations revealed that the phase offset has no impact on the application or performance of the discussed measurement approaches.

In view of the NF being calculated by the simulation model of Hertzian dipoles, the time-harmonic NF

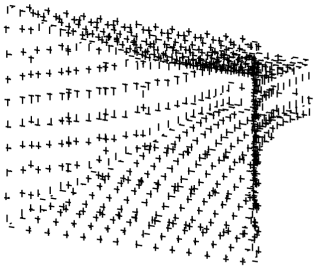

Figure 7.14: Schematic view of the arrangement of the 2232 Hertzian dipoles serving as equivalent sources by representing the horn antenna.

samples are calculated for the carrier frequency as well as for the upper and lower sideband frequencies. Starting from this, the frequency spectrum is composed in the NF such that it corresponds to the time signals that are present at the single measurement positions. However, the actual time signals are calculated by evaluating the inverse Fourier transformation for the desired time samples and measurement position. Furthermore, the measurement of the NF time signals at the different positions is considered by the STFT that is used to calculate the NF samples which would be measured by a VNA. The window length of the STFT T_{meas} is chosen according to the LTM and STM approaches while the further processing of the field is also done with respect to the two measurement methods. Eventually, the measured FF time signal is compared with a reference time signal that is directly calculated from the dipole model. The different simulation steps are shown as block diagram in Fig. 7.15.

The frequency spectrum of an amplitude modulation contains three frequency peaks: the carrier frequency ω_0, the upper sideband frequency $\omega_0 + \omega_{\mathrm{m}}$ and the lower sideband frequency $\omega_0 - \omega_{\mathrm{m}}$. Since the spectrum of a real-valued time signal is symmetric, the same frequency components occur at negative mirror frequencies. The time signal is given by the inverse Fourier transform, see (7.2). As the single frequency components of (7.11) with (7.48) can be written as Dirac-impulses, the evaluation of the inverse Fourier integral leads to

$$\boldsymbol{\mathcal{E}}(\boldsymbol{r},t) = \Re\left\{\left[\boldsymbol{E}(\boldsymbol{r},\omega_0) + \frac{\boldsymbol{M}}{2}\boldsymbol{E}(\omega_0-\omega_{\mathrm{m}},\boldsymbol{r})\,\mathrm{e}^{-\mathrm{j}\omega_{\mathrm{m}}t} + \frac{\boldsymbol{M}}{2}\boldsymbol{E}(\boldsymbol{r},\omega_0+\omega_{\mathrm{m}})\,\mathrm{e}^{\mathrm{j}\omega_{\mathrm{m}}t}\right]\mathrm{e}^{\mathrm{j}\omega_0 t}\right\}. \tag{7.49}$$

Equation (7.49) describes the real-valued time signal as it would be seen by a measurement receiver. However, since the modulation frequency is orders of magnitudes lower than the carrier frequency, it is more efficient to compute and analyze the fields in the baseband. According to (7.6), the baseband time signal $\boldsymbol{\mathcal{E}}_{\mathrm{bb}}(t,\boldsymbol{r})$ of $\boldsymbol{\mathcal{E}}(\boldsymbol{r},t)$ denotes to

$$\boldsymbol{\mathcal{E}}_{\mathrm{bb}}(\boldsymbol{r},t) = \boldsymbol{E}(\boldsymbol{r},\omega_0) + \frac{\boldsymbol{M}}{2}\boldsymbol{E}(\boldsymbol{r},\omega_0-\omega_{\mathrm{m}})\,\mathrm{e}^{-\mathrm{j}\omega_{\mathrm{m}}t} + \frac{\boldsymbol{M}}{2}\boldsymbol{E}(\boldsymbol{r},\omega_0+\omega_{\mathrm{m}})\,\mathrm{e}^{\mathrm{j}\omega_{\mathrm{m}}t}. \tag{7.50}$$

Looking at (7.50), it is especially important to note that the NFs $\boldsymbol{E}(\boldsymbol{r},\omega_i)$ are calculated for the actual modulation frequencies including the carrier frequency, regardless of the following calculation in the baseband. For the simulations, a spherical measurement geometry has been chosen which is surrounding the AUT and has a radius of $r = 1$ m.

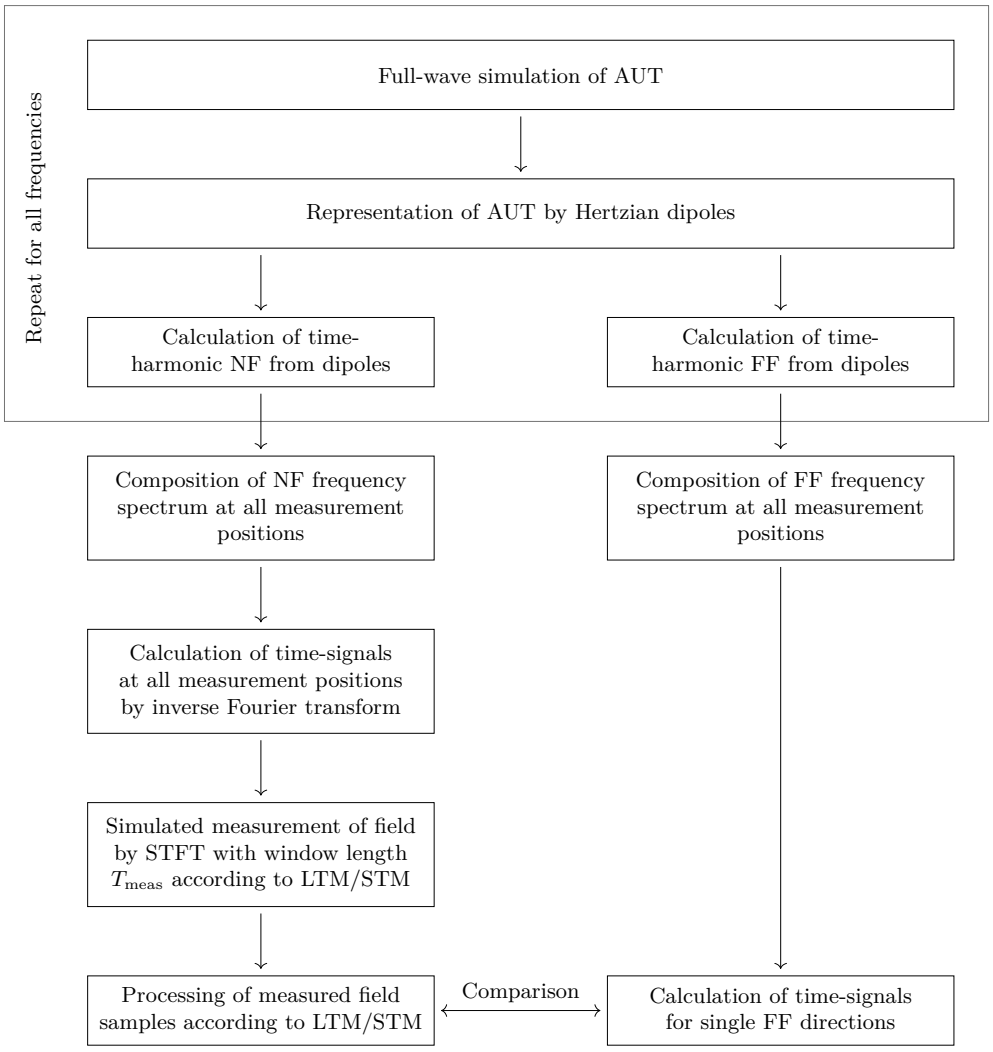

Figure 7.15: Block diagram outlining the single steps of simulations with modulated fields in which a time-harmonic dipole representation of the AUT was employed. The modulated field signals are processed according to the LTM and STM approaches, while a reference signal is directly calculated from the dipole model.

7.4.2 Long-Time Measurement Approach

The LTM was realized as described in Section 7.2, i.e., the individual spectral frequencies were transformed to the FF using a time-harmonic NFFFT. For this, the modulated field signal was calculated at the single measurement positions with a measurement time of $T_{\text{meas}} = 30\,\text{ms}$. Regarding the modulation frequency of 500 Hz, 15 modulation periods were measured at each of the different NF positions. The time axes for the different measurement positions had an incremental offset of 1 s to account for the change of position and since the field signal will be measured sequentially at the different positions in real NF measurements. The example of the normalized NF signal in the main beam of the horn antenna is depicted in Fig. 7.16 (a), while its corresponding frequency spectrum is depicted in Fig. 7.16 (b). As expected, the NF spectrum contains three frequency peaks which match with the carrier and the modulation sideband frequencies. It can also be seen in Fig. 7.16 (b) that, due to the linear scale and regarding the modulation index of 0.5, the magnitude of the sideband frequencies is one fourth of the carrier peak.

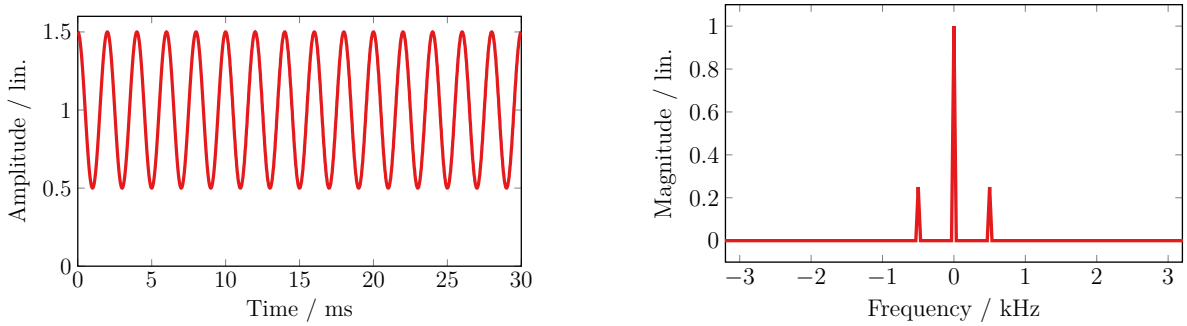

(a) (b)

Figure 7.16: Modulated NF signal at the center of the main beam of the AUT (a). The corresponding frequency spectrum (b) contains three frequency peaks which match the carrier and modulation sideband frequencies.

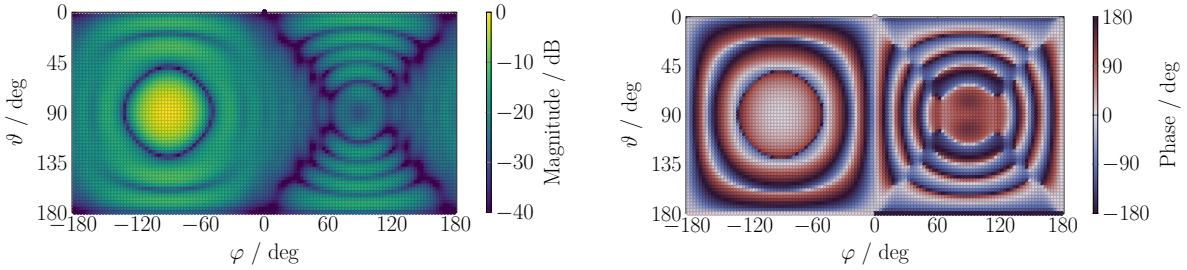

(a) (b)

Figure 7.17: Three-dimensional spherical NF for an instantaneous timestamp in magnitude (a) and phase (b). The main beam of the horn antenna occurs at ($\vartheta = 90°, \varphi = -90°$).

Evaluating the NF for a single instantaneous timestamp results in a snapshot of the NF which can be treated as time-harmonic. In this way it is possible to plot the full three-dimensional NF, which is shown in Figs. 7.17 (a) and (b) in magnitude and phase, relatively.

According to the LTM approach, the single frequencies of the NF spectrum for all measurement positions are together transformed to the FF. There, the spectrum is composed again with respect to the actual measurement frequencies while the remaining frequencies, which have not been involved in the transformation, are filled with zeros such that the number of samples of the FF spectrum is equal to that of the NF spectrum. The resulting frequency spectrum from the NFFFT of Fig. 7.16 (b) is depicted in Fig. 7.18 (a). Here, it can be observed that the magnitude ratio between the carrier and the sideband frequency peaks is again one fourth and is preserved throughout the NFFFT. Finally, the modulated FF signal results from the inverse Fourier transform of the composed frequency spectrum. The resulting modulated FF signal, again in the middle of the main beam, is shown in Fig. 7.18 (b) alongside a reference signal which results from the direct calculation of the field from the horn dipole model. The same reference is also shown in the FF spectrum. In addition to the field signals, the error between the transformed and the reference FF signal, according to (2.32), is given in Fig. 7.18 (b). With an error level of about $-100\,\mathrm{dB}$, it can be justified that the LTM approach does not add any additional error to the measurement and transformation of modulated fields.

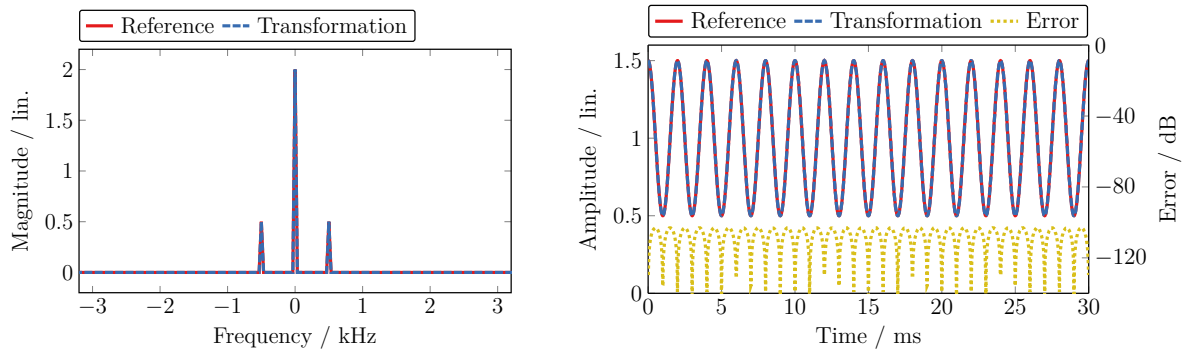

(a) (b)

Figure 7.18: Frequency spectrum resulting from the NFFFT and re-combination of the single spectral lines (a) and corresponding time signals. The reference signal has been directly calculated from the dipole model while the error includes the deviation in magnitude and phase.

7.4.3 Short-Time Measurement Approach

While the LTM method does not introduce an additional error for the simulated case of step measurements, its comparably long measurement time has a detrimental influence on measurements with moving antennas, e.g., as in UAV-based field measurements. The STM approach has been proposed to overcome this problem as discussed in Section 7.2. Its applicability is shown in the following with the help of numerical simulations of a horn antenna as AUT that is represented by Hertzian dipoles where the same simulation model as for the LTM was used. In the examples, an AM has been chosen as it nicely demonstrates how the STM approach works. However, simulations and measurements show that the same concept can also be applied to frequency or phase modulated signals.

Measurement with Modulation Period

Within the STM approach, measured NF samples with equal modulation states are transformed together to the FF, where it becomes clear that the ensurance of a similar modulation state is crucial to the method. One way to accomplish this is the measurement of the field with the modulation period, i.e., the time between two measurements, the measurement period, is equal to the period of the modulation signal. This ensures similar modulation states for all measurements as the measurement is always started for the same temporal position regarding the modulation period. However, the actual captured value of the modulation depends on the initial offset and can be adjusted. An overview of the modulation signals for different measurement locations is schematically depicted in Fig. 7.19. Important is the fact that the field samples across all measurement locations share the same modulation state, i.e., the i-th field sample of all measurement positions shares the same modulation state m_i, equal to a simultaneous measurement of the field at all positions. This is a consequence of the fact that the measurement is synchronized with the modulation period, although the realization of the synchronization can vary. One specific implementation is the measurement of a single field value with each modulation period, i.e., the measurement receiver records only one sample at a time while the time between two adjacent samples is equal to the modulation period. Regarding a moving field probe, this means that each measured field sample must be assigned to a different position and, thus, no two field samples of equal modulation states are at the same position. If one changes the implementation in such a way that each modulation period triggers a sequence of measurements, then several field samples can be recorded per measurement, provided that the sampling rate is chosen sufficiently high. Even with a moving probe, this will cover less spatial

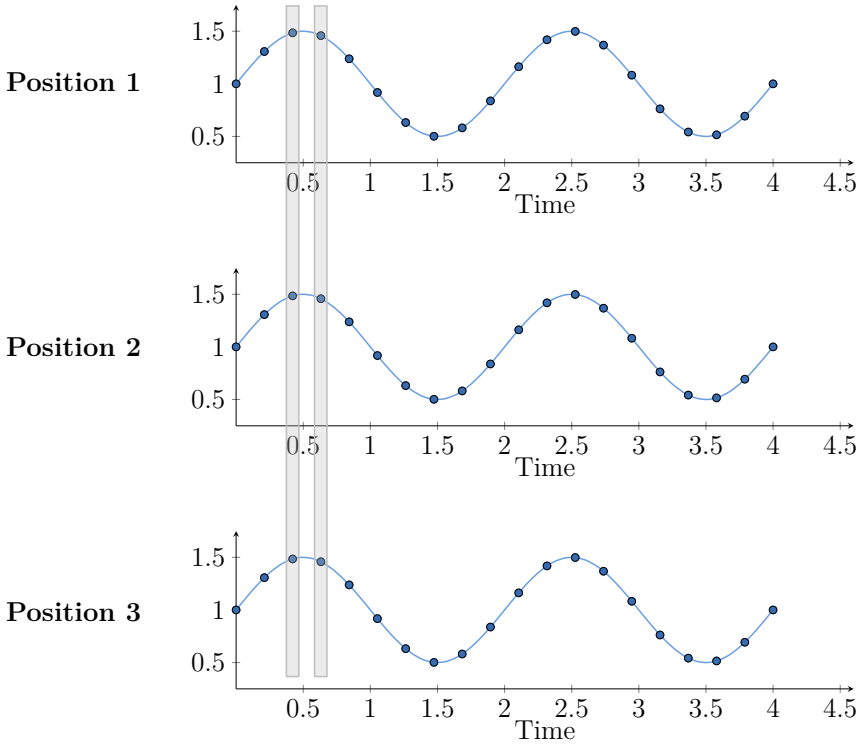

Figure 7.19: Schematic comparison of the modulation signals at different measurement locations for the case where the time difference between two measurements is equal to the modulation period. All samples at the same time position in all signals are transformed together to the FF.

variance, allowing multiple field samples to be measured at nearly the same position. However, the disadvantage of this approach is the stability and repeatability of the high sampling rate of the measurement sequence across all measurement positions, otherwise the individual field samples will not match. For the simulations, this second approach has been chosen. The NF resulting from the theoretical measurement of the time signal and for a transformable dataset with similar modulation state m_i, is depicted in Figs. 7.20 (a) and (b) in magnitude and phase, respectively. Since the plotted field is similar to the time-harmonic carrier field, weighted with the modulation state m_i, it is equal to Fig. 7.17, where the field of the carrier resulting from the LTM approach was plotted. The time-varying NF signal in the main beam of the AUT is shown in Fig. 7.21 (a), while the single measurement samples are marked. The corresponding FF signal is depicted in Fig. 7.21 (b), where it is plotted against the reference FF signal that has been directly calculated from the dipole model. Both curves are almost identical which is also reflected by the error that is less than $-105\,\mathrm{dB}$ for all positions and times. This proves that the STM approach, realized by the synchronization of the measurements to the modulation period, does not introduce an additional error into the measurement for step measurements. However, an important drawback of this approach is that the time between two measurements needs to be fully synchronized to the period of the modulation signal. While this can be easily achieved in simulations, it can become challenging in real measurements. This is because, the synchronization between two independent clocks is delicate and the measurement and modulation periods are likely to drift apart over time. Another possible implementation is the filtering and usage of the modulation signal as trigger for the measurement receiver which, however, requires some effort regarding a dedicated circuit or real-time processing step to make the modulation signal usable as trigger input.

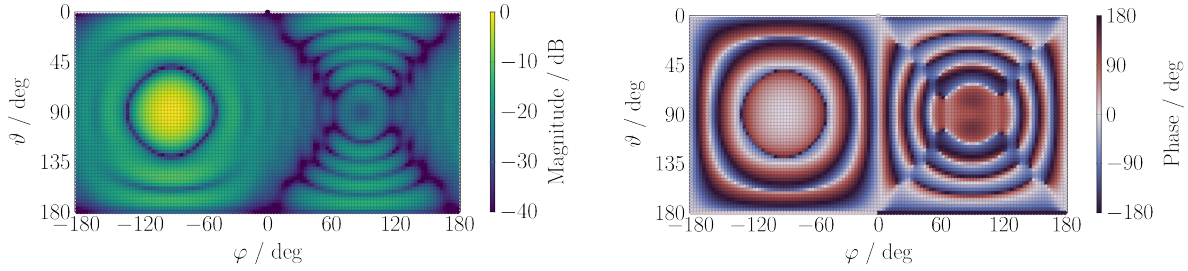

Figure 7.20: Three-dimensional spherical NF of a transformable dataset for a modulation state m_i in magnitude (a) and phase (b). The main beam of the horn antenna occurs at ($\vartheta = 90°, \varphi = -90°$).

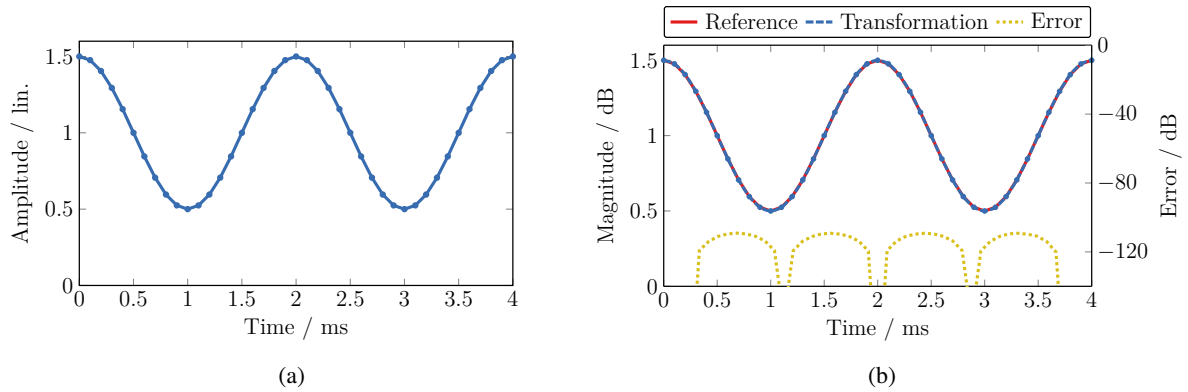

Figure 7.21: Measured time signal in the NF (a) and corresponding FF signal (b). The single measurements for different modulation states are marked while the complex error between the transformed FF signal and a reference signal, that was directly calculated from the dipole model, has been calculated.

Equal Value Interval

The outlined synchronization issue between the measurement time and the modulation signal can be overcome following a different path. Given that the sample rate is substantially higher than the modulation frequency, i.e., the time difference between two subsequent measurements is significantly smaller than the modulation period, then the field samples which are transformed together to the FF can be selected regarding their modulation state. Figure 7.22 shows a schematic of the modulated NF signals at different measurement positions. It can be clearly seen that the phases of the signals are not aligned and, therefore, the i-th measurement sample does not share the same modulation state m_i at all positions. However, the field samples of the same modulation state can be determined by comparison. For this, all field samples within a certain amplitude interval around a modulation state $m_i \pm \epsilon$ are extracted and transformed using the NFFFT. The comparison can be challenging since the absolute field amplitude of the different positions changes regarding the field distribution of the AUT. However, coherent NF measurements require a phase reference signal which also contains the modulation information. Depending on the setup, the reference signal can be used for the evaluation and extraction of the field samples. If this extraction is repeated for different modulation states m_i, the modulation signal can be reconstructed in the FF under consideration of the occurrence of the respective modulation states within the modulation signal. From simulations, the modulated NF signal in the main beam of the horn antenna is depicted in Fig. 7.23 (a). Here, the values of the modulation states together with the intervals, which are trans-

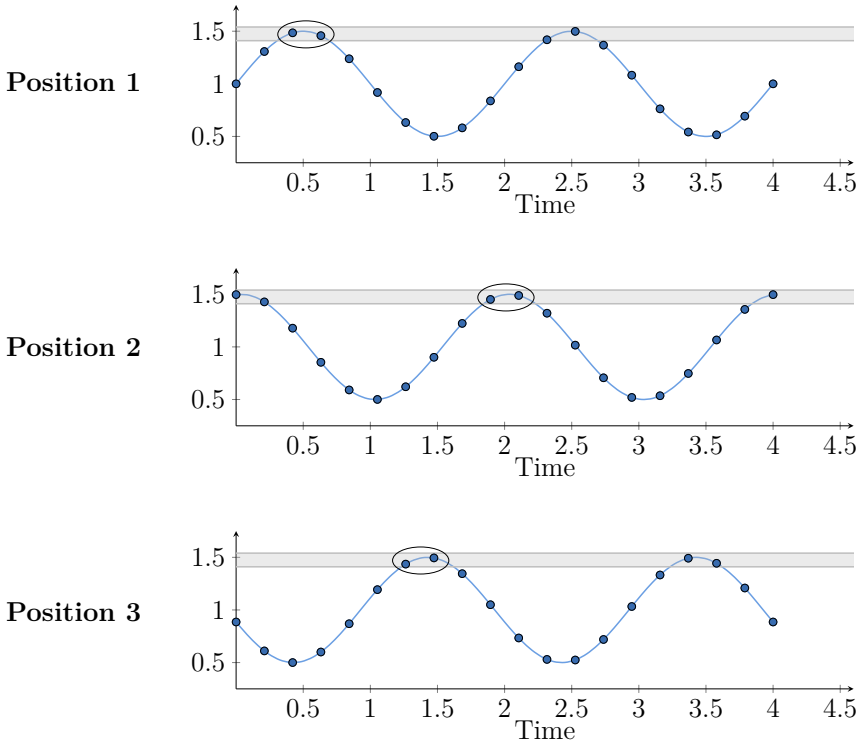

Figure 7.22: Schematic comparison of the modulation signals at different measurement locations for the case where the field samples with similar modulation states are extracted and combined to a transformable dataset.

formed to the FF, are marked. The modulation occurring in the time signal in the FF is a direct result of the NFFFT where the order of the samples and their mutual dependence regarding the time axis must be taken into account. The resulting FF signal in the main beam of the AUT is depicted in Fig. 7.23 (b), where also the error of the transformed time signal with respect to a reference signal, which has been directly calculated from the dipole model, is given. In these simulations, the sampling frequency of 410.224 kHz was chosen to be significantly higher than the modulation frequency and as an odd value to prevent that the sampling frequency is a multiple of the modulation frequency. In general, this is not necessary and is only to demonstrate that the sampling and modulation frequency are indeed unrelated. To make sure that the NF signals at different measurement positions are not synchronized, an individually random phase offset has been added to the signals at the single NF positions. Inspecting the FF signal in Fig. 7.23 (b) reveals that the error is significantly larger than for the case where the sampling and the modulation frequency are aligned. This is a consequence of the interval $m_i \pm \epsilon$ which has been chosen to 0.5 % of the amplitude hub of the modulation. The interval must be chosen according to the sampling rate such that a sufficient number of field values is included in the NFFFT. However, in this specific case, the FF error is still well below −60 dB which is lower than what can usually be achieved in NF measurements.

Dismissing Modulation Content

The LTM, as well as the STM, approach are based on the assumption that the modulated field signal of an antenna shall be determined in the FF, while it is measured in the NF. However, in the case where only the FF radiation pattern is of interest and not the modulation itself, the transformation of the field

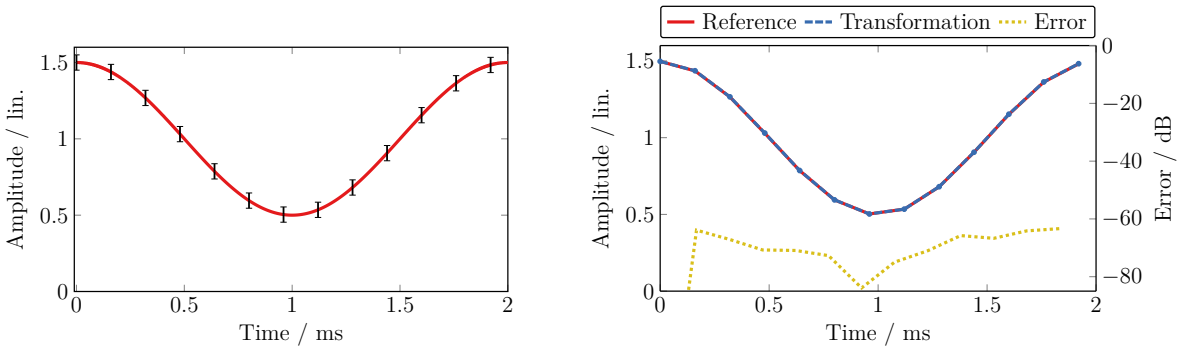

(a) (b)

Figure 7.23: Intervals of NF samples that are transformed together to the FF (a) and corresponding FF signal (b) in comparison to the reference. The shown signals occur in the main beam of the horn antenna at ($\vartheta = 90°, \varphi = -90°$).

becomes trivial since the modulation content can be dismissed. In this case, the measurement is performed according to the STM approach while, instead of extracting field samples of similar modulation state, the measurement signal is divided by the reference signal. This division removes the modulation as it is incorporated in the measurement as well as the reference signal. In contrast to the STM approach described before, the measurement period and time can be chosen arbitrarily. The only relevant considerations for both values are the movement speed of the antennas and the occurring noise.

7.5 Verification by Measurement

The basic applicability of the STM approach has been shown by numerical simulations while, next, the actual implementation in hardware is discussed. This is especially important since the simulations are based on the assumption that the actual modulation signal is available as reference and can be employed to determine the instantaneous modulation state. However, in real measurements this cannot be assumed at all. Instead, it is very likely that a test signal cannot be fed to the AUT and, also, that the feeding signal of the AUT cannot be accessed. Given this situation, a measurement setup based on an external reference is needed. In the following, measurements are presented that show a possible implementation of the STM approach and its applicability and behavior within real measurements. The section follows the structure of the corresponding publications [Faul et al. 2021a] and [Faul et al. 2023] in which the measurement results have been published.

7.5.1 Measurement Setup

The measurements investigating the STM approach have been performed in an anechoic chamber at the TUM. A cylindrical NF measurement setup was used, where the double-ridged horn antenna DRH400 [RFSpin 2013] served as AUT and was mounted on a wooden mast on a turntable. Opposite of the AUT, at a distance of 1.74 m, another double-ridged horn antenna of type HF906 [R&S 2022b] was mounted on a vertical linear positioner. This antenna served as field probe within the measurements. The radius of the measurement cylinder was equal to the distance between the two antennas and the height of the scan area was 1.5 m. A picture of the measurement setup is depicted in Fig. 7.24 (a), while Fig. 7.24 (b) shows a schematic of the setup, including the RF connections. Within the measurements, the AUT was transmitting and connected to a signal generator of type R&S SMC100a [R&S 2022c]. A

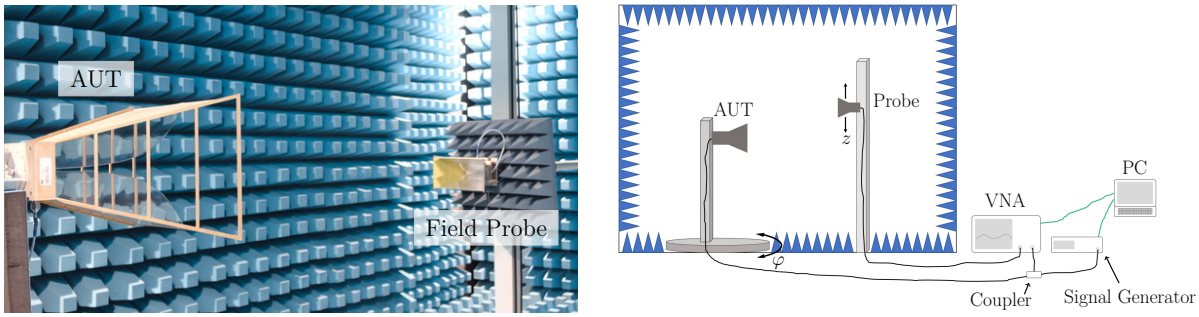

(a) (b)

Figure 7.24: Picture (a) of the used measurement setup where the two double-ridged horn antennas were facing each other. The schematic overview (b) shows the placement of the antennas in the anechoic chamber, including the RF equipment and corresponding connections. (b) [Faul et al. 2023]

two-port VNA of type R&S ZVK [R&S 2022g] was employed as measurement receiver while only the incoming b-waves were measured. The probe antenna was connected to one channel of the VNA, while the other channel was connected to the feed signal of the AUT via a directional coupler. Hence, the feed signal served as reference for the determination of the measurement samples of same modulation state m_i, similar as in Section 7.4. Furthermore, the reference signal is also needed as phase reference since the used NFFFT expects complex field values. In general, this measurement setup represents the case where the feeding signal of the AUT can be accessed. In cases where this is not possible, a reference signal can be gained from a second static reference antenna which is, e.g., outlined in the measurement example of air navigation systems in Chapter 8.

In principle, different implementations of measurements following the STM approach are possible. At first sight, the realization with an oscilloscope as measurement receiver seems to be most straight forward as multiple channels can be measured at the same time and, therefore, the modulation signal can be sampled continuously. Still, an implementation with a VNA as measurement receiver has been chosen as there are some advantages in using a VNA over an oscilloscope. First, the dynamic range of a VNA is usually larger than that of an oscilloscope, being about 100 dB to 130 dB. In comparison, oscilloscopes often have only 8 bit analog-digital (AD)-converters, which leads to a dynamic range of 48 dB.[2] The VNA is measuring in zero-span mode, i.e., no frequency sweep is performed and all measurements are conducted at the center frequency. Because of that the data acquisition is comparably fast and the sweep time depends only on the chosen RBW and the number of measurement samples. Further, the zero-span mode has the advantage that the modulation signal is directly measured and no additional demodulation has to be performed on the measured field signal. Another very important difference in the usage of a VNA over an oscilloscope is that the internal filter of the VNA suppresses external noise, which can be chosen in terms of RBW. In contrast, an oscilloscope always measures all frequencies within its broad bandwidth that can only be changed with the help of additional external filters.

It shall also be mentioned that the actual radiation patterns measured with this setup are not fully correct due to the availability of scattering objects in the measurement chamber. This is a consequence of the fact that the measurement chamber has not been designed for antenna measurements, rather than for EMC measurements. Despite being one of the main characteristics of any antenna, the exact radiation

[2]These values are the result of a comparison between different VNAs and oscilloscopes. The VNAs of type R&S ZVL [R&S 2022f], ZVA [R&S 2022e] and ZVK [R&S 2022g] and oscilloscopes of type Agilent MSO7104B [Agilent 2010] and LeCroy WaveMaster 808Zi-B [LeCroy 2021] have been taken into account. It shall be noted that both oscilloscopes provide modes which offer an even higher resolution, e.g., up to 12 bit for the Agilent MSO7104B. However, in this case, measurements are averaged to achieve this resolution which is not feasible for the usage together with the STM approach.

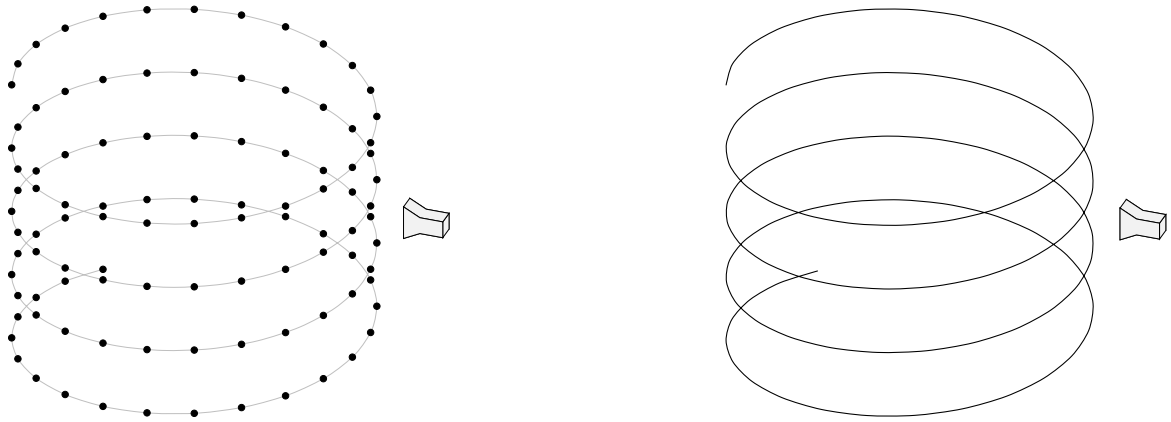

(a) (b)

Figure 7.25: Illustration of the scan grids resulting from the different measurement scenarios. Within step measurements (a), the field probe stops at the different measurement locations, while it keeps moving on the cylindrical surface within a continuous measurement scenario (b).

pattern of the AUT is not relevant within these test measurements as they shall reveal the applicability of the STM approach. Therefore, only the relative accuracy between subsequent measurements is crucial instead of the absolute accuracy. The limiting factor, however, is the precision of the positioners which is far from accuracies observed in sophisticated NF chambers. Still, as a result of several test measurements, the repeatability of the measurement setup was determined to $-40\,\mathrm{dB}$ within the valid angles of the scan area.

Two different kinds of measurements have been performed: measurements with a static and measurements with a continuously moving field probe. First, step measurements have been performed in which the field probe is virtually moved to the desired measurement location and remains at this specific location during the actual measurement. Then, it is moved to the next location where the next measurement is conducted. The second type of measurements are those, in which the field probe is virtually moving on horizontal lines on the cylindrical measurement surface with constant speed. While the field probe moves virtually around the AUT, in reality, it moves only in vertical direction while the AUT is rotated during these measurements. The resulting measurement grids of both types are exemplary depicted in Figs. 7.25 (a) and (b).

7.5.2 Measurements with a Static Field Probe

The measurements with the static field probe, also called step measurements, have been performed on a regular grid of the cylindrical surface. The field samples have been processed as described in Section 7.2, while the modulation signal was re-composed in the FF. Especially for the reconstruction of the modulation in the FF, a priori knowledge about the modulation signal is taken into account, e.g., whether the symmetry of the modulation signal allows for the combination of measurement samples of same modulation states but from different times within a modulation period.

In the measurements, the signal generator, feeding the AUT, was tuned to a carrier frequency of $f_0 = 1\,\mathrm{GHz}$. Furthermore, an AM was set up with a modulation frequency of $f_\mathrm{m} = 50\,\mathrm{Hz}$ and a modulation index of $M = 0.5$. The RBW of the VNA was chosen to 3 kHz and, therefore, the acquisition time of a single field sample was $T_\mathrm{meas} = 1/RBW = 0.3\,\mathrm{ms}$. The measured NF signal in the middle of the main beam, i.e., at $z = 0\,\mathrm{m}$ and $\varphi = 0°$, is depicted in Fig. 7.26 (a). Carefully looking at the measured antenna

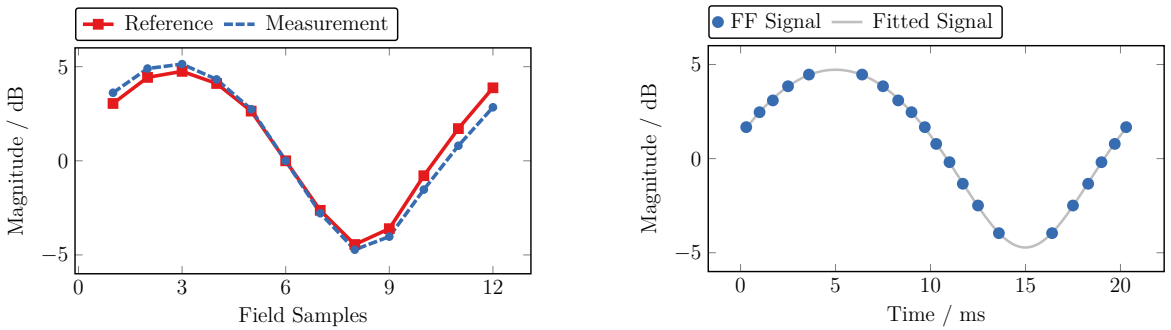

(a) (b)

Figure 7.26: The modulated NF signal (a) is recorded for all different measurement locations and processed according to the short-time measurement approach. The resulting FF signal (b) inevitably shares the same modulation form. [Faul et al. 2023]

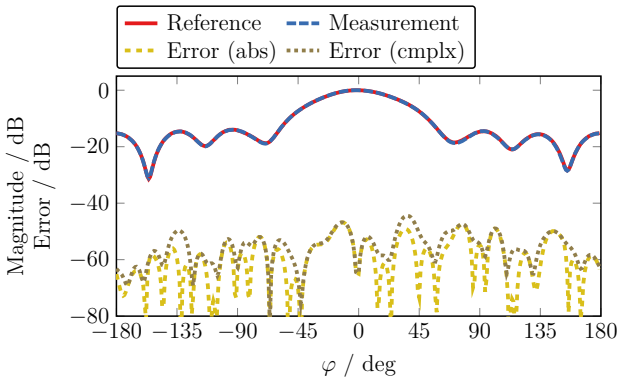

Figure 7.27: Horizontal main cut of the FF at $\vartheta = 90°$, evaluated for a fixed modulation state m_i. The FF of a time-harmonic reference measurement is compared to the one of the STM. [Faul et al. 2023]

signal, as well as the reference signal, reveals that the modulation is not exactly sinusoidal and rather stretched. This finding is an artifact of the logarithmic scale as the modulation of the linear field signal is indeed of sinusoidal form. From the NF signal, the corresponding FF signal has been derived by field transformation. It is depicted in Fig. 7.26 (b), again for the middle of the main beam which is $\vartheta = 90°$ and $\varphi = 0°$ in this case. Similar as before, also the FF signal looks not exactly sinusoidal due to the logarithmic scale. As a consequence, the fitting of the sine function to the transformed FF samples has to be performed with respect to the linear representation of the field signal.

While Fig. 7.26 (b) shows the change of the FF in the middle of the main beam over time, the spatial change of the FF is given in form of the horizontal FF main cut at $\vartheta = 90°$ of the cylindrical measurement surface in Fig. 7.27. The field is depicted for one fixed modulation state m_i. The plot shows error curves that have been calculated from the comparison of the STM measurement and a time-harmonic reference measurement according to the error measures introduced in Section 2.6, one with and one without the consideration of the phase. Regarding the measurement in Fig. 7.27, both error measures are on a similar level which expresses that the STM approach does not introduce an additional error into the measurement. It can also be seen that the complex error measure is slightly higher for some spatial directions of the FF which is no effect of the STM approach and fully due to the measurement setup. In fact, a similar situation can be observed also in other measurements. In the following, only

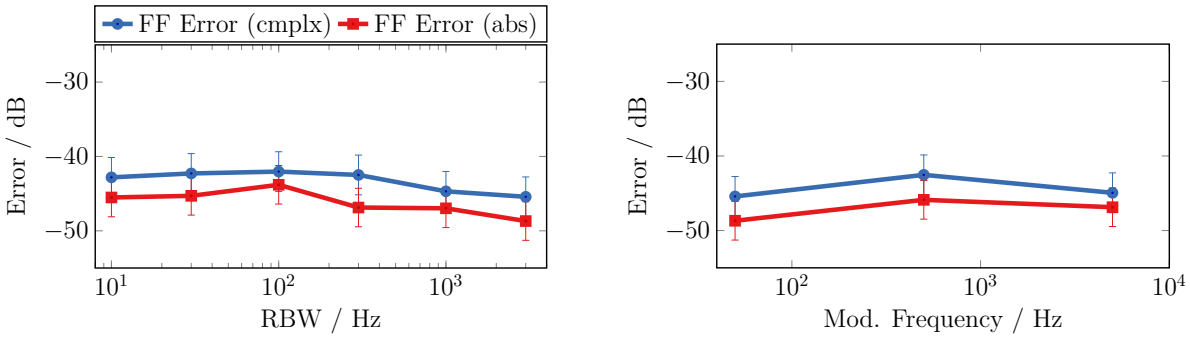

(a) (b)

Figure 7.28: Multiple measurements for different RBWs (a) and modulation frequencies (b). The absolute (red) and complex (blue) measures of the maximum FF error are shown in comparison. [Faul et al. 2023]

the horizontal FF main cut is evaluated due to the fact that the valid angle in vertical direction is very small as a consequence of the small height of the cylindrical scan geometry. To reveal the measurement scenarios in which the STM approach fails and cannot be used anymore, the different parameters of the AM and data acquisition are changed.

First, the RBW of the VNA is changed. Figure 7.28 (a) shows the maximum FF error of the NFFFT for different RBWs, while it can be observed that the error neither increases nor decreases significantly. Here, it is important to recall that the observation time of a VNA is directly linked to its RBW while lower RBWs implicate longer measurement times. Moreover, the observation or measurement time T_{meas} must be seen in relation to the period of the modulation signal T_{mod} or, equally, to its frequency f_{m}. An easy way to inspect the measurement time, respectively RBW, is by defining a measurement-modulation-ratio (MMR) as

$$MMR = \frac{T_{\text{meas}}}{T_{\text{mod}}} = \frac{f_{\text{m}}}{RBW} = \frac{1}{T_{\text{mod}} RBW} . \tag{7.51}$$

With that, measurement times which are longer than the respective modulation period are indicated by $MMR > 1$. In this case, the modulation signal is averaged such that it is not available anymore in the recorded field samples and, hence, cannot be reconstructed in the FF according to the STM approach. In the measurements, however, the transformation error does not increase even for measurement times that are longer than the modulation period. Within a second measurement series, the modulation frequency f_{m} was swept between 50 Hz and 5 kHz for a fixed RBW of 3 kHz, except for the measurement with $f_{\text{m}} = 5$ kHz where the RBW was 10 kHz. The maximum FF errors for the different frequencies are depicted in Fig. 7.28 (b). Regarding the relation pointed out by (7.51), it becomes clear that a change of the modulation frequency has a similar effect as a change of the RBW. Therefore, a similar behavior of the measurement error is expected. Likewise, in these measurements, no increase of the FF error can be observed. Besides the frequency of the modulation signal, also its intensity has been changed. This was done in terms of the modulation index M for a modulation frequency of 50 Hz and an RBW of 3 kHz. Similar as before, the FF error is shown in Fig. 7.29 (a). Also in these measurements, no significant change of the FF error can be observed. However, it is worth noting that a modulation index close to one can cause problems, depending on the offset of the AM signal since the resulting minimal values can be very close, or even inside, the noise floor of the measurement setup.

Additional to the parameters of the modulation signal, also the carrier frequency f_0, respectively measurement frequency, has been changed within the measurements. The maximum FF error of the horizontal main cut is shown in Fig. 7.29 (b). Here, it can be observed that the FF error increases for higher measurement frequencies. However, this observation is misleading as it is fully due to the measurement

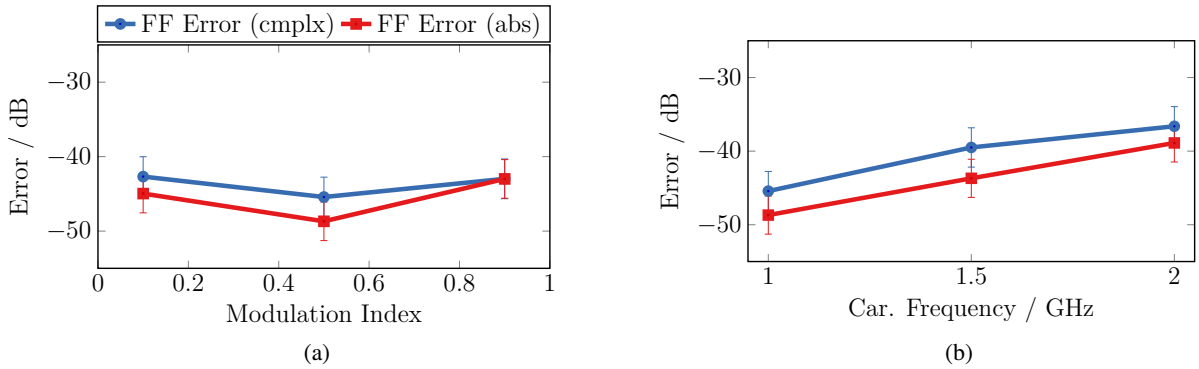

Figure 7.29: Multiple measurements for different modulation indices of the AM (a) and carrier frequencies (b). The absolute (red) and complex (blue) measures of the maximum FF error are shown in comparison. [Faul et al. 2023]

setup rather than due to the STM approach. As already mentioned, the anechoic measurement chamber has not been designed for antenna measurements and, as a consequence, the positioners do not fulfill the requirements for high-precision positioning which is needed in antenna NF measurements. Due to the smaller wavelength, the positioners need to be more and more precise with increasing frequency within NF measurements which is, however, not the case for the given setup. The assumption that the STM is independent of the carrier frequency is supported by the fact that the same increase in the FF error has been also found for time-harmonic measurements with the measurement setup. Also, numerical simulations come to the same result that the STM approach can be applied independently of the carrier frequency as long as all prerequisites are fulfilled.

To further prove that the measurement approach is not only applicable to AM signals, measurements with a frequency modulated field have been performed. In these measurements, the carrier frequency was again 1 GHz, while the signal generator was set up to provide an frequency modulation (FM) signal with a modulation frequency of 50 Hz. The principle of forming transformable data sets within the STM approach can basically also be applied to FM signals, where a key problem is that the instantaneous frequency cannot be determined as easy as the instantaneous amplitude of an AM signal in the time-domain. However, looking at the frequency-domain and with the help of a linear frequency slope, e.g., a filter curve, a simple edge demodulation can be performed which is a conversion of the FM to an AM. Eventually, the resulting AM can be processed in the exact same manner as before. For the conducted measurements, the input filter of the VNA was employed. Though, the key problem of this approach was that this input filter is undocumented and no filter curve was available. Therefore, the linear part of the filter curve has been determined by several test measurements, before the actual measurements of the modulated fields were performed. In principle, the usage of a known external filter instead of the internal one may be able to enhance the accuracy of the FM to AM conversion. Figure 7.30 shows the maximum FF error of measurements with different frequency deviations between 50 Hz and 1 kHz. Also here, no relevant change of the maximum FF error can be observed.

While the STM approach asks for the extraction of field samples that share a common modulation state, the idea might come up to use all field samples, regardless of their respective modulation state, within the NFFFT. Depending on the recorded modulation states and their distribution, the transformation of all samples can lead to the correct FF pattern which could also be observed during the transformation of the measurements described above. However, the inclusion of all field samples results in a larger NF error of the NFFFT, while the modulation signal cannot be found in the FF. This is a consequence of an averaging that is done by the NFFFT as multiple field samples occur at similar positions. Given the fact that the modulation signal is not available in the FF, the transformation of all measurement samples

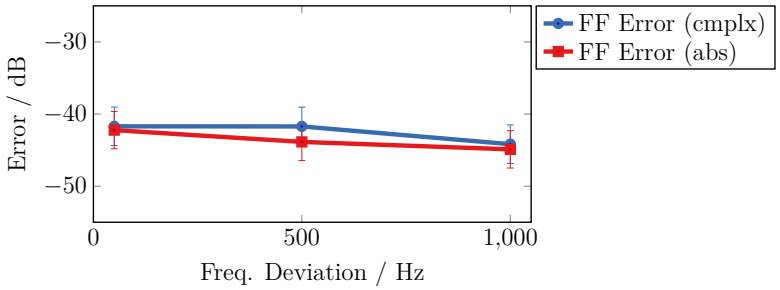

Figure 7.30: Measurements for different frequency deviations of the FM signal for a modulation frequency of 50 Hz. The absolute (red) and complex (blue) measures of the maximum FF error are shown in comparison. [Faul et al. 2023]

does only make sense when there is no interest in the modulated field signal. Still, also in this case, the division by the reference signal as described in Section 7.4 might be the better choice.

7.5.3 Measurements with a Moving Field Probe

The measurements with the static field probe in Section 7.5.2 did not reveal any error for the application of the STM approach exceeding that of the used measurement setup. However, as already mentioned, a UAV cannot hover at a specific position for a longer time. Instead, the field field probe will be moving during the measurement of the single field samples within UAV-based field measurements. To include this in-situ measurement scenario and make the measurements in the chamber more realistic, measurements have been performed in which the turntable was constantly moving during data acquisition. This is equal to a field probe which is constantly moving on the cylindrical scan surface, according to Fig. 7.25 (b). The rotation speed of the table was $v_{\text{move}} = 12.4\,^\circ\,\text{s}^{-1}$, which is equal to a movement speed of $0.375\,\text{m}\,\text{s}^{-1}$ according to the dimensions of the measurement setup.

To enable a comparison with the measurements before, also here, a carrier frequency of 1 GHz and an AM have been chosen, while the rotation speed was set to its maximum. This is a consequence of the expectation that the FF error increases with larger movement speeds and longer measurement times, respectively larger MMRs, since more spatial extent is covered. To enforce a somehow extreme situation, the RBW has been reduced to 10 Hz to achieve a comparably long measurement time of $T_{\text{meas}} = 100\,\text{ms}$. Therefore, within the measurements, the MMR is changed by changing the modulation frequency which also needs to be comparably low to comply with the low RBW. Figure 7.31 (a) shows the maximum FF error for modulation frequencies between 1 Hz and 5 Hz. According to the plot, the modulation frequency has no impact on the measurement error also in the case of a continuous movement of the field probe. Another measurement sweep, depicted in Fig. 7.31 (b), shows that also the change of the modulation index, for a fixed modulation frequency of 1 Hz, does not have a mentionable impact on the FF error.

7.6 Distance and Time Constraints

The measurements in Section 7.5 showed that the STM approach is practicable and can also be applied to real measurement data. The measurements also confirmed that the measurement bandwidth needs to be larger than the bandwidth of the modulation signal since the modulation cannot be reconstructed otherwise. Within the measurements, none of the tested parameter sweeps revealed a noteworthy increase in the maximum FF error which was always similar to the time-harmonic reference measurements. However, this does not imply that the STM does never introduce any error in NF measurement of modulated

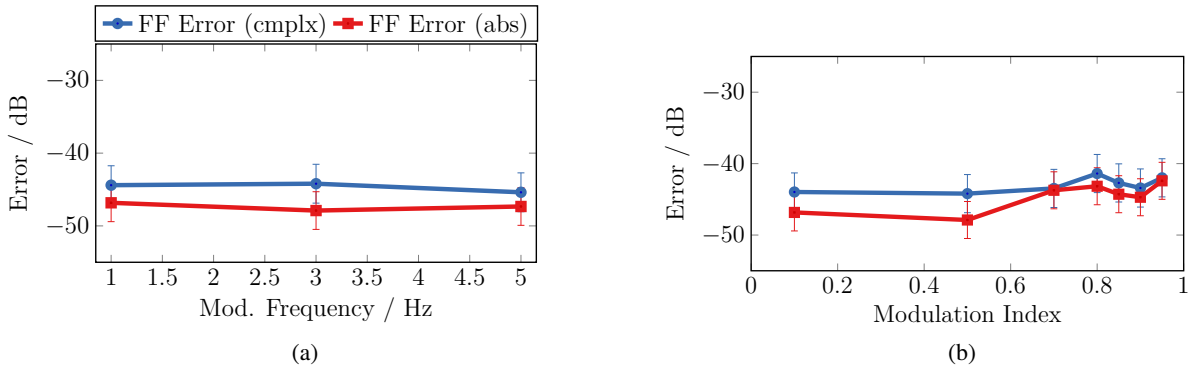

Figure 7.31: Measurements for different modulation frequencies (a) and a sweep of the modulation index (b) for the case of a continuously moving field probe. The absolute (red) and complex (blue) measures of the maximum FF error are shown in comparison. [Faul et al. 2023]

fields and can be applied in all cases. It is rather a consequence of the limitations of the measurement setup as will be pointed out in this section. A similar observation has been made in Section 7.3.4, where the field error introduced by the modulation has been analytically calculated for a Hertzian dipole as radiating source. While these investigations can only be taken as indications, the error is analyzed in a more realistic measurement scenario through numerical simulations in this chapter. In contrast to Section 7.3.4, this section investigates the FF error. In the following, simulations with similar parameter sweeps as for the measurements in Section 7.5 are discussed with the intention to reveal the limitations and constraints of the STM approach.

7.6.1 Simulation Model

Numerical simulations have been performed with the same model of a horn antenna as for the simulations in Section 7.4, i.e., a horn antenna was represented by time-harmonic Hertzian dipoles. Similar as before, the time signal was derived from the calculation of the time-harmonic fields for the carrier and the sideband frequencies. Here, a carrier frequency of 3 GHz and an AM were chosen. The NF was calculated on a cylindrical measurement surface with radius r and a height of 6 m. The methodology of the evaluation of the simulations was similar as for the measurements to enable a comparison with them. However, for the simulations, only the more restrictive complex error is shown which includes the phase of the FF. It is calculated according to (2.32), where the reference was the time-harmonic FF that has been directly calculated from the dipole model. Moreover, the error is only evaluated inside the valid angles which are defined by the height and radius of the cylindrical measurement surface as described in Section 2.4. Similar as before, only the maximum error of the horizontal FF main cut at $\vartheta = 90°$ is shown, which is, however, just for simplicity and not a restriction of generality. Complementary to the described measurements, simulations for the cases of step measurements as well as for continuous measurements with a moving field probe have been performed. Here, as for any other dipole simulation in this thesis and for simplicity, a single Hertzian dipole was assumed as field probe.

7.6.2 Distance Constraints

According to the wavenumber k and the relationship between the phase distribution and the frequency of the field, it is assumed that the error of the STM approach is dependent on the modulation frequency. For this, the radius r of the measurement cylinder has been changed during the simulations. The modulation index of the AM was $M = 0.5$, while the case of step measurements was assumed. In this case, errors

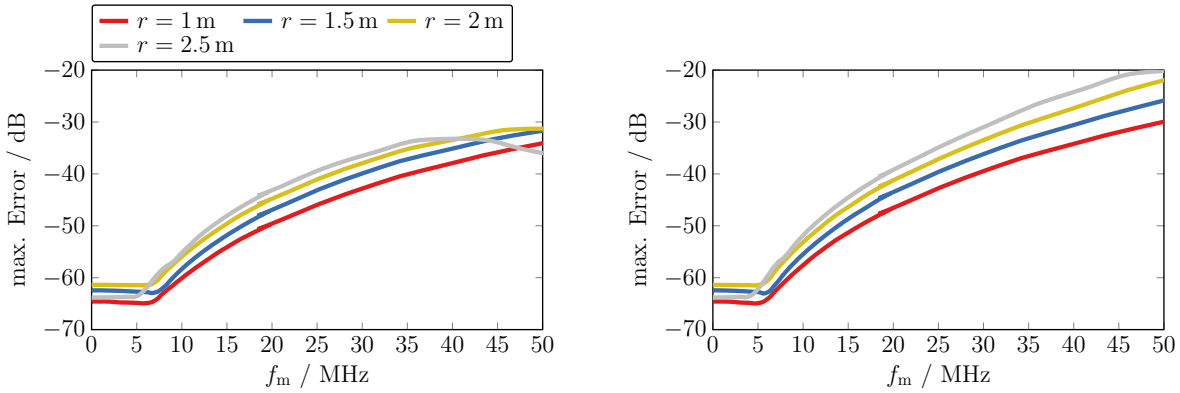

Figure 7.32: Maximum error of the FF cut at $\vartheta = 90°$ for different modulation frequencies f_m and measurement radii r. In addition, the modulation index has been changed between the simulations, where it was chosen to $M = 0.5$ (a) and $M = 0.9$ (b). © 2021 IEEE, [Faul and Eibert 2021]

due to the moving field probe are prevented. The maximum error of the horizontal FF cut is plotted over the modulation frequency f_m in Fig. 7.32 (a). The figure clearly reveals that the error increases with increasing modulation frequency and also with increasing measurement distance, respectively with the radius r of the cylinder. Overall, the impact of the radius is almost negligible, while the changing modulation frequency causes changes in the order of tens of decibels. Regarding the simulation, it is also found that the error does not change significantly for modulation frequencies below 5 MHz. Figure 7.32 (b) shows the same simulation as Fig. 7.32 (a) but for a modulation index of $M = 0.9$. In comparison, the error increases faster with the modulation frequency, while, at the same time, the absolute magnitude of the error is higher for the different modulation frequencies. Furthermore, it can be seen that the differences between the error curves for different measurement radii increase with increasing modulation frequency. However, this effect is not significant for errors below −50 dB, or even −40 dB, which are common error levels within NF antenna measurements. In addition, the error change for different measurement distances is still negligible in comparison to the change due to the different modulation frequencies. Overall, also in this case, there is almost no change for modulation frequencies below 5 MHz.

In addition to the variation of the radius, simulations were performed with a mean radius of $r = 1.5$ m, while the exact radius was blurred for the single measurements. The actual measurement radii were within an interval $r \pm \Delta r/2$, while the radii of the single positions were randomly chosen within these boundaries. The modulation signal was again an AM with a modulation index of 0.5. The corresponding maximum FF error is depicted in Fig. 7.33. Similar as for the simulations before, the error increases with the modulation frequency. Furthermore, the error seems to be independent of the uncertainty value Δr, at least within the tested range and with the usage of FIAFTA as NFFFT algorithm. In total, the simulations in this section reveal that a low FF error can only be achieved if the measurement radius r is significantly shorter than the wavelength of the modulation signal, i.e., $\| r\| \ll \lambda_\mathrm{m}$. In the simulations, no significant increase of the error from the noise level could be observed for modulation frequencies lower than 5 MHz. With the consideration of the maximum radius in the simulations $r = 2.5$ m, a guideline for the application of the STM can be derived, stating that $\| r\| < \lambda_\mathrm{m}/20$ must be fulfilled regarding the NF measurement distance, where λ_m is the wavelength of the modulation signal.

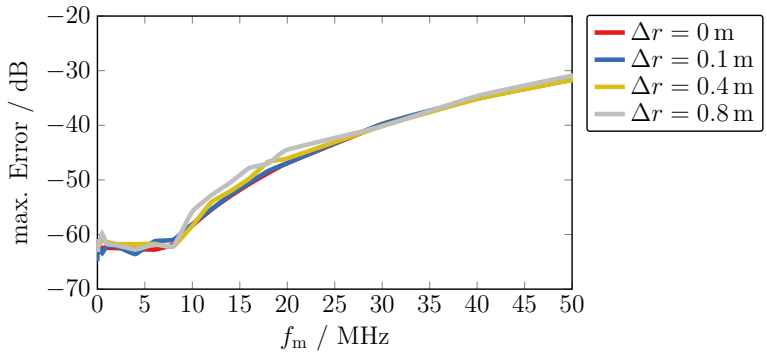

Figure 7.33: Maximum FF error for different modulation frequencies f_m. The mean measurement radius of $r = 1.5\,\mathrm{m}$ was blurred as random offsets within an interval $\pm\Delta r/2$ have been added for the different measurement locations. © 2021 IEEE, [Faul and Eibert 2021]

7.6.3 Time Constraints

The STM is based on the premise that the modulation signal can be treated as constant during one single measurement. This implies that the measurement time T_{meas} must be significantly shorter than the period of the modulation signal T_{mod}. A short measurement time increases the position accuracy as the moving field probe does not travel too far during that time. In contrast to that, a long measurement time blurs the measurement position and with that reduces the position accuracy, but it also increases the signal-to-noise ratio (SNR) which is very much desired in measurements. In the end, a trade-off has to be found, where the simulations can, again, provide guidelines.

There is an essential difference for the time constraints regarding step measurements, in which the measurement locations are static during the single measurement intervals, and for dynamic measurements, where the measurement location changes during the measurements due to the probe movement. The time ΔT between two consecutive measurements is crucial. It must either be chosen to match with the period of the modulation signal or, if ΔT is chosen randomly, a filtering approach must be applied in the post-processing to combine the measured field samples into transformable data sets, as already described in Section 7.2. The measurement time T_{meas}, however, is not relevant within the case of step measurements, since the modulation state m_i will be the same for all measurements. In the following, the dynamic case with a continuous probe movement is considered for the simulations as it is the relevant case regarding UAV-based NF field measurements. It is further assumed that the single measurements start at the same modulation state regarding the phase of the modulation signal.

Similar as for the distance constraints, simulations with a modulation frequency of $f_m = 50\,\mathrm{Hz}$ and a modulation index $M = 0.5$ were performed. The measurement radius was 1.5 m, while the field probe was constantly moving with a velocity v. This velocity v was changed between different simulations, where the resulting maximum FF error is shown in Fig. 7.34. Within these simulations, the measurement time was swept from 1 µs to 12 ms, while the horizontal axis in the plot is given in terms of the MMR, i.e., the ratio of the measurement time T_{meas} to the modulation period T_{mod}. It can be easily seen that the error increases for faster flight speeds and, more significant, for larger MMR values, which is equal to longer measurement times. This result is expected, as both, a larger velocity for a constant measurement time and a longer measurement time for a constant velocity, lead to an increasing spatial averaging of the modulated field due to the probe movement during data acquisition. Here, it is important to mention that the largest simulated speed of $7\,\mathrm{m\,s^{-1}}$ is a rather theoretical case and not realistic since the actual flight speed of a UAV is significantly lower in field measurements, e.g., the maximum flight speed during the UAV-based measurements in Chapter 5 was only $1\,\mathrm{m\,s^{-1}}$.

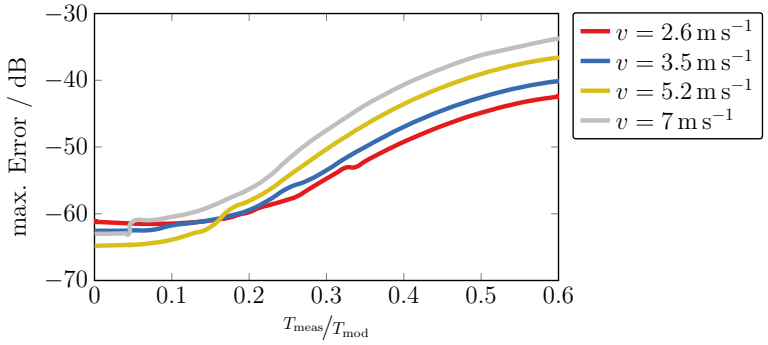

Figure 7.34: Maximum error of the FF cut at $\vartheta = 90°$ for different movement velocities v of the field probe and for different measurement times T_{meas}. The measurement time on the horizontal axis of the plot is given relative to the modulation period in terms of the MMR. © 2021 IEEE, [Faul and Eibert 2021]

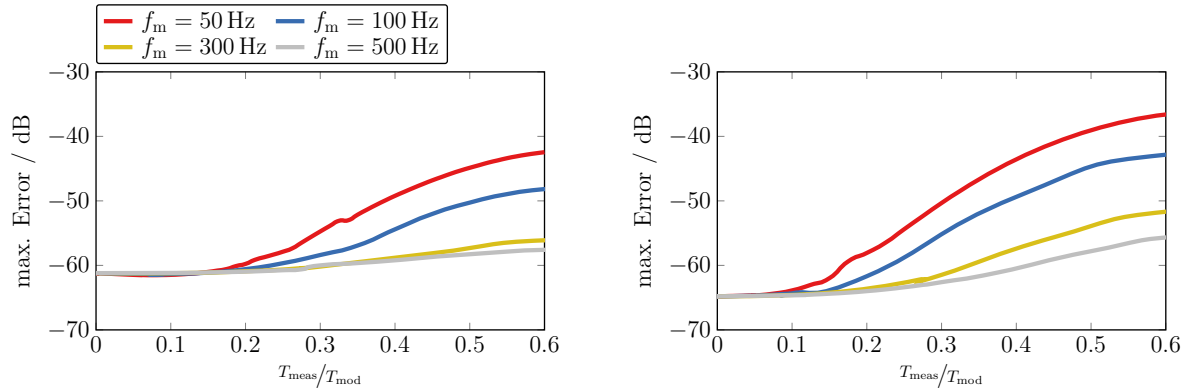

Figure 7.35: Maximum error of the horizontal FF cut for various modulation frequencies f_{m} and two different movement velocities of $v = 2.6\,\mathrm{m\,s^{-1}}$ (a) and $v = 5.2\,\mathrm{m\,s^{-1}}$ (b). The measurement time on the horizontal axes of the plots is given in terms of the MMR. © 2021 IEEE, [Faul and Eibert 2021]

Furthermore, simulations for different modulation frequencies f_{m} but with fixed movement velocities of $v = 2.6\,\mathrm{m\,s^{-1}}$ and $v = 5.2\,\mathrm{m\,s^{-1}}$ have been performed. The results are depicted in Figs. 7.35 (a) and (b). Again, in these simulations, it is found that the error increases with the MMR. The measurement error also increases with the velocity, which can be observed when comparing Figs. 7.35 (a) and (b). In contrast, the FF error decreases with increasing modulation frequency and for a fixed MMR value. While this seems to be counterintuitive at first, the MMR, given on the horizontal plot axis, is relative to the modulation period where larger modulation frequencies entail shorter modulation periods. This implies that, for a specific MMR value, the measurement time decreases with increasing modulation frequency, which means that the error due to the UAV-movement also decreases. The comparison of Figs. 7.35 (a) and (b) reveals that the error does not scale equally regarding the different movement velocities. Therefore, it can be concluded that the error according to the measurement time is dominant over the error that is caused by the movement of the field probe. Furthermore, the modulation index M was varied for a constant movement velocity of the field probe of $2.6\,\mathrm{m\,s^{-1}}$. The modulation frequency was, again, chosen to 50 Hz, while the measurement time was swept from 3 µs to 12 ms. The maximum FF error is shown in Fig. 7.36. It can be easily seen that the measurement error increases for larger MMR values, but also for larger modulation indices. However, a saturation seems to exist with respect

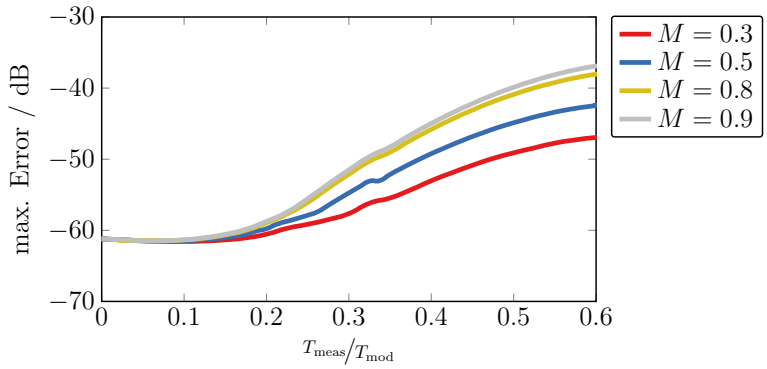

Figure 7.36: Maximum FF error for different modulation indices M and different measurement times T_{meas}, which is given in terms of MMR values. The modulation frequency was 50 Hz at a constant movement velocity of 2.6 m s^{-1}. © 2021 IEEE, [Faul and Eibert 2021]

to the modulation index as the FF error for $M = 0.8$ and $M = 0.9$ is almost similar. Though, larger modulation indices have not been tested as they are not relevant for practical measurements, due to the small magnitude values resulting from such modulation indices as mentioned above.

Overall, the simulations in this section show that the FF error of the measurement increases with longer measurement times T_{meas} in the case of a moving field probe since the spatial measurement position is blurred and the recorded field is integrated. According to the simulations, no significant increase of the error occurs for $MMR \leq 0.1$, which is equal to $T_{\mathrm{meas}} \leq 0.1\, T_{\mathrm{mod}}$. This finding can act as a guideline for the application of the STM approach. Still, the guidelines in this section have to be considered in addition to the requirements discussed in Section 7.2. In general, the measurement time T_{meas} must be chosen such that a sampling of the modulation signal is achieved. This implies that there are multiple measurements during one period of the modulation signal. Within the STM approach, the quality of the reconstruction of the modulation signal mainly depends on T_{meas} as shorter measurement times allow for an higher sampling rate.

7.7 Chapter Summary

Two methods for the measurement of modulated fields have been described in this chapter, the long-time measurement and the short-time measurement approaches. The main difference between both approaches is the measurement time which needs to be sufficiently long with respect to the lowest frequency and the necessary spectral resolution within the LTM. In the STM, in contrast, the measurement time is reduced to such an extent that the modulation signal can be treated as constant during the single measurements. Both approaches have been analytically described, before their applicability was demonstrated by numerical simulations. Due to the fact that primarily only the STM is interesting when it comes to UAV-based field measurements, this approach has been further investigated in NF measurements in an anechoic chamber. Eventually, to reveal the limits and constraints of the STM, numerical simulations have been performed where several parameters have been swept. As a result, guidelines for the application of the STM have been derived. To dismiss an influence of the STM approach onto the measured field data, the measurement radius r needs to fulfill $\|r\| < \lambda_{\mathrm{m}}/20$. Furthermore, the MMR must be smaller than 0.1, which is equal to $T_{\mathrm{meas}} \leq 0.1\, T_{\mathrm{mod}}$.

Chapter 8

Measurement of the Doppler VHF Omnidirectional Range

The VHF Omnidirectional Radio Range (VOR) is a ground-based NAVAID for aviation which allows planes to determine their bearing with respect to the NAVAID itself, i.e., a pilot knows the angle at which he is flying regarding a fixed landmark. The reception of multiple VOR signals enables an aircraft to determine its horizontal location by triangulation. VORs have been established internationally in 1949 and are nowadays more and more replaced by GNSSs. However, even in the case of full replacement for flight operations, VORs are likely to be kept as backup systems for several years since a VOR works independent of any other navigation system and does not rely on external information, e.g., satellite signals. Today, VORs are still considered primary NAVAIDs for the instrument flight of airplanes throughout several countries.

VORs work in the VHF range and those stations are often located at elevated scenery due to the almost optical propagation of VHF radio waves. An improved version of the standard VOR is the Doppler VHF Omnidirectional Radio Range (DVOR) which, as the name suggests, makes use of the Doppler effect. Even though the operation principle is different, the signal structure is almost the same such that the receiver in a plane can deal with both types. The DVOR provides more accurate navigation information as the bearing error is rarely larger than 1° in comparison to the VOR where it is usually below 2.5°. To check the accuracy of the VOR and DVOR stations, measurements have to be performed on a regular basis where the exact testing procedure is defined by the International Civil Aviation Organization (ICAO) [ICAO 2000].

So far, VORs and DVORs are measured with the help of crewed planes. For this, a plane, equipped with a specific measurement receiver, flies along predefined paths while the received navigation signal is checked against former measurements and, nowadays, also against GNSS locations. Moving forward, the introduction of UAV-based measurement systems in this field can make the verification of such navigation system much easier and more environmentally friendly. It can also provide additional information, such as the radiation patterns of the individual antennas. Up to now, there have been multiple concepts and field tests towards the measurement of VORs with the help of UAVs [Demule and Theißen 2018; Oliveira Costa et al. 2020] as well as for the detection of interference with buildings or wind farms [Schrader et al. 2016, 2019]. However, going one step further, NF measurements can improve the verification of NAVAIDs significantly and can even help with antenna diagnostics. Another reason to promote NF measurements for the verification of VORs is the operating frequency of about 110 MHz, which requires comparably large distances for measurements under FF conditions due to the large AUT size. In this case, measuring the field around the VOR would require the UAV to fly several hundred meters around the NAVAID to test its field signals in all directions. While this is feasible using airplanes or helicopters, such measurements can easily become challenging when using UAVs because the energy

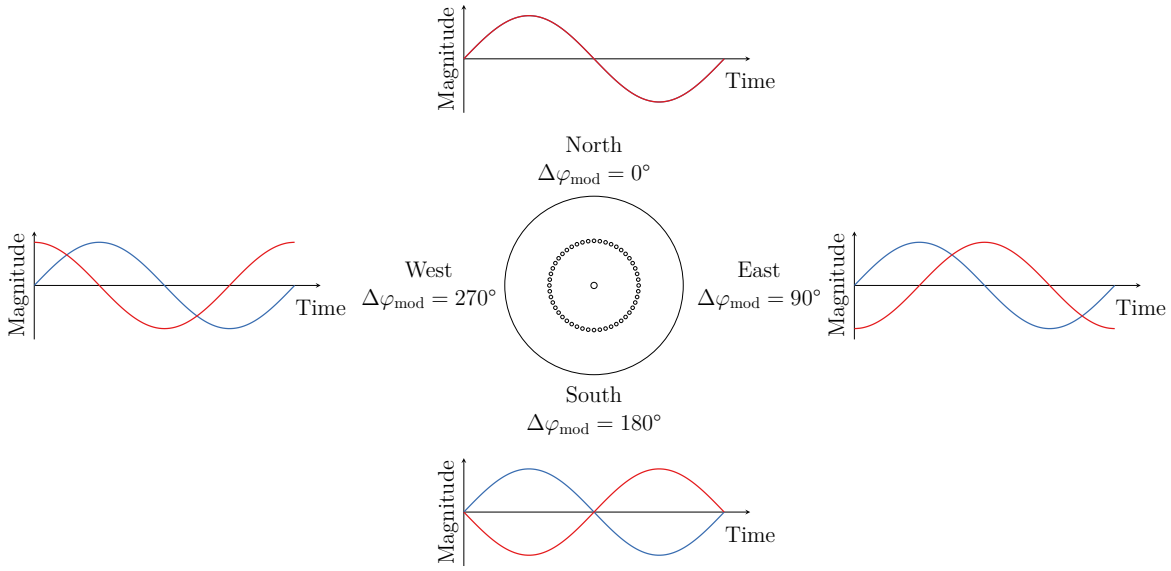

Figure 8.1: Phase difference between the AM (blue) and the FM (red) signals for different spatial directions from the DVOR. The phase difference can be directly used as navigation information as it is 0° in north-direction, increasing in clockwise direction.

required for long flights is often not available, especially when measurement equipment must be carried. In contrast, NF measurements avoid this problem since the field can be measured on a surface close to the DVOR, where the FF radiation pattern is calculated in the post-processing from the NF data using an NFFFT. However, as discussed in Section 7, modulated field signals need a special treatment when it comes to the NFFFT of such fields.

In the following, measurements towards the verification of a DVOR are discussed. First, the operation principle of the DVOR is reviewed, before the approach for the NF measurement and transformation of the field, radiated by such a flight navigation system, is discussed. Here, especially the STM method is taken into account where simulations show its advantage over the LTM approach. Finally, measurement results from first field tests are discussed.

8.1 DVOR Operation Principle

The DVOR is an improved version of the VOR where the resulting navigation signals are similar although the underlying operation principle is different. In the following, only the implementation of the DVOR is discussed since measurements have been performed on such a system. However, some of the discussion does also apply to the conventional VOR. In addition to the given explanation, the working principle of the DVOR is also covered well in the literature [Powell 1981; Helfrick 2007].

The DVOR operates in the frequency range from 108 MHz to 117.95 MHz with a channel width of 50 kHz, while the frequencies up to 111.95 MHz are shared with the ILS. As already mentioned, the DVOR provides its navigation information in terms of radials that allow planes to navigate relative to the DVOR. The radials are established by the comparison of the phase of an AM and an FM signal or, more specific, the navigation information is the phase difference between the AM and FM signals which is different for distinct spatial directions. This is schematically shown in Fig. 8.1. Assuming a top view as in the figure, the phase difference is zero in north direction and increasing clockwise around the DVOR station. It can also be seen in Fig. 8.1 that the DVOR consists of a ring of multiple antennas and an

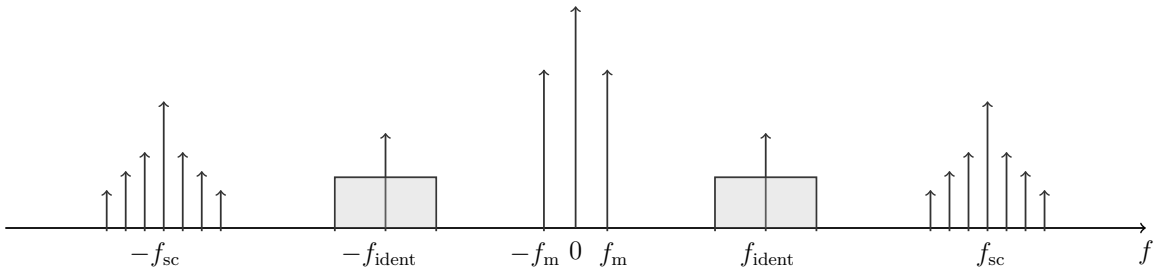

Figure 8.2: Frequency spectrum of the DVOR signal relative to the carrier frequency f_0. A 30 Hz AM is directly modulated onto the carrier f_0, while an FM signal around the subcarrier frequency of $f_{sc} = 9960$ Hz results from the virtual rotation of the active element on the antenna ring. Morse identification and voice signals f_{ident} are additionally present in the frequency range between the carrier and the subcarrier frequencies.

additional antenna in the center of the ring. The center antenna radiates an AM signal with a modulation frequency of $f_m = 30$ Hz and a modulation index of 0.3. The AM signal is directly modulated onto the carrier frequency f_0 and its phase is equal in any direction from the DVOR station. Therefore, it serves as reference signal. The exact number of antennas forming the ring around the center antenna depends on the specific implementation of the DVOR while it is an even number of usually 48 or 50 antennas. Each antenna of the antenna ring radiates a subcarrier frequency f_{sc} of 9960 Hz, i.e., the actual radiated frequency is $f_0 + f_{sc}$. Furthermore, the ring antennas are not all active at the same time where one antenna after another radiates the signal on the subcarrier frequency in counter-clockwise order, i.e., only one antenna is active at a time, creating a quasi-rotating radiator on the ring. The antenna opposite to the active antenna on the ring radiates the signal on the negative subcarrier frequency modulated on the carrier $f_0 - f_{sc}$, while this signal also virtually rotates on the ring. With this an FM is created by the radiation of the antenna ring as an observer recognizes a frequency change due to the Doppler effect. Here, it shall be explicitly mentioned that the antenna signal is electronically rotated and no mechanical rotation or movement of any antenna is involved. The active element of the antenna ring is switched in a way that the radiator virtually moves around the ring with 30 Hz, i.e., one element is only active for $1/(48 \cdot 30\,\text{Hz}) = 0.69$ ms assuming a DVOR with 48 ring antennas. Therefore, the modulation frequency f_{fm} of the FM is 30 Hz, while the radius of the DVOR is chosen in such a way that a peak frequency deviation of $\Delta f = 480$ Hz is created. Both values together lead to an FM modulation index of $\Delta f / f_{fm} = 16$.

The resulting frequency spectrum of the complete DVOR signal is schematically depicted in Fig. 8.2. Besides the positive and negative sideband frequencies of the AM and the FM, an additional identification morse code signal is present in the frequency spectrum at a 1020 Hz tone, modulated on the carrier. Also an optional voice signal can exist in the frequency range of 300 kHz to 3000 kHz. Therefore, the actual spectral parts which contain the navigation information must be extracted from the complete signal with the help of bandpass filters before the AM and FM phases can be compared.

All antennas of a DVOR are Alford loop antennas (ALAs). An isolated ALA has a radiation pattern similar to that of a dipole, i.e., it is almost omnidirectional in horizontal direction regarding the horizontal main cut of the FF radiation pattern. Within a DVOR, all antennas are mounted on a metallic ground plane with about 40 m in diameter. This ground plane, or counterweight, changes the radiation pattern of the single antennas, where, as a consequence, a null in vertical direction above the DVOR exists in which the navigation information is not valid. This null is, therefore, also known as cone of silence. Since the polarization of the ALA is horizontal, the polarization of the DVOR field is also horizontal.

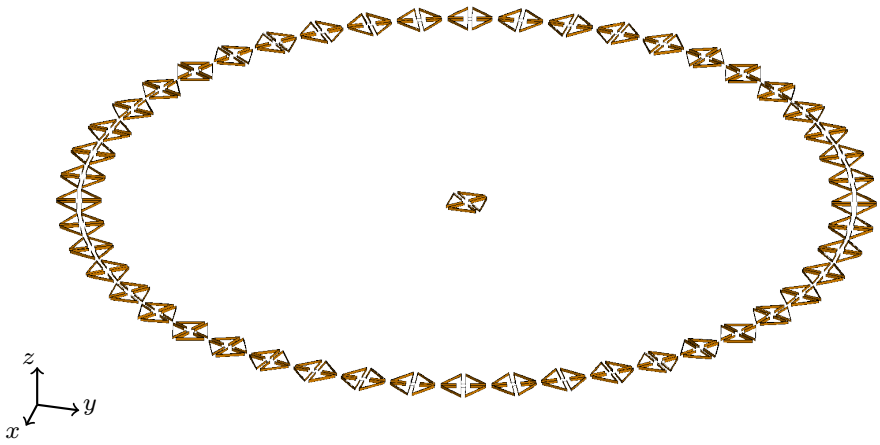

Figure 8.3: Simulation model of a DVOR. All antennas are similar ALAs, where the antenna ring consists of 48 elements, which are rotated such that always the same edge points to the center of the ring.

8.2 DVOR Modulated Field Processing

Two different methods for the measurement and transformation of modulated fields have been discussed in Chapter 7. Both approaches, the LTM and the STM, are principally applicable for the measurement of the modulated field of a DVOR where the reconstruction of the modulation signal in the FF is of interest as this allows the validation of the navigation information. To investigate the differences of the single methods, numerical simulations have been performed. For this, the model of a DVOR has been built in Altair FEKO [Altair 2022] where the dimensions and details of the DVOR Ottersberg in the east of Munich, Germany have been considered, as far as the information could be obtained from available sources [Airport Systems 1991; SELEX 2005]. The simulation model is schematically depicted in Fig. 8.3, where the characteristic antenna ring can be clearly seen. The ring has a radius of 6.7 m and consists of 48 ALAs which are all 1.35 m above a perfect electric conductor (PEC) ground plane. The ALA is a loop antenna of quadratic shape. It is horizontally polarized and has an almost omnidirectional radiation pattern in azimuthal direction. A schematic of the antenna structure including the geometrical dimensions and its FF radiation pattern is depicted in Fig. 8.4. Within the antenna ring of the DVOR, the single ALAs are oriented such that the same edges of all antennas point to the center of the ring. In addition to the 48 ALAs of the antenna ring, there is another ALA in the middle of the ring, the center antenna, whose horizontal orientation does not matter. All ALAs are equal within the simulation model. Still, the ALAs used in reality are more advanced but their exact dimensions are not known. Therefore, plausible dimensions have been chosen where the metal parts were 50 mm high and the length of one edge was 0.5 m. Despite the fact that the simulation is inevitably erroneous in terms of the exact radiation pattern of the single antenna elements due to the barely known dimensions, the simulations are plausible in the sense that they basically match the literature regarding the overall radiation pattern and cone of silence. Moreover, the exact radiation pattern of the DVOR is not crucial to showcase the principal application of the STM and LTM approaches. As already described in Section 8.1, the center ALA radiates a 30 Hz AM that is directly modulated onto the carrier. The antenna ring, in contrast, creates an FM with a modulation frequency of 30 Hz by virtually rotating the active antenna element around the ring where always only one antenna is radiating. All ring antenna elements radiate at a subcarrier frequency of 9960 Hz.

Within the simulations, only the radiation of the antenna ring was considered since the static center

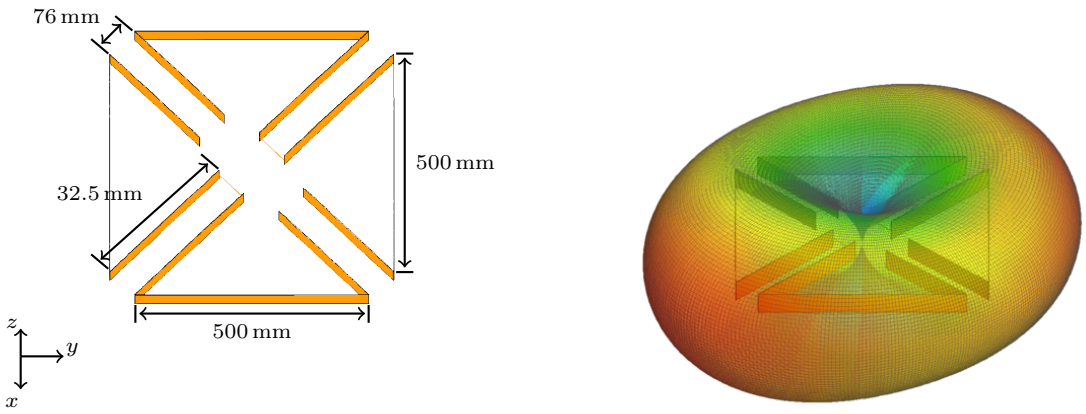

(a) (b)

Figure 8.4: Simulation model of the ALA with the geometrical dimensions used within the numerical simulations (a). The characteristic, almost omnidirectional, FF radiation pattern of a single ALA is shown in (b), where red indicates large and blue small field values.

antenna can be treated in the measurements exactly as the horn antenna in Chapter 7 due to the fact that it is only one single static radiator. The radiation of the single ring elements has been calculated in FEKO while the processing of the modulated signals was performed in MATLAB. The complete simulation concept is depicted as block diagram in Fig. 8.5. First, the time-harmonic NFs and FFs of all 48 ring antennas have been calculated by numerical simulations. The time-harmonic FF pattern of the first ring antenna is depicted in Fig. 8.6 as 2D plot. The figure clearly shows that the field maximum is at about $\vartheta = 60°$, while the fluctuations of the field magnitude along the azimuthal axis are due to the fact that the radiation pattern of the ALA is not exactly omnidirectional. After importing the time-harmonic fields into MATLAB, the modulated NF signal is calculated. Since only one antenna element in the ring is active and radiating at a given time t_i, the number of the active element n_{act} is determined by

$$n_{\text{act}}\left(t_i\right) = \left(\left\lfloor 48 f_{\text{fm}}\left(t_i - t_0\right)\right\rfloor \mod 48\right) + 1\,, \tag{8.1}$$

where $f_{\text{fm}} = 30\,\text{Hz}$ is the modulation frequency and t_0 a static time offset that is needed for adjusting the FM relative to the AM and, thus, the navigation information of the DVOR. Within the simulations, $t_0 = 0\,\text{s}$ applies. Furthermore, $\lfloor . \rfloor$ is the floor and mod the modulo function. The floor function rounds a real number x down to the next integer. It is defined by

$$\lfloor x \rfloor = \max\{a \in \mathbb{Z} \mid a \leq x\}\,. \tag{8.2}$$

The modulo function delivers the least positive residue of a division. Dividing x by m, the modulo function is defined as

$$x \bmod m = x - \left\lfloor \frac{x}{m} \right\rfloor m\,. \tag{8.3}$$

According to the time base and (8.1), the NF signal is constructed by appending the field samples of the active antennas to each other. The resulting time signal is a baseband signal which is desired and similar to Section 7.4. The NF has been calculated on a cylindrical scan surface with a radius of 30 m and a height of 100 m, where a NF time signal exists for every field position on this scan surface. The further processing of the field data is according to the LTM and STM methods. The FIAFTA is again employed to transform the NF to the FF, where currents on a triangular mesh are used as equivalent sources. The

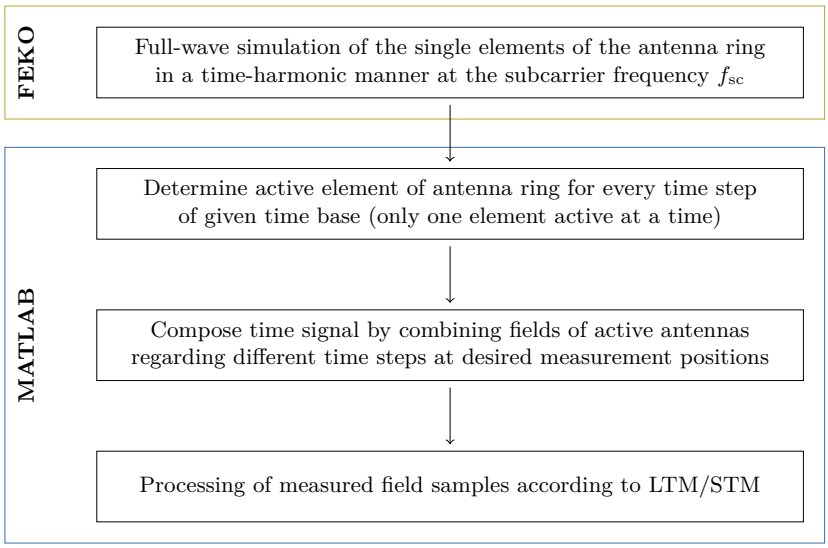

Figure 8.5: Block diagram of the concept for the simulation of the DVOR antenna ring, describing the interaction between the numerical simulations in FEKO and further processing of the field data in MATLAB.

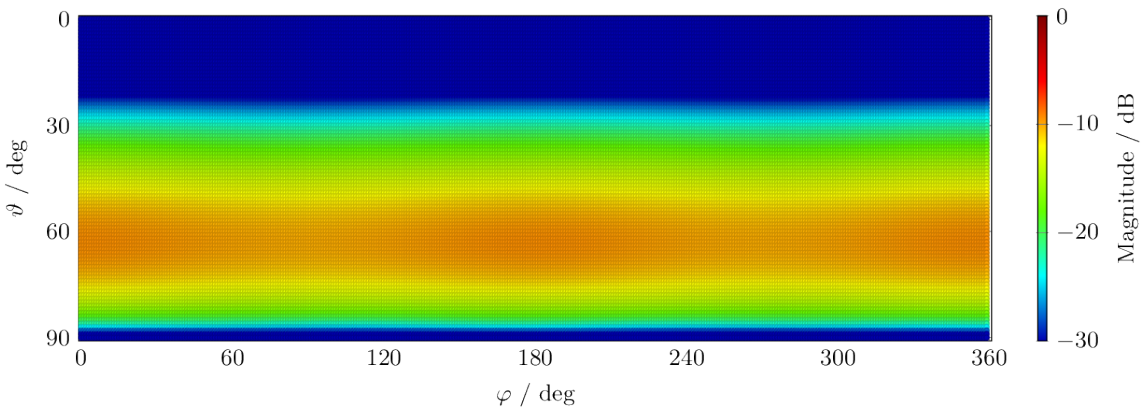

Figure 8.6: Time-harmonic FF radiation pattern of a single ALA of the antenna ring as 2D plot, considering a PEC ground plane.

mesh consist of 48 cylinders that are arranged in a circle as they represent the single elements of the antenna ring.

The time signal of the NF in y-direction at the measurement position $(x, y, z) = (30\,\text{m}, 0\,\text{m}, 73.5\,\text{m})$ is shown in Fig. 8.7 (a) and (b) in amplitude and phase, respectively. The field amplitude is fluctuating since the polarization changes as the radiating element is virtually rotating around the antenna ring. At the same time, the distance of the radiating element to the observation position changes which causes a phase of sinusoidal form. Following the LTM approach, the full time signals are taken, from which spectra for the single measurement positions are calculated by the Fourier transform. Figure 8.8 (a) shows the NF spectrum corresponding to the time signal in Fig. 8.7. After transforming the single spectral lines to the FF, the spectrum can be composed again in the FF where the resulting FF spectrum is depicted in Fig. 8.8 (b), for $(\vartheta, \varphi) = (60°, 0°)$ as this is the direction of the largest field magnitude according

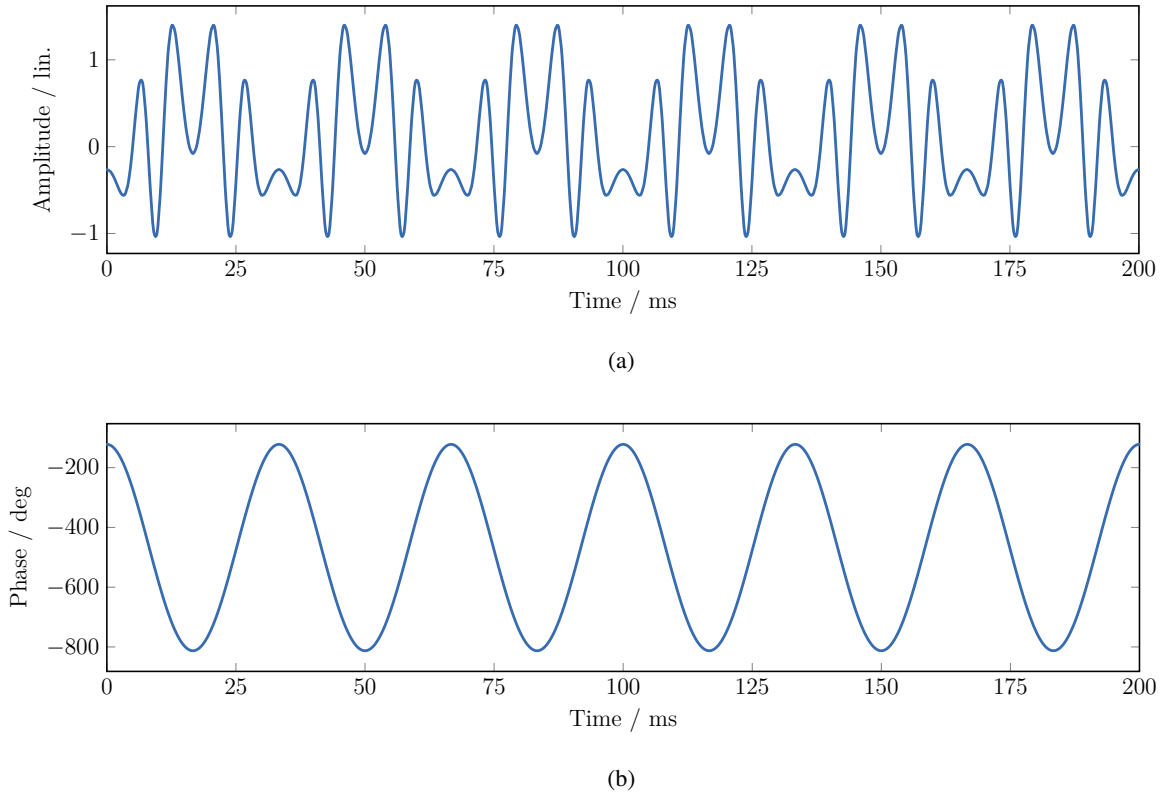

Figure 8.7: NF time signal in amplitude (a) and phase (b) at $(x, y, z) = (30\,\text{m}, 0\,\text{m}, 73.5\,\text{m})$. The position has been chosen to be close to the NF maximum.

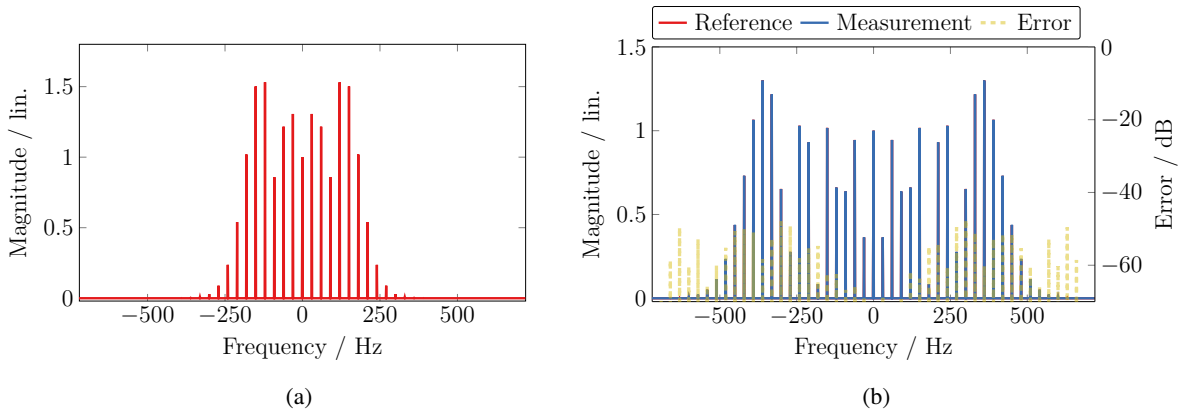

Figure 8.8: Frequency spectrum corresponding to the time signal in Fig. 8.7. The spectrum is given in the NF (a) and FF (b) where the latter is obtained from the NF spectrum with the help of a NFFFT. Also, the FF spectrum is compared to a reference that is directly calculated from the time-harmonic FFs of the single ALAs.

to Fig. 8.6. The FF spectrum is shown in comparison to a reference spectrum which is obtained by Fourier transforming the FF signal that is created in a similar way as described above from the time-harmonic FFs of the single antenna elements in the ring. The error in Fig. 8.8 (b) is calculated with consideration of the phase deviation according to (2.32). The maximum FF error is found to be the accuracy of the simulation as verified separately by the direct NFFFT of the time-harmonic NFs of the

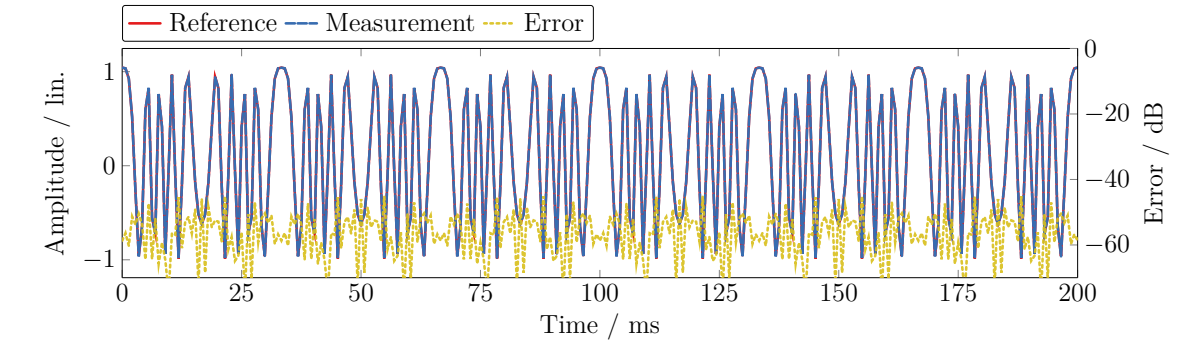

(a)

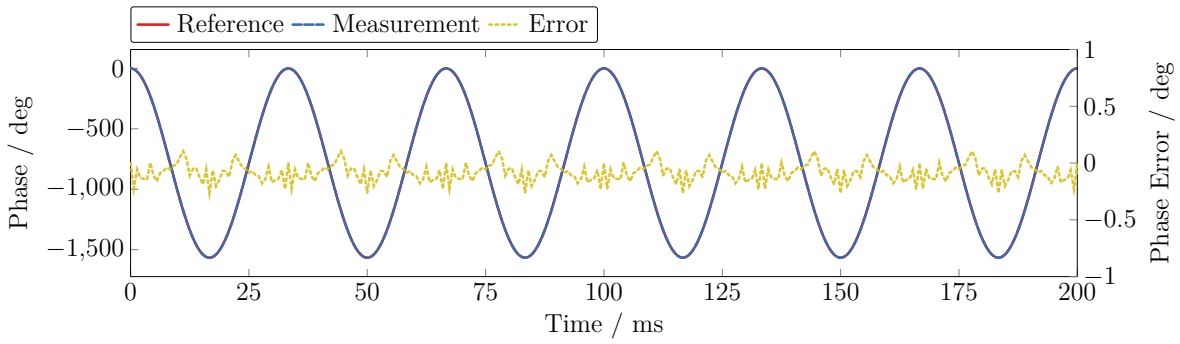

(b)

Figure 8.9: FF time signal in amplitude (a) and phase (b) at $(\vartheta, \varphi) = (60°, 0°)$. The position corresponds to the NF position. The time signal is compared to a reference that is directly calculated from the time-harmonic FFs of the single ALAs and is similar to the reference spectrum.

antennas. Eventually, the time signals in the FF can be calculated from the FF spectra with the help of the inverse Fourier transform. The resulting FF signal in magnitude and phase of the horizontal field component $\boldsymbol{\mathcal{E}}_{\varphi}$ and for $(\vartheta, \varphi) = (60°, 0°)$ is depicted in Figs. 8.9 (a) and (b). The error level, found in the FF spectrum in Fig. 8.8 (b), is also reflected in the time domain. The signal amplitude has the typical form of an FM where the phase is of sinusoidal form. Within the NFFFT, currents on a mesh have been used as equivalent sources which are depicted in Fig. 8.10 for the transformation of a single spectral line. Overall, the simulation shows that the LTM approach is suitable for the measurement and transformation of a DVOR where the modulation signal is preserved and available in the FF. This is a mandatory prerequisite for the validation of such a navigation system.

Besides the LTM, also the STM approach can be used for the NF measurement and transformation of modulated fields as demonstrated for a single horn antenna in Chapter 7. The STM can also be employed for the measurement of the DVOR signals as both modulation signals, the AM as well as the FM, are periodic. Similar as before, the FM signal, arising from the virtually rotating radiator of the antenna ring, has been transformed to the FF using the STM approach. For this, the same concept, model and numerical simulations have been employed where, in fact, the STM was applied to the identical NF signals that have been used for the LTM and are exemplary depicted in Fig. 8.7. The time sampling was chosen in such a way that always only one specific ring antenna was active, i.e., the time between two NF measurements was $1/30\,\mathrm{Hz}$ while the time offset was changed for the measurement of the single antenna ring elements. The resulting FF signal is depicted in Figs. 8.11 (a) and (b) in magnitude and phase, respectively, and for the FF direction of $(\vartheta, \varphi) = (60°, 0°)$. Similar as before, the transformed time signal is compared to a reference signal that is calculated directly from the time-harmonic FF obtained

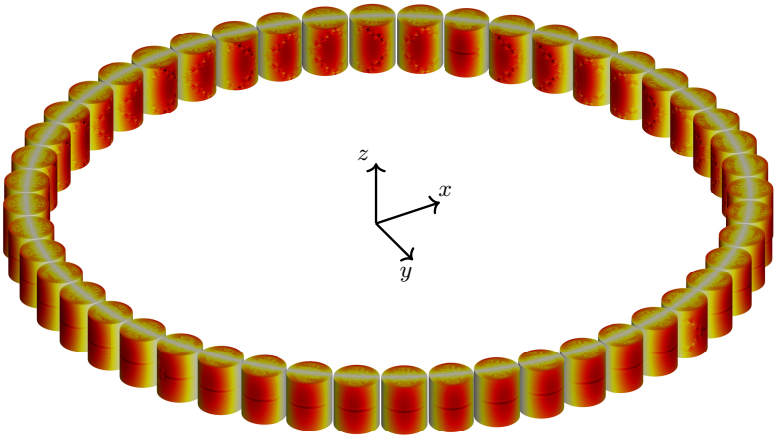

Figure 8.10: Distribution of the equivalent currents on the mesh for the NFFFT of a single spectral line following the LTM approach.

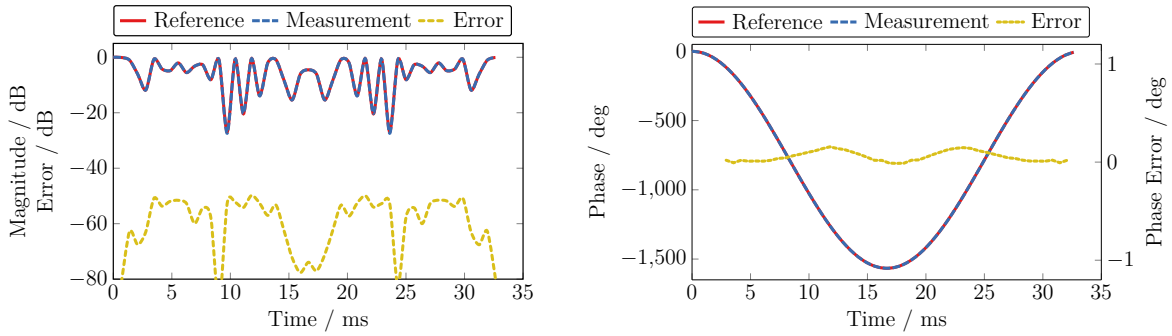

(a) (b)

Figure 8.11: FF time signal in magnitude (a) and phase (b) at $(\vartheta, \varphi) = (60°, 0°)$. The transformed time signal is compared to a reference that is directly calculated from the time-harmonic FFs of the single ALAs according to the STM method.

from the numerical simulations. As expected, the error level is similar as for the LTM which proves that both methods can be equally applied if the time signal needs to be verified in the FF. However, the comparison of the equivalent currents used by the NFFFT within the STM and the LTM reveals a major difference between both approaches. In Fig. 8.10 it was shown that the equivalent currents for the transformation of a single spectral line are distributed over all cylinders of the mesh, i.e., over all elements of the antenna ring. This is a consequence of the fact that one spectral line contains information from the whole duration that is needed for the measurement at one position. In contrast, the equivalent currents used for the NFFFT of a single modulation state within the STM are depicted in Fig. 8.12. Here, it can be easily seen that the currents are concentrated at one single element of the antenna ring. This is a consequence of the fact that, within the STM approach, one modulation state inevitably belongs to one specific antenna element, i.e., if only one modulation state is transformed, only field samples of one single active antenna are considered within the NFFFT. Even if both measurement approaches are equal in terms of resulting time signals, the difference in the equivalent currents is crucial when it comes to antenna diagnostics as the STM approach allows for a finer spatial resolution. This makes the STM the preferred measurement approach for the measurement of navigation systems with spatially distributed

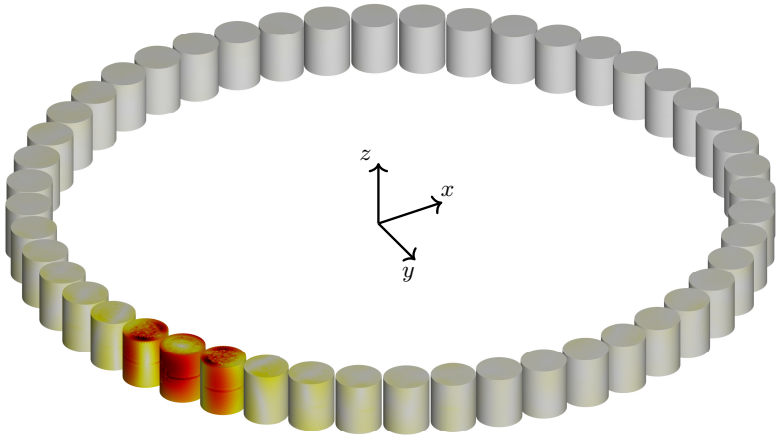

Figure 8.12: Distribution of the equivalent current on the mesh for the NFFFT of a single modulation state line following the STM approach.

radiating elements such as the DVOR.

8.3 Measurement Approach

Following the investigations in Section 8.2, a concept for the measurement of a DVOR can be derived by combining the realization of UAV-based measurements with the STM approach.

First of all and similar to the measurements which have been presented in Chapter 5, the field probe is moved by a UAV around the DVOR. Here, a cylindrical scan geometry is a good choice as it can be easily realized with a UAV, while all relevant field parts are covered in this way due to to the null of the field in vertical direction. If an optical fiber link is used to connect the field probe with a measurement receiver on the ground, a cylindrical measurement geometry does also prevent problems like tangling up the fiber or moving it across the DVOR station as it would be needed, e.g., for a hemispherical scan geometry. However, principally any measurement geometry can be chosen that covers the relevant field parts of the DVOR, especially if the FIAFTA is used as NFFFT since it allows for irregular spatial sampling of the field.

As discussed before, the navigation information of the DVOR can be derived by the comparison of the AM and the FM, while there are additional frequency bands present in the spectrum. Therefore, the AM and FM signals need to be extracted from the spectrum at first. Instead of measuring the full DVOR signal and extracting the navigation information in a second step, the AM and FM signals can be filtered and recorded such that only the relevant parts of the frequency spectrum are measured. This makes the measurement more efficient and can be realized, e.g., by splitting the field probe signal before bandpass filters for the carrier and subcarrier frequencies are applied to measure only the AM, respectively FM. Here, it is important that both signal paths have the same group delay while both signals have to be measured synchronously with two independent channels of a VNA. At the same time, and in addition to the split of the field probe signal, the same signal flow is necessary for a static reference antenna. This reference antenna is necessary to provide a phase reference within the measurement setup since the exciting signal of the DVOR antennas cannot be accessed. The full signal flow together with the usage of a four port VNA is schematically depicted in Fig. 8.13. Within this measurement setup, the phases of the AM and FM signals are preserved for the single spatial directions. This is a mandatory prerequisite for the evaluation of the navigation signal in the FF. Therefore, it is only logical that the

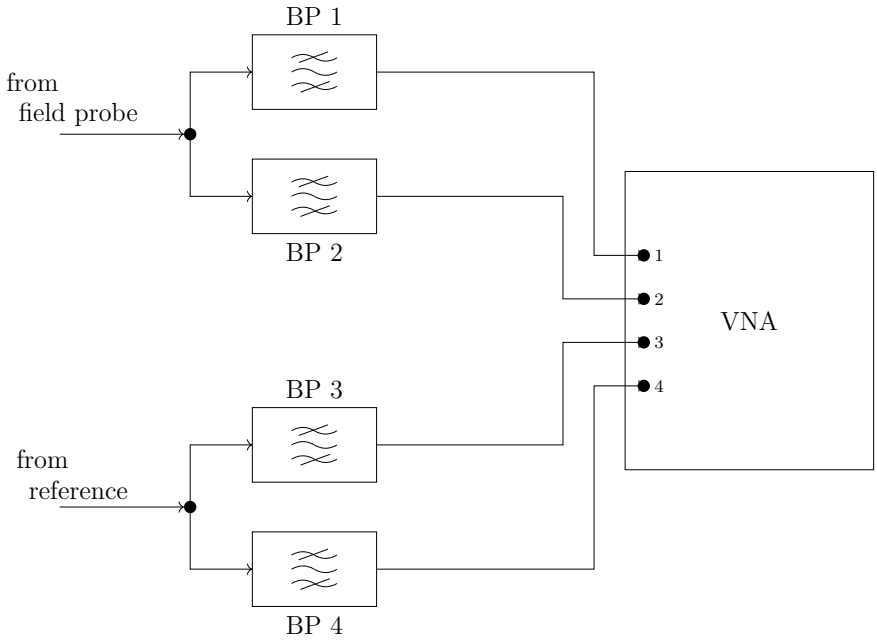

Figure 8.13: Signal flow for the simultaneous measurement of the AM and FM signals of the center antenna and the antenna ring. The signals from both, the field probe as well as from the reference antenna, are splitted, filtered and measured with independent but coupled channels of a VNA.

navigation signal of the DVOR can be determined from the two modulation signals, while it can be verified by the comparison with recorded GNSS positions that can be retrieved directly from the UAV logfiles. Even if the reference signal is primarily necessary as phase reference for the evaluation of the measured NF, it can also be used to sort the measured field samples within the STM approach, similar as in Section 7.5. Overall, a precise and detailed analysis of the DVOR operation state requires the usage of the STM approach.

8.4 Measurement Setup

After the creation of a concept for the measurement of a DVOR, first UAV-based NF measurements have been performed on the DVOR Ottersberg (OTT) to prove the assumptions of the DVOR operation and test the general applicability of the STM. The OTT is located in the municipality Pliening about 30 km east of Munich, Germany where it is, as most of the VORs and DVORs, built in the open country and not surrounded by buildings and other potential scatterers. A picture of the DVOR is shown in Fig. 8.14. In the picture, some of the ring antennas can be seen while the metallic counterweight is prominently dominating. The height of the counterweight above ground is about 5.5 m. The DVOR is surrounded by a fence which prevented a direct and precise measurement of the DVOR dimensions as well as its exact location in the measurement coordinate system. As a workaround, the upper edge of the fence was measured at several positions while a reference position was marked to allow for a synchronization between two measurements on different days. Further, the position of the DVOR was assumed to be the center of the circle formed by the fence. For the field measurements, the UAV was flying around the DVOR on a cylindrical geometry. In contrast to the UAV-based measurements in Chapters 4 and 5, a hexacopter based on the Tarot 680 Pro frame was used. The reason for the exchange of the UAV is that the Tarot 680 Pro is larger than the F550 frame and designed for more payload. It is equipped with

Figure 8.14: Picture of the DVOR Ottersberg where the counterweight or artificial ground plane is prominently visible. The reference antenna is also depicted which was mounted on a stand and served as phase reference for the measurements.

Figure 8.15: UAV including field probe during a measurement flight. A ring dipole antenna served as field probe which was mounted to the front of the UAV, even in front of the front motors.

larger rotors while higher-capacity batteries can be used at the same time which, in turn, increases the flight duration. However, the key electronic components, like flight controller and sensors, are similar to the UAV described in Chapter 4. Hence, the employed Tarot 680 Pro also uses a Pixhawk Cube [PX4 2022] in combination with Ardupilot [ArduPilot 2022]. Also, the companion ground control station is the exact same as for the measurements discussed before.

For the DVOR measurements, a folded ring dipole was employed as field probe. It was mounted to the front of the UAV, where the antenna and the UAV frame cannot considerably be separated, especially regarding the long wavelength of about 2.7 m. Figure 8.15 shows the UAV including the ring dipole during flight. The ring dipole itself has a radius of about 0.55 m and was designed to work in the VHF band. The operation or carrier frequency of the OTT and, hence, the measurement frequency was 112.3 MHz. The antenna is well impedance-matched at this frequency. In addition to the flying part, a second ring dipole, serving as reference antenna, was mounted on a stand about 4.68 m above ground as depicted in the left part of Fig. 8.14. The antenna was placed on a fixed location outside of the

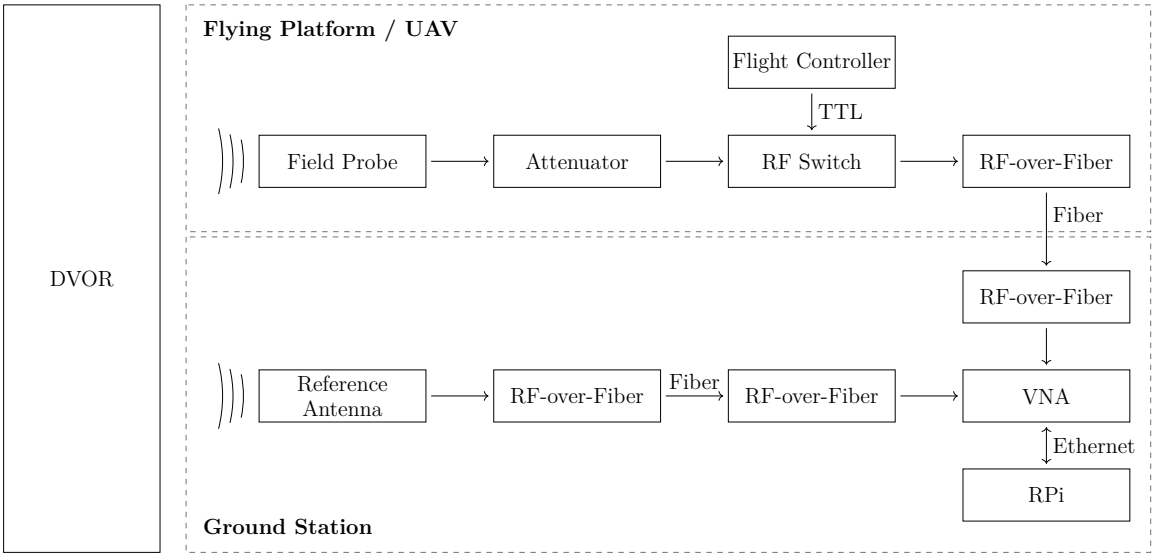

Figure 8.16: RF part of the setup for the measurement of the modulated field signals of a DVOR. The flying and ground parts of the setup used almost the same components, while an attenuation and a switch were inserted on the UAV to cope with the high field values and data synchronization.

measurement plane and not moved during the measurements. In the post-processing, the signal of this antenna was also used for the selection of the measurement samples which can be transformed together to the FF regarding the STM approach. Both, the field probe and reference antenna, were connected via RF-over-fiber links [ViaLiteHD 2020] to a two-port VNA of type R&S ZVK [R&S 2022g] which was employed as measurement receiver. The ZVK itself was working in zerospan mode, which means that no frequency sweep was performed and always the center frequency was measured. The VNA was, further, set up in such a way that it only recorded the incoming *b*-waves of both channels, i.e., the internal generator was not used and no test signal was sent by the VNA. A schematic overview of the RF part of the measurement setup is depicted in Fig. 8.16. Here, it can be seen that the signal path of the field probe on the UAV does include an additional attenuation before the RF-over-fiber converter. This attenuation has been inserted to prevent a distortion of the field signal due to clipping as the DVOR is fed with a power of 75 W which results in comparably large field values. Furthermore, an RF switch was inserted in the signal path of the field probe on the UAV-side. The switch is controlled by the flight controller and enables the time synchronization of the UAV with the ground station as described in Section 4.4.3. This synchronization is especially important for the presented measurement setup since no laser tracker can be used due to the necessary height of the measurement cylinder, which was about 60 m, and the inevitably interruption of the laser link. Thus, only the position data from the RTK system are used which also satisfy the $\lambda/50$-rule by virtue of the larger wavelength in the VHF band.

8.5 Measurement Results

First, the AM signal, transmitted by the center antenna of the DVOR, was investigated. For this, a measurement with the described setup was performed, where the measurement frequency was equal to the DVOR carrier frequency of 112.3 MHz and the RBW was chosen to 1 kHz to filter only the AM. The VNA operated in zerospan mode which means that effectively the modulation signal, radiated by the center antenna, has been measured in the time domain. Figure 8.17 shows the signal received by the field probe on the UAV as well as the field signal received by the static reference antenna on

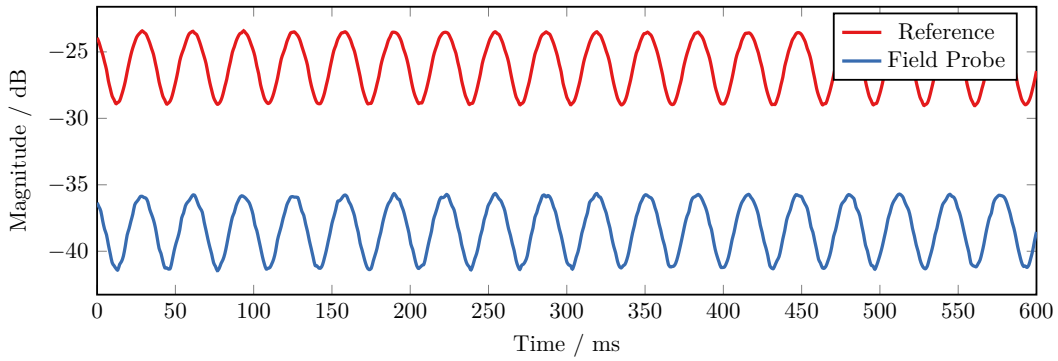

Figure 8.17: Timeline of the DVOR NF signal measured by the flying field probe and static reference antenna in comparison. The VNA was set up in a way that it filtered and recorded only the AM that is radiated by the center antenna.

the ground. Since the internal memory of the VNA is limited, only a certain number of data samples can be recorded in one sweep which resulted in a sweep time of 600 ms regarding the chosen VNA settings. Therefore, the *b*-waves of both channels were simultaneously recorded in "blocks" of 600 ms and transferred to the controlling PC before the next measurement was started. Figure 8.17 shows one of these data blocks where the AM of 30 Hz can be clearly seen. The modulation of both signals, from the field probe and reference antenna, are different in terms of magnitude which is, among others, a consequence of the 20 dB attenuation that is present in the UAV signal path to prevent damage to the measurement equipment due to the large field values radiated by the DVOR. The measured NF is depicted in Fig. 8.18 where the modulation has been dismissed by normalizing the field probe data to the data obtained by the reference antenna. As seen in the figure, only a part of the cylindrical measurement surface has been covered which, of course, limits the valid angles of the resulting FF but is sufficient to check the field distribution of the DVOR and also to check the measurement equipment and the applicability of the measurement approach. Figure 8.18 also shows the measured reference locations of the fence that surrounds the DVOR. Eventually, the NF has been transformed to the FF with the help of the FIAFTA where a PEC ground was assumed. A vertical cut through the FF within the valid angles is shown in Fig. 8.19 (a). The figure shows the comparison of the same FF cut for the NFFFT in which the field probe was assumed to be a Hertzian dipole as well as for the NFFFT in which a probe correction has been performed using the probe pattern. The radiation pattern of the field probe was determined by a numerical simulation of the dipole ring antenna together with a simple model of the UAV due to the fact that the available anechoic chambers and NF systems are not specified for measurements at such low frequencies. Still, the comparison of the two FF cuts demonstrates that a probe correction of the measured field data is important and has an influence on the resulting FF radiation pattern, especially in the upper parts of the measurement cylinder. The measurement of a sector of the cylindrical measurement surface around the DVOR has been performed several times where multiple parameter settings have been tested. Figure 8.19 (b) shows the comparison between two such measurements in terms of a vertical FF cut. Here, both measurements were performed with the same settings of the NFFFT, including probe correction and the consideration of ground. It can be seen that the deviation in the upper parts of the field, closer to 0°, is large which is due to the fact that these parts are clearly beyond the scope of the valid angles. In comparison to the time-harmonic measurements in Part II of this thesis, the deviation between the two DVOR measurements is significantly larger. However, this comparison shall not be drawn since the two measurement situations are largely different and there are several reasons for the deviation of the two measurements. Therefore, no deviation curve is given. Due to the fact that the measurements have to be carried out on-site, the whole measurement

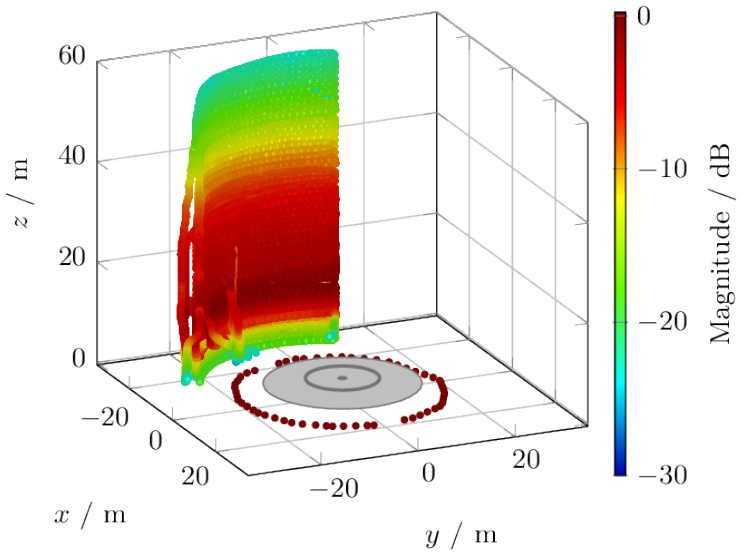

Figure 8.18: Time-harmonic representation of the measured NF as part of a cylindrical measurement geometry. The position of the DVOR is schematically shown as well as the measured reference positions of its surrounding fence.

setup needs to be packed and built up for each measurement campaign, e.g, different days led to different positions of the antennas, corresponding cable lengths and multiple calibrations of the DVOR position. Furthermore, the two depicted vertical cuts show different sectors of the cylindrical scan surface, i.e., different angular ranges in azimuth, and are, therefore, not directly comparable due to the imperfect omnidirectionality of the radiation pattern of the ALA. Still, the measurement of the center antenna reveals that the signal form as well as the radiation pattern are as expected and are, thus, an important preliminary test for the application of the STM approach and for a real measurement campaign in which the field is measured on a full cylinder.

In addition, also the field of the antenna ring has been principally investigated. Most important is the detection of the measurement state for the successful application of the STM. In contrast to the amplitude, the phase of the field signal can only be detected with respect to a reference, i.e., the ratio between the field signals of two antennas needs to be calculated. While, in principle, the modulation states of the antenna ring modulation can be detected from the ratio of the flying field probe and the static reference antenna by some filtering, they may not be precise due to the movement of the UAV. Therefore, a second reference antenna is introduced which is equally mounted on a stand. To fulfill the demands of three input signals, a four port VNA of type R&S ZVA [R&S 2022e] was used as measurement receiver. Similar as before, it was set up in a way such that only the incoming b-waves were measured and the internal generator was turned off. Further, the VNA was measuring in zerospan mode with a center frequency of 112.31 MHz and an RBW of 1 kHz. The result of the measurement is again the time signal that is modulated on the sub-carrier frequency or, here, the modulation signal which is created by the virtually rotating active element. Figure 8.20 shows the phase of the ratio between the two static reference antennas. The rotation or modulation frequency of 30 Hz can be clearly seen. However, it is conspicuous that the phase does not show a clean sinusoidal form as has been found for the AM. This might be primarily an effect of the RBW which needs to be aligned with the measurement frequency and the DVOR spectrum, while some phase variation is also expected to be caused by the used RF-over-fiber links since the investigations in Section 6.2.3 show a large variation of the phase regarding

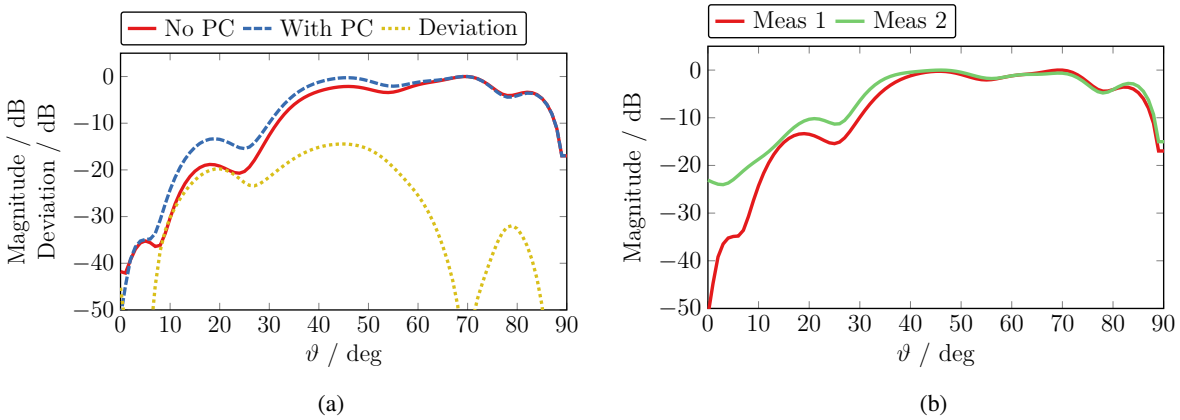

Figure 8.19: Vertical ϑ-cut of the transformed FF pattern as result of the DVOR measurement. The comparison of the NFFFT with and without probe correction (a) reveals the impact of the field probe especially in the upper parts of the cylinder. The similarity of two measurements (b) shows the principle repeatability of the measurement.

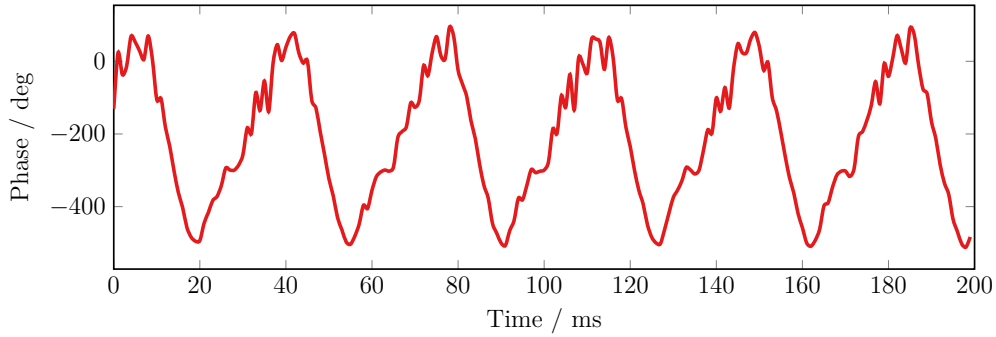

Figure 8.20: Phase of the virtually rotating active element of the antenna ring. The phase has been obtained from the ratio between two static reference antennas and can be used for the extraction of transformable data sets following the STM approach.

environmental influence. Nevertheless, the time signal shows that the STM approach can be principally employed for the measurement of the antenna ring where the tracking of the varying phase allows for the determination of the different modulation states. In view of the measurement results, the overhead of the additional reference antenna is acceptable.

8.6 Chapter Summary

The measurement of the modulated fields of a DVOR has been addressed in this chapter which can also be taken as example for the measurement of other similar NAVAIDs. After reviewing the operation principle of a DVOR, it has been shown with the help of numerical simulations that the LTM as well as the STM methods are suitable for the measurement and transformation of the modulated fields of a DVOR. However, it was also outlined that the STM approach has the advantage that the single elements of the antenna ring can be resolved which makes antenna diagnostics possible. In addition, an implementation of a measurement setup has been presented that allows for the evaluation of the navigation signal if the AM and FM are measured simultaneously. Eventually, measurements showed that the basic assump-

tions about the signal forms are correct and that the detection of the single modulation states within the STM approach is possible. Nonetheless, only principal test measurements have been performed while the measurement of the field on a closed cylindrical surface is still to be done.

Part IV

Finale

Chapter 9

Conclusion and Outlook

In this thesis, UAV-based NF measurements of continuously modulated electromagnetic fields have been addressed. After reviewing some basics of antenna measurement and UAV operation, the realization of coherent UAV-based NF measurements has been demonstrated in the second part of the thesis. The different components of the measurement setup have been described, while it became clear that there are several options of how to look at the measurement setup: it can be divided into an RF and a flight part as well as, on another level, into a flying part in the air and a static part on the ground. The different classifications are useful when comparing the UAV-based setup to traditional antenna measurements or other UAV applications. Also, the interaction between the hardware and software components has been outlined where most of the employed components were of consumer grade. The setup used optical fibers to establish an RF as well as a data connection between the flying platform and the ground station. This is an important step to obtain a common phase reference and, therefore, for the realization of true coherent field measurements. The application of the measurement setup was shown within planar and cylindrical in-situ measurements of a horn antenna. All measurements used spatial oversampling to reduce the field error, where an error level of better than -30 dB was achieved with the presented measurement setup. In addition to the measurements, an analysis of the different error sources within the measurement setup has been performed as this is a prerequisite for the further improvement of UAV-based measurements using similar setups. Accordingly, the single components of the measurement setup have been investigated where corresponding numerical simulations revealed the impact of the different parameters. From this, it has been found that the position accuracy is crucial and the corresponding position measurement system must be chosen accordingly. Yet, this is largely known for NF antenna measurements and, therefore, it comes as no surprise that it also applies to measurements with UAVs. Still, the differences of the UAV-based to the traditional measurement setup requires additional care for some components. Regarding the RF part of the measurement setup, the fiber connection was found to be delicate with a significant impact on the accuracy of the measurement results. Also, from the measurements as well as from the error investigations, it becomes clear that a cylindrical scan surface is desirable for UAV-based field measurements as it significantly lowers the impact of the field probe on the measured field data and also reduces the influence of the rotating rotor blades.

The third part of this thesis concerned the measurement and subsequent NFFFT of continuously modulated fields. Here, two distinct approaches have been introduced where the main difference between both methods is the measurement time at the single measurement positions. The LTM uses a measurement time that is so long that the single frequencies can be distinguished in the frequency spectrum, which allows for an individual transformation to the FF. The STM approach, in contrast, is based on a measurement time that is so short that the modulation can be treated as constant during the measurement interval where effectively only the carrier is measured. Both measurement approaches, LTM and STM, have been discussed in detail and demonstrated by numerical simulations as well as measurements. It has

also been outlined that the STM method is more suitable to be used in combination with UAV-based field measurements as the significantly shorter measurement time reduces the position error that arises from the unceasing movement of the UAV during a measurement. Furthermore, the uncertainties and constraints were investigated in numerical simulations where it has been found that the STM method can be applied without the introduction of any additional error if the measurement radius r fulfills $\|r\| < \lambda_m/20$ and the measurement time and modulation period comply with $T_{meas} \leq 0.1\, T_{mod}$.

Both topics, UAV-based NF measurements as well as the measurement of modulated fields, were eventually combined in the measurement of a DVOR, an air navigation system that is based on continuously modulated fields. In this connection, it has been shown with the help of numerical simulations that the STM also enables antenna diagnostics regarding a modulated and spatially distributed antenna system such as the DVOR since the single radiating elements of the antenna ring can be distinguished, while the occurring position error within UAV-based field measurements is minimized. Even if the general measurement concept allows for the verification of the navigation signal, only test measurements were made which demonstrated that the STM can be applied and the system characterization can be done as intended. The measurement of large antenna systems still suffers from the fact that the flight time of a UAV is limited by its battery capacity and overall mass. However, the vision for UAV-based antenna measurements is a fully autonomous measurement system where the UAV covers a predefined measurement area of interest while it autonomously takes care of the sample density. A real-time evaluation of the NFFFT delivers the FF radiation pattern with increasing valid angle and accuracy. Furthermore, the envisioned system also checks the measured field data for plausibility and automatically re-measures field samples that are suspicious.

As true for any evolving technology, there is lots of room for improvement of UAV-based field measurements. The power supply is clearly a demanding topic as a supply shortage limits the flight time and, with that, the dimensions of the measurement geometry. There are already ideas and experiments with solutions like tethering and combustion engine powered UAVs. Besides the power supply, an optimization of the flight path can help to speed up measurements and even reduce errors. The possible flight height of the cylindrical scan surface can be increased by the usage of a gimbal for the laser tracker target, while the usage of a specifically designed gimbal for the probe antenna would improve the SNR as the main beam of the field probe is illuminated throughout the measurement and as a consequence the rotor influence is lowered. Even more crucial is the implementation of a recurring calibration of the used RF-over-fiber links which is expected to significantly improve the field data in terms of robustness against environmental influences. Such a calibration can be either done in between two measurement flights or even during the actual measurements. Lastly, an extra sensor board for recording the orientation can improve the position accuracy, especially when it is reliably triggered together with the measurement equipment on the ground.

Even if the vision of a fully autonomous UAV-based NF measurement system is not fully realized yet, this thesis has made several important contributions towards a successful implementation as the general applicability of coherent UAV-based NF measurements has been demonstrated, showing that an acceptable error level can be reached. Moreover, the methods for the measurement of modulated fields pave the way for new application areas where UAVs can help with the in-situ characterization of antenna systems.

List of Abbreviations

2D	two-dimensional
3D	three-dimensional
6D	six-dimensional
AD	analog-digital
ALA	Alford loop antenna
AM	amplitude modulation
AUT	antenna under test
BDS	BeiDou navigation satellite system
CATR	compact antenna test range
cp	co-polarized field component
DA	digital-analog
DC	direct current
DGNSS	differential GNSS
DGPS	differential GPS
DVOR	Doppler VHF Omnidirectional Radio Range
EMC	electromagnetic compatibility
EMI	electromagnetic interference
ESC	electronic speed controller
ETH	Ethernet
FC	flight controller
FF	far field
FFT	fast Fourier transform
FGPS	fake GPS
FIAFTA	fast irregular antenna field transformation algorithm
FM	frequency modulation
FT	Fourier transform
GCS	ground control station
GNSS	global navigation satellite system
GPIO	general-purpose input/output
GPS	Global Positioning System
HPBW	half power beam width

ICAO International Civil Aviation Organization
IFT inverse Fourier transform
ILS Instrument Landing System
IMU inertial measurement unit
IO input/output
LIDAR light detection and ranging
LiPo lithium polymer
LO local oscillator
LT laser tracker
LTM long-time measurement
MMR measurement-modulation-ratio
MoM method of moments
NAVAID navigational aid
NF near field
NFFFT near-field to far-field transformation
NIST National Institute of Standards and Technology
OTT DVOR Ottersberg
PC personal computer
PCB printed circuit board
PEC perfect electric conductor
PLF polarization loss factor
PM phase modulation
PSU power supply unit
PWM pulse width modulation
RADAR radio detection and ranging
RBW resolution bandwidth
RF radio frequency
RPi Raspberry Pi
RTK real-time kinematic
RX receiver
SBR sideband ratio
SMA SubMiniature version A
SMR spherically mounted retroreflector
SNR signal-to-noise ratio
STFT short-time Fourier transform
STM short-time measurement
TH time-harmonic
TUM Technical University of Munich
TX transmitter

UAV uncrewed aerial vehicle
UHF ultra high frequency
USB Universal Serial Bus
VHF very high frequency
VNA vector network analyzer
VOR VHF Omnidirectional Radio Range
VSWR voltage standing wave ratio
VTOL vertical take-off and landing
WGS 84 World Geodetic System 1984
xp cross-polarized field component

List of Symbols

Symbol	Unit	Description
Physical quantities		
$\boldsymbol{\mathcal{E}}$	$\mathrm{V\,m^{-1}}$	electric field in time domain
$\boldsymbol{\mathcal{H}}$	$\mathrm{A\,m^{-1}}$	magnetic field in time domain
$\boldsymbol{E}$	$\mathrm{V\,m^{-1}}$	time-harmonic electric field
$\boldsymbol{H}$	$\mathrm{A\,m^{-1}}$	time-harmonic magnetic field
η	Ω	wave impedance
P_{rad}	W	total power radiated
P_{in}	W	input power
$\boldsymbol{S}$	$\mathrm{W\,m^{-2}}$	power density
Z	Ω	impedance
R	Ω	resistance
X	Ω	reactance
I	A	electric current
U	V	voltage
Q	A s	electric charge
ψ	deg	polarization mismatch angle
f	Hz	temporal frequency
ω	$\mathrm{s^{-1}}$	angular frequency
f_0, ω_0	Hz, $\mathrm{s^{-1}}$	carrier frequency
f_{m}, ω_{m}	Hz, $\mathrm{s^{-1}}$	modulation frequency
f_{sc}, ω_{sc}	Hz, $\mathrm{s^{-1}}$	frequency of subcarrier
λ	m	wavelength
k	$\mathrm{m^{-1}}$	wavenumber
Δf	Hz	frequency resolution
RBW	Hz	resolution bandwidth
t, τ	s	time
T	s	signal duration/length
T_{meas}	s	measurement time
T_{mod}	s	modulation period

Symbol	Unit	Description
ΔT	s	time between two adjacent measurement samples
ΔT_{meas}	s	time between two consecutive measurements
v	$\text{m}\,\text{s}^{-1}$	velocity
c	$\text{m}\,\text{s}^{-1}$	speed of light
ε	$\text{A}\,\text{s}\,\text{V}^{-1}\,\text{m}^{-1}$	electric permittivity
μ	$\text{V}\,\text{s}\,\text{A}^{-1}\,\text{m}^{-1}$	magnetic permeability
r, d	m	distance
r_{earth}	m	radius of the earth
r_{min}	m	radius of minimum sphere enclosing AUT
d_{ant}	m	maximum aperture size of antenna
r_{meas}, d_{meas}	m	measurement distance
Δr	m	distance between two measurement positions
lat	deg	latitude (GNSS position)
lon	deg	longitude (GNSS position)
alt	m	altitude (GNSS position)
Vectors		
$\boldsymbol{r}$, $\boldsymbol{p}$		observation position
$\boldsymbol{r}_{\text{lt}} = (x, y, z)$		position in laser tracker coordinate system
$\boldsymbol{r}_{\text{aut}} = (u, v, w)$		position in AUT coordinate system
(u', v', w')		position in UAV coordinate system
(lat, lon, alt)		GNSS position
$\tilde{\boldsymbol{r}}$		position determined from GNSS position, relative to (lat_0, lon_0, alt_0)
Others		
$\boldsymbol{D}$		antenna directivity
$\boldsymbol{G}$		antenna gain
ξ		antenna efficiency
Γ		reflection coefficient
ϵ		deviation between two fields / field error
$\epsilon_{\text{abs/cmplx}}$		deviation between two fields ex-/including phase
σ		standard deviation
$\boldsymbol{M}$		modulation index
m_i		single modulation state
Accents and Operators		
$\hat{\boldsymbol{u}}_{\text{x}}$		unit vector in x-direction

Symbol	Unit	Description
$\overset{*}{\boldsymbol{E}}$		field normalized to its maximum
$\lvert x \rvert$		absolute value of x
$\lfloor x \rfloor$		floor function (see (8.2))
$\mathfrak{R}\,[z]$		real part of z
$\mathcal{F}\,\{s(t)\}$		Fourier transform of $s(t)$
$\mathcal{F}^{-1}\,\{S(f)\}$		inverse Fourier transform of $S(f)$
$\mathcal{H}\{s(t)\}$		Hilbert transform of $s(t)$
$\overline{x}$		mean value
Notation and Functions[1]		
$s(t)$		time-dependent signal
$s_{\mathrm{a}}(t)$		analytic signal
$s_{\mathrm{bb}}(t)$		baseband signal
$m(t)$		modulation signal
$w(t)$		window function

[1]For simplicity, all functions in this list are only noted with a dependence on time while they may also depend on other variables when used in this thesis.

Bibliography

Agilent Technologies (2010), *InfiniiVision 7000B Series Oscilloscopes*, 3rd, 54695-97025, User's Manual.

Airport Systems International (1991), *Operations and Maintenance Manual - Model 1150 Doppler VOR (DVOR) Antenna*, No. 570002-0001, Revised April 1993, Overland Park, KS, USA.

Allen, J. (1977), "Short Term Spectral Analysis, Synthesis, and Modification by Discrete Fourier Transform", *IEEE Transactions on Acoustics, Speech, and Signal Processing*, vol. 25, no. 3, pp. 235–238, DOI: 10.1109/TASSP.1977.1162950.

Altair (2022), *Altair HyperWorks FEKO 2017.2*, URL: https://www.altair.com/feko (visited on July 9, 2022).

Álvarez-Narciandi, G., J. Laviada, Y. Álvarez-López, G. Ducournau, C. Luxey, C. Belem-Goncalves, F. Gianesello, N. Nachabe, C. D. Rio, and F. Las-Heras Andrés (2021), "Freehand System for Antenna Diagnosis Based on Amplitude-Only Data", *IEEE Transactions on Antennas and Propagation*, vol. 69, no. 8, pp. 4988–4998, DOI: 10.1109/TAP.2021.3060082.

ArduPilot (2022), *ArduPilot, Open Source Drone Software. Versatile, Trusted, Open.* URL: https://ardupilot.org/ (visited on Feb. 12, 2022).

Azhar, A. and T. F. Eibert (2021), "A Dual-Polarized Tapered Slot Antenna for UAV-Based Collection of Locally Coherent Field Data", *15th European Conference on Antennas and Propagation (EuCAP)*, Düsseldorf, Germany, pp. 1–4, DOI: 10.23919/EuCAP51087.2021.9411166.

Balanis, C. A. (1992), "Antenna Theory: A Review", *Proceedings of the IEEE*, vol. 80, no. 1, pp. 7–23, DOI: 10.1109/5.119564.

Balanis, C. A. (2005), *Antenna Theory - Analysis and Design*, Third Edition, Hoboken, NJ, USA: John Wiley & Sons.

Balanis, C. A. (2012), *Advanced Engineering Electromagnetics*, Second Edition, Hoboken, NJ, USA: John Wiley & Sons,

Barnes, C. (1963), *Full-Scale HF Antenna Pattern Measurements Made With Transmitter Towed by Aircraft*, research rep., Menlo Park, California: Stanford Research Institute.

Bolli, P., G. Pupillo, F. Paonessa, G. Virone, S. J. Wijnholds, and A. M. Lingua (2018), "Near-Field Experimental Verification of the EM Models for the LOFAR Radio Telescope", *IEEE Antennas and Wireless Propagation Letters*, vol. 17, no. 4, pp. 613–616, DOI: 10.1109/LAWP.2018.2805999.

Brittain, J. E. (2004), "Electrical Engineering Hall of Fame: Guglielmo Marconi", *Proceedings of the IEEE*, vol. 92, no. 9, pp. 1501–1504, DOI: 10.1109/JPROC.2004.832946.

Bronstein, I. N., K. A. Semendjajew, G. Musiol, and H. Mühlig (2012), *Taschenbuch der Mathematik*, vol. 8, Wissenschaftlicher Verlag Harri Deutsch.

Chang, C., C. Monstein, A. Refregier, A. Amara, A. Glauser, and S. Casura (2015), "Beam Calibration of Radio Telescopes with Drones", *Publications of the Astronomical Society of the Pacific*, vol. 127, no. 957, pp. 1131–1143, DOI: 10.1086/683467.

Chen, V. C., F. Li, S. Ho, and H. Wechsler (2006), "Micro-Doppler Effect in Radar: Phenomenon, Model, and Simulation Study", *IEEE Transactions on Aerospace and Electronic Systems*, vol. 42, no. 1, pp. 2–21, DOI: 10.1109/TAES.2006.1603402.

CST (2020), *CST Microwave Studio 2019*, URL: https://www.cst.com/products/cstmws (visited on Jan. 11, 2020).

Culotta-López, C., S. Gregson, A. Buchi, C. Rizzo, D. Trifon, S. Skeidsvoll, I. Barbary, and J. Espeland (2021), "On the Uncertainty Sources of Drone-Based Outdoor Far-Field Antenna Measurements", *43rd Annual Symposium of the Antenna Measurement Techniques Association (AMTA)*, pp. 1–6, DOI: 10.23919/AMTA52830.2021.9620638.

Defense Mapping Agency Washington DC (1991), *Department of Defense World Geodetic System 1984, Its Definition and Relationships with Local Geodetic Systems*, tech. rep., version 2, Department of Defense, p. 169.

Demule, H. and K. Theißen (2018), "Using UAV Multicopters as an Extension of ILS Ground Measurements: This Innovative Idea has Already Become Reality in Switzerland!", *International Flight Inspection Symposium* (Monterey, California).

DJI (2022), *Flame Wheel ARF Kit*, URL: https://www.dji.com/de/flame-wheel-arf/spec (visited on Feb. 12, 2022).

Du, G.-X., Q. Quan, and K.-Y. Cai (2015), "Controllability Analysis and Degraded Control for a Class of Hexacopters Subject to Rotor Failures", *Journal of Intelligent and Robotic Systems*, vol. 78, pp. 143–157, DOI: 10.1007/s10846-014-0103-0.

Eibert, T., T. Fritzel, C. Schmidt, and H.-J. Steiner (2013), "Method and Device for Measuring a Radiation Field", US8 410 987 B2 (United States).

Eibert, T. F., Ismatullah, E. Kaliyaperumal, and C. H. Schmidt (2010), "Inverse Equivalent Surface Current Method with Hierarchical Higher Order Basis Functions, Full Probe Correction and Multilevel Fast Multipole Acceleration (Invited Paper)", *Progress In Electromagnetics Research*, vol. 106, pp. 377–394, DOI: 10.2528/PIER10061604.

Eibert, T. F., E. Kilic, C. Lopez, R. A. M. Mauermayer, O. Neitz, and G. Schnattinger (2015), "Electromagnetic Field Transformations for Measurements and Simulations (Invited Paper)", *Progress In Electromagnetics Research*, vol. 151, pp. 127–150, DOI: 10.2528/PIER14121105.

Eibert, T. F. and R. A. M. Mauermayer (2018), "Equivalent Sources Based Near-field Far-field Transformation Above Dielectric Half Space", *Proc. 40th Annual Meeting and Symposium of the Antenna Measurement Techniques Association (AMTA)*, Williamsburg, VA.

Eibert, T. F. and C. H. Schmidt (2009), "Multilevel Fast Multipole Accelerated Inverse Equivalent Current Method Employing Rao–Wilton–Glisson Discretization of Electric and Magnetic Surface Currents", *IEEE Transactions on Antennas and Propagation*, vol. 57, no. 4, pp. 1178–1185, DOI: 10.1109/TAP.2009.2015828.

Engel, M., A. Heinzel, E. Schreiber, S. Dill, and M. Peichl (2021), "Recent Results of a UAV-based Synthetic Aperture Radar for Remote Sensing Applications", *13th European Conference on Synthetic Aperture Radar (EUSAR)*, pp. 1–5.

FARO (2013), *Datasheet - FARO Vantage Features, Benefits & and Technical Specifications*.

FARO (2016), *FARO Laser Tracker Vantage Benutzerhandbuch*, 3rd ed.

Faul, F. T., J. Daubmeier, and T. F. Eibert (2021a), "Short-Time Measurement and Transformation of Continuously Modulated Time-Harmonic Fields", *Kleinheubacher Tagung*, Miltenberg, Germany, DOI: 10.23919/IEEECONF54431.2021.9598410.

Faul, F. T., J. Daubmeier, and T. F. Eibert (2023), "Measurement and Transformation of Continuously Modulated Fields Using a Short-Time Measurement Approach", *Advances in Radio Science*, vol. 20, pp. 9–15, DOI: 10.5194/ars-20-9-2023.

Faul, F. T. and T. F. Eibert (2021), "Errors and Prerequisites of the Short-Time Measurement and Transformation of Continuously Modulated Fields", *43rd Annual Symposium of the Antenna Measurement Techniques Association (AMTA)*, DOI: 10.23919/AMTA52830.2021.9620725.

Faul, F. T., J. Kornprobst, T. Fritzel, H.-J. Steiner, R. Strauß, A. Weiß, R. Geise, and T. F. Eibert (2019), "Near-field Measurement of Continuously Modulated Fields Employing the Time-harmonic Near- to

Far-field Transformation", *Advances in Radio Science*, vol. 17, pp. 83–89, DOI: 10.5194/ars-17-83-2019.

Faul, F. T., D. Korthauer, and T. F. Eibert (2021b), "Impact of Rotor Blade Rotation of UAVs on Electromagnetic Field Measurements", *IEEE Transactions on Instrumentation and Measurement*, vol. 70, pp. 1–9, DOI: 10.1109/TIM.2021.3109354.

Faul, F. T., D. Korthauer, and T. F. Eibert (2021c), "Impact of the Rotor Blade Rotation of a UAV on an Installed Field Probing Antenna", *XXXIV URSI General Assembly and Scientific Symposium (URSI GASS)*, Rome, Italy, DOI: 10.23919/URSIGASS51995.2021.9560501.

Faul, F. T., H.-J. Steiner, and T. F. Eibert (2020), "Near-Field Antenna Measurements with Manual Collection of the Measurement Samples", *Advances in Radio Science*, vol. 18, pp. 17–22, DOI: 10.5194/ars-18-17-2020.

Friis, Harald T. (1946), "A Note on a Simple Transmission Formula", *Proceedings of the IRE*, vol. 34, no. 5, pp. 254–256, DOI: 10.1109/JRPROC.1946.234568.

Fritzel, T., H.-J. Steiner, J. Hartmann, and J. Habersack (2002), "Revolutionary New Outdoor Testing with a Mobile Airborne Nearfield Test Facility (ANTF)", *24th Annual Symposium of the Antenna Measurement Techniques Association (AMTA)* (2002), Cleveland, Ohio.

Fritzel, T., H.-J. Steiner, and R. Strauß (2019), "Advances in the Development of an Industrial UAV for Large-Scale Near-Field Antenna Measurements", *13th European Conference on Antennas and Propagation (EuCAP)*, pp. 1–3.

Fritzel, T., R. Strauß, H. Steiner, C. Eisner, and T. Eibert (2016), "Introduction into an UAV-based Nearfield System for In-situ and Large-scale Antenna Measurements (Invited paper)", *IEEE Conference on Antenna Measurements Applications (CAMA)*, pp. 1–3, DOI: 10.1109/CAMA.2016.7815762.

García-Fernández, M., Y. Álvarez López, A. Arboleya, B. González-Valdés, Y. Rodríguez-Vaqueiro, M. E. De Cos Gómez, and F. Las-Heras Andrés (2017), "Antenna Diagnostics and Characterization Using Unmanned Aerial Vehicles", *IEEE Access*, vol. 5, pp. 23563–23575, DOI: 10.1109/ACCESS.2017.2754985.

García-Fernández, M., Y. Álvarez López, and F. Las-Heras Andrés (2018a), "Evaluation of an Unmanned Aerial System for Antenna Diagnostics and Characterization", *12th European Conference on Antennas and Propagation (EuCAP)*, pp. 1–5, DOI: 10.1049/cp.2018.0899.

García-Fernández, M., Y. Álvarez López, and F. Las-Heras Andrés (2018b), "On the Use of Unmanned Aerial Vehicles for Antenna and Coverage Diagnostics in Mobile Networks", *IEEE Communications Magazine*, vol. 56, no. 7, pp. 72–78, DOI: 10.1109/MCOM.2018.1700991.

García-Fernández, M., Y. Álvarez López, and F. Las-Heras Andrés (2019a), "Advances in Antenna Measurement and Characterization Using Unmanned Aerial Vehicles", *13th European Conference on Antennas and Propagation (EuCAP)*, pp. 1–5.

García-Fernández, M., Y. Álvarez López, and F. Las-Heras Andrés (2019b), "Unmanned Aerial System for Antenna Measurement and Diagnosis: Evaluation and Testing", *IET Microwaves, Antennas Propagation*, vol. 13, no. 13, pp. 2224–2231, DOI: 10.1049/iet-map.2018.6167.

García-Fernández, M., G. Álvarez Narciandi, A. Arboleya, C. Vázquez Antuña, F. Las-Heras Andrés, and Y. Álvarez López (2021), "Development of an Airborne-Based GPR System for Landmine and IED Detection: Antenna Analysis and Intercomparison", *IEEE Access*, vol. 9, pp. 127382–127396, DOI: 10.1109/ACCESS.2021.3112058.

Geise, A., O. Neitz, J. Migl, H.-J. Steiner, T. Fritzel, C. Hunscher, and T. F. Eibert (2019), "A Crane Based Portable Antenna Measurement System — System Description and Validation", *IEEE Transactions on Antennas and Propagation*, vol. 67 (5), pp. 3346–3357, DOI: 10.1109/TAP.2019.2900373.

Girod, B., R. Rabenstein, and A. Stenger (2001), *Signals and Systems*, Chichester, United Kingdom: John Wiley & Sons.

Hansen, J. E., ed. (2008), *Spherical Near-Field Antenna Measurements*, Second Edition, Electromagnetic waves series, London, United Kingdom: The Institution of Engineering and Technology.

Hansen, T. B. and A. D. Yaghjian (1995), "Formulation of Probe-corrected Planar Near-field Scanning in the Time Domain", *IEEE Transactions on Antennas and Propagation*, vol. 43, no. 6, pp. 569–584, DOI: 10.1109/8.387172.

Helfrick, A. (2007), *Principles of Avionics*, Fourth Edition, Leesburg, VA, USA: Avionics Communications Inc.

Hindman, G. and A. C. Newell (2006), "Simplified Spherical Near-field Accuracy Assessment", *Annual Symposium of the Antenna Measurement Techniques Association (AMTA)*.

Hoffmann, R. (2005), *Grundlagen der Frequenzanalyse*, Renningen, Germany: expert Verlag.

Hohensinn, Roland, Raphael Stauffer, Marcus Franz Glaner, Iván Darío Herrera Pinzón, Elie Vuadens, Yara Rossi, John Clinton, and Markus Rothacher (2022), "Low-Cost GNSS and Real-Time PPP: Assessing the Precision of the u-blox ZED-F9P for Kinematic Monitoring Applications", *Remote Sensing*, vol. 14, no. 20, DOI: 10.3390/rs14205100.

IEEE (1969), *IEEE Standard Definitions of Terms for Antennas*, DOI: 10.1109/TAP.1969.1139442.

IEEE (2012), *IEEE Std 1720-2012 – Recommended Practice for Near-Field Antenna Measurements*, DOI: 10.1109/IEEESTD.2012.6375745.

IEEE (2014), *IEEE Standard for Definitions of Terms for Antennas*, DOI: 10.1109/IEEESTD.2014.6758443.

International Civil Aviation Organization (ICAO) (2000), *Manual on Testing of Radio Navigation Aids, Testing of Ground-based Radio Navigation Systems*, Volume I, Fourth Edition.

Joy, E. and D. Paris (1972), "Spatial Sampling and Filtering in Near-field Measurements", *IEEE Transactions on Antennas and Propagation*, vol. 20, no. 3, pp. 253–261, DOI: 10.1109/TAP.1972.1140193.

Joy, E. B. (1988), "A Brief History of the Development of the Near-field Measurement Technique at the Georgia Institute of Technology", *IEEE Transactions on Antennas and Propagation*, vol. 36, no. 6, pp. 740–745, DOI: 10.1109/8.1175.

Kemper, M. and S. Fatikow (2006), "Impact of the Center of Gravity in Quadrotor Helicopter Controller Design", *Proceedings IFAC Symposium on Mechatronic Systems*, vol. 39, 16, pp. 157–162, DOI: 10.3182/20060912-3-DE-2911.00030.

Khristenko, A. V., M. O. Konovalenko, M. E. Rovkin, V. A. Khlusov, A. V. Marchenko, A. A. Sutulin, and N. D. Malyutin (2018), "Magnitude and Spectrum of Electromagnetic Wave Scattered by Small Quadcopter in X -Band", *IEEE Transactions on Antennas and Propagation*, vol. 66, no. 4, pp. 1977–1984, DOI: 10.1109/TAP.2018.2800640.

Klaer, P., A. Huang, P. Sévigny, S. Rajan, S. Pant, P. Patnaik, and B. Balaji (2020), "An Investigation of Rotary Drone HERM Line Spectrum under Manoeuvering Conditions", *Sensors*, vol. 20, no. 20, DOI: 10.3390/s20205940.

Kraus, J. (1985), "Antennas since Hertz and Marconi", *IEEE Transactions on Antennas and Propagation*, vol. 33, no. 2, pp. 131–137, DOI: 10.1109/TAP.1985.1143550.

Landau, H., X. Chen, S. Klose, R. Leandro, and U. Vollath (2009), "Trimble's RTK and DGPS Solutions in Comparison with Precise Point Positioning", *Observing our Changing Earth*, ed. by Michael G. Sideris, Berlin, Heidelberg: Springer Berlin Heidelberg, pp. 709–718.

Magnussen, Ø., G. Hovland, and M. Ottestad (2014), "Multicopter UAV Design Optimization", *IEEE/ASME 10th International Conference on Mechatronic and Embedded Systems and Applications (MESA)*, pp. 1–6, DOI: 10.1109/MESA.2014.6935598.

Mahony, R., V. Kumar, and P. Corke (2012), "Multirotor Aerial Vehicles: Modeling, Estimation, and Control of Quadrotor", *IEEE Robotics & Automation Magazine*, vol. 19, no. 3, pp. 20–32, DOI: 10.1109/MRA.2012.2206474.

MathWorks (2022), *MATLAB*, URL: https://www.mathworks.com/products/matlab.html (visited on June 20, 2022).

Mauermayer, R. A. M. and T. F. Eibert (2018), "Spherical Field Transformation Above Perfectly Electrically Conducting Ground Planes", *IEEE Transactions on Antennas and Propagation*, vol. 66, no. 3, pp. 1465–1478, DOI: 10.1109/TAP.2018.2794406.

Moritz, H. (2000), "Geodetic Reference System 1980", *Journal of Geodesy*, vol. 74, no. 1, pp. 128–133, DOI: 10.1007/s001900050278.

Nearfield Systems Incorporated (NSI) (2008), *NSI-SC-5635 Rotation Stage, Positioners*.

Nearfield Systems Incorporated (NSI) (2011), *NSI-700S-50 Spherical Near-field Measurement System*.

Nearfield Systems Incorporated (NSI) (2014), *NSI-300V-8x8 Vertical Planar Near-field Measurement System, Vertical Planar*.

Neipp, C., A. Hernández, J. J. Rodes, A. Márquez, T. Beléndez, and A. Beléndez (2003), "An Analysis of the Classical Doppler Effect", *European Journal of Physics*, vol. 24, no. 5, pp. 497–505, DOI: 10.1088/0143-0807/24/5/306.

Newell, A. C. (1988), "Error Analysis Techniques for Planar Near-field Measurements", *IEEE Transactions on Antennas and Propagation*, vol. 36, no. 6, pp. 754–768, DOI: 10.1109/8.1177.

Newell, A. C. and D. Lee (2000), "Application of the NIST 18 Term Error Model to Cylindrical Near-Field Antenna Measurements", *Annual Symposium of the Antenna Measurement Techniques Association (AMTA)*.

Nguyen, Nang Van and Wonjae Cho (2023), "Performance Evaluation of a Typical Low-Cost Multi-Frequency Multi-GNSS Device for Positioning and Navigation in Agriculture – Part 2: Dynamic Testing", *AgriEngineering*, vol. 5, no. 1, pp. 127–140, DOI: 10.3390/agriengineering5010008.

Nguyen, Nang Van, Wonjae Cho, and Kazunobu Hayashi (2021), "Performance Evaluation of a Typical Low-cost Multi-frequency Multi-GNSS Device for Positioning and Navigation in Agriculture – Part 1: Static Testing", *Smart Agricultural Technology*, vol. 1, p. 100004, DOI: 10.1016/j.atech.2021.100004.

NXP Semiconductors (2014), *Product Data Sheet: SA630, Single-Pole Double-Throw (SPDT) Switch*, version 3.

Oetting, C.-C. and L. Klinkenbusch (2005), "Near-to-far-field Transformation by a Time-domain Spherical-multipole Analysis", *IEEE Transactions on Antennas and Propagation*, vol. 53, no. 6, pp. 2054–2063, DOI: 10.1109/TAP.2005.848465.

Oliveira Costa, D. de, N. M. F. Oliveira, and R. d'Amore (2020), "The Feasibility of Remotely Piloted Aircrafts for VOR Flight Inspection", *Sensors*, vol. 20, no. 7, DOI: 10.3390/s20071947.

Paonessa, F., G. Virone, L. Ciorba, G. Addamo, M. Lumia, G. Dassano, M. Zannoni, C. Franceschet, and O. A. Peverini (2020), "Design and Verification of a Q-Band Test-Source for UAV-Based Radiation Pattern Measurements", *IEEE Transactions on Instrumentation and Measurement*, pp. 1–1, DOI: 10.1109/TIM.2020.3031127.

Paonessa, F. et al. (2016), "VHF/UHF Antenna Pattern Measurement with Unmanned Aerial Vehicles", *IEEE Metrology for Aerospace (MetroAeroSpace)*, pp. 87–91, DOI: 10.1109/MetroAeroSpace.2016.7573191.

Papoulis, A. and S. U. Pillai (2002), *Probability, Random Variables, and Stochastic Processes*, Fourth Edition, New York, USA: McGraw-Hill.

Parini, C., S. Gregson, J. McCormick, D. Janse van Rensburg, and T. Eibert (2020a), *Theory and Practice of Modern Antenna Range Measurements*, Second Edition, vol. 1, Stevenage, United Kingdom: The Institution of Engineering and Technology.

Parini, C., S. Gregson, J. McCormick, D. Janse van Rensburg, and T. Eibert (2020b), *Theory and Practice of Modern Antenna Range Measurements*, Second Edition, vol. 2, Stevenage, United Kingdom: The Institution of Engineering and Technology.

Paulus, A. (2016), "A Comprehensive Error Prediction Model for Near-Field Antenna Measurements", Master's Thesis, München: Technische Universität München.

Pavković, D., M. Krznar, M. Cipek, D. Zorc, and M. Trstenjak (2020), "Internal Combustion Engine Control System Design Suitable for Hybrid Propulsion Applications", *International Conference on Unmanned Aircraft Systems (ICUAS)*, pp. 1614–1619, DOI: 10.1109/ICUAS48674.2020.9214002.

Peters, J. (1967), *Einführung in die allgemeine Informationstheorie*, First Edition, Heidelberg, Germany: Springer, 266 pp., DOI: 10.1007/978-3-642-86500-8.

PNI (2022), *RM3100 Geomagnetic Sensor*, URL: https://www.pnicorp.com/rm3100/ (visited on Feb. 12, 2022).

Powell, J. (1981), *Aircraft Radio Systems*, London, United Kingdom: Pitman.

Punzet, S., F. T. Faul, T. Mittereder, C. Oettl, M. Ganser, M. Häusler, and T. F. Eibert (2022), "Fully Coherent UAV-based Near-Field Measurement and Transformation of the S67-15m Ground Station Antenna at the German Space Operations Center in Weilheim", *16th European Conference on Antennas and Propagation (EuCAP)*, Madrid, Spain, pp. 1–5, DOI: 10.23919/EuCAP53622.2022.9769018.

PX4 Autopilot (2022), *Hex Cube Black Flight Controller*, URL: https://docs.px4.io/main/en/flight_controller/pixhawk-2.html (visited on Feb. 12, 2022).

Quan, Q. (2017), *Introduction to Multicopter Design and Control*, Singapore: Springer Nature, DOI: 10.1007/978-981-10-3382-7.

Qureshi, M. A. (2013a), "Near-Field Error Analysis and Efficient Sampling Techniques for the Fast Irregular Antenna Field Transformation Algorithm", Dissertation, München: Technische Universität München.

Qureshi, M. A., C. H. Schmidt, and T. F. Eibert (2013b), "Efficient Near-Field Far-Field Transformation for Nonredundant Sampling Representation on Arbitrary Surfaces in Near-Field Antenna Measurements", *IEEE Transactions on Antennas and Propagation*, vol. 61, no. 4, pp. 2025–2033, DOI: 10.1109/TAP.2012.2231932.

Qureshi, M. A., C. H. Schmidt, and T. F. Eibert (2013c), "Near-Field Error Analysis for Arbitrary Scanning Grids Using Fast Irregular Antenna Field Transformation Algorithm", *Progress In Electromagnetics Research B*, vol. 48, pp. 197–220, DOI: 10.2528/pierb12121502.

Rahman, S. and D. A. Robertson (2018), "Radar Micro-Doppler Signatures of Drones and Birds at K-band and W-band", *Scientific Reports*, vol. 8, no. 17396, pp. 2045–2322, DOI: 10.1038/s41598-018-35880-9.

Regoli, L. H., M. B. Moldwin, M. Pellioni, B. Bronner, K. Hite, A. Sheinker, and B. M. Ponder (2018), "Investigation of a Low-cost Magneto-inductive Magnetometer for Space Science Applications", *Geoscientific Instrumentation, Methods and Data Systems*, vol. 7, no. 1, pp. 129–142, DOI: 10.5194/gi-7-129-2018.

RFSpin (2013), *Double Ridged Broadband Horn Antenna DRH400*.

Ritchie, M., F. Fioranelli, H. Griffiths, and B. Torvik (2015), "Micro-drone RCS Analysis", *IEEE Radar Conference*, pp. 452–456, DOI: 10.1109/RadarConf.2015.7411926.

Rizwan, A., D. Biswas, and V. Ramachandra (2017), "Impact of UAV Structure on Antenna Radiation Patterns at Different Frequencies", *IEEE International Conference on Antenna Innovations Modern Technologies for Ground, Aircraft and Satellite Applications (iAIM)*, pp. 1–5, DOI: 10.1109/IAIM.2017.8402597.

Rohde & Schwarz (2022a), *R&S FSIQ Signal Analyzer*, URL: https://www.rohde-schwarz.com/product/fsiq-productstartpage_63493-9479.html (visited on Feb. 12, 2022).

Rohde & Schwarz (2022b), *R&S HF906 Antenna*, URL: https://www.rohde-schwarz.com/product/hf906-productstartpage_63493-9337.html (visited on Feb. 12, 2022).

Rohde & Schwarz (2022c), *R&S SMC100A Signal Generator*, URL: https://www.rohde-schwarz.com/products/test-and-measurement/analog-signal-generators/rs-smc100a-signal-generator_63493-10181.html (visited on Sept. 15, 2022).

Rohde & Schwarz (2022d), *R&S SMIQ Vector Signal Generator*, URL: https://www.rohde-schwarz.com/product/smiq-productstartpage_63493-7561.html (visited on Feb. 12, 2022).

Rohde & Schwarz (2022e), *R&S ZVA Vector Network Analyzer*, URL: https://www.rohde-schwarz.com/products/test-and-measurement/network-analyzers/rs-zva-vector-network-analyzer_63493-9660.html (visited on Feb. 12, 2022).

Rohde & Schwarz (2022f), *R&S ZVL Vector Network Analyzers*, URL: https://www.rohde-schwarz.com/products/test-and-measurement/network-analyzers/rs-zvl-vector-network-analyzer_63493-9014.html (visited on Feb. 12, 2022).

Rohde & Schwarz (2022g), *R&S ZVx Vector Network Analyzer Family*, URL: https://www.rohde-schwarz.com/cz/product/zvx-productstartpage_63493-8172.html (visited on May 29, 2022).

Rupprecht, W. (1993), *Signale und Übertragungssysteme, Modelle und Verfahren für die Informationstechnik*, Springer-Verlag Berlin Heidelberg, DOI: 10.1007/978-3-642-95711-6.

Schrader, T., J. Bredemeyer, M. Mihalachi, J. Rohde, and T. Kleine-Ostmann (2016), "Concept and Design of a UAS-based Platform for Measurements of RF Signal-in-space", *Advances in Radio Science*, vol. 14, pp. 1–9, DOI: 10.5194/ars-14-1-2016.

Schrader, T., J. Bredemeyer, M. Mihalachi, D. Ulm, T. Kleine-Ostmann, C. Stupperich, S. Sandmann, and H. Garbe (2019), "High-resolution Signal-in-space Measurements of VHF Omnidirectional Ranges Using UAS", *Advances in Radio Science*, vol. 17, pp. 1–10, DOI: 10.5194/ars-17-1-2019.

SELEX Sistemi Integrati (2005), *Operations and Maintenance Manual - Model 1150 Doppler VHF Omnirange (DVOR)*, No. 571150-0002 Rev G April 2003, Overland Park, KS, USA.

Selvan, K. T. and R. Janaswamy (2017), "Fraunhofer and Fresnel Distances: Unified derivation for aperture antennas", *IEEE Antennas and Propagation Magazine*, vol. 59, no. 4, pp. 12–15, DOI: 10.1109/MAP.2017.2706648.

Slater, D. (1991), *Near-Field Antenna Measurements*, First Edition, Norwood, MA, United States: Artech House.

Smith, G. S. (1997), *An Introduction to Classical Electromagnetic Radiation*, First Edition, Cambridge, United Kingdom: Cambridge University Press.

Sommer, D., A. S. C. R. Irigireddy, J. Parkhurst, K. Pepin, and E. R. Nastrucci (2020), "UAV-Based Measuring System for Terrestrial Navigation and Landing Aid Signals", *AIAA/IEEE 39th Digital Avionics Systems Conference (DASC)*, pp. 1–7, DOI: 10.1109/DASC50938.2020.9256447.

Stahl, P., T. Seren, C. Rößler, and M. Hornung (2018), "Development and Performance Comparison of Optimized Electric Fixed-Wing VTOL UAV Configurations", *31st Congress of the International Council of the Aeronautical Sciences*.

Steiner, H.-J. and T. Fritzel (1993), "Concept and Design of a Cylindrical Outdoor Near-Field Test Range for High Precision RF-Measurements", *15th Annual Symposium of the Antenna Measurement Techniques Association (AMTA)* (Dallas, Texas).

Steiner, H.-J., T. Fritzel, A. Geise, C. Schmidt, and M. Paquay (2015), "First Results of Innovative Mobile Near-field Antenna Measurement System for Extreme Large DUTs", *9th European Conference on Antennas and Propagation (EuCAP)*, pp. 1–5.

Steiner, H.-J., T. Fritzel, J. Habersack, T. Jakob, A. McCormick, and J. R. Holloway (1994), "Qualified and High Performance Test Results of the Cylindrical Outdoor Near-Field Test Range", *16th Annual Symposium of the Antenna Measurement Techniques Association (AMTA)* (Long Beach, California).

Teledyne LeCroy (2021), *WaveMaster 8 Zi-B*, URL: https://teledynelecroy.com/oscilloscope/wavemaster-sda-dda-8-zi-b-oscilloscopes/wavemaster-808zi-b (visited on Sept. 12, 2022).

Teng, E., F. Mokaya, J. D. Falcao, P. Zhang, C. R. Dominguez, and B. Iannucci (2015), "Aerial Sensing and Characterization of Three-Dimensional RF Fields", *2nd International Workshop on Robotic Sensor Networks*, Seattle, Washington, USA, pp. 1–6.

Torvik, B., K. E. Olsen, and H. Griffiths (2016), "Classification of Birds and UAVs Based on Radar Polarimetry", *IEEE Geoscience and Remote Sensing Letters*, vol. 13, no. 9, pp. 1305–1309, DOI: 10.1109/LGRS.2016.2582538.

u-blox (2021a), *NEO-M8 - Datasheet, u-blox M8 Concurrent GNSS Modules*, UBX-15031086, version R11.

u-blox (2021b), *ZED-F9P-04B - Datasheet, u-blox F9 high precision GNSS module*, UBX-21044850, version R01.

u-blox (2022), *ZED-F9P module*, URL: https://www.u-blox.com/en/product/zed-f9p-module (visited on Feb. 3, 2022).

Valavanis, K. P. and G. J. Vachtsevanos, eds. (2015), *Handbook of Unmanned Aerial Vehicles*, First Edition, Dordrecht: Springer Science+Business Media, DOI: 10.1007/978-90-481-9707-1.

ViaLiteHD (2020), *RF Fibre Optic Link*, URL: https://www.vialite.com/wp-content/uploads/2017/10/ViaLiteHD-RF-Link-Handbook-HRx-HB-7.pdf (visited on Feb. 12, 2022).

Vincenty, T. (1975), "Direct and Inverse Solutions of Geodesics on the Ellipsoid with Application of Nested Equations", *Survey Review*, vol. XXIII (176).

Virone, G., A. M. Lingua, M. Piras, A. Cina, F. Perini, J. Monari, F. Paonessa, O. A. Peverini, G. Addamo, and R. Tascone (2014), "Antenna Pattern Verification System Based on a Micro Unmanned Aerial Vehicle (UAV)", *IEEE Antennas and Wireless Propagation Letters*, vol. 13, pp. 169–172, DOI: 10.1109/LAWP.2014.2298250.

Virone, G., F. Paonessa, M. Lumia, L. Ciorba, G. Addamo, P. Bolli, and O. A. Peverini (2021), "Effect of Conductive Propellers on VHF UAV-based Antenna Measurements: Simulated Results", *15th European Conference on Antennas and Propagation (EuCAP)*, Düsseldorf, Germany, pp. 1–4, DOI: 10.23919/EuCAP51087.2021.9411266.

Walendziuk, W., D. Oldziej, and M. Slowik (2020), "Power Supply System Analysis for Tethered Drones Application", *International Conference Mechatronic Systems and Materials (MSM)*, pp. 1–6, DOI: 10.1109/MSM49833.2020.9202196.

Wit, J. J. M. de, R. I. A. Harmanny, and G. Prémel-Cabic (2012), "Micro-Doppler Analysis of Small UAVs", *9th European Radar Conference*, pp. 210–213.

Yaghjian, A. D. (1975), *Upper-Bound Errors in Far-Field Antenna Parameters Determined From Planar Near-Field Measurements, Part 1: Analysis*, tech. rep., National Bureau of Standards.

Yinusa, K. A. and T. F. Eibert (2013), "A Multi-Probe Antenna Measurement Technique With Echo Suppression Capability", *IEEE Transactions on Antennas and Propagation*, vol. 61, no. 10, pp. 5008–5016, DOI: 10.1109/TAP.2013.2271495.

Zhao, Y. and Y. Su (2020), "The Extraction of Micro-Doppler Signal With EMD Algorithm for Radar-Based Small UAVs' Detection", *IEEE Transactions on Instrumentation and Measurement*, vol. 69, no. 3, pp. 929–940, DOI: 10.1109/TIM.2019.2905751.

Zikou, L., C. Papachristos, and A. Tzes (2015), "The Power-over-Tether System For Powering Small UAVs: Tethering-line Tension Control Synthesis", *23rd Mediterranean Conference on Control and Automation (MED)*, pp. 681–687, DOI: 10.1109/MED.2015.7158825.

Zogg, J.-M. (2011), *GPS und GNSS: Grundlagen der Ortung und Navigation mit Satelliten*, u-blox.

Publications of the Author

Faul, F. T., J. Kornprobst, T. Fritzel, H.-J. Steiner, R. Strauss, A. Weiss, R. Geise, and T. F. Eibert (2018), "A Concept Study of Near-Field Measurements and Corresponding Field Transformations of the Modulated Fields of Air Navigation Systems", *Kleinheubacher Tagung*, Miltenberg, Germany.

Faul, F. T., J. Kornprobst, T. Fritzel, H.-J. Steiner, R. Strauß, A. Weiß, R. Geise, and T. F. Eibert (2019a), "Near-field Measurement of Continuously Modulated Fields Employing the Time-harmonic Near- to Far-field Transformation", *Advances in Radio Science*, vol. 17, pp. 83–89, DOI: 10.5194/ars-17-83-2019.

Faul, F. T., H.-J. Steiner, and T. F. Eibert (2019b), "Near-Field Antenna Measurements with Manual Collection of the Measurement Samples", *Kleinheubacher Tagung*, Miltenberg, Germany.

Geise, R., A. Weiss, T. Fritzel, R. Strauß, F. T. Faul, and T. F. Eibert (2019a), "Interference Measurements of a High Power Cable-Bound Unmanned Aerial Vehicle", *13th European Conference on Antennas and Propagation (EuCAP)*.

Geise, R., A. Weiss, B. Neubauer, T. Fritzel, R. Strauss, H. Steiner, F. Faul, T. Eibert, and J. Honda (2019b), "Nearfield Inspection of Navigation Systems with UAVs – First Results from the NAVANT Project", *EIWAC - 6th ENRI International Workshop on ATM/CNS*.

Faul, F. T., H.-J. Steiner, and T. F. Eibert (2020), "Near-Field Antenna Measurements with Manual Collection of the Measurement Samples", *Advances in Radio Science*, vol. 18, pp. 17–22, DOI: 10.5194/ars-18-17-2020.

Weiß, A., R. Geise, B. Neubauer, F. Faul, T. Eibert, T. Fritzel, H. Steiner, and R. Strauß (2020), "RF-Signal Receiver for UAV-Based Characterisation of Aeronautical Navigation Systems", *14th European Conference on Antennas and Propagation (EuCAP)*, pp. 1–5, DOI: 10.23919/EuCAP48036.2020.9136061.

Faul, F. T., J. Daubmeier, and T. F. Eibert (2021a), "Short-Time Measurement and Transformation of Continuously Modulated Time-Harmonic Fields", *Kleinheubacher Tagung*, Miltenberg, Germany, DOI: 10.23919/IEEECONF54431.2021.9598410.

Faul, F. T. and T. F. Eibert (2021a), "Errors and Prerequisites of the Short-Time Measurement and Transformation of Continuously Modulated Fields", *43rd Annual Symposium of the Antenna Measurement Techniques Association (AMTA)*, DOI: 10.23919/AMTA52830.2021.9620725.

Faul, F. T. and T. F. Eibert (2021b), "Flight Path Planning Using Graph Theory in UAV-based Antenna Measurements", *XXXIV URSI General Assembly and Scientific Symposium (URSI GASS)*, Rome, Italy.

Faul, F. T. and T. F. Eibert (2021c), "Setup and Error Analysis of a Fully Coherent UAV-based Near-Field Measurement System", *15th European Conference on Antennas and Propagation (EuCAP)*, Düsseldorf, Germany, pp. 1–4, DOI: 10.23919/EuCAP51087.2021.9411307.

Faul, F. T., D. Korthauer, and T. F. Eibert (2021b), "Impact of Rotor Blade Rotation of UAVs on Electromagnetic Field Measurements", *IEEE Transactions on Instrumentation and Measurement*, vol. 70, pp. 1–9, DOI: 10.1109/TIM.2021.3109354.

Faul, F. T., D. Korthauer, and T. F. Eibert (2021c), "Impact of the Rotor Blade Rotation of a UAV on an Installed Field Probing Antenna", *XXXIV URSI General Assembly and Scientific Symposium (URSI GASS)*, Rome, Italy, DOI: 10.23919/URSIGASS51995.2021.9560501.

Geise, R., A. Weiss, B. Neubauer, T. Fritzel, R. Strauß, H. Steiner, F. Faul, T. Eibert, and J. Honda (2021), "Nearfield Inspection of Navigation Systems with UAVs — First Results from the NAVANT Project", *Air Traffic Management and Systems IV*, ed. by Electronic Navigation Research Institute, Singapore: Springer Singapore, pp. 337–351, DOI: 10.1007/978-981-33-4669-7_20.

Faul, F. T. and T. F. Eibert (2022a), "Coherent Near-Field Measurements Using Unmanned Aerial Vehicles", *16th European Conference on Antennas and Propagation (EuCAP); AMTA Scientific Workshop: Expanding the Limits - Antenna Metrology Using UAVs*, Madrid, Spain.

Faul, F. T. and T. F. Eibert (2022b), "Error Analysis of UAV-based Near-Field Antenna Measurements", *United States National Committee of URSI National Radio Science Meeting (USNC-URSI NRSM)*, Boulder, Colorado, USA.

Punzet, S., F. T. Faul, T. Mittereder, C. Oettl, M. Ganser, M. Häusler, and T. F. Eibert (2022), "Fully Coherent UAV-based Near-Field Measurement and Transformation of the S67-15m Ground Station Antenna at the German Space Operations Center in Weilheim", *16th European Conference on Antennas and Propagation (EuCAP)*, Madrid, Spain, pp. 1–5, DOI: 10.23919/EuCAP53622.2022.9769018.

Eibert, T. F., S. Punzet, T. Mittereder, F. T. Faul, and A. H. Paulus (2023), "UAV-Based Near-Field Measurements at a Doppler Very High Frequency Omnidirectional Radio Range", *17th European Conference on Antennas and Propagation (EuCAP)*, Florence, Italy, pp. 1–5, DOI: 10.23919/EuCAP57121.2023.10133603.

Faul, F. T., J. Daubmeier, and T. F. Eibert (2023), "Measurement and Transformation of Continuously Modulated Fields Using a Short-Time Measurement Approach", *Advances in Radio Science*, vol. 20, pp. 9–15, DOI: 10.5194/ars-20-9-2023.

Supervised Student Projects

Bouazizi, Amir (2019), “Darstellung und Auswertung des Flugpfades einer Drohne”, Bachelor’s Thesis, Munich, Germany: Technical University of Munich.

Korthauer, Daniel (2019), “Investigation on the Precision of GPS Receivers and the Calculation of Heading”, Bachelor’s Thesis, Munich, Germany: Technical University of Munich.

Mitterer, Christoph (2019), “Neukonzeption des Versuchs zur Messung der elektromagnetischen Umweltverträglichkeit im Hochfrequenztechnik Praktikum”, Bachelor’s Thesis, Munich, Germany: Technical University of Munich.

Muhr, Florian (2019), “Influence of a Hexacopter on the Far-Field of a Probe Antenna”, Bachelor’s Thesis, Munich, Germany: Technical University of Munich.

Daubmeier, Jana (2021), “Verification of the Short-Time Measurement Approach for Continuously Modulated Fields”, Master’s Thesis, Munich, Germany: Technical University of Munich.

Peychev, Dimitar (2021), “Antenna Design for Drone-Borne Near Field Measurement of VOR Infrastructure”, Master’s Thesis, Munich, Germany: Technical University of Munich.

Korthauer, Daniel (2022), “Automation and Characterization of an EMC-Measurement Chamber”, Forschungspraxis, Munich, Germany: Technical University of Munich.